Application of a Convolutional Neural Network (CNN) for Droplet Detection in an Aeroengine Bearing Chamber

Katrina Farbrother

Thesis submitted to The University of Nottingham
for the degree of Doctor of Philosophy

September, 2023

Abstract

Global efforts to reduce emissions mean that there is a a great need for aeroengine manufacturers to develop more efficient designs. Improvements to efficiency require rotating parts to be able to operate in a higher temperature environment. Therefore, better design capability is needed for improvement of the cooling system. A greater understanding of engine transmission systems is essential to achieving this.

Concentric highly rotating shafts run down the centre of an aeroengine. Bearings support these rotating shafts and are key elements with respect to lubrication and cooling requirements because of high rotational speeds and a high temperature environment. The bearings are housed in bearing chambers which are supplied with oil for cooling and lubrication via a continuous feed. Sealing airflow prevents oil from escaping the bearing chamber, creating a complex two-phase flow environment. Oil passes through the bearing and is shed into the bearing chamber before being scavenged and recirculated around the oil system.

Heat and oil management in a bearing chamber is highly dependent on understanding where the oil is and what form it is in (film, droplets etc.). Design capability can be improved with a better understanding of two-phase flow behaviour and also through the improved modelling capability this facilitates.

The work presented in this thesis investigates oil shedding from a large civil aeroengine High Pressure (HP) location bearing. Oil is supplied to the bearing via under race feeds and passes through the bearing, forming droplets, ligaments and/or sheets as it is ejected from the bearing and bearing cage. An oil film forms on the bearing housing and passes over the shedding edge into the bearing chamber. More droplet generation occurs from breakup of the oil film that separates from the front face (the vertical surface on the static outer race) at this point. This work looks at oil passing over the shedding edge between the bearing housing and the front face. Two strands of work are presented in this thesis. In the first an AI approach to detecting and characterising shedding oil is developed, and in the second the main focus is investigating the effect of

operating conditions on droplet diameter and speed, as well as qualitative discussion of other features observed.

The specially designed Bearing Shedding Rig (BSR) at the University of Nottingham has visual access to a large civil aeroengine HP location bearing, allowing high speed imaging to be performed for investigation of two phase flow behaviour. Operating speed, oil flow rate and applied axial load can be varied on the BSR to investigate their effect on droplet generation. In this work, high-speed imaging is performed on the co-current (where shear force and gravity act in the same direction) and counter-current (where shear force and gravity act opposite directions) positions in the bearing chamber. Thousands of images are obtained for each operating condition meaning an automated technique to extract data is essential.

The work presented in this thesis demonstrates a significant improvement to the understanding of two phase flow in an aeroengine bearing chamber. Qualitative analysis of images shows a change in wetted surface area of the front face with increasing operating speed and/or higher oil flow rate. Increasing either of these variables correlates to increased production of ligaments, complex three-dimensional structures and higher number of droplets in the bearing chamber. Four behavioural regimes have been identified for conditions investigated at speeds up to 7000 rpm on the co-current side of the bearing chamber. They are defined as follows:

- **Regime 1:** Droplets are present and there is no/minimal film on the front face.
- **Regime 2:** Droplets are present and a small film coverage on front face (bubbles are contained in the film).
- **Regime 3:** Droplets are present and there is a large film coverage (film is thicker and more wavy than in regime 2).
- **Regime 4:** All features of regime 3 are present, in addition to large complex oil structures passing through the bearing chamber (breakup of these structures is often observed).

Increasing operating speed and oil flow rate both contribute to change in regime but axial load has negligible observed effect.

An analysis tool for droplet detection in a visually complex aeroengine representative environment has been delivered in this work. A Convolutional Neural Network (CNN) has been trained for droplet detection in the BSR, where simpler methods such as implementation of circle detection perform poorly. The accuracy of detection by

this approach has been validated against manually labelled data, meaning that automated processing is possible for large quantities of data - on a scale that would not be feasible using a manual approach. The CNN produces accurate droplet diameter and position information, allowing calculation of droplet speed when an image sequence is processed. In this work droplet diameter and speed data has been obtained on the co-current and counter-current sides of the bearing chamber for speeds between 1000 rpm and 12 000 rpm providing aeroengine relevant data for future design and validation of existing and new computational models, facilitating improved design capabilities. The maximum surface shaft speed reached in this operating range is approximately $150\,\mathrm{m\,s^{-1}}$. The shaft rotation accelerates air in the bearing chamber, however droplet speeds are expected to be significantly lower than the surface shaft speed since the majority of droplets are shed from a static surface.

Detailed analysis of a single test condition (7000 rpm, $5.2\,\mathrm{l\,min^{-1}}$ oil flow rate and 20 kN axial load) is performed.The modal droplet diameter was found to be between 0.6 mm and 0.8 mm and only a very small proportion of droplets above 3.0 mm diameter were observed. Two peaks in the droplet speed probability distribution were identified at this test point suggesting there may be multiple mechanisms of droplet generation in the bearing chamber. The lower speed peak (at $1\,\mathrm{m\,s^{-1}}$) consists of generally smaller diameter droplets compared to the higher speed peak (at $3\,\mathrm{m\,s^{-1}}$) which is made up of a greater range of droplet diameters.

Trends in droplet properties were investigated for changes in operating speed, applied axial load and oil flow rate supplied to the bearing. It was determined that the droplet diameter distribution can be well represented by Rosin-Rammler fit. The idea was proposed by Nicoli [1] for computational modelling but had not been investigated at all in experimental work prior to this. This provides the ability to describe the distribution using only the three Rosin-Rammler parameters. Inspection of the variables in the Rosin-Rammler distribution for different operating conditions aid analysis of the effect of changing conditions on droplet diameter distribution and provide a representative diameter distribution for design purposes or validation of computational models. The spread of the distribution does not vary significantly or with an identified trend in relation to operating conditions, meaning that a similarly shaped diameter distribution is seen at all operating conditions investigated. The position of modal droplet diameter is found to be constant for speeds up to 7000 rpm at 0.8 mm on the co-current side of the bearing chamber and 0.7 mm on the 9 o'clock side. Above 7000 rpm droplet diameter increases with operating speed to approximately 1.0 mm on both sides of the bearing chamber. No significant effect on droplet diameter is observed with change in either

oil flow rate supplied to the bearing chamber or applied axial load.

Droplet speeds are generally fairly similar on both sides of the bearing chamber for each operating speed, indicating that rotating air speed is dominant over the effects of gravity, but tend to higher speeds at the co-current position where gravity and shear act in the same direction - approximately $0.5\,\mathrm{m\,s^{-1}}$ faster than on the 9 o'clock side where shear and gravity act in opposite directions. No correlation is identified between droplet speed and operating speed, but it was noted that at 1000 rpm droplets observed were in the order of $1\,\mathrm{m\,s^{-1}}$ slower than at other operating speeds. Variation in applied axial load did not affect droplet speed. However, lower droplet speeds are seen at higher oil flow rates.

List of Publications

Katrina Farbrother, Paloma Paleo Cageao, Kathy Johnson, and Stephen Ambrose. Investigation of Droplet Shedding in an Aeroengine Bearing Chamber Using Convolutional Neural Networks. Proceedings of the ASME Turbo Expo 2022: Turbomachinery Technical Conference and Exposition. Volume 8A. Rotterdam, Netherlands. June 13–17, 2022. V08AT22A013. doi: 10.1115/GT2022-82275.

Acknowledgements

I would like to thank my supervisors Kathy Johnson and Stephen Ambrose for their guidance throughout the PhD both through supervision meetings and additional support with technical work and motivation – especially throughout the uncertainty of the pandemic with all its associated disruption to routines and ways of working. I would also like to thank my internal examiner Donald Giddings for the feedback, genuine enthusiasm and interest in my work in each annual review meeting.

I am very grateful for the opportunity I have had to further my studies at the University of Nottingham through this PhD. In this time I have had the chance to learn about Convolutional Neural Networks (CNNs) and their implementation for challenging experimental images – an area was not originally planned for the PhD but has been of great interest. None of this would have been possible without use of the Bearing Shedding Rig (BSR), designed and built for Rolls-Royce funded projects, and the various funding sources that contributed towards this PhD: the EPSRC, G2TRC and the University of Nottingham.

Thanks also go to Graham Johnson and the rest of the G2TRC technical team for training and support with the BSR used for experimental work in this PhD, as well as Paloma Paleo Cageao, Michael Walsh and Avick Sinha for their help with high-speed imaging and lighting, and running of the test rig. I would also like to thank all members of the G2TRC for making the research group such a welcoming and supportive place. Last but not least, I would like to thank my friends and family for being understanding and encouraging throughout the entirety of the PhD and helping me to keep motivated through challenging parts of the process.

Nomenclature

Symbols

Latin Symbols

Symbol	*Meaning*	*Unit*
A	Area	m^2
d	Droplet diameter	mm
D	Disk diameter	m
f	Frequency of droplet production for one ligament	s^{-1}
h	Heat transfer coefficient	-
k	Constant in the Rosin-Rammler equation	-
K'	Constant	-
$\dot{m}$	Mass flow rate	$kg\,s^{-1}$
n	Rotational speed	s^{-1}
N	Number of ligaments	-
Q	Volumetric oil flow rate	$m^3\,s^{-1}$
Q'	Non-dimensional volume flow rate	-
r	Radius	m
r_s	Radius of bearing slot	m
SMD	Sauter Mean Diameter, $SMD = \frac{\mu d^3}{\mu d^2}$	mm
$\overline{T}$	Mean temperature	K
t	Film thickness	m
v	Droplet speed	$m\,s^{-1}$
$\dot{V}$	Volume flow rate	$m^3\,s^{-1}$

Greek Symbols

Symbol	*Meaning*	*Unit*
β	Scaling factor in the Rosin-Rammler equation	-
Γ	Oil flowrate/circumference of static, $\Gamma = Q/2\pi r_s$	$\mathrm{m^2\,s^{-1}}$
μ	Dynamic viscosity	$\mathrm{kg\,m^{-1}\,s^{-1}}$
ν	Kinematic viscosity	$\mathrm{m^2\,s^{-1}}$
ρ	Density	$\mathrm{kg\,m^{-3}}$
σ	Surface tension	$\mathrm{N\,m^{-1}}$
ϕ	Location parameter in the Rosin-Rammler equation	-
ω	Shaft rotational speed	$\mathrm{rad\,s^{-1}}$

Subscripts

Symbol	*Meaning*
a	Air
ch	Chamber
o	Oil
s	Shaft
t	Transient
U	Circumference
1	Inner cylinder
2	Outer cylinder

Non-dimensional Groups

Liquid Reynolds number

$$Re_{liq} = \frac{\Gamma}{\nu_{oil}} \tag{0.1}$$

Non-dimensional droplet diameter

$$d^* = \frac{d}{t} \tag{0.2}$$

Non-dimensional droplet speed

$$v^* = \frac{v}{r\omega} \tag{0.3}$$

Ohnesorge number

$$Oh = \frac{\mu}{\sqrt{(d\sigma\rho)}} \tag{0.4}$$

Reynolds number

$$Re = \frac{du\rho}{\mu} \tag{0.5}$$

Rotational Reynolds number

$$Re_\omega = \frac{\omega r^2}{\nu_{air}} \tag{0.6}$$

Taylor number

$$Ta = \frac{2(\frac{r_1}{r_2})^2(r_2 - r_1)^4}{1 - (\frac{r_1}{r_2})^2}\left(\frac{\omega_1}{\nu}\right)^2 \tag{0.7}$$

Splashing parameter

$$K = WeOh^{-0.4} \tag{0.8}$$

Weber number

$$We = \frac{\rho V^2 d}{\sigma} \tag{0.9}$$

Abbreviations

Abbreviation	*Meaning*
BSR	Bearing Shedding Rig
CNN	Convolutional Neural Network
FOHE	Fuel-Oil Heat Exchanger
G2TRC	Gas Turbine and Transmissions Research Centre
HP	High Pressure
HS	High-Speed
LDA	Laser Doppler Anemometry
NN	Neural Network
PDPA	Phase Doppler Particle Analyser
PIV	Particle Image Velocimetry
P1	12 o'clock position in the BSR
P2	3 o'clock position in the BSR
P3	6 o'clock position in the BSR
P4	9 o'clock position in the BSR
ROI	Region of Interest
TDC	Top Dead Centre

Contents

1 Introduction **1**

1.1 Background 1

1.2 Aeroengine Bearings 3

1.3 Oil Systems 3

1.4 Oil Flow Phenomena 4

1.5 Aims and Objectives 7

1.6 Thesis Chapter Outline 8

2 Literature Review **11**

2.1 Airflow in a Bearing Chamber 11

2.2 Droplet Generation in the Bearing Chamber 14

2.3 Droplets in a Shear Gas Flow 16

2.3.1 Droplet Deflection 16

2.3.2 Film Formation 16

2.4 Shear-Driven Films 18

2.4.1 Film Thickness 18

2.4.2 Flow Regimes 23

2.5 Droplet-Film Impingement 26

2.6 Film Separation and Disintegration 29

2.7 Droplet/Ligament Disintegration 33

2.8 Residence Time 37

2.9 Automated Droplet Detection and Tracking 39

2.9.1 Droplet Detection Using Conventional Methods in the Literature 39

2.9.2 Droplet Detection Using a Convolutional Neural Network (CNN) 40
2.9.3 Droplet Tracking . . . 41
2.10 Summary of Literature . . . 42

3 Experimental Methodology 44
3.1 Bearing Shedding Rig (BSR) . . . 44
3.1.1 Overview . . . 44
3.1.2 Drive . . . 47
3.1.3 Loading . . . 47
3.1.4 Bearing Chambers . . . 47
3.1.5 Oil System . . . 48
3.2 High-Speed Imaging . . . 50
3.3 Experimental Data Collection . . . 51
3.4 Experimental Methodology Summary . . . 53

4 Droplet Detection using a Conventional Method compared to a Convolutional Neural Network (CNN) 54
4.1 Conventional Detection . . . 54
4.2 Convolutional Neural Network (CNN) Theory . . . 57
4.3 Droplet Detection Methodology . . . 63
4.3.1 CNN Droplet Detection Process Overview . . . 63
4.3.2 Image Pre-Processing . . . 64
4.3.3 Transfer Learning From a Pre-Trained CNN . . . 64
4.3.4 Labelled Data for Training the CNN . . . 67
4.3.5 Selection of Potential Pre-Trained CNNs . . . 68
4.3.6 CNN Implementation and Data Extraction . . . 69
4.3.7 Droplet Tracking . . . 70
4.3.8 Calculation and Quantitative Analysis . . . 70
4.4 Assessment of Droplet Detection CNNs . . . 71
4.4.1 Comparison of Detection Data to Ground Truth . . . 71
4.4.2 Metrics . . . 75

4.4.3 CNN Selection 82
4.4.4 Validity and Applicability of Method 84
4.5 Droplet Detection Method Summary 85

5 Experimental Results and Discussion **86**
5.1 Qualitative Analysis 87
5.1.1 Change in Operating Speed 87
5.1.2 Change in Oil Flow Rate 87
5.1.3 Change in Axial Load 88
5.1.4 Shedding Regimes 88
5.2 Results From a Single Operating Condition 98
5.3 Diameter Distribution 102
5.3.1 Effect of Operating Speed on Diameter Distribution 103
5.3.2 Effect of Oil Flow Rate on Diameter Distribution 116
5.3.3 Effect of Axial Load on Diameter Distribution 122
5.3.4 Diameter Distribution Summary 123
5.4 Droplet Speed Distribution 127
5.4.1 Effect of Operating Speed on Droplet Speed Distribution 129
5.4.2 Effect of Oil Flow Rate on Droplet Speed Distribution 139
5.4.3 Effect of Axial Load on Droplet Speed Distribution 139
5.5 Experimental Results Summary 142

6 Conclusions and Future Work **147**
6.1 Main Findings From the Thesis 147
6.1.1 Qualitative Work 147
6.1.2 Development of the Convolutional Neural Network (CNN) . . . 148
6.1.3 Quantitative Work 149
6.2 Contribution to Knowledge 150
6.3 Recommendations for Future Work 151

Appendices **163**

A Effect of Operating Speed on Diameter Distribution for the AERIS Dataset 164

B Droplet Speed Distribution 173

CHAPTER 1

Introduction

This chapter introduces the work presented in this thesis, why it is needed and what this work intends to achieve. The importance of improved understanding of two phase flow in an aeroengine bearing chamber for limiting the environmental impact of civil air travel is discussed and the reader is introduced to the location and function of the bearing chamber and oil system. Finally, the aims and objectives are presented followed by the thesis chapter outline.

1.1 Background

The COVID-19 pandemic had a dramatic impact on civil aviation in 2020, returning the number of passenger arrival and departures from UK airports to levels not experienced since 1986 [2]. However, data shown in Fig. 1.1 indicates that the industry is rapidly recovering towards pre-pandemic levels and Shparberg and Lange [3] forecast a 3.6% annual increase in passenger traffic (CAGR - Compound Annual Growth Rate) between 2019 and 2041, meaning that the environmental impact of civil aviation is expected to increase significantly. Despite continual improvement in aeroengine specific fuel consumption, aviation in 2010 contributed to 2% of global CO_2 emissions and is predicted to increase to 5% by 2040 [4]. Increasing trends in civil air travel mean there is a significant global interest in reducing the environmental impact of the industry. However substantial improvement is needed per passenger kilometre if net global CO_2 emissions from civil aviation is to be reduced. Flightpath 2050 [5] outlines specific targets for the reduction of emissions per passenger kilometre as compared to typical new aircraft in 2000: 75% reduction in CO_2 emissions and a 90% reduction in NO_x emissions. This is a major challenge for future aircraft design.

Reduced emissions can be achieved using alternative fuels, such as Hydrogen or SAF,

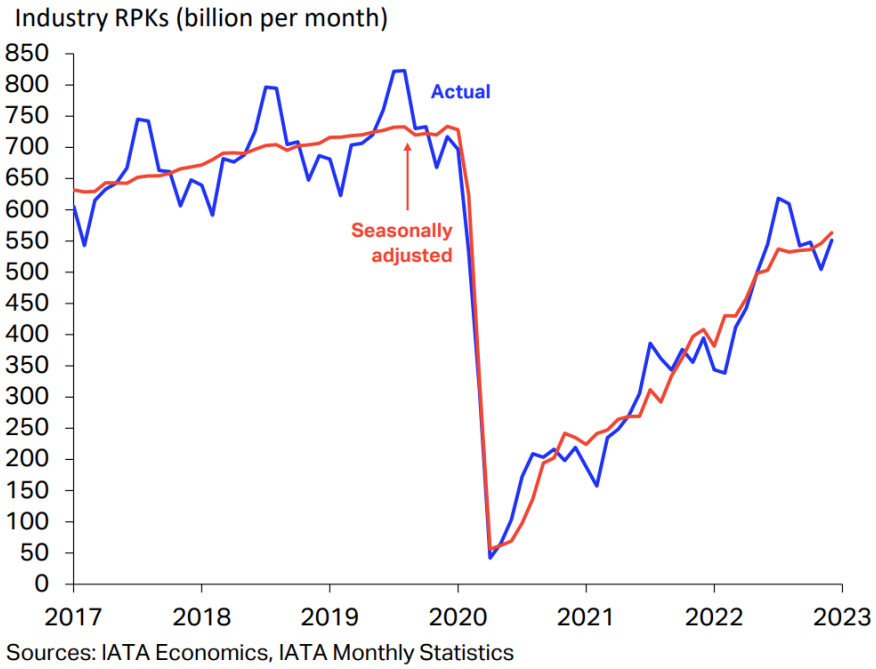


Figure 1.1: Global air passenger data based on revenue passenger-kilometers (RPKs) between 2017 and 2022 [6].

or with new engine designs that have higher propulsion and thermal efficiencies. The latter can be achieved by increasing the overall bypass ratio and the turbine rotor inlet temperature. There is therefore a need for aeroengines to operate under higher temperatures and with higher shaft speeds. A three-shaft aeroengine has low, intermediate and high pressure compressors on separate concentric shafts. These shafts are supported by bearings which must be capable of transmitting large loads in a highly rotating high temperature environment, meaning the bearings must be cooled and lubricated by a continuous oil supply. Changes to aeroengine design for greater efficiency require better design capability for improvement of the cooling system. A greater understanding of engine transmission systems is essential to designing a more effective cooling system.

The oil used to cool and lubricate the bearing degrades at high temperatures, meaning the oil must be replaced regularly. The maximum temperature experienced by the oil must be reduced to minimise degradation. This can be done by designing for high heat transfer within the oil leading to a more evenly distributed bulk oil temperature, while still providing adequate cooling and lubrication. Improved design capability, without the expense of engine testing, requires improved modelling capability. However, experimental work is needed to provide boundary conditions and validation data for Computational Fluid Dynamics (CFD) modelling of two phase flow in the bearing chamber.

1.2 Aeroengine Bearings

Bearings support the shafts in an aeroengine, providing very small rotational resistance. Ball bearings (also referred to as location bearings), unlike roller bearings, are able to transmit axial loads as well as radial loads and therefore provide axial location to the shaft. Typically one ball bearing and one or more roller bearings are used to support each shaft. The position of bearings in a typical three-shaft engine is shown in Fig. 1.2. Continuous high-speed operation of these bearings requires cooling and lubrication to prevent excessive wear and damage of parts. The majority of the oil supplied is used for cooling - only a small amount is required for lubrication. The oil system is described in detail in Section 1.3.

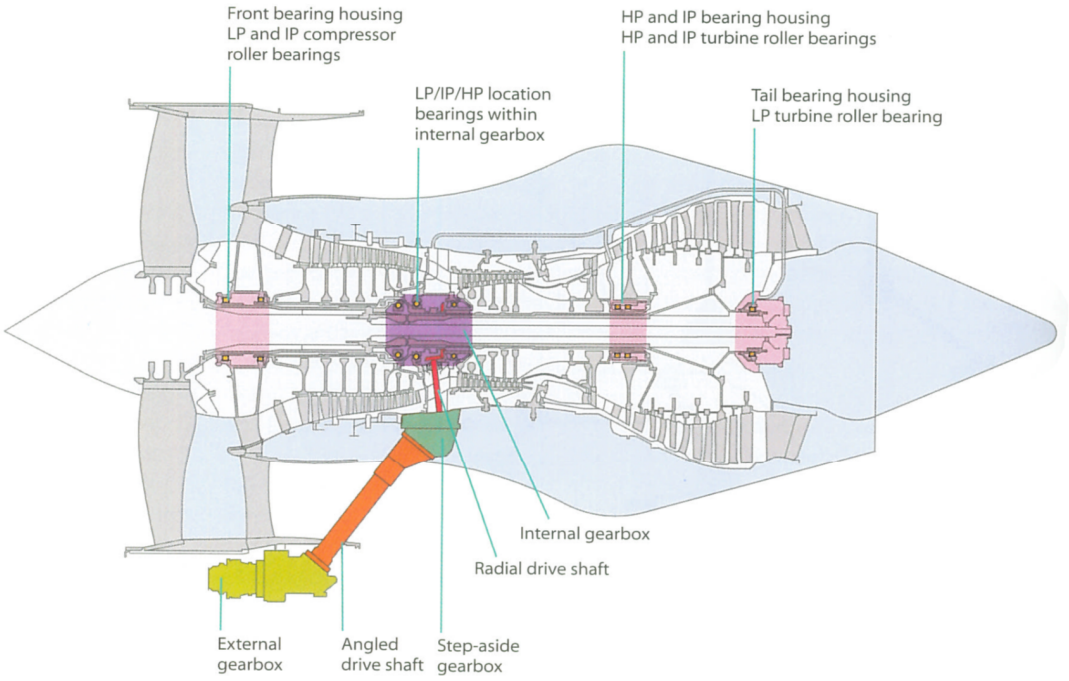


Figure 1.2: Position of bearing in a three-shaft engine [7].

1.3 Oil Systems

Oil is supplied to the mechanical transmission components for cooling, lubrication and corrosion protection. Bearings are one such component and exist in a high-temperature, highly rotating environment. Full flow oil systems are commonly used as they allow smaller pumps than would be needed for an alternative equivalent system such as a pressure relief valve system and are able to achieve an oil flow rate closer to optimum throughout the engine speed range [7]. A simplified schematic of a full flow oil system

is shown in Fig. 1.3.

The Gas Turbine and Transmissions Research Centre (G2TRC) at the University of Nottingham created a test facility representative of elements of an aeroengine bearing chamber - this is the Bearing Shedding Rig (BSR) shown diagrammatically in Fig. 1.4. Feed jets supply oil to the inner race and centrifugal force delivers oil via narrow channels to the front, middle and rear of the bearing. Heat is transferred from the bearing to the cool oil, which leaves the bearing in a complex manner via droplets, ligaments and sheets. These behaviours can be observed in Fig. 1.5. Sealing air enters through the labyrinth seals indicated in Fig. 1.3, preventing oil from escaping the bearing chamber. A vent at the top of the bearing chamber leads to a breather, which separates the oil from the air, exhausting the air and returning most of the oil to the tank. Large droplets are centrifuged by the swirl flow in the breather, while most smaller droplets are separated using a porous metallic foam. The majority of the oil leaves the bearing chamber by a scavenge at the bottom of the bearing chamber. The scavenge is designed to remove oil from the bearing chamber after only a small residence time in order to minimise the risk of coking and chemical decomposition of the oil.

Displacement pumps drive oil from the scavenge to the oil tank via a de-aerator, magnetic chip detector and filter. This removes entrained air as well as metal particles and dirt originating from transmission system that could otherwise cause damage, reducing the life of components in the transmission system. Oil leaves the tank and heat is exchanged with the fuel in the fuel oil heat exchanger in order to cool the oil and bring the fuel up to a higher temperature prior to combustion. A high-pressure feed delivers the cool oil to the bearings via an under-race feed, oil travels through the bearing, is collected by the scavenge and the cycle is repeated. The bearing is described in greater detail in Section 1.4 and Chapter 3.

1.4 Oil Flow Phenomena

Oil exhibits a highly complex behaviour within the bearing and bearing chamber, forming films, ligaments and droplets. An overview of these behaviours is presented here, and a more detailed discussion is given throughout Chapter 2. The Bearing Shedding Rig (BSR) at the University of Nottingham, described in Chapter 3, is used to investigate oil flow in the bearing chamber. The BSR has a large civil aeroengine HP location bearing to facilitate investigation of oil shedding. Oil outside of the bearing is indicated in blue in Figs. 1.4 and 1.5, where Fig. 1.5 shows both a schematic and optical imaging close the bearing in images taken from a test facility containing an aeroengine bear-

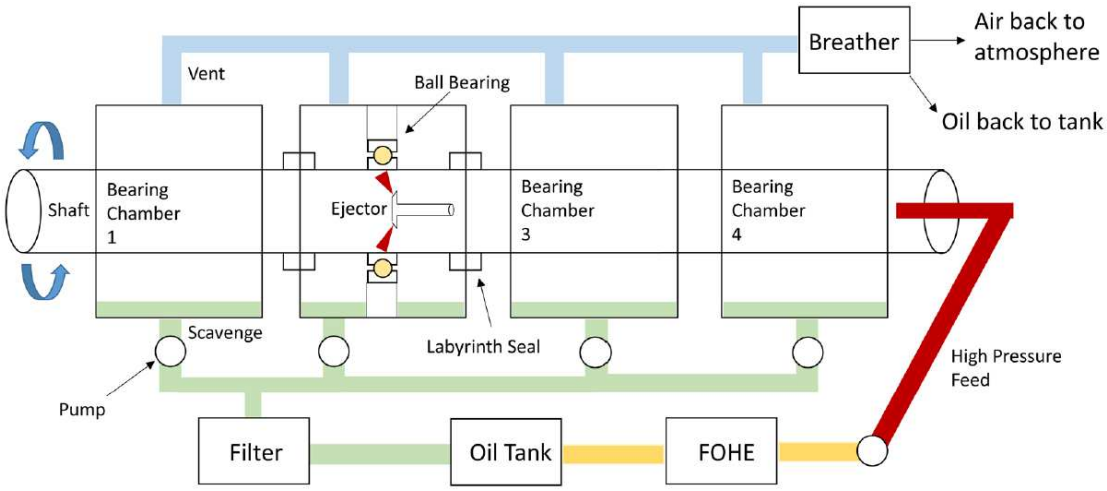


Figure 1.3: Schematic of a simplified full flow oil system. Note that the green, yellow, red and blue indicate the presence of oil [8].

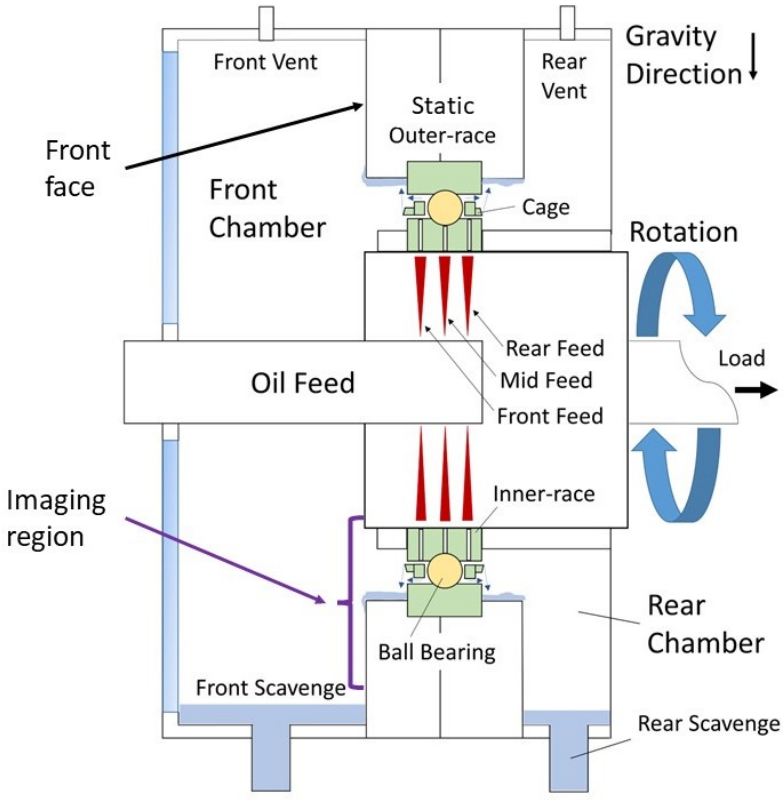


Figure 1.4: Schematic of bearing shedding rig working section (adapted from Hee [8]).

ing and simplified surrounding geometry. An oil film on the bearing housing, formed by oil leaving the bearing, is driven by a circumferential airflow. Optical images were taken by Hee [8] at circumferential positions of 0°, 90°, 180° and 270° from top dead centre (TDC) using the G2TRC bearing shedding rig described in detail in Section 3.1. Images Fig. 1.5c and Fig. 1.5d include images showing a radially ejected sheet at the bearing cage (labelled on the image as "Focus: 30 mm"). The ejected oil can be seen to impinge onto the moving film on the bearing housing and could generate splashing. At the shedding edge (at the front face of the bearing housing - labelled on the image as "Focus: 0 mm" in Fig. 1.5) the oil film can be seen to escape over the front face with a different flow behaviour at each combination of circumferential position and speed, generating droplets, ligaments and sheets. This difference is due to the change in the force balance acting on the oil due to gravity and shear. In Fig. 1.5a shows operation at 3000 rpm and 5000 rpm. Ligaments are clearly visible at 3000 rpm and held together by surface tension until breakup by Plateau-Rayleigh instability forms droplets. Increasing the speed to 5000 rpm increases the shear force and causes shear breakup to occur, generating a larger number of droplets. A clear difference in behaviour can also be seen for each circumferential position when comparing images in Fig. 1.5. The 3 o'clock position has a relatively smooth film passing over the shedding edge and remaining attached to the front face and a few droplets can be seen at a lesser radial position. These droplets are likely generated by either splashing (droplets from the bearing colliding with the film on the bearing housing) or by shear stripping. At the 6 o'clock position the radially falling film becomes significantly more wavy. At the 9 o'clock position more three-dimensional oil structures form at the shedding edge due to the opposing shear and gravitational forces causing there to be a falling film but also driving oil upwards. The three-dimensional structures are very prone to break-up and tend to generate large, slow moving droplets. Ligaments are observed at the shedding edge at the 12 o'clock position. These again are prone to break-up leading to droplet generation - these may also be seen entering the 3 o'clock imaging region.

Oil close to the bearing enters the bearing chamber past the front face in a complex manner which is yet to be fully investigated. Much of the same physics applies in the bearing chamber as that discussed for behaviour close to the bearing. An oil film forms on the outer bearing chamber wall and is affected by both gravity and a shearing airflow, and droplets may be carried by the airflow or may impinge on the film as before. The oil films on the bearing housing and bearing chamber wall have been previously investigated, but the transition of the oil from one region to the other has not been previously investigated, hence the need for this thesis. Having identified a need for improved heat and oil management capability in an aeroengine bearing chamber, the

specific aims and objectives are defined in Section 1.5.

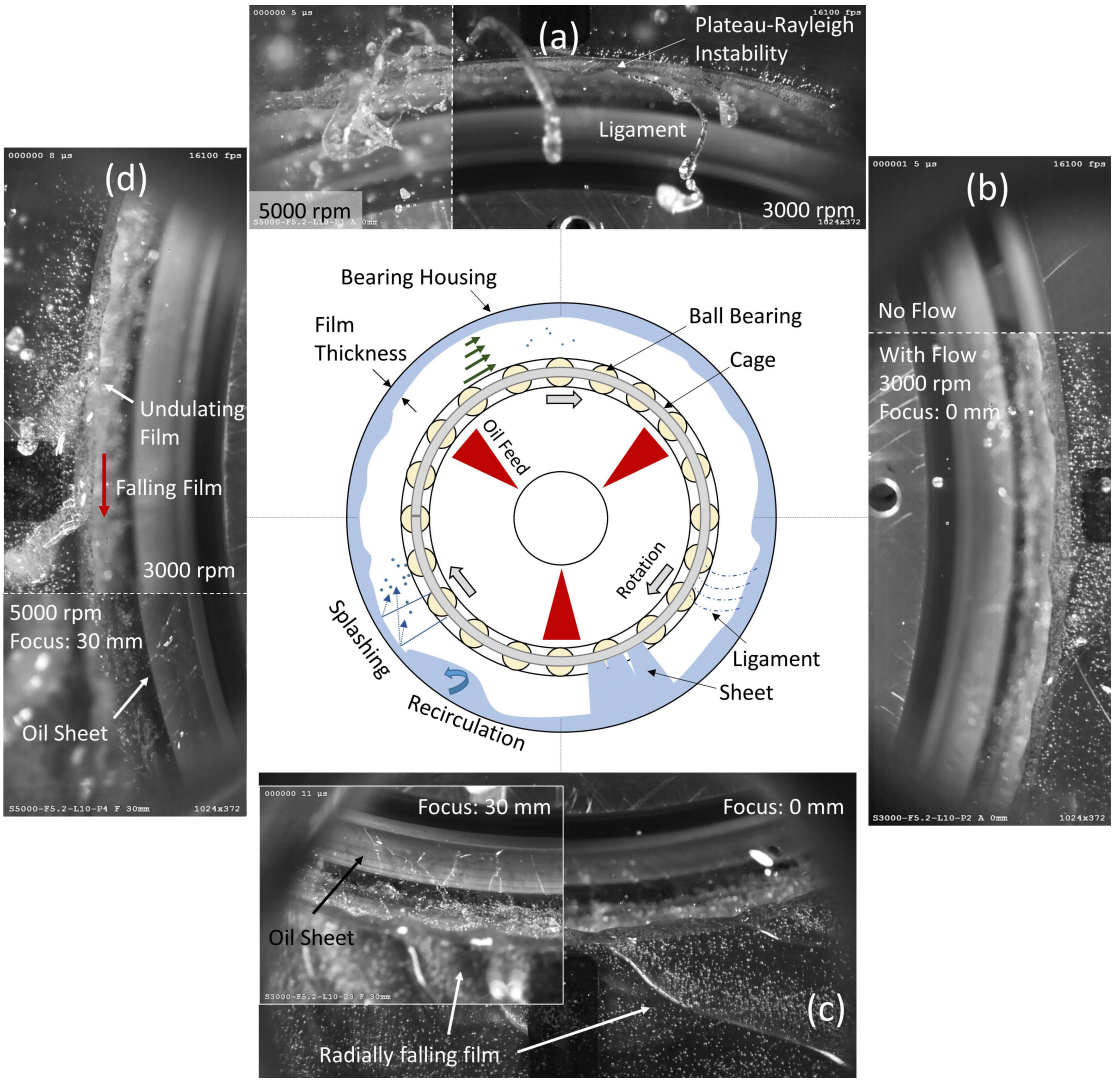


Figure 1.5: Flow phenomena close to an aeroengine bearing (adapted from Hee [8]).

1.5 Aims and Objectives

The aim is to improve heat and oil management for more efficient aeroengines through understanding of the oil shedding process in a ball bearing and to provide high quality validation data that supports improved modelling capability. The objectives of this research are:

1. To investigate the process of oil entering the front bearing chamber of the bearing shedding rig, including breakup and separation over the lip of the bearing housing, in order to characterise flow regimes and the effect of operational parameters.

2. To measure the diameter and velocity of droplets entering the bearing chamber over a range of operating conditions at different circumferential positions in order to provide validation data for computational modelling of oil behaviour passing over the shedding edge or to be used as an inlet condition in modelling the bearing chamber.
3. Identify key operating conditions and their influence on oil shedding.
4. To improve bearing chamber modelling capability beyond the current state of the art by providing a detailed and comprehensive set of validation data.

1.6 Thesis Chapter Outline

This section outlines the main topics of each chapter of the thesis.

Chapter 2: Literature Review The literature review summarises previous experimental studies with regard to how oil behaves in an aeroengine bearing chamber and identifies gaps in knowledge for further investigation. The two phase flow is highly complex with oil being present in a number of different forms (droplet, film, sheet, ligament, mist) and moving between these forms on its journey from entry to exit. Many elements of two phase flow behaviour relevant to an aeroengine bearing chamber have been previously investigated, generating a reasonable body of prior work that gives a level of understanding of likely behaviours. This literature review identifies areas where further work is required to advance current knowledge. Little is known about the mechanisms of oil shedding from an aeroengine ball bearing, leading to a weakness in design and computational modelling capability in this region.

Prior literature provides a reasonable understanding of single phase flow in the bearing chamber in addition to significant fundamental works considering two phase flow in simplified geometries, including droplet behaviour and film formation in a shear gas flow, shear driven films, droplet-film impingement and droplet generation by spinning discs and cups. However, injecting a liquid jet into a crossflow does not include a rotational component and spinning discs or spinning cups consider oil break up from the edge of a rotating surface rather than a static surface as in an aeroengine bearing chamber (or as in the Bearing Shedding Rig (BSR) used for experimental work in this project). Therefore, while the simplified experimental setups are similar enough to provide comparison and initial validation of modelling approaches, a difference in behaviour is expected in an aeroengine bearing chamber representative geometry.

A considerable gap in prior knowledge from the literature exists regarding droplet generation as oil enters a bearing chamber. This includes data regarding droplet diameter, speed, direction of travel and path taken through the bearing chamber. Experimental droplet data is highly valuable for improved understanding of two phase flow behaviour and for validation of existing and future computational modelling approaches.

Convolutional Neural Networks (CNNs) have been used for visually similar particle detection in the literature and are a promising method for accurate droplet detection from high-speed experimental images. A CNN is trained on a visually similar set of labelled data and is able to detect features in order to make an output prediction. In this thesis the output type is semantic segmentation, meaning that each pixel of the image is assigned either the classification of *droplet* or *not droplet*. Droplet data can be extracted from the CNN output for every image frame, giving position, speed and diameter information.

Chapter 3: Experimental Methodology This section provides details of the Bearing Shedding Rig (BSR), data acquisition through high-speed imaging and subsequent image processing. This includes high-speed camera and lighting set-up, as well as a description of the method for experimental high-speed image data collection Chapter 4 covers the approach used to extract numerical data from the high-speed images for quantitative analysis using automated droplet detection by use of a CNN. Chapter 5 goes on to present and discuss the experimental results obtained via this methodology.

Chapter 4: Droplet Detection using a Convolutional Neural Network (CNN) Chapter 4 details the implementation of the CNN detecting droplets in images taken from the BSR. The droplet detection CNN is trained using a manually labelled set of representative sample images from the BSR to perform complex feature recognition for droplet detection. Labelling an image requires manual identification of each droplet to produce a colour coded image that indicates the classification (*droplet* or *not droplet*) of each pixel - a time intensive process. The trained CNN uses semantic segmentation to produce an output mask (like the images labelled in training) to indicate the droplets detected per image. Droplet detection is achieved with a good level of accuracy, outperforming the conventional method used in prior work. The minimum feasible droplet diameter for detection is limited by spatial resolution of images at around four pixel diameter for this application - approximately 0.25 mm. Droplets larger than this threshold can be detected and tracked to give a good representation of true values. Therefore, the method for droplet detection and tracking developed in this project is considered

to be appropriate for experimental work of this type. The described methodology is applied to high speed images from the BSR and results are presented in Chapter 5.

Chapter 5: Experimental Results and Discussion Results from experimental work are presented for moderate and high speeds on the co-current and counter-current sides of the bearing chamber. Experimental results are obtained using the experimental methodology and processing techniques presented in Chapters 3 and 4, including qualitative and quantitative analysis of two phase flow behaviour in an aeroengine bearing chamber.

Qualitative analysis is performed to inspect the effect of changing operating speed, oil flow rate and axial load on oil behaviour on the 3 o'clock side of the bearing chamber. Four behavioural regimes have been identified and defined for conditions investigated at speeds up to 7000 rpm.

Detailed analysis of a single test point is discussed and droplet diameters obtained from CNN droplet detection are compared to true values to assess the level of agreement. Droplet diameter, speed and position information is also inspected and discussed for the sample operating condition.

Trends in droplet properties are investigated for changes in operating speed, applied axial load and oil flow rate supplied to the bearing. Additionally, the Rosin-Rammler fit is shown to provide a good representation of droplet diameter probability distribution both sides of the bearing chamber. Inspection of the variables in the Rosin-Rammler for different operating conditions aid analysis of the effect of changing conditions on droplet diameter distribution.

Chapter 6: Conclusions and Future Work The main findings and contribution to knowledge of this research are summarised and recommendations for future work are made.

CHAPTER 2

Literature Review

This chapter presents a review of existing literature surrounding experimental work relevant to single phase (Section 2.1) and two phase flow in an aeroengine bearing chamber (Sections 2.2 to 2.8) in addition to literature relevant to automated droplet detection in Section 2.9. Many prior experimental works covers fundamentals, rather than investigating a realistic bearing chamber.

2.1 Airflow in a Bearing Chamber

Airflow and gravity are the biggest influences on oil behaviour in a bearing chamber, therefore it is critical that their effects are fully understood. Bearing chambers must be sealed to prevent oil from escaping to the rest of the engine. This is done by applying a positive pressure across the small gap such that there is a small continuous inflow of high pressure air into the chambers. The air entering through the seals is supplied from one of the compressor stages and is therefore at very high temperature. Additionally, a shear airflow is generated close to the bearing and in the bearing chamber by the shaft rotation. This airflow creates a shear force at the air-oil interface, accelerating the oil film close to the bearing. The simplicity of single phase flow compared to two-phase flow, means that there is value in establishing a complete understanding of the airflow field in the bearing chamber before extending the problem to include the complex interactions between oil and air. This is the approach taken by Lee et al. [9], who performed experimental single phase flow investigations in a bearing chamber geometry using Particle Image Velocimetry (PIV) and were able to model the flow field with reasonable agreement to experimental data. Flow features within the bearing chamber were found to be highly dependent on chamber geometry and shaft rotation, highlighting the importance of physical bearing chamber design and influence of operating conditions.

Rotating Couette flow occurs in an annular flow region between two concentric cylinders as in Fig. 2.1. The flow is driven by the relative rotation of these cylinders and the tangential velocity component dominates the flow. A simplified bearing chamber geometry can be approximated as meeting this description, in that an annular gap exists between the bearing chamber wall, idealised as a static cylinder, and the highly rotating shaft. Taylor number indicates the stability of flow in an annulus between concentric cylinders with relative rotation. At critical Taylor number, steady viscous Couette flow becomes unstable and counter rotating toroidal vortices form due to a centrifugal-driven instability. The three-dimensional vortex pairs, commonly known as Taylor vortices, span the space between the inner cylinder and outer cylinder.

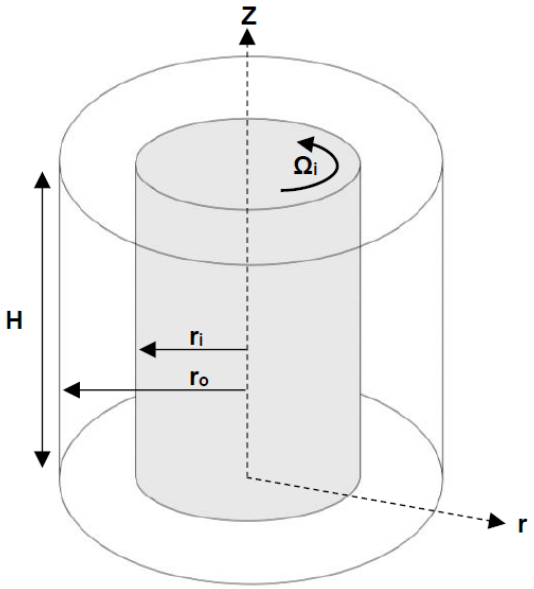


Figure 2.1: Cylindrical Couette flow with rotating inner cylinder [1].

The vortices are more energetic at higher rotational speeds, meaning the operating speed of experiments is significant to the results. Most experiments consider Taylor-Couette flow at speeds in the order of 2000 rpm [10], which is substantially below aeroengine operating conditions. Further differences between idealised Taylor-Couette flow and the flow in a bearing chamber exist because the true geometry is more complex than two concentric cylinders and is of finite length, meaning flow is significantly affected by end effects. Near the end of a cylinder negative centrifuging, caused by the static end plate, drives the fluid radially inward creating large re-circulations which interact with existing vortices [11]. It is therefore very difficult to predict flow in bearing chamber using Taylor-Couette flow, meaning that experimental data and computational modelling is necessary.

A more extensive experimental investigation into pure airflow in a bearing chamber,

and its dependency on shaft speed and sealing flow rates, was performed by Gorse et al. [12]. In this work, the air flow field was resolved in the bearing chamber of a test rig using 3D Laser Doppler Anemometry (LDA). The shaft speed was varied between 3000 rpm and 13 000 rpm, and the sealing flow rate was varied between 6.2 g s^{-1} and 16.9 g s^{-1}. The resulting flow field is shown to be highly dependent on the ratio of shaft surface velocity to axial inlet velocity. When the velocity ratio is greater than 4.2, two vortices dominated by shaft rotation exist in the chamber. This behaviour is termed as Rotational Speed Driven Mode (RSDM). Reducing the velocity ratio below 4.2 led to the existence of one sealing air driven vortex only - this is known as Sealing Air Driven Mode (SADM). RSDM and SADM flows are shown in Fig. 2.2a and Fig. 2.2b respectively.

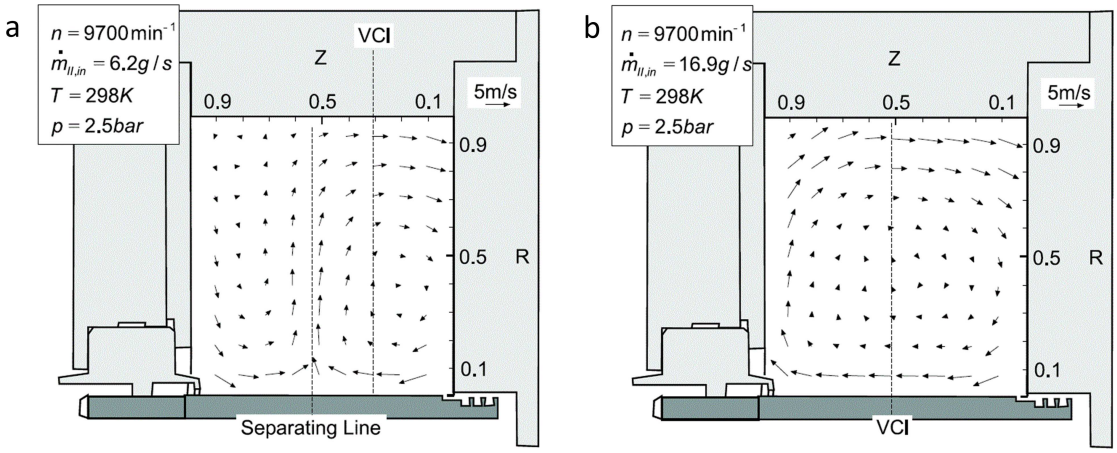


Figure 2.2: Pure airflow in a bearing chamber under (a) RSDM and (b) SADM [12].

Lee [10] performed a similar air-only study using Particle Image Velocimetry (PIV) to examine single-phase flow in a bearing chamber. Tangential velocities were captured with high spatial resolution and accuracy to provide velocity profiles and an improved understanding of flow features for validation of computational modelling.

In a later study, Gorse et al. [13] was able to predict pure airflow with good accuracy using an analytical approach, but less able to accurately predict oil behaviour in the bearing chamber due the assumptions made for two-phase flow, indicating that a significant amount of work was required to extend single-phase predictive capability to two-phase cases.

Further investigation into the airflow field was performed by Aidarinis and Goulas [14] using 2D Laser Doppler Anemometry (LDA). Operating speeds were investigated up to 7000 rpm with a sealing airflow of 23 g s^{-1} and 33 g s^{-1} and with a fixed oil flow rate of 2.5 L min^{-1}. This experimental work provides validation data for computational modelling and allowed the development of a CFD model to predict the airflow field in

an aeroengine bearing chamber.

There is good level of existing literature on single phase flow in an aeroengine bearing chamber. Experimental data is necessary even in an air only situation as it is difficult to predict flow in a bearing chamber using Taylor-Couette flow. LDA and PIV experimental data provides good understanding of air-only behaviour. However, to obtain understanding in real bearing chamber operation, oil needs to be included.

2.2 Droplet Generation in the Bearing Chamber

Understanding droplet generation is important for understanding of overall oil behaviour in the bearing chamber. Generation of droplets close to the bearing (e.g. droplets shed from the cage) contribute to film formation on the static. Further droplet generation occurs when the film reaches the edge of the static. The diameter and velocity of these droplets influences the path taken to the outer wall before scavenge, which influences the residence time of oil and consequently the temperature reached and degree to which oil degradation occurs.

Droplet generation by roller bearings was experimentally investigated by Glahn et al. [15] for shaft speeds up to 16 000 rpm using Phase Doppler Particle Analyser (PDPA). This work produced droplet diameter and velocity data for droplets shed from a roller bearing. The variation of droplet radial and tangential velocity with change in shaft speed is shown in Fig. 2.3. The droplet diameter distribution is presented in Fig. 2.4 for operation at 12 000 rpm with an oil flow rate of $100\,\mathrm{L\,h^{-1}}$ and a sealing air flow rate of $10\,\mathrm{g\,s^{-1}}$. The diameter distribution is concentrated around 70 µm to 80 µm but extends up to a small proportion of droplets at 500 µm.

A later investigation into droplet generation by roller bearings was performed by Gorse et al. [16] at rotational speeds between 4000 rpm and 12 000 rpm with varied oil flow rate and gaseous cross flow. It was found that droplet generation can be reduced by designing the bearing support with smoothed edges, operating at high rotational speed and increasing the oil flow rate. However, the most significant design guideline was that the pressure difference across the bearing must be reduced to a minimum in order to reduce axial airflow to minimise droplet generation. No similar studies consider two-phase flow in ball bearings with a pressure difference across the bearing. The effect of axial airflow on ball bearing shedding is therefore of interest to future investigation.

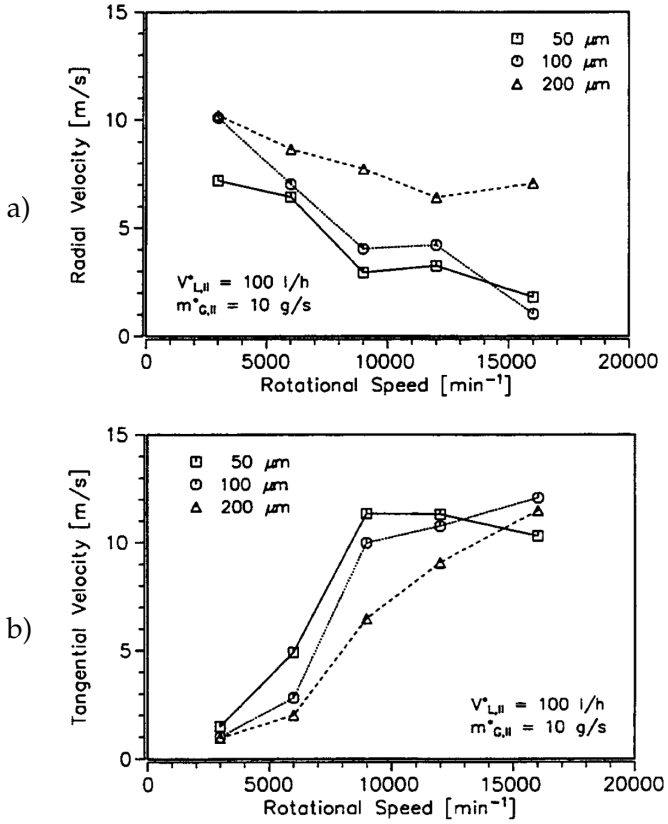


Figure 2.3: Mean a) radial and b) tangential particle velocities versus rotational speed [15].

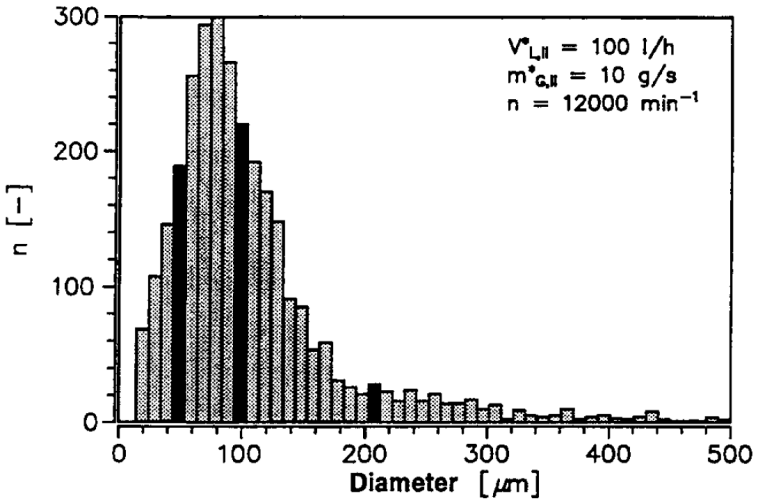


Figure 2.4: Droplet diameter histogram at 12 000 rpm, oil flow rate of 100 l h^{-1} and a sealing air flow rate of 10 g s^{-1} [15].

2.3 Droplets in a Shear Gas Flow

Paths taken by oil droplets that are ejected into the bearing chamber must be understood to allow computer modelling of the bearing chamber and for understanding of droplet residence time in the bearing chamber. Therefore, it is important to understand how droplet trajectory is influenced by the shearing airflow.

2.3.1 Droplet Deflection

Momentum transfer between the airflow and oil droplets causes the droplet trajectory to be deflected, meaning that droplets generated by the bearing follow the air flow field towards the front plate [16]. The process is most easily observed in simple experimental geometries where a liquid jet is injected into a cross flow. Small diameter droplets are deflected to a greater extent than larger droplets which have sufficient momentum to reach the opposite wall for many shear airflow velocities [17, 18]. This phenomenon can be seen in optical imaging of experimental work shown in Fig. 2.5, or more easily in the numerical simulation shown in Fig. 2.6 where droplets are coloured by size. Experimental data from this geometry was used by Nicoli et al. [19] to validate CFD modelling of jet-breakup and film formation before applying the model to a more complex bearing chamber geometry.

Deflection of droplets is significant in the context of bearing chambers in that it is desirable that most droplets reach the bearing chamber walls quickly to form a liquid film. This means that droplet entrainment in the airflow is minimised and heat transfer is optimised. Excessive residence time means that droplet temperature becomes high (contributing to oil degradation) and contributes to increased windage power loss. Droplet residence time in the bearing chamber are discussed in Section 2.8.

2.3.2 Film Formation

Oil films are formed on the bearing housing from oil leaving the bearing and on the outer bearing chamber wall, as seen in Fig. 1.4. The behaviour and formation of the oil film is critical to understanding heat transfer in the bearing chamber. Experimental work considering film formation has been performed for the simplified set-up shown in Fig. 2.7 in a number of studies [17, 18]. A jet is injected into a cross-flow and primary atomisation causes the jet to break up into droplets which are deflected by the shear gas flow. Droplets that reach the wall accumulate to form a film [17]. The largest diameter droplets are deflected the least, meaning that they are the most likely to reach the wall

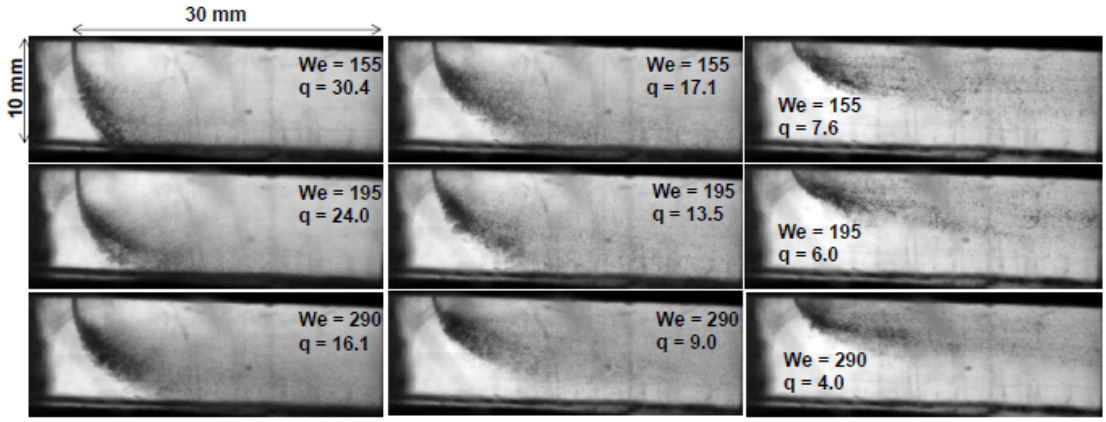


Figure 2.5: Spray trajectory and penetration as a function of Weber number (We) and momentum-flux ratio (q) (q is momentum-flux ratio of the liquid jet to the normal air flow) [17].

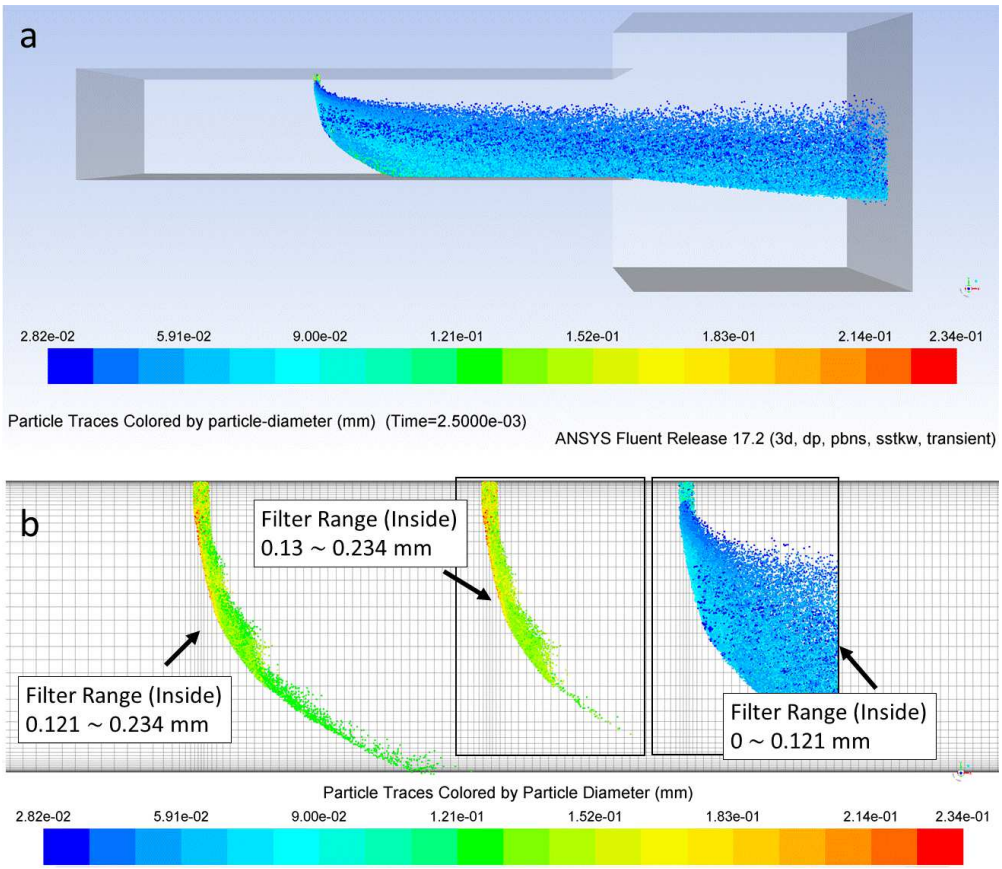


Figure 2.6: Numerical simulation of a liquid jet injected into a cross flow [20].

and contribute to the film. Once the film is formed, further droplet impingements may cause splashing, as discussed in detail in Section 2.5. Droplets in the bearing chamber form a film on the outer wall in the same way. Behaviour of the film in the shear air flow generated by the rotating shaft is discussed in Section 2.4.

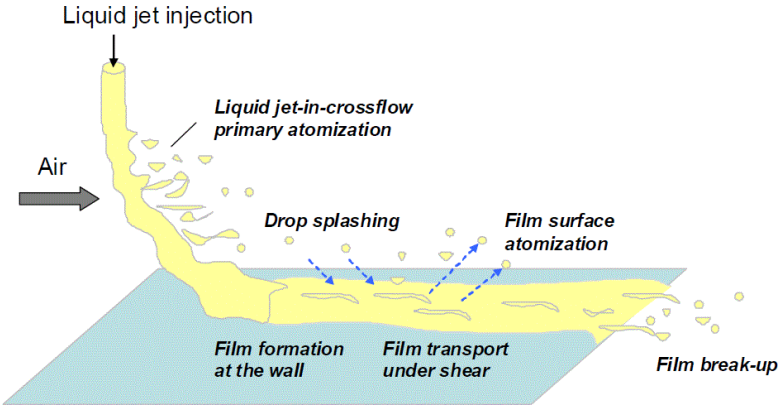


Figure 2.7: Liquid jet injected into a shear flow before primary atomization, wall film formation and eventual film breakup [17].

2.4 Shear-Driven Films

Shear stress at the air-oil interface is caused by the relative velocity between the oil film and the air in the bearing chamber, which is accelerated circumferentially by shaft rotation. Hence air velocity, and consequently shear stress, is proportional to shaft speed. The shear stress drives the film, affecting the oil distribution in the bearing chamber.

2.4.1 Film Thickness

The effect of shear air velocity on film thickness on a horizontal flat wall was investigated by Shedd et al. [17]. It was observed that, for a given oil flow rate, increased shear air velocity correlates to an reduced film thickness (shown in Fig. 2.8). Film thickness is also shown in Fig. 2.8 to increase with an increased oil flow rate for a given shearing air velocity i.e. the film velocity is unchanged so a higher oil flow rate leads to a thicker film. Given that an increase in shaft speed correlates to increased air velocity in a bearing chamber, this bears significant resemblance to the experimental investigation of the relationship between shaft speed and film thickness performed by Wittig et al. [21]. Film thickness measurements recorded using an ultrasonic sensor showed that a thinner, more uniformly distributed film is formed on the bearing chamber wall at higher shaft speeds. Reduced film thickness on the bearing chamber wall at higher

shaft speeds (for a given geometry and Reynolds number) occurs due to conservation of flow rate when the film is accelerated to a higher velocity by the airflow [22]. This trend was also observed by Gorse et al. [13] for films in the bearing chamber, and by Hee et al. [23] for films on the bearing housing. Note that a significant difference to the films exists compared to the flat horizontal wall case due to the effect of gravity and the presence of the vent and scavenge in the bearing chamber.

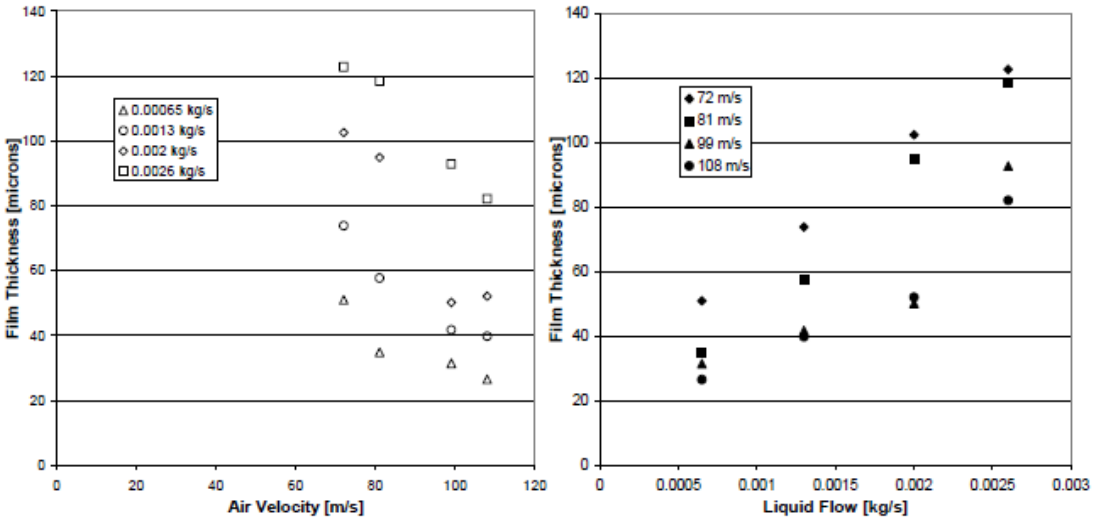


Figure 2.8: Film thickness on a flat plate as a function of shearing air velocity (left) and as a function of liquid flow rate (right) [17].

Hee et al. [23] examines the film thickness close to an aeroengine ball bearing using the same specialist test facility used in the current PhD investigation. The Bearing Shedding Rig (BSR) was designed to investigate oil behaviour as it exits an aeroengine-representative ball bearing. The study considers film on the static bearing housing (axial locations A and B in Fig. 2.9) and between the bearing cage and static outer race (axial location C in Fig. 2.9). The Bearing Shedding Rig (BSR) is discussed in detail in Section 3.1. Windows located at the front of the bearing shedding rig allow film thickness data to be obtained using optical imaging at circumferential positions of 90° and 270° from top dead centre. The film surface is wavy and therefore has a time-dependent thickness profile, meaning that image processing is required to achieve steady-state film thickness measurement. Median stacking produces a higher signal to noise ratio than can be achieved through time-averaging, producing a clearer (less hazy) air-oil interface, and is able to exclude droplets breaking-off from the edge and moving across the area of focus from the resulting image [23]. The difference between these two image processing techniques is shown in Fig. 2.10. Peaks in pixel intensity gradient against radial position from the median stacked image (shown in Fig. 2.11) were used to identify the air-oil and oil-solid interfaces and calculate film thickness.

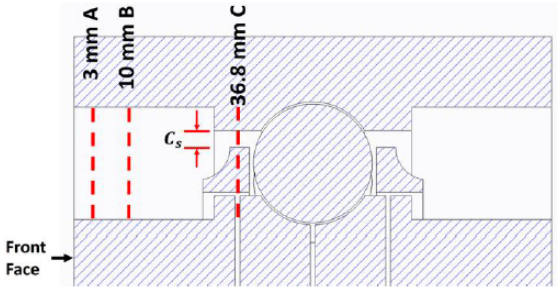


Figure 2.9: Axial planes for film thickness measurement [23].

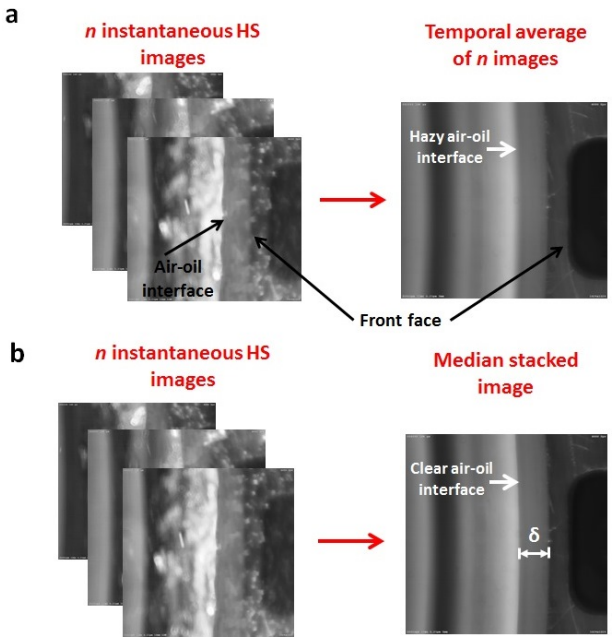


Figure 2.10: Time-averaged and median stacked image processing [23].

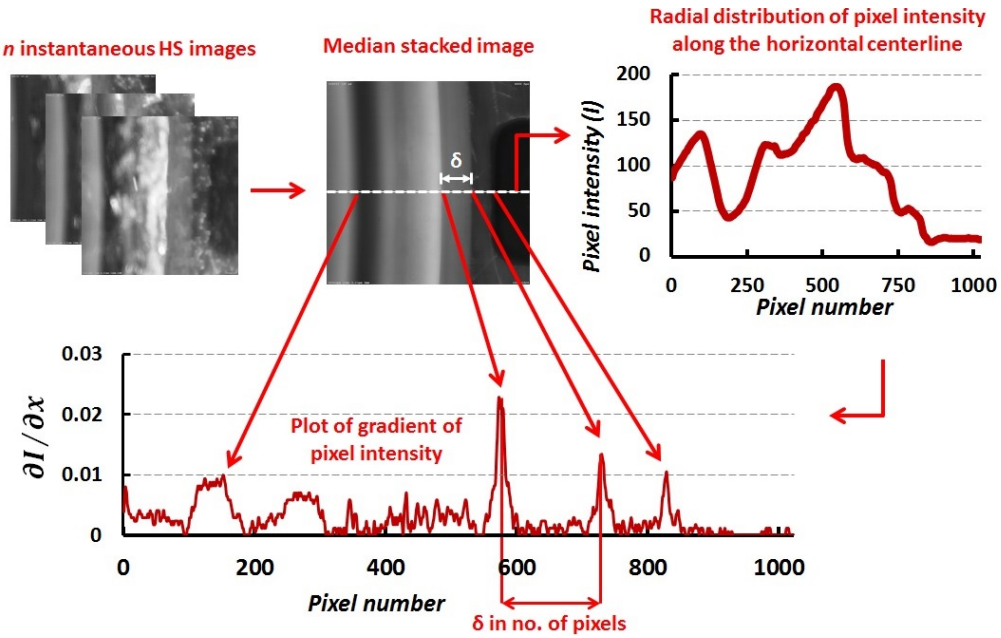


Figure 2.11: Determination of oil film thickness, δ [23].

The effect of shaft rotational speed, axial load and oil flow rate on film thickness on the bearing housing in co- and counter-current regions in axial planes A, B and C is shown in Fig. 2.12. Hee et al. [23] found that at a low shaft speed of 3000 rpm, films tend to be thicker in the counter-current region than the co-current region (especially at axial planes further from the front face), however film heights on either side of the bearing housing are more similar at shaft speeds of 5000 rpm and 7000 rpm. The same trend was observed by Gorse et al. [13] for rotational speeds in the range 4000 rpm to 16 000 rpm. At low speed, Gorse et al. [13] found the oil accumulated at the bottom of the chamber (when gravity is dominant compared to shear) and at higher speed shear becomes more dominant and the oil film is more uniformly distributed around the chamber annulus.

Hee [8] (using the BSR) found that film thickness on the static housing close to the bearing decreased when operating at 7000 rpm compared to 3000 rpm in order to conserve the mass and momentum of the film. The change in film thickness is significant: from 2.1 mm at 3000 rpm to 0.7 mm at 7000 rpm. However, oil flow rate supplied to the bearing did not have a substantial effect on thickness of the film close to the bearing [8].

Similar trends were observed by Sinha et al. [24] who also used the BSR to investigate oil films near to the bearing. Long wave, short wave and uniform film interface shapes were found to occur depending on the shaft speed. Film thickness decreases with shaft speed (as found by Hee [8]) and trends towards a minimum value at high speed - from 2.3 mm at 1000 rpm to 0.4 mm at 8000 rpm where minimum film thickness is reached [24]. The film was also found to be thicker at the 9 o'clock position than at the 3 o'clock position. Larger droplets are expected to be generated at operating conditions/circumferential positions where thicker films exist.

It was suggested by Glahn and Wittig [22] that gravity is more dominant (compared to inter-facial shear) at lower shaft speeds, which would explain why the difference in film thickness on the co- and counter-current sides of the bearing housing is greater at low speed. The film is thicker on the counter-current side under these conditions because gravity slows the film by acting in the opposite direction to the shear force, creating a region of recirculation within the film. Kurz and Bauer [25] defines two distinct regimes:

- Gravity driven oil flow at low speeds - oil pools at the bottom of the chamber and there is a thin film on the rest of the wall.
- Shearing dominated oil flow at high speeds - the oil film is more evenly distributed.

Hee et al. [23] found that, contrary to the findings of Shedd et al. [17] (considering a film on a flat plate), changing the oil flow rate had no significant affect on film thickness close to the bearing. However, increasing axial bearing load from 10 kN to 30 kN was found to increase film thickness, as seen in Fig. 2.12.

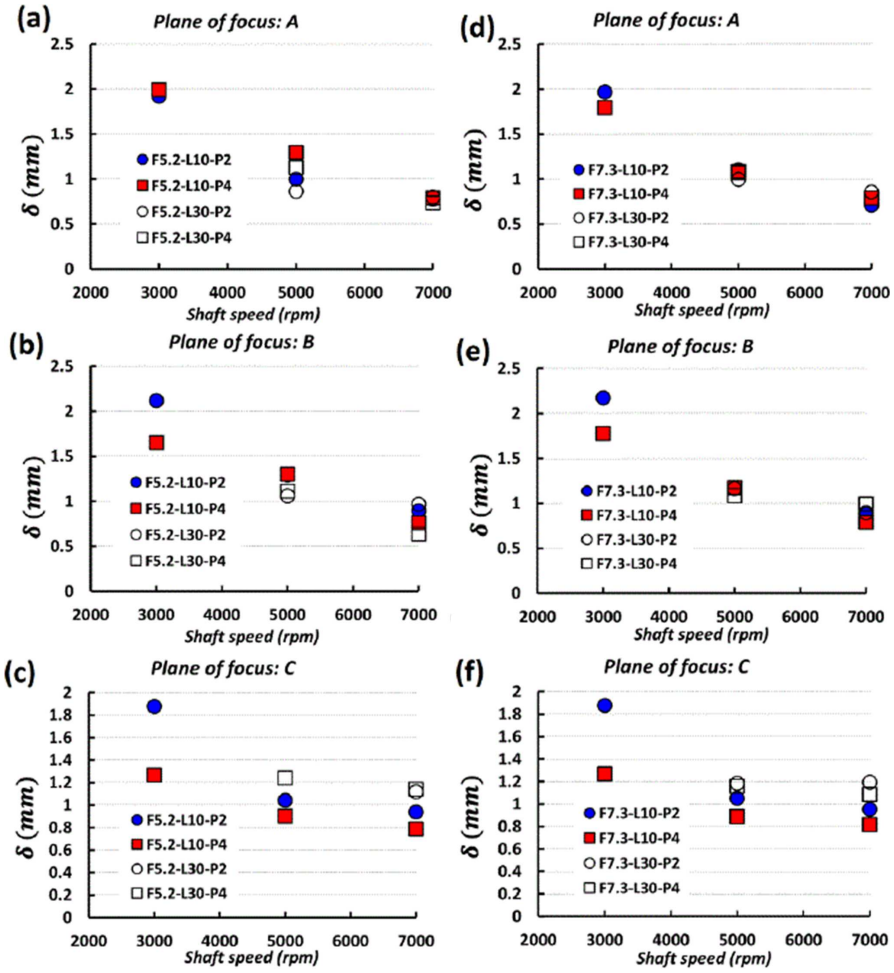


Figure 2.12: Effect of shaft rotational speed, bearing axial load and oil flow rate on film thickness in co- and counter-current regions close to the bearing in axial planes A, B and C. [23].

Existing prior work provides information of how shear air flow affects film thickness on both a flat plate and in a curved bearing chamber environment. Film thickness on bearing housing is affected by both shaft speed and axial load [23]. Film thickness in this region is likely to influence droplet generation in the bearing chamber as the film passes over the shedding edge.

2.4.2 Flow Regimes

Shear and gravity are the main influences on oil behaviour close to the bearing and in the bearing chamber. The way in which these two factors interact determines the oil film flow regime. On the co-current side gravity and shear act in the same direction, causing a relatively thin film. However, on the counter-current side, gravity and shear act in opposite directions, leading to a thicker film including an unstable recirculation region [23, 26]. This region of recirculating oil flow is where the flow transitions from gravity dominated pool flow to shear dominated smooth flow.

Due to the difficulty of analysing the flow field close to the bearing or in the bearing chamber, Hashmi et al. [26] used a simplified test rig to investigate the effect of shear and gravity on a film. The test rig is a straight channel which can be inclined up to an angle of 25° with a gas flow which can be induced in either the same direction as the fluid flow (representing co-current regime) or in the opposite direction (representing counter-current regime). Fig. 2.13 shows the effect of increasing shear airflow velocity on a horizontal film. Increasing the gas velocity causes the waves to transition from smooth to wavy. A single three dimensional (3D) wave forms across the channel before breaking up into a number of smaller 3D waves. Further increase in airflow velocity increases both the amplitude and frequency of 3D waves, and droplets are sometimes atomised from the film in a process known as shear stripping. This is in line with the regime changes seen by Sinha et al. [24] between long wave, short wave and uniform film with increasing shaft speed (corresponding to increased velocity of the shear airflow) in a bearing chamber environment.

In the co-current regime, the film surface is not significantly affected by airflow velocity, but is highly dependent on incline angle (i.e. equivalent to different circumferential positions on the bearing housing/bearing chamber wall). Wave amplitude and frequency is shown in Fig. 2.14 to decrease with increased inclination of the film.

In the counter-current regime three distinct waveforms were observed by Hashmi et al. [26]. All categories of waveform can be seen in Fig. 2.15a at incline angles up to 5° but only the latter two can be observed in Fig. 2.15b at angles above 10°. At a low incline angle and shear airflow velocity, category 1 waves are small surface disturbances. Increasing shear airflow velocity and/or inclination of the film leads to category 2 periodic solitary waves which span the channel, with small disturbances between the waves. The tip of these waves point in the direction of gravity and droplets are sometimes stripped from the wave tips. Further increase in shear airflow velocity causes the waves to transition into the third category. At this point the waves cease to be period-

ically distributed and increase in frequency. The space between waves is occupied by 3D waves of variable amplitude and droplet shedding from the wave tips is common.

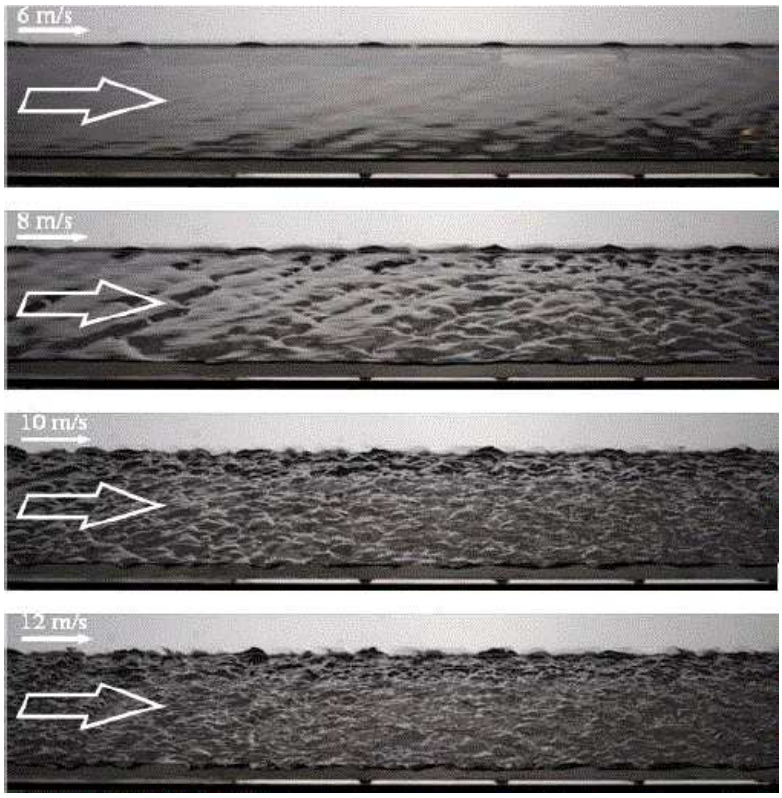


Figure 2.13: Waveforms resulting from varying shear airflow velocity on a horizontal film [26].

This matches the findings of Hee et al. [23] who investigated the film on the bearing housing. Maximum undulation was observed in the shock regime at the transition between gravity dominated pool flow and shear dominated smooth flow. It is noted that reduced net tangential drag on the counter-current side of the bearing chamber caused the film in this region to be more affected by axial oil flow, leading to increased waviness.

A high relative velocity between the air and oil film in the bearing chamber causes Kelvin-Helmholtz (KH) instabilities to form at the interface. These instabilities contribute to KH wave formation and, without damping mechanisms (e.g. gravity, viscosity and surface tension), the perturbations increase with time [17, 20, 27, 28]. Shear stripping occurs when the shear stress overcomes the damping mechanisms, allowing the growth of KH instability [8]. At this point, small droplets are separated from the film at the wave tip. Shear stripping predominantly occurs in the counter-current regime, and is unlikely in the co-current regime where waves are significantly more stable [26].

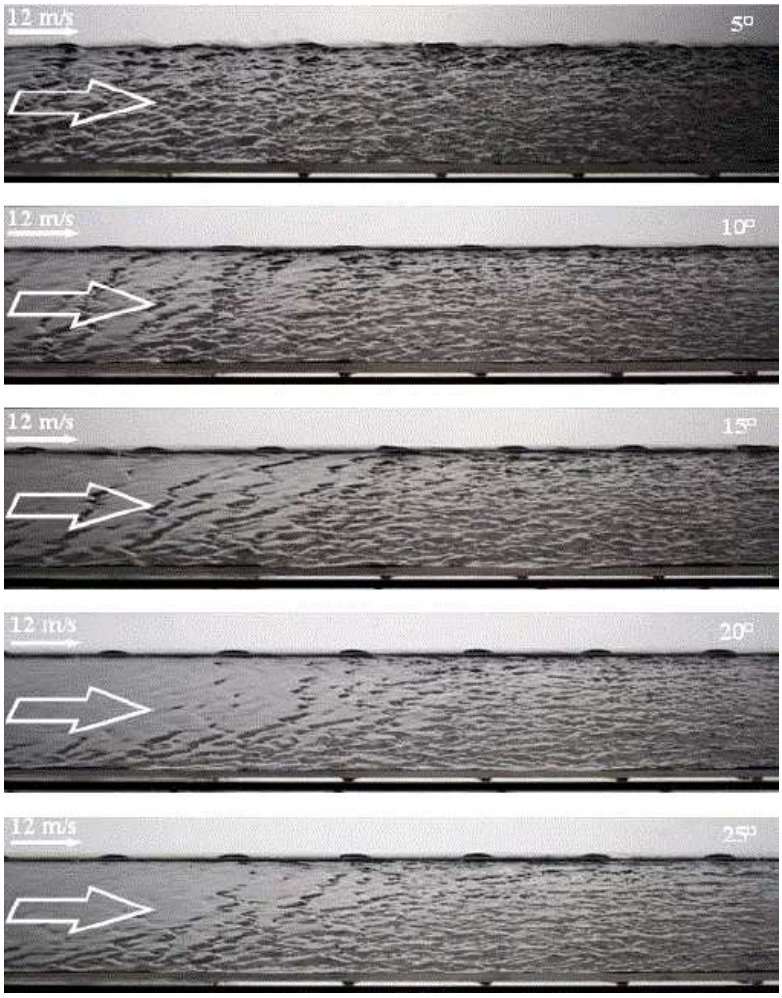


Figure 2.14: Waveforms resulting from co-current shear airflow on a film at varying angles of incline [26].

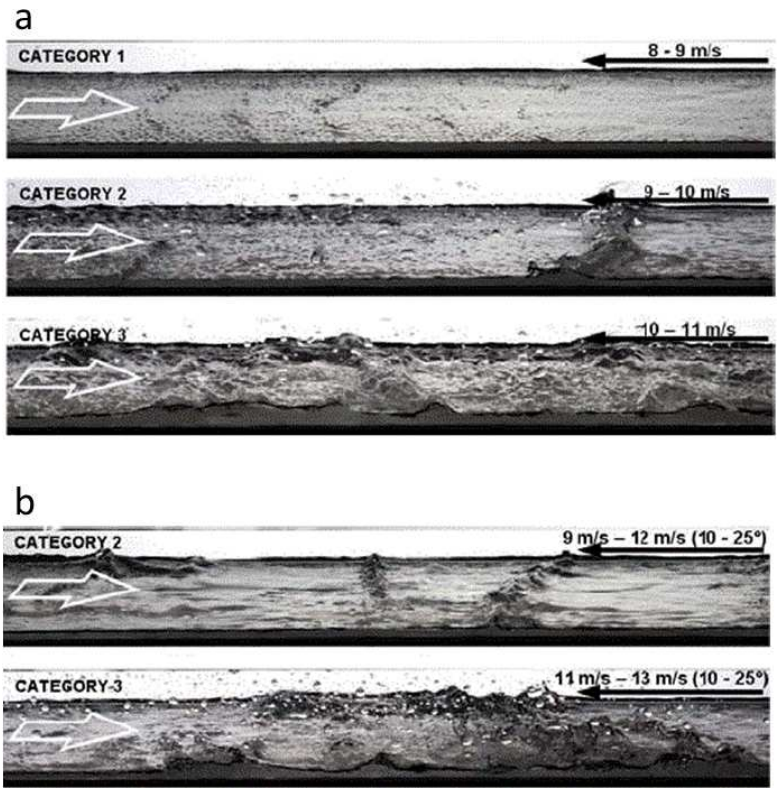


Figure 2.15: Waveforms resulting from counter-current shear airflow on a film (a) inclined up to 5° (b) inclined over 10° [26].

2.5 Droplet-Film Impingement

Droplets frequently impinge with the films on the bearing housing and bearing chamber wall, sometimes causing smaller secondary droplets to be ejected from the film into the airflow. Understanding and being able to predict the outcome of such droplet-film impingements is critical to improving bearing chamber design. Of particular importance is predictive capability of whether splashing will result from an impingement and the size and velocity of any secondary droplets.

A great number of parameters and behaviours have been investigated in relation to droplet-film impingements. Importantly among these is the characterisation of impingement outcome [29–32]:

- Floating/bouncing - the droplet either floats on the surface of the film before attaching, or (given slightly higher kinetic energy) bounces on the film surface.
- Deposition (Fig. 2.16a) - the droplet attaches to the surface quickly with little disturbance to the film (no secondary droplets are produced).
- Crown formation (Fig. 2.16b) - a hemispherical cavity forms, surrounded by a

curtain of fluid which extends above the surface of the film. The crown propagates outwards before collapsing and rejoining the film.

- Crown splashing (Fig. 2.16c) - secondary droplets are produced from the rim of the crown.
- Jet formation - collapse of the cavity at the impingement site causes fluid to be ejected vertically, forming a jet.
- Jet breakup - one or more secondary droplets are formed due to Rayleigh instability of the jet.



Figure 2.16: Droplet-film impingement outcomes: (a) deposition, (b) crown fromation and (c) crown splash [29].

Splashing parameter, K, is commonly used to predict the impingement outcome, including whether or not splashing will occur (i.e. whether secondary droplets will be produced). Several equations have been proposed to define the splashing parameter, but among the most frequently used is Eq. (2.1) defined by Cossali et al. [30].

$$K = WeOh^{-0.4} \tag{2.1}$$

The transition between crown formation and crown splash for normal impact on static films exists at $K = 2100$ [29, 33]. Later experimental work on droplet impingement on a static liquid film by Okawa et al. [34] found that more secondary droplets are produced by an impinging droplet with a higher impact Weber number. The mass ratio of secondary droplets to the primary droplet is found to be predicted by Eq. (2.2), where K_{ex} is calculated in Eq. (2.3), excess Weber number, We_{ex} is calculated in Eq. (2.4) and early critical Weber number, $We_{c,early}$ is calculated as in Eq. (2.5).

$$R_{mass} = 1.55x10^{-9}K_{ex}^2 \tag{2.2}$$

$$K_{ex} = We_{ex}Oh^{-4} \tag{2.3}$$

$$We_{ex} = We - We_{c,early} \tag{2.4}$$

$$We_{c,early} = 8123Oh^{0.581} \tag{2.5}$$

Okawa et al. [35] determined that $K = 2100$ is also a good fit for the boundary between splashing and non-splashing for impingement angles below 50°, where the angle is defined as the angle between the velocity vector of the primary drop and the normal vector to water surface. However, at higher impingement angles, splashing does not occur until a higher value of splashing parameter and the impingement outcome is asymmetric. At higher impingement angles, the prow is directed closer to the film surface, as seen in Fig. 2.17. Okawa et al. [35] supposes that the reason that no secondary droplets are produced at impingement angles over 70° (even with high splashing parameter) is that a higher proportion of the kinetic energy of the impinging droplet produces subsurface effects so that little of the impingement outcome is visible above the surface of the film.

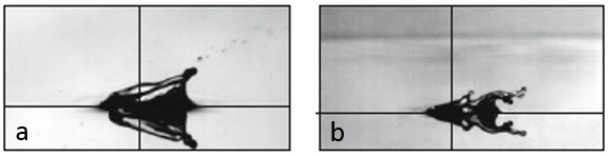


Figure 2.17: Outcome of oblique droplet impingement on a static film at an angle of (a) 24° (b) 49° [35].

Chen et al. [36] performed a numerical investigation into splashing dynamics using the lattice Boltzmann flux solver and the diffuse interface method for droplet-film impingements between 45° and 75°. This work produced the correlation shown in Eq. (2.6) for the splashing limit of droplet impingement on a thin film at an oblique angle of 45° to 75°.

$$K_L = Oh^{-0.66}We = 3966 \tag{2.6}$$

Sinha et al. [37] took this research a step further by investigating droplet impingement onto a curved liquid film. At low impingement angles, the transition to crown splashing occurred around $K = 2100$ and was found to increase at higher impingement angles, in strong agreement with prior work by Okawa et al. [35]. However, a higher critical splashing parameter was identified for impingement onto a curved surface than for the equivalent impingement angle onto an inclined film.

In addition to splashing parameter, the impingement outcome is also influenced by the shape of the droplet (spherical, deformed, oscillating, internal circulation), impingement angle, shear airflow and impact surface (i.e. film thickness, waviness and physi-

cal properties of liquid films) [32]. In practice, droplets in bearing applications impinge onto a moving, wavy film and will most often occur at an oblique angle, meaning that data on non-normal impingements is highly relevant. These impingements occur on the film on the bearing housing and on the outer wall of the bearing chamber, potentially causing secondary droplets to be generated in both cases.

2.6 Film Separation and Disintegration

Oil films form on surfaces near the bearing but are likely to separate from these surfaces as the film passes over an edge, as seen in Fig. 1.5. The separated oil is ejected into the chamber and forms part of the body of oil that must be tracked and modelled.

Film separation occurs when a film reaches an edge with sufficient inertia to overcome restoring forces. This behaviour is expected to occur as the oil film on the bearing housing passes over the front face into the bearing chamber and has been observed from the bearing cage by Santhosh et al. [38]. At the onset, only partial separation occurs (as seen in Fig. 2.18), but the proportion of the film that separates from the wall increases with the ratio of inertial force to restoring force [39]. Understanding how the film separates over aeroengine relevant geometries at high operating speed provides information to aid the development and validation of numerical modelling techniques. In order to develop effective computational modelling of such geometries, modelling approaches for simpler geometries must first be validated - this is what was done by Nicoli et al. [19].

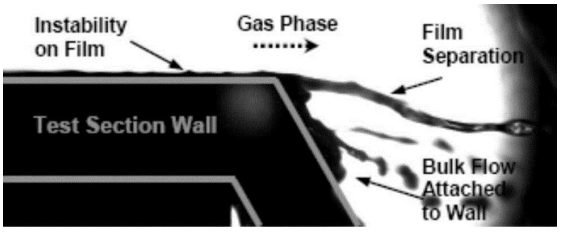


Figure 2.18: Partial film separation in a shearing gas flow [39].

Work by Glahn et al. [40] looks at liquid disintegration from rotary discs and cups. This situation resembles oil disintegration from parts in the bearing chamber (e.g. from rotational elements such as the bearing cage) but is not representative of droplets shedding from static elements in an aeroengine bearing chamber. Breakup has been extensively investigated for rotating discs and cups and can occur through a number of different mechanisms (in all cases, liquid elements leave the solid surface tangentially):

- Direct drop formation (Fig. 2.19a) – centrifugal force causes the liquid to separate

from the edge of the solid surface in uniformly sized discrete droplets. These droplets are larger than those produced in shear stripping [18].

- Ligament formation (Fig. 2.19b) – occurs when flow rate or rotational speed is increased from direct drop formation, causing ligaments to be produced from the edge of the solid surface. The number of ligaments increases with flow rate.
- Film formation (Fig. 2.19c) – occurs when flow rate or rotational speed is further increased from ligament formation to the point where ligaments can no longer accommodate the flow of liquid. At this point, a thin sheet forms radially from the edge of the solid surface.

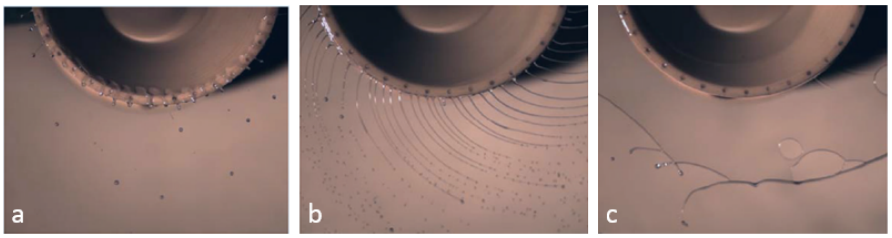


Figure 2.19: Breakup mechanisms from the rim of a cup (a) direct droplet formation (b) ligament formation (c) film formation [41].

Frost [42] produced correlations for the number of ligaments, disintegration frequency and drop size produced from ligament formation from a spinning disc (shown in Eqs. (2.1) to (2.3) respectively). These correlations are valid for oil shedding from a rotating surface, such as the bearing cage, but not from a static surface. Droplets shed from the cage will impact on the static where a film is formed and then shed as it passes over the lip of the front face. Paleo Cageao et al. [43] found there to be significant reduction in tangential velocity of the oil shed via a static element compared to when oil is shed directly from a rotating surface.

$$N = 0.29\left(\frac{\omega\rho D^2}{\mu}\right)^{0.93}\left(\frac{\sigma D\rho}{\mu^2}\right)^{-0.44} \tag{2.1}$$

$$\frac{fD^3}{Q} = \left(\frac{\omega D^3}{Q}\right)^{1.33} \tag{2.2}$$

$$d = 1.87\left(\frac{Q^{0.44}\sigma^{0.15}\mu^{0.017}}{D^{0.80}\omega^{0.75}\rho^{0.16}}\right) \tag{2.3}$$

Breakup mechanisms from the bearing cage are shown by Santhosh et al. [38] to be very similar to those of rotating discs and cups. This is determined by comparison of prior work to oil shedding from the cage of an aeroengine-representative ball bearing

(using the G2TRC bearing shedding rig). In this work, direct drop formation is defined as before but additional distinctions between other breakup mechanisms are defined as follows:

- Primary ligaments (Fig. 2.20b) - ligaments form directly from the lip of the solid surface.
- Laminar sheet (Fig. 2.20c) - a smooth film extends radially from edge until the equilibrium radius, at which point the sheet experiences further breakup.
- Ruffled sheet (Fig. 2.20e) - forms in much the same way as the laminar sheet, but also exhibits waves perpendicular to the liquid flow-lines created by the shear gas flow. Ruffled sheets were also observed in rotating cup experiments by Fraser et al. [44] where wave disintegration was found to be the dominant mechanism for breakup of the sheet.
- Secondary ligaments (Fig. 2.20f) - these are different from primary ligaments because they do not originate directly from the solid surface, but instead are formed by the breakup of a ruffled sheet.

In prior work, it was found that liquid flow rate has negligible effect on the spray characteristic, while rotational speed of the disc greatly impacts the diameter of droplets produced [40]. Smaller diameter droplets are generated with increasing rotational speed until a minimum diameter is reached, at which point droplet diameter becomes insensitive to further increase in rotational speed [40, 41]. Much of the experimental work on droplets in bearing chambers considers rotational speeds below aeroengine-representative conditions [9, 20, 23, 38], meaning that droplets in an aeroengine bearing chamber may be smaller than those observed in experimental work - unless the rotational speed corresponding to minimum droplet diameter is less than or equal to experimental shaft speeds. Further investigation into the applicability of droplet size observed in experiments may be warranted.

Frost [42] determined well-defined transition points between direct drop, ligament and sheet formation. However Santhosh et al. [38] found that, despite similarity in breakup mechanisms, transition between mechanisms occurs at a different point for each geometry type. It was concluded that, while correlations for rotating cups were closer than those for discs, none of the previous empirical equations were able to accurately predict transition between breakup mechanisms from the bearing cage. It is therefore expected that the correlations will also be unable predict transition between breakup

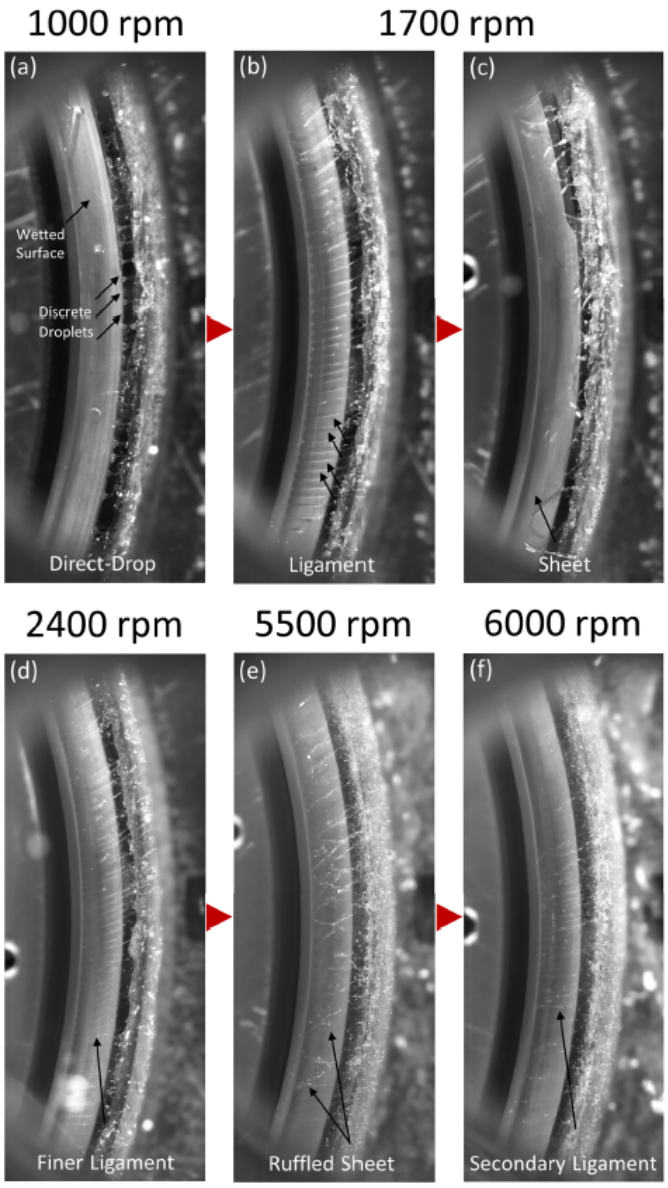


Figure 2.20: High-speed visualisation of disintegration modes [8].

mechanisms from the lip of the bearing housing. Despite the inability to predict transition between breakup behaviours, general trends observed in disc and cup experiments can be applied to bearing chambers with reasonable confidence.

Hee [8] found that for oil shedding from the bearing cage, direct drop formation occurred below 1700 rpm. Primary ligaments and laminar sheets were observed together in different parts of the cage edge (due to variable oil flow rates caused by eccentricity) between 1700 rpm and 4300 rpm. At rotational speeds above 4300 rpm a ruffled sheet forms. The speed at which secondary ligaments first exist is not defined.

Santhosh et al. [38] proposed Eq. (2.4), where K', x and y are constants to be determined. Eq. (2.4) may also be applicable to film breakup over the lip of the bearing housing, although it is likely that the constants would be different than those for breakup from the cage.

$$Q' = K'We^{x}Re^{y} \tag{2.4}$$

Glahn et al. [45, 46] investigated the velocity of droplets emerging from either axial passages or radial holes in rotating cylinders as seen in Fig. 2.21a and Fig. 2.21b respectively. A correlation is provided (used for both cases) with respect to the velocity of the rim of the cylinder:

$$\frac{\overline{V_d}}{V_{rim}} = 1.5 - 0.1327ln(We^{*0.5}) \tag{2.5}$$

If this is a reasonable approximation for the velocity of droplets entering the bearing chamber after breakup of the film, this information greatly improves knowledge of inlet conditions for numerical modelling. However, it is likely that droplet velocity will vary with the mechanism of film disintegration and with shedding from static elements compared to rotating elements (as per Paleo Cageao et al. [43]). Therefore, given that the experiment performed by Glahn et al. [45, 46] does not replicate geometry of the bearing housing and chamber, it is unlikely that the correlation is applicable.Despite this, the data is useful for validation of theoretical models and is used as such by Zhu et al. [47]. The proposed model provides additional information about droplet behaviour: increased droplet velocity and lower droplet temperatures are seen for higher droplet diameters.

2.7 Droplet/Ligament Disintegration

Ligaments and large droplets tend to undergo breakup in highly rotating and shear environments. Breakup of ligaments to droplets was investigated in early rotating cup

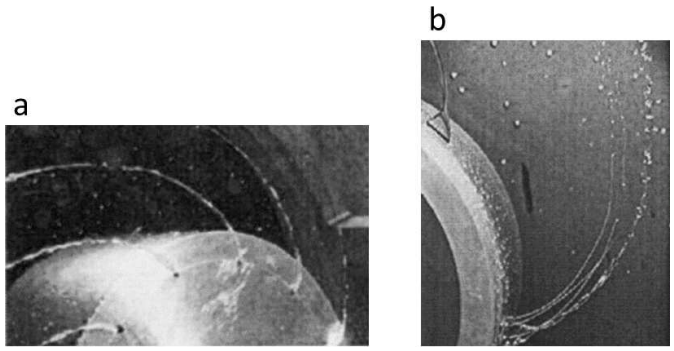


Figure 2.21: Droplets emerging from (a) axial passages in a rotating cylinder (b) radial holes in a rotating cylinder [45, 46].

experiments by Hinze and Milborn [48]. Ligaments were found to breakup by Rayleigh instability in the same way that a straight liquid column does. Droplets produced by ligament breakup are expected to have the same diameter if the following assumptions are met:

- ligaments are of equal diameter
- breakup occurs at the same distance from the edge
- disturbances with optimum wavelength cause breakup
- ligament stretching does not affect breakup

In practice, this is rarely the case. Ligaments tend to breakup at different distances from edge and are therefore not of equal diameter at the point of breakup. Additionally, breakup often occurs, not by optimum wavelength (at which there is a maximum rate of increase of disturbance), but by a singular disturbance with the inclusion of ligament stretching. The ligament stretching process means larger droplets are generated, with a thin trailing tail. This tail then breaks up into a number of very small droplets. Breakup by this mechanism creates two distinct droplet size groups (clearly visible in Fig. 2.22), depending on whether droplets originated from the large lead droplet, or the thin trailing tail.

Droplet generation by ligament formation and subsequent breakup creates a more uniform distribution than by direct droplet generation from a spinning cup [48]. In direct drop formation, the film is disturbed by the airflow, causing irregular perturbations to be formed. A significant contribution to the non-uniformity of droplets generated by direct droplet formation is the high number of very small droplets produced by breakup of the very thin threads that often connect the clots of liquid.

Once droplets are formed, through either direct drop formation or from the breakup

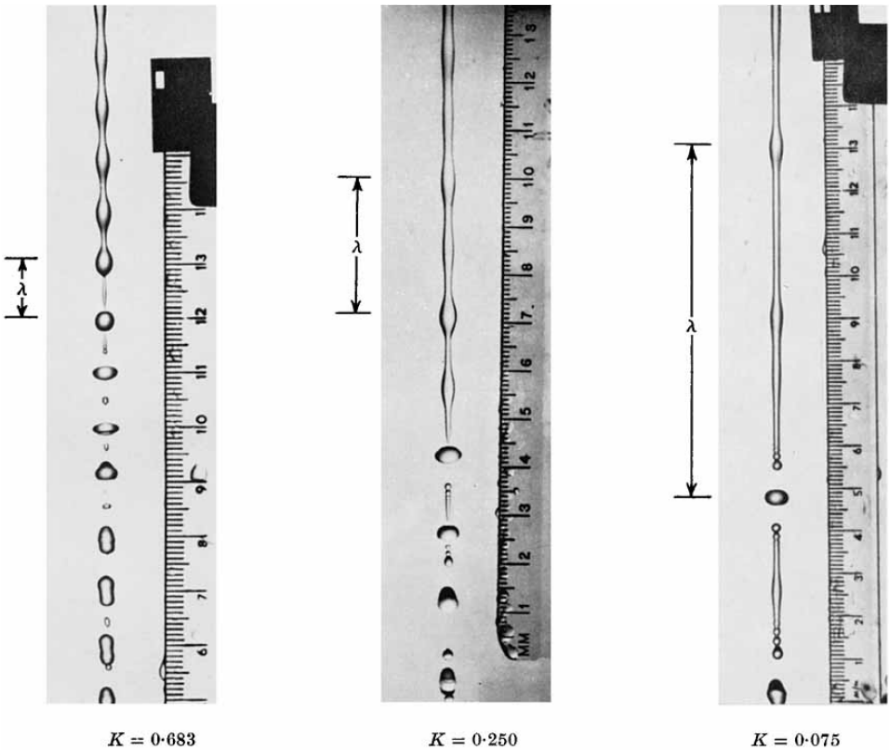


Figure 2.22: Unstable breakdown of water jets at three different wave-numbers, with wavelength λ [49].

of ligaments, they may undergo Kelvin-Helmhotz-Rayleigh-Taylor (KH-RT) breakup shown in Fig. 2.23. Kelvin-Helmhotz (KH) and Rayleigh-Taylor (RT) instabilities are generated by the effect of air-droplet shear force, causing small droplets to be stripped from the parent droplet and leading to the disintegration of the parent drop into a number of smaller droplets [50, 51]. Droplets only breakup if the wavelength of instabilities is less than the droplet diameter. The drop separates into a number of smaller drops due to RT instability and KH waves with a much shorter wavelength cause micro-meter size droplets to break off from the edge [51].

Alternatively, droplets may go through bag breakup. The stages of bag breakup shown in Fig. 2.24 are described as:

(i) Initial spherical droplet

(ii) Deformed to a disc/pancake shape

(iii) Bag growth occurs with further deformation

(iv) The bag begins to burst, producing smaller droplets

(v) Bag fragmentation produces more small droplets

(vi) Toroidal ring breakup occurs

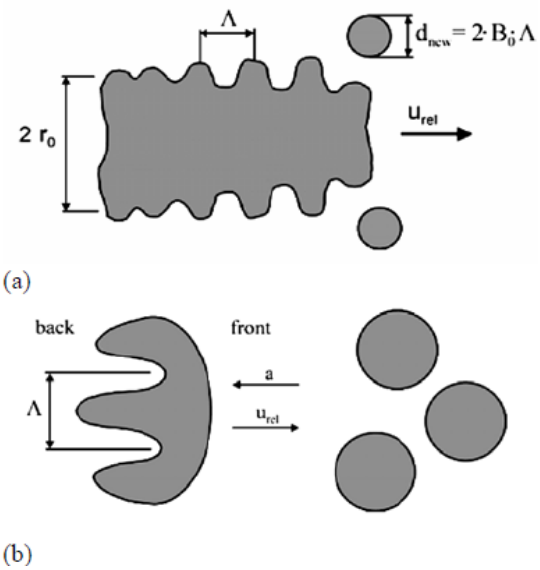


Figure 2.23: Droplet breakup through (a) Kelvin-Helmholtz instability and (b) Rayleigh-Taylor instability [51].

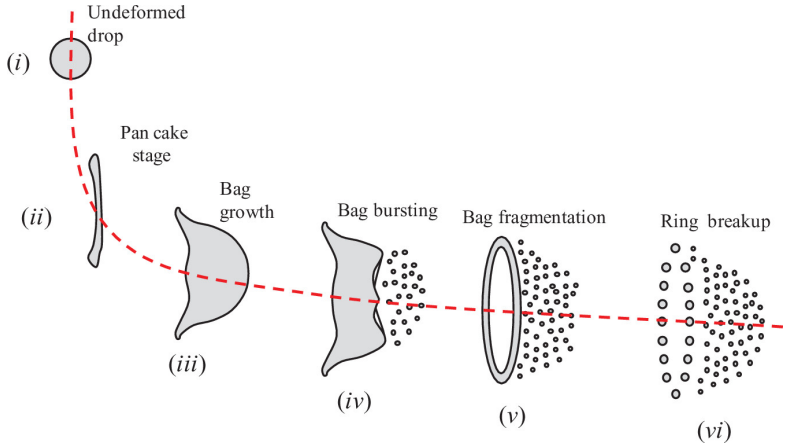


Figure 2.24: Bag breakup process [52].

2.8 Residence Time

The length of time that oil resides in the bearing chamber is significant to the effectiveness of cooling and prevention of oil degradation. To efficiently cool the bearing chamber, the design should be such that heat is quickly transferred to the oil and then the oil is efficiently scavenged, removing heat from the system. The persistence of hot oil does not help to cool the bearing chamber, but does contribute to oil degradation and increase the risk of coking.

Residence time in the bearing chamber has not been investigated to the authors knowledge. However, work has been performed considering the trajectory of droplets entering the bearing chamber and travelling towards the outer wall. It was discussed in Section 2.3.1 that smaller droplets are deflected by a shear airflow to a greater extent than large droplets, as in Fig. 2.27. These studies are in agreement with Sun et al. [53], Fang and Chen [54] who found that smaller diameter droplets experience greater deflection in the bearing chamber in both the circumferential and axial directions, as shown in Figs. 2.25 and 2.27. For a given droplet velocity, high deflection in the circumferential direction leads to an increase in time taken for the droplet to reach the wall film, meaning a higher residence time. It is possible that very small droplets may become entrained in the airflow. Smaller droplets are also found to have a lower velocity (as shown in Fig. 2.26), meaning that the time taken for them to reach the outer wall is significantly higher than that of larger droplets. The effect of droplet deformation on trajectory was investigated in a similar study by Chen et al. [55] who found that deformed droplets experience a more curved trajectory and lower velocity than spherical droplets.

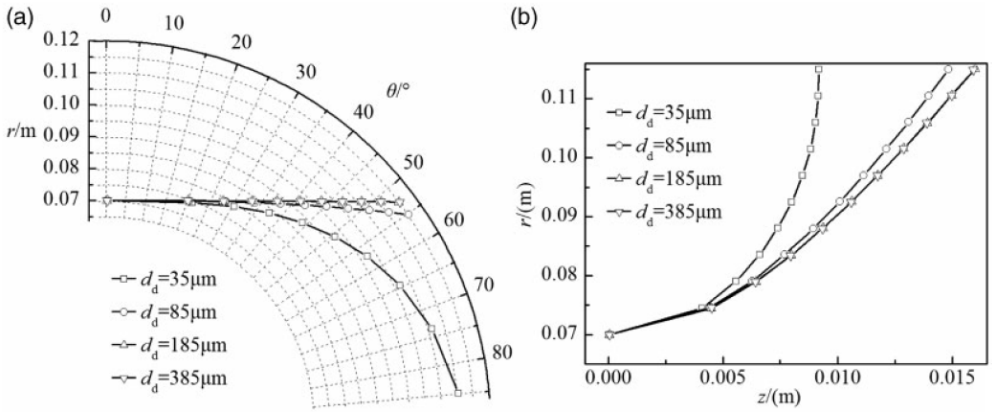


Figure 2.25: Effect of droplet diameter on trajectory (a) r-θ plane (b) r-z plane [53].

The effect of droplet size and shape on the time taken to reach the wall film highlights the need to accurately represent droplets entering the bearing chamber in future nu-

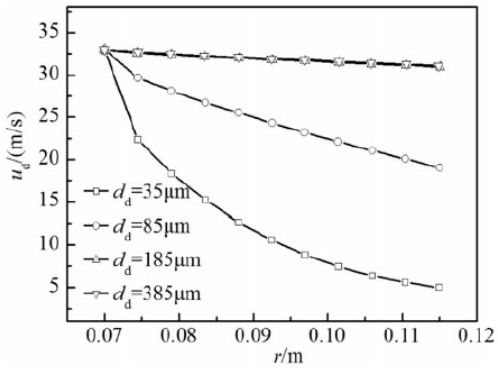


Figure 2.26: Effect of droplet diameter on velocity [53].

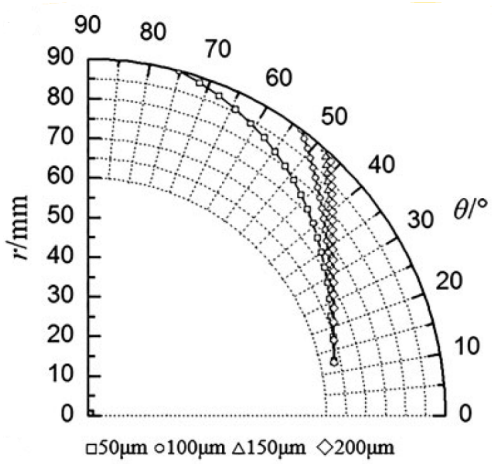


Figure 2.27: Effect of droplet diameter on trajectory in the r-θ plane [54].

merical modelling, hence the need for further work in this area.

2.9 Automated Droplet Detection and Tracking

Automation of the particle detection and tracking process is essential for processing large quantities of image data. This allows particle data to be obtained in order to provide a snapshot of the number, size and velocity of particles in the region investigated. Similar studies often investigate bubbles in a liquid or droplets in the air, both of which require a similar process [56–63].

2.9.1 Droplet Detection Using Conventional Methods in the Literature

Detection of droplets, bubbles or particles in experimental imaging is often performed using a conventional method, as detailed in this section. Geometry-based methods (e.g. the Hough Transform which is used for feature extraction in an image) are commonly used for detecting circular/near-circular objects. The Hough transform isolates features of a particular shape in an image to identify parameters of a curve to fit a set of edge points [64]. The edge description must be obtained separately from a feature detecting operator e.g. Sobel or Canny edge detection. The Hough transform can only be used for simple curves e.g. in circle detection.

Mitchell et al. [57] uses circle detection in MATLAB to detect a single falling droplet in images taken using a high-speed camera. High accuracy detection is achieved using this method in the simple visual environment where the droplet is spherical.

Shao et al. [56] uses the combination an intensity metric and intensity gradient with circular Hough transform to segment bubbles in experimental images for the purpose of measuring the size of bubbles. The limitation of this approach in other applications is the assumption of spherical bubbles/droplets/particles and the need for a relatively homogenous background. Conversely, droplets are often non-spherical and experimental images often have complex lighting conditions and/or features in the background that droplets are travelling past.

A MATLAB script was developed by Vasques et al. [58] for detecting bubbles entrained in a liquid film. Implementation of the Brightness Based Laser Induced Fluorescence (BBLIF) technique means that bubbles have a well-defined outline. The two step approach implements Canny edge detection then filters non-bubble objects using the *regionprops* function in MATLAB, so that only objects with a light border and dark centre are included. Next, the function *imfindcircles* uses the Hough Transform to detect circles

for multiple non-overlapping diameter ranges. This approach is not directly applicable to other experimental set-ups with a different lighting distribution across the objects being detected. A Convolutional Neural Network (CNN) is designed to make predictions from an input image. The output can be classification of the image (e.g. this is an image of a cat), or detection of where in an image a particular feature is. This is of use in many applications including medical imaging and for use in self-driving vehicles.

2.9.2 Droplet Detection Using a Convolutional Neural Network (CNN)

This section considers literature using CNNs for detection of droplets or similar applications and how the accuracy of prediction capability compared to alternative conventional methods. A CNN is a Neural Network (NN) with a convolutional layer, making it able to process two-dimensional image information as opposed to individual pixel values. Information is passed through the CNN as a series of mathematical functions, producing a numerical output. For a segmentation problem such as identifying regions of an image that contain a droplet, the output indicates the classification of each pixel in the image. The advantage of a CNN is that it is able to perform two-dimensional feature recognition learned from a representative set of training images (rather than comparatively simple rules such as circle detection) and is therefore able to perform accurately in more complex visual environments and detect droplets with a range of shapes, sizes and lighting distributions. A detailed description of how a CNN functions (including detail of the convolutional layer) and how it is trained is presented in Chapter 4.

Ilonen et al. [59] examines different methods for bubble detection and size distribution estimation in images. It is concluded that for some applications it may be most appropriate to use direct bubble size distribution estimation method as it is the fastest technique and does not require detection of individual droplets. However, using a CNN do detect droplets and subsequently obtaining the diameter distribution is higher accuracy [59] and yields additional information that can be used to inspect droplet paths and velocity. The paper considers a problem with mostly spherical droplets with relatively even lighting so circle detection is appropriate for a geometry-based approach. Geometry-based approaches have many possible false positives, are sensitive to noise and have false negatives when bubbles are not visually outlined in the way expected by the model - in such cases use of a CNN is likely to produce more accurate results.

Multiple studies found using a CNN produces high accuracy predictions [60, 61, 65]. Chaussonnet et al. [60] is able to achieve good accuracy for highly challenging degraded optical conditions including overlapping droplets following primary atom-

ization using a CNN for segmentation and detection of droplets. Poletaev et al. [61] trained a neural network ensemble using synthetic images (similar appearance to experimental images) to examine gas-liquid bubbly flows. The application includes overlapping, blurred and non-spherical bubbles. Higher identification accuracy and lower processing time was achieved using a CNN to classify bubbles and find their centroid position compared to using non-convolutional neural networks. Malakhov et al. [65] use CNNs because of the capability to detect and segment bubbles on the wall and ignore those that have detached. The two CNN architectures U-net [66] and Mask R-CNN [67] were considered and the Mask R-CNN was found to deliver higher accuracy results.

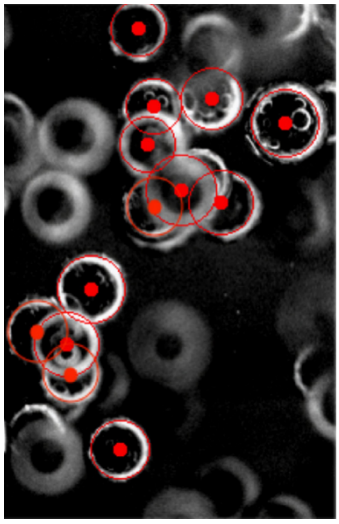


Figure 2.28: Example of bubble detection by Poletaev et al. [61] using an NN based method.

An investigation into the effect of the number of layers in a CNN was performed by He et al. [68]. Application of an 18-layer and a 34-layer ResNet on the ImageNet dataset [69] showed a notable reduction in prediction error with an increase in network depth. Error in deeper ResNets (20 to 110 layers) was investigated using the CIFAR-10 dataset [70]. A significant reduction in prediction error was made in increasing from 20-layers to 32-layers, however less significant changes were seen with further increases to 44, 56 and 110 layers.

2.9.3 Droplet Tracking

A simple approach to obtaining droplet velocity is to match droplets across neighbouring frames of an images sequence within a set distance of the starting position without assigning droplet IDs. This is the approach used by Vasques et al. [58], however there are several downsides to this approach.

- There is no way to correlate velocity and diameter of droplets.
- Incidences of a single droplet may be incorrectly paired across frames.
- Droplet statistics use the number of instances of detection rather than the number of droplets with given characteristics.
- Only works in a sparse environment when particles are consistently detected.

To prevent these issues, a tracking method which assigns an ID to each droplet can be implemented instead, such as the tracking function available from Blair and Dufresne [71]. This is a MATLAB adaption of Crocker and Grier [72]. The required format is a single array, in which each row corresponds to an incidence of droplet detection. Each incidence of detection has the following information associated:

- x-position of the centroid
- y-position of the centroid
- equivalent diameter
- image number in which the detection occurred

The tracking function then tracks droplets through the image sequence and assigns an ID to each incidence of detection. The ID is maintained for a droplet for as long as it can be identified as the single droplet moving through time. There are cases where the droplet may not be able to be matched to its earlier path, in which case a new ID is generated for the same droplet. Once droplet IDs are assigned, further calculations can be performed to provide velocity data and information regarding the path taken by individual droplets. This approach allows correlations between droplet diameter, position, speed and direction of travel to be investigated, as well as the ability to consider the probability distribution of each variable.

2.10 Summary of Literature

This literature review summarises the current state of knowledge with regard to how oil behaves in an aeroengine bearing chamber. The two phase flow is highly complex with oil being present in a number of different forms (droplet, film, sheet, ligament, mist) and moving between these forms on its journey from entry to exit. Researchers have looked a many of the elements of flow relevant to a bearing chamber and there is a reasonable body of prior work that gives a level of understanding of likely behaviours.

This review also highlights areas where current knowledge is weak or absent. In particular, very little is known about how oil sheds from an aeroengine ball bearing and this leads to a weakness in capability to model the two-phase behaviour.

A reasonable understanding of single phase flow in the bearing chamber is currently available in addition to significant fundamental works considering two-phase flow in simplified geometries including droplet behaviour and film formation in a shear gas flow, shear driven films, droplet-film impingement and droplet generation by spinning discs and cups. It should be noted however that the injecting a liquid jet into a cross flow does not include a rotational component and spinning discs and spinning cups consider oil breakup from the lip of a rotating surface, rather than a static surface as in the bearing chamber of the bearing shedding rig used for experimental work in this project. Therefore, while these simplified experimental setups are similar enough to provide comparison and initial validation of modelling approaches, a difference in behaviour is expected in an aeroengine bearing chamber representative geometry.

A considerable gap in knowledge exists around droplet generation as oil enters bearing chamber, including data regarding droplet diameter, speed, direction of travel and path taken through the chamber. Experimental droplet data will be of great value for validation of existing and future CFD modelling of two-phase flow behaviour in an aeroengine bearing chamber. The use of Convolutional Neural Networks (CNNs) is a promising method for accurate droplet detection from high-speed experimental images and is the approach developed and analysed in this thesis.

CHAPTER 3

Experimental Methodology

In this chapter, a description of the experimental equipment is provided, including details of the Bearing Shedding Rig (BSR), high-speed camera and lighting equipment. Following this, the method for experimental data collection is presented.

3.1 Bearing Shedding Rig (BSR)

3.1.1 Overview

The BSR is a specialist test facility designed, manufactured and commissioned in 2013 as part of the Innovate UK-funded project SILOET to investigate oil shedding from a large civil aeroengine HP location bearing. The rear of the bearing, as it would be installed in the engine, is oriented towards the front of the bearing shedding rig. The general arrangement of the bearing shedding rig is shown in Fig. 3.1. The actual rig is shown in Fig. 3.2 and further information is given in the cross-section shown in Fig. 3.3. The bearing shedding rig consists of a driven section and a working section as indicated in Fig. 3.3. The working section is where optical imaging data is collected, while the driven section is everything rear of the bearing. The bearing and main shaft are driven by an electric motor through a flexible coupling.

The rig has good visual access to the front chamber via windows positioned on the front of the bearing shedding rig to allow observation of oil behaviour. High-speed imaging of oil behaviour close to the bearing and in the bearing chamber is possible using this rig. This ability allows investigation of how the film on the bearing housing enters the bearing chamber over the front face at different circumferential positions. The operational limits of the rig as currently commissioned are given in Table 3.1.

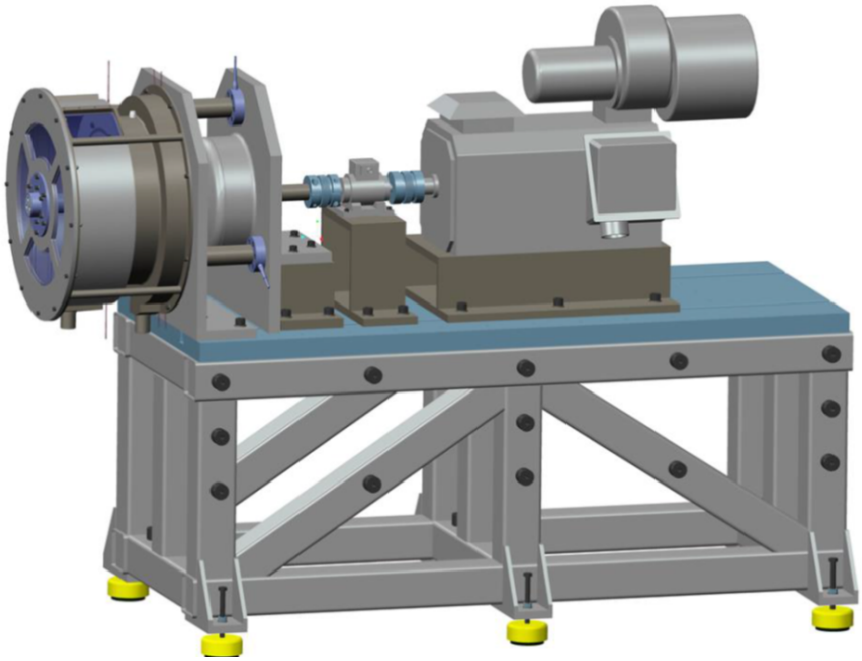


Figure 3.1: Bearing shedding rig general arrangement.

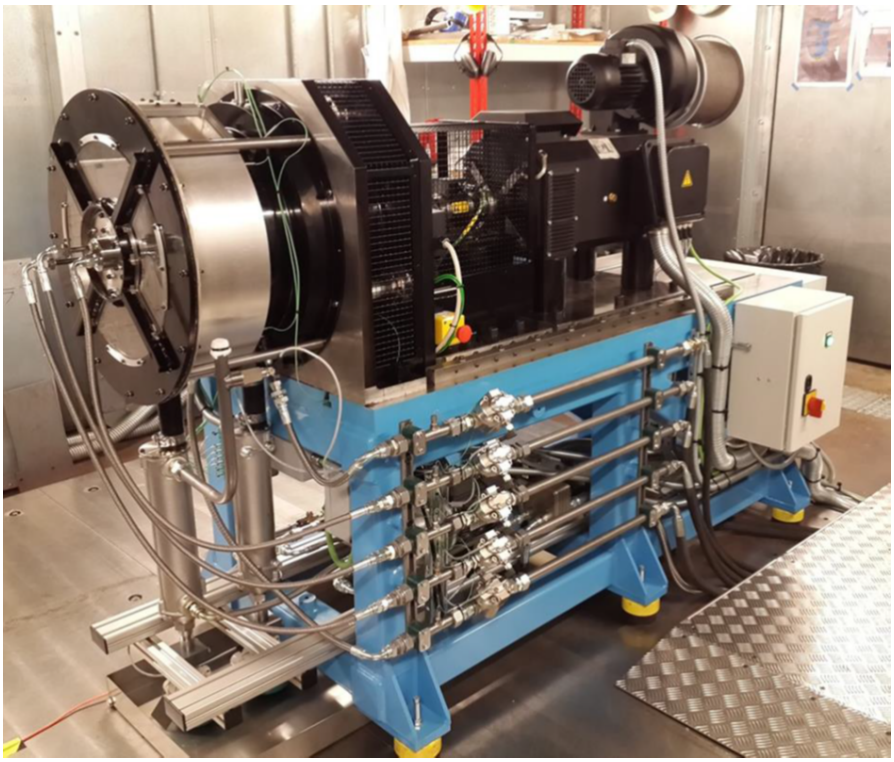


Figure 3.2: G2TRC bearing shedding rig.

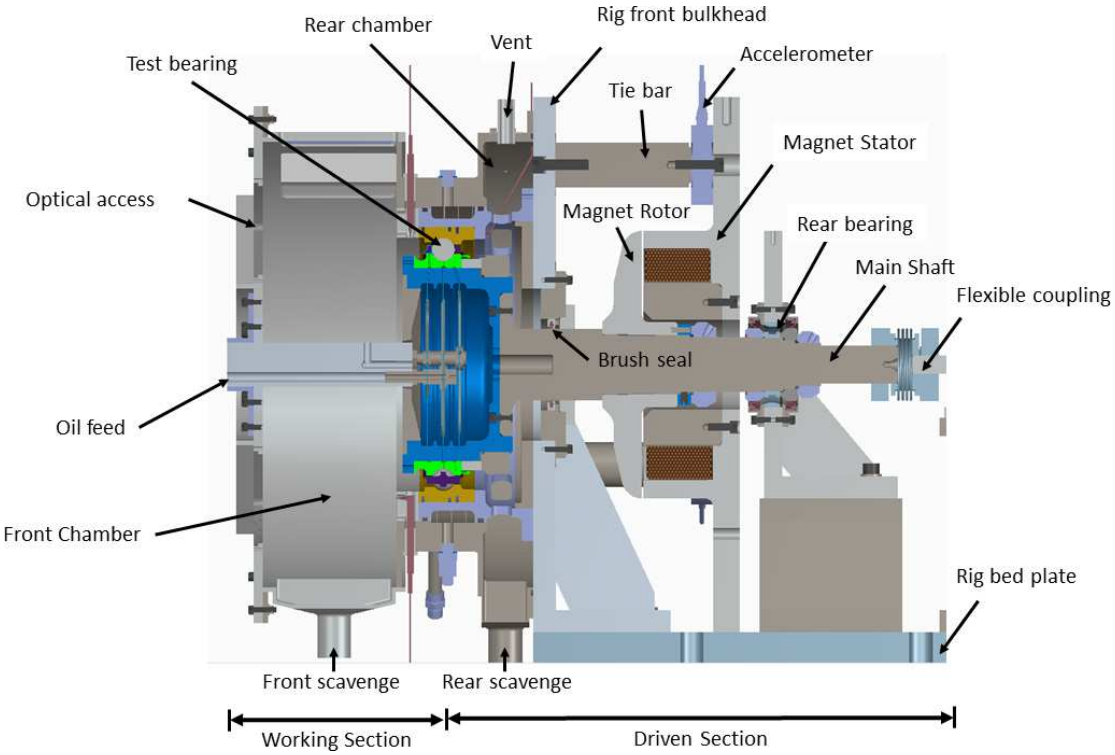


Figure 3.3: Schematic of bearing shedding rig.

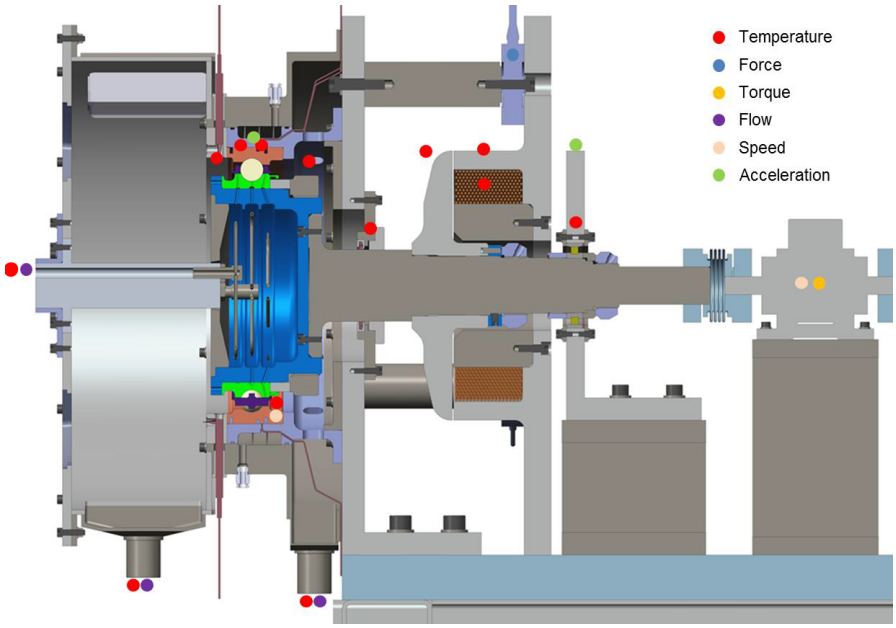


Figure 3.4: Measurement instrumentation built into the BSR.

Table 3.1: Rig Operational limits [73]

Parameter	**Units**	**Commissioned**	
		Min	Max
Shaft Speed	rpm	-	13000
Chamber Pressure	bar g	-0.1	0.1
Maximum Rig Temperature	°C	-	165
Bearing Axial Load	kN	5	35
Total Bearing Oil Feed	$l\,min^{-1}$	3	11
Oil Feed Temperature	°C	35	35

3.1.2 Drive

The rig is driven by an electric 49 kW direct-drive motor and is intended to run up to a top speed of 13 000 rpm [73]. A uni-directional brush seal stops oil from leaking from the rear chamber. Inclusion of this seal means that the rig is only able to rotate in a clockwise direction (as viewed from the front of the rig). The shaft is supported by both the test ball bearing (a large civil aeroengine HP bearing) and a grease lubricated sealed roller bearing at the rear.

3.1.3 Loading

Axial load must be applied to the test bearing to make the contact angle and forces in the bearing representative of those in an aeroengine. This is achieved using an electromagnet which can deliver a uniaxial load between 0 kN and 35 kN, although a minimum axial load of 5 kN is applied during operation [73]. No radial loading is applied to the test bearing beyond that provided by the weight of the shaft.

The axial load is regulated in a closed control loop using process variable feedback provided by three compression load cells mounted at base of the tie bars. The load cells react to axial load applied by electromagnet to the grounded front bulkhead. However, the load cell signal is not exactly representative of the load applied to the bearing.

3.1.4 Bearing Chambers

The front and rear bearing chambers can be seen in Fig. 3.3 to be separated by the test bearing. It should be noted that the rear of the bearing, as it would be installed in the engine, is oriented towards the front of the bearing shedding rig. A separate scavenge exists in each of the two chambers, allowing measurement of oil flows leaving either

side of the bearing. Oil reaches the scavenges by the effect of gravity. Both chambers are vented to the atmosphere, so no differential pressure can be applied across the bearing. This is different from an actual bearing chamber which is pressurised to prevent oil from escaping. The pressure creates an air inflow which influences the mode of air flow in chamber - as investigated for single phase flow by Gorse et al. [12] and discussed in Section 2.1. It is expected that having the chambers vented to atmospheric pressure in the BSR will influence droplet generation in the bearing chamber. The findings by Gorse et al. [16] suggested that increased axial airflow correlates to increased droplet generation. Therefore it is anticipated that droplet generation in this work shall be less than in an aeroengine bearing chamber.

The front chamber has four borosilicate glass windows, at 0°, 90°, 180° and 270° from Top Dead Centre (TDC), which provide optical access and can be removed to provide instrument access. Additional lighting can be provided through the front windows and through windows on the outer chamber wall as shown in Fig. 3.5. Lighting is discussed further in Section 3.2.

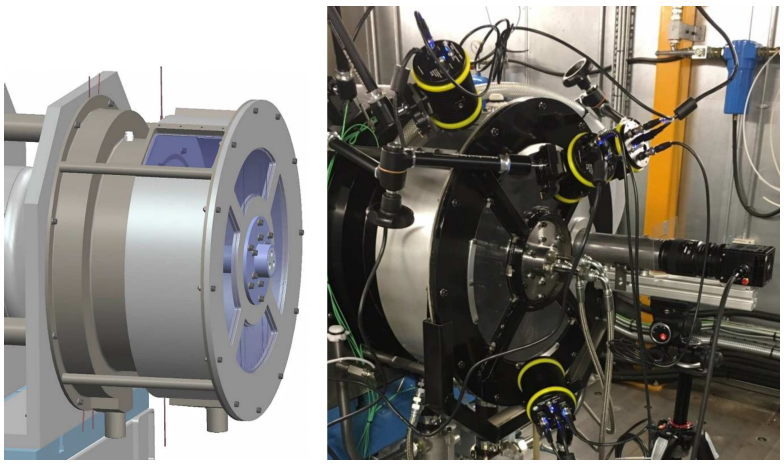


Figure 3.5: Optical access to the front chamber with HS camera (IDT, OS4-S3-M-04) and additional lighting (120E Veritas) set-up for imaging at P2.

3.1.5 Oil System

The oil system on the bearing shedding is a closed-loop system in which oil is supplied to the bearing via delivery tubes, oil enters the bearing chambers where it is then scavenged, filtered and cooled before being pumped back towards the bearing to repeat the cycle. A simplified schematic of the bearing shedding rig oil system is shown in Fig. 3.6.

The physical properties of oil are dependant on temperature, meaning that accurate temperature control is essential to obtaining repeatable data from testing. A feedback

system controls feed pressure and temperature to achieve the desired oil flow rate is delivered at a constant temperature of 35 °C, preventing variation in viscosity or surface tension between tests. The temperature in an aeroengine is much higher than is feasible in experimental work, therefore using the same oil would not lead to aeroengine representative results. The oil used in the BSR was selected as part of the commissioning process in the Innovate UK-funded project SILOET. Non-dimensional groups for rig operation were compared with confidential engine temperature and pressure data and 3 cSt oil (*AeroShell Turbine Oil (ASTO) 390*) was selected. This is the same oil used in all prior work with BSR.

Oil is supplied to the bearing via an under-race feed. Fig. 3.7 shows oil delivery tubes supplying oil to axial channels at three axial locations. Cross-flow between the axial channels is minimised in the design so that oil flow rate to each axial channel can be varied independently allowing the effect of axial distribution of oil supply to be investigated. The oil is centrifuged from the axial channels through separate channels to arrive at the front, mid and rear of the bearing.

A scavenge pumps extracts oil from sumps in the front and rear bearing chambers. The sumps are held at 50% volumetric capacity - apart from at overshoot during initial start-up. Transient phenomenon can be identified by variation in level meter and thermocouple readings, allowing the operator to perform data acquisition only when steady state is achieved i.e. when the oil level in the sump and bearing temperature reach constant value. The flow rate from the front and rear scavenges is representative of oil flow rate leaving either side of the bearing.

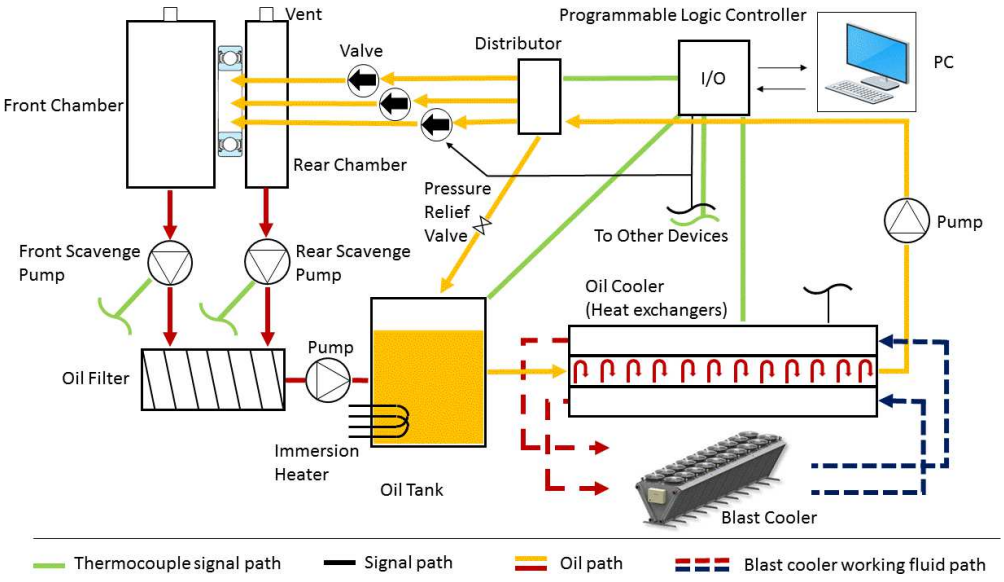


Figure 3.6: Schematic of the bearing shedding rig oil system [8].

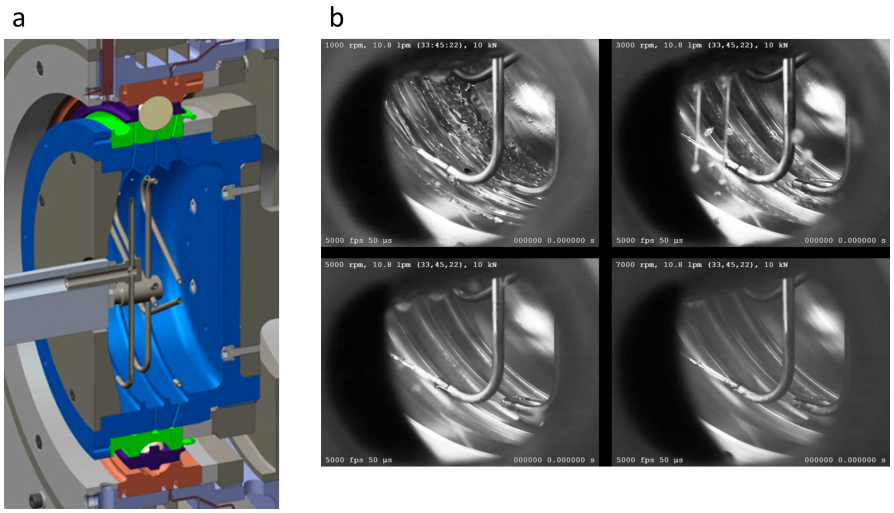


Figure 3.7: (a) oil feed locations (b) oil delivery at 180° from TDC.

3.2 High-Speed Imaging

Two phase flow in the bearing shedding rig is investigated using high-speed optical imaging. LED light sources can be synchronised with the high-speed imaging so additional lighting is provided (as shown in Fig. 3.5) when the camera records an image. Synchronising the lights in this way instead of providing continuous illumination minimises heating of the light head and surrounding parts. The camera used in this work is an IDT, OS4-S3-M-04 and the model of lights used is 120E Veritas.

High-speed (HS) optical imaging can be performed at locations P1, P2, P3 and P4 (0°, 90°, 180° and 270° from TDC respectively) shown in Fig. 3.8. The high-speed camera is mounted on a horizontal traverse allowing precise movement over 50 mm range to focus the image on different axial planes shown in Fig. 3.9. The horizontal traverse has a graduation of 0.5 mm, meaning the camera positioning can be adjusted accurately by very small increments.

Image acquisition and post-processing is performed using *Motion Studio* software. The high-speed camera can be used with either a normal zoom lens (*Nikon AF Micro Nikkor* 60 mm *f/2.8D*) or a long distance microscope (LDM). The sample HS image shown in Fig. 3.10 has a 1024x372 pixel resolution and images a 111.7 mm by 40.5 mm area, as compared to the LDM HS image which has a 1024x1024 pixel resolution and images a 15.25 mm by 15.25 mm area. The optical resolution of images taken using the zoom lens and LDM are compared in Table 3.2. Despite the higher optical resolution of the LDM HS images, HS imaging with a normal zoom lens is to be used in this study due to it's ability to capture image data over a larger area. In order to fully capture the behaviour of oil passing over the lip of the bearing housing, a 1024x1024 pixel image

needs to be captured so that more of the front face is shown, as in Fig. 3.11. A sample image taken on the P2 side (Fig. 3.12) indicates the features observed in HS images.

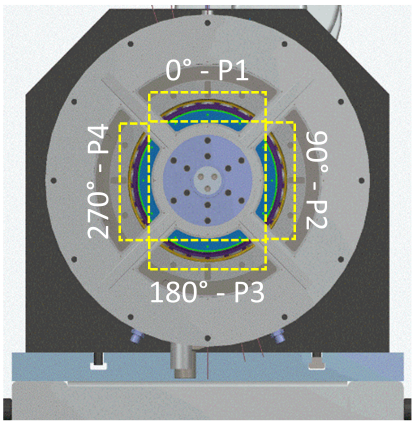


Figure 3.8: Front view of the bearing shedding rig showing the four viewing positions.

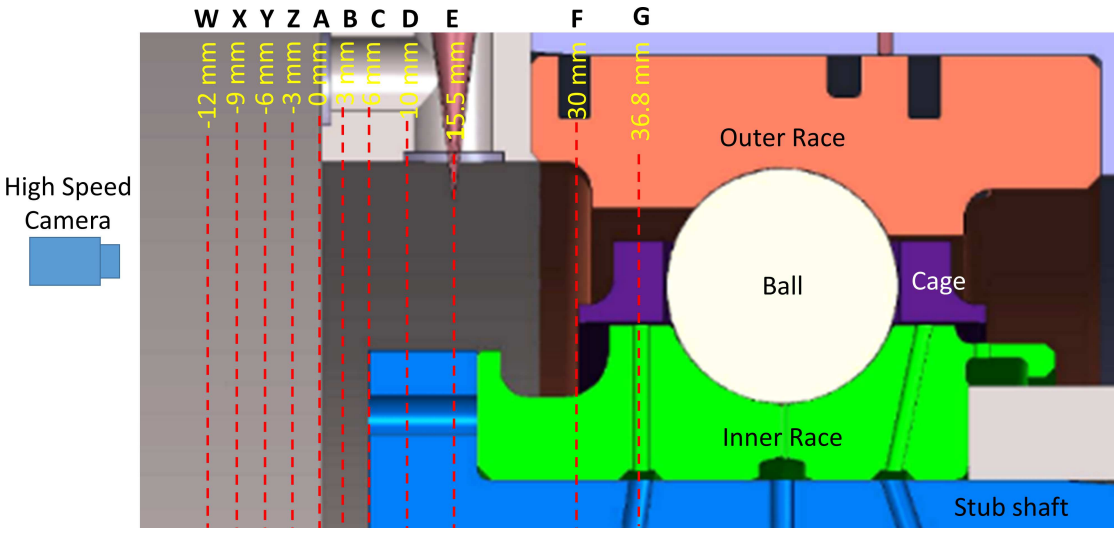


Figure 3.9: Section view of the bearing shedding rig showing the axial planes at which high-speed images are acquired.

The file naming convention used includes information of test conditions to prevent confusion of data. File names are of the form 'SXXXX-FYY-LZZ-PN-Q', where XXXX is the shaft speed [rpm], YY is the oil flow rate [$\mathrm{l\,min^{-1}}$], ZZ is the bearing axial load [kN], N is the viewing position (corresponding to P1, P2, P3 or P4) and Q is the axial plane.

3.3 Experimental Data Collection

The first stage in beginning experimental work is to set-up the HS camera and LED lights for the circumferential position being considered (P1/P2/P3/P4). This requires

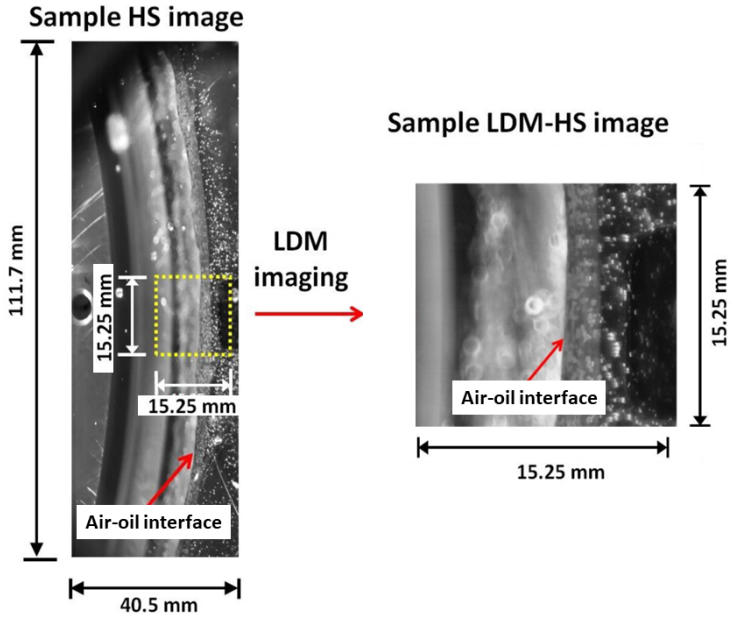


Figure 3.10: Comparison of HS and LDM HS images from Santhosh et al. [73] focussing on the axial plane 0 mm from the front face.

Table 3.2: Resolution of HS and LDM HS images [8]

Description	HS	LDM HS
Horizontal pixel	372	1024
Horizontal length /mm	40.5	15.25
Optical resolution /µm/pixel	108	14.9

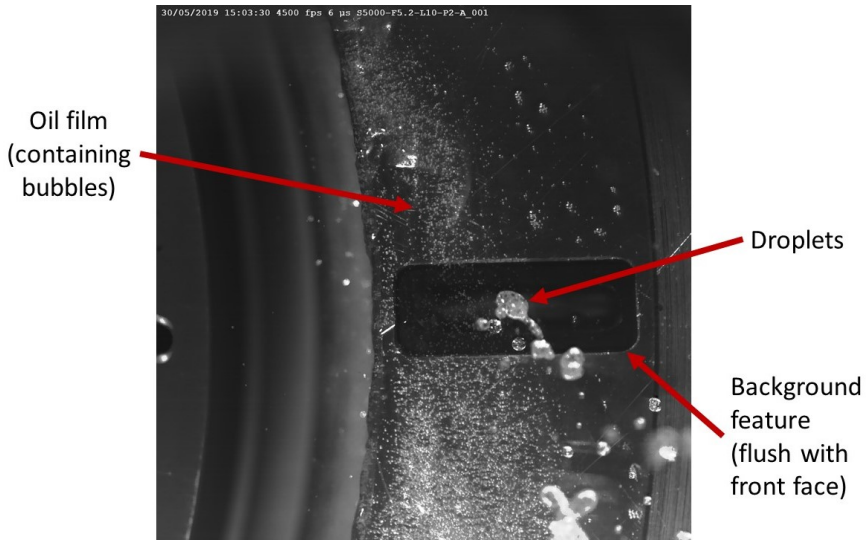


Figure 3.11: 1024x1024 pixel HS image taken as part of this work, showing oil passing over the front face (S5000-F5.2-L10-P2-A).

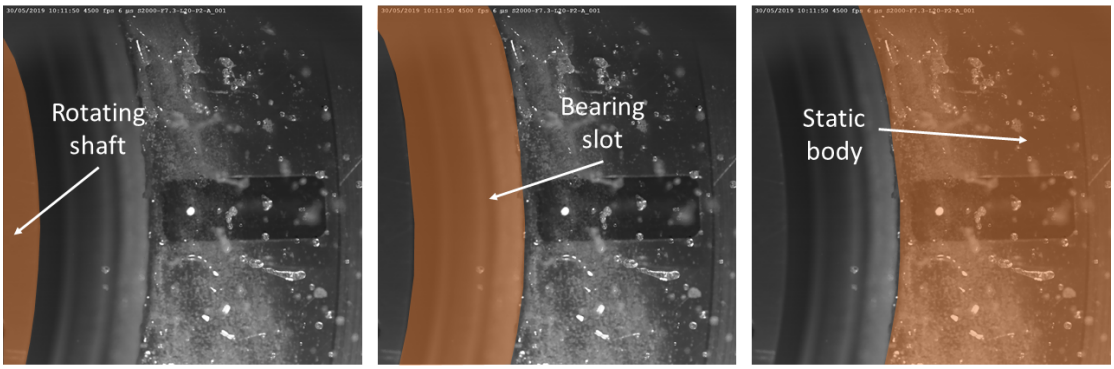


Figure 3.12: Sample HS image taken at P2 labelled to indicate the features visible in the BSR from the instrument access point.

removing the glass window in the relevant position to allow instrument access. The HS camera is then focussed on plane A (indicated in Fig. 3.9) with the horizontal traverse set to the zero position, and the lights are positioned to provide even illumination across the region of interest.

The BSR is driven to the first test point and conditions are maintained. Once thermal stability is reached and the sump level becomes steady, image acquisition is performed using a frame rate of 4500 fps. The process is then repeated for subsequent operating conditions at the set circumferential position. Once all test points are captured for a given circumferential position, the HS camera and lights are moved to the next circumferential position to be considered and image acquisition is repeated for selected test points.

3.4 Experimental Methodology Summary

This chapter presented details of the BSR, including high-speed camera and lighting set-up, as well as a description of the method for experimental high-speed image data collection. Chapter 4 covers the approach used to extract numerical data from the high-speed images for quantitative analysis using automated droplet detection by use of a Convolutional Neural Network (CNN). Chapter 5 goes on to present and discuss the experimental results obtained via this methodology.

CHAPTER 4

Droplet Detection using a Conventional Method compared to a Convolutional Neural Network (CNN)

In this chapter, the process of extracting droplet data using a conventional method of droplet detection in HS images from BSR is compared to a novel Convolutional Neural Network (CNN) methodology. The methodology presented includes droplet tracking through the imaging region, facilitating the analysis of correlations in droplet diameter and speed. Detection accuracy is assessed both in comparison to ground truth data and using metrics. This method provides droplet diameter data that is representative of true conditions and allows for examination of in-plane velocity and behaviour at multiple circumferential positions, but does not include axial droplet velocity information. This data provides an enhanced understanding of two phase flow in an aeroengine bearing chamber. The data can also be used for validation of future computational modelling approaches.

4.1 Conventional Detection

Initial attempts at droplet detection were made through an automated method used in prior work by Vasques et al. [58], Mitchell et al. [74]. These works establish a conventional approach to droplet detection that does not require manual selection of individual droplets in each image frame as the prior state of the art. Image pre-processing removes the temporal average from each image to reduce the effect of static droplets

and features on detection. An adaption of the *MATLAB* script from Vasques et al. [58] was used. This is similar to the detection method used by Mitchell et al. [74] for a single droplet impinging onto a film. Circle detection (for three non-overlapping diameter ranges) and identification of regions with a different brightness intensity to the surrounding image was implemented. Before outputting the droplet diameters and centroid coordinate positions, the script checks for detections in the same location (within a given threshold) to prevent multiple detections of the same droplet occurring.

With an even light intensity across the frame and brightly illuminated spherical droplets (in comparison to background brightness), this method is suitable, however it struggles in non-ideal conditions. Key issues noted are:

- Very small droplets (less than 5 pixel diameter) cannot be identified using circle detection.
- Small droplets (close to the minimum detectable diameter of 5 pixels) are often not detected.
- Droplets with low brightness are often not detected.
- Droplets with inconsistent brightness are often detected with very poor accuracy i.e. only part of the droplet will be detected or multiple small droplets are detected instead of one large droplet.
- Non-spherical droplets are poorly detected - often partial detection.
- Detection of false positives i.e. non-droplet features (such as entrained bubbles, complex three-dimensional oil structures and bright regions on the surface of the oil due to reflections) are detected as droplets.

Using a conventional method of detection, many droplets are not detected (false negatives), some detections occur where there is no droplet (false positives) and some droplets are poorly/inaccurately detected. Detection of a single droplet can be inconsistent between image frames, causing the detected droplet to change diameter or fluctuate in position. An example of this situation is shown in Fig. 4.1 where there are two droplets near the centre of the image that are detected as two (one is only partially detected), then as three overlapping similar sized droplets, then as two similar size droplets plus one small overlapping position - none of which are good representations of the two. Additionally, a droplet towards the lower left corner is not properly detected, only small regions of reflection are detected. This is a common problem across the detections and makes tracking individual droplets more challenging as well is adding considerable uncertainty to results.

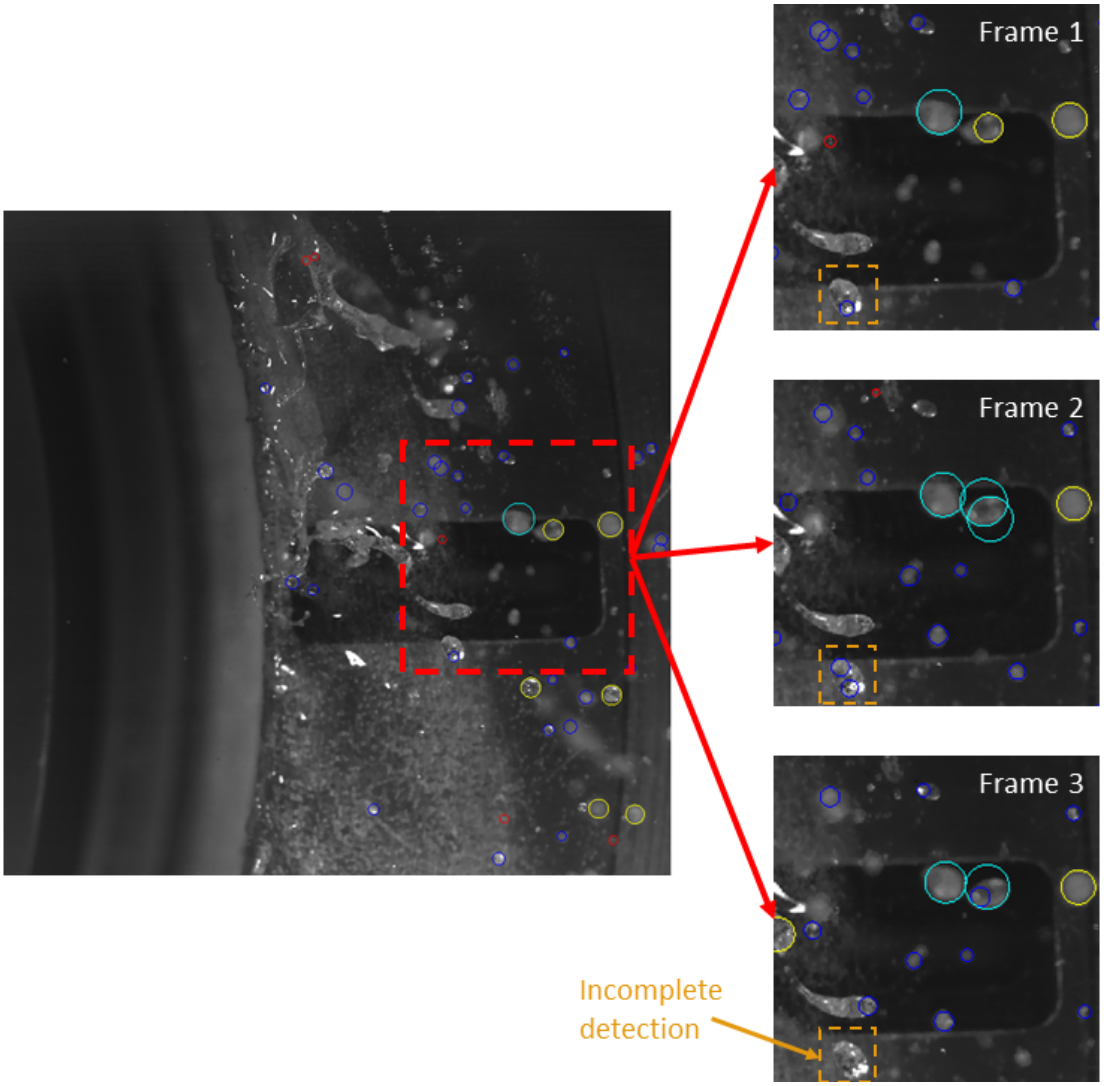


Figure 4.1: Example of droplet detection by the conventional method over a zoomed in area for a sequence of three images.

4.2 Convolutional Neural Network (CNN) Theory

Training and implementing a CNN for droplet detection, or similar, is a time intensive process. A significant level of manual image labelling is required to provide the training, test and validation datasets prior to the relatively computationally expensive process of training and implementing the CNN. However, the pay-off is higher accuracy detection and the potential to detect particles in a more complex environment. Visually similar applications of CNN detections include detection of: particles in multiphase flow [63], agglomerated & partially sintered particles [75], falling droplets [76] and bubbles [61, 77–81]. As such, CNNs are used in many two phase flow detection problems, but never before in an aeroengine bearing chamber.

This section draws heavily from Nielsen [82] in explaining CNN theory. A Neural Network (NN) is a set of algorithms, inspired by the way the brain functions, that is able to learn complex feature recognition to make predictions from an input. A NN has an input layer, one or more hidden layers and an output layer. An example of a simple NN, consisting of only fully connected layers, is shown in Fig. 4.2 and discussed more fully by Nielsen [82]. Activations in one layer are determined by activations in previous layers as information is passed through the network. The activations are calculated as in Eq. (4.1), where $\mathbf{a}^{(n)}$ is column vector of activations in layer n, $\mathbf{b}$ is column vector of biases corresponding to each node on layer n and $\mathbf{W}$ is a matrix containing weights corresponding to every connection between nodes in layer n and layer $(n-1)$. The weight is proportional to the strength of the connection and the bias is proportional to how active or inactive the node tends to be.

$$\mathbf{a}^{(n)} = \sigma(\mathbf{W}\mathbf{a}^{(n-1)} + \mathbf{b}) \tag{4.1}$$

There can be any number of hidden layers, although an increased number of layers increases the computational cost of the network. The output layer produces a numerical value corresponding to the prediction. Semantic segmentation (also known as pixel classification) classifies each pixel in an image into a semantic class [83]. This effectively means that the network is able to predict an overlay of the original image which is colour-coded according to the classes trained in the network. There are many applications of semantic segmentation in the literature including scene understanding (e.g. for autonomous vehicles) [84, 85], detection of nano-particles [86] and bubble detection [81]. Ilonen et al. [59] find that a CNN is able to achieve a higher bubble detection accuracy compared to other methods, although it is not the fastest approach. When real-time data is required, direct bubble size estimation methods were found to be most

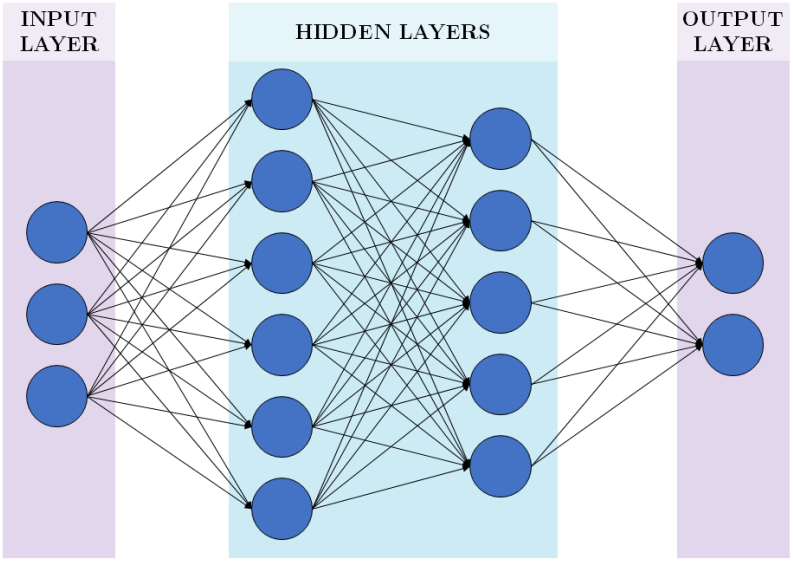


Figure 4.2: Structure of a simple neural network consisting of only fully connected layers.

appropriate however, when speed is not a limiting factor, bubble detection with a CNN is proposed as the best choice. This is due to the high accuracy and inclusion of spatial location information.

A NN is trained using pre-labelled data. Each connection between nodes has a *weight* and a *bias*, as per Eq. (4.1). The NN will adjust the weights and biases to improve its performance on correctly predict outputs in the training data. The way in which the NN determines how to adjust its weights and biases is by finding the minimum of the cost function. For each training example, the NN calculates the sum of the difference between the network outputs and the ground truth output squared as shown in Eq. (4.2) where n is the number of output nodes. This value is the cost of a single training example. The cost is very low when the network makes a prediction with reasonable accuracy i.e. high activation of the correct answer and low activation of all incorrect answers, where the activation corresponds to the probability of the given output. The cost function is the average cost over the set of training data. Prior to training, weights and biases are set at random so initial predictions are likely to have moderate activations on all outputs and produce a very high cost function. In short, minimising the cost function by adjusting the weights and biases improves the accuracy of NN prediction. After training, the NN should be able to make good predictions for similar input data that it has never seen before i.e. anything outside of the training dataset. A subset of the labelled data (not used for training the NN) can be used to test the accuracy by allowing the network to make a prediction and comparison to ground truth.

This allows the calculation of accuracy metrics such as Intersect over Union (IoU) and Boundary F1 (BF) score, discussed in detail in Section 4.4.2.

$$cost = (prediction_1 - truth_1)^2 + (prediction_2 - truth_2)^2 + ... + (prediction_n - truth_n)^2 \tag{4.2}$$

For the purpose of explaining the process of minimising the cost function when training the NN, it is easiest to imagine a one-dimensional problem i.e. where there is one input to the cost function (one connection between nodes, meaning one weight and bias) as in Fig. 4.3. For a simple one-dimensional case, the minima could be calculated explicitly using calculus, however this is not feasible/possible when the problem is expanded up to hundreds or thousands of network connections, weights and biases as in more realistic problems. Instead the network is initialised with a random set of weights and biases and the gradient of the cost function is calculated at that point. The gradient indicates the direction in which the weights and biases must be adjusted. The adjustment of weights and biases and calculation of the gradient of the cost function are repeated until a local minimum is reached. It should be noted that minimising the cost function increases the performance over the entire training dataset and not necessarily for every individual input sample (i.e. it is possible that a training example that was predicted correctly before could now be predicted incorrectly or with less certainty) since the cost function is calculated over the entire training set. This process is called gradient descent.

The magnitude of adjustment made to weights and biases is generally made to be proportional to the gradient of the cost function, preventing overshoot of the minima or excessive time to reach the minima. It should be noted that the final solution may not be the global minima. For this reason, it is valuable to train the network from multiple random initialisations and select the network that produces the best prediction accuracy. Initialising the CNN with a different set of weights and biases means that it is likely to reach a different minima, and therefore the global minima is more likely to be obtained, at which point the prediction accuracy will be best.

From here, it is relatively easy to think of a two-dimensional optimisation landscape where there are two inputs (weights and biases) influencing the cost function. In this case there would be a three-dimensional surface and gradient descent can be pictured as a ball rolling down the hill and eventually settling in a hollow. Increasing the number of inputs to the cost function adds more dimensions to the optimisation landscape, making it impossible to visually represent, however the concept does not change. To illustrate the complexity of this, a fully connected NN used to recognise digits in the

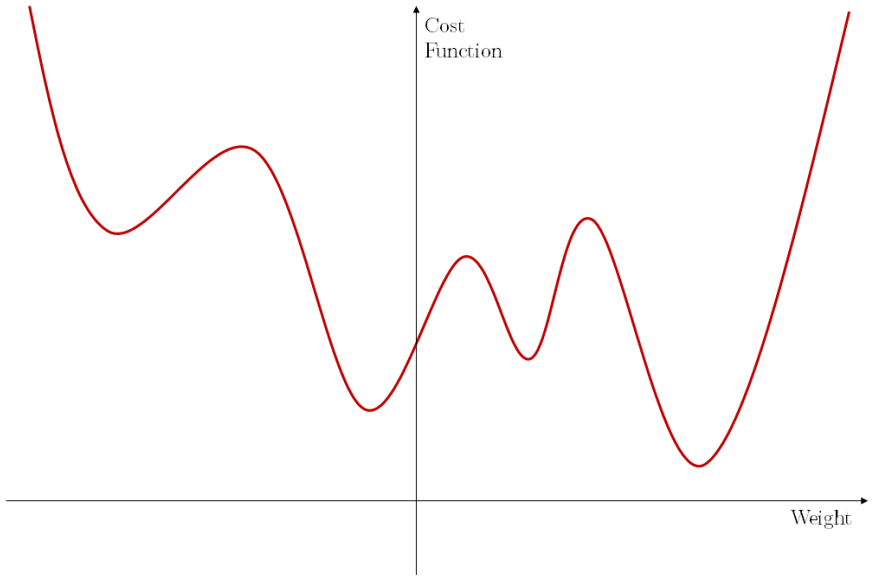


Figure 4.3: Example of variation of the value of the cost function with change in weight.

MNIST dataset has 28 x 28 (=784) input nodes. If there are two hidden layers, each with 16 nodes, and 10 output classes (for digits 0 to 9) then there will be 13,002 weights and biases in the NN.

Computers take a long time to sum the cost of a single training example, therefore processing every gradient descent step for the entire dataset in one go is hugely expensive and requires large amounts of memory. Instead, the training dataset is randomly grouped into a set of "mini-batches" and back propagation is performed for each mini-batch. Back propagation is an algorithm used for calculating the gradient of the cost function (explained in detail by Nielsen [82]). Compared to minimising the output of the cost function based on the whole dataset, using mini batches provides a less direct route (the direction of "nudges"/adjustments to weights and biases towards the minima are less accurate), but allows each step to be made far more quickly so that the minima is found much faster overall.

Information from a two-dimensional input image is extracted in a different way when using a CNN compared to when using other types of NN. Instead of extracting the data from individual pixels and passing it downstream, information is taken from a local receptive field. This is a region of the image from which connections are made to the subsequent layer. The convolutional layer itself uses local receptive fields and shared weights, making the CNN able to process two-dimensional information. A CNN is designed to make predictions from an input image. The output can be classification of the image or detection of where in an image a particular feature is. A pooling layer

normally follows immediately after the convolutional layer to collate the information from each region.

The position of the local receptive field steps across the image (also known as the sliding window approach) in a way that corresponds to the nodes in the first hidden layer. In Fig. 4.4 a receptive field of 5 x 5 pixels with a stride length of one is shown. This simply means that data from a 5 x 5 pixel region corresponds to a single node in the first hidden layer and that the local receptive field shifts by one pixel (either horizontally or vertically) for the next node in the corresponding direction. The setup in this example means that the first hidden layer is 24 x 24 nodes. It should be noted that the size of the local receptive field and stride length can be different from that shown in this example, however the numbers will be maintained in this explanation for simplicity.

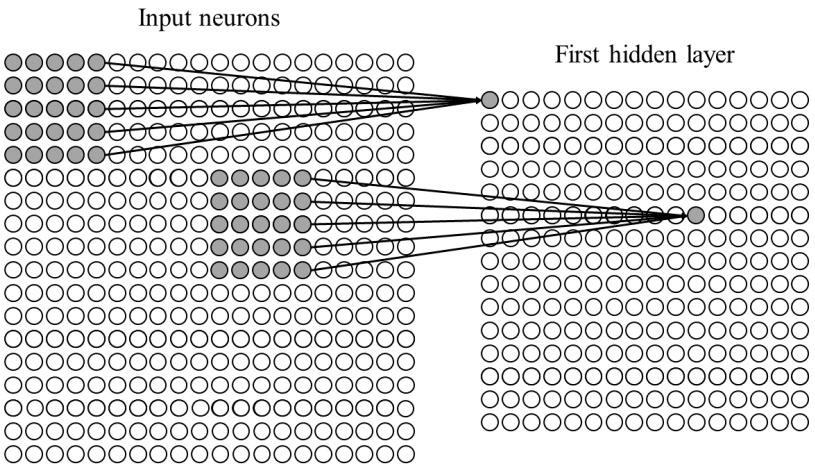


Figure 4.4: Mapping of input neurons to the first hidden layer of a CNN (image adapted from Nielsen [82]).

Each local receptive field in this example has 5 x 5 weights and a single bias connecting to the corresponding node in the first hidden layer. All the nodes in the first hidden layer are used to detect the same feature. The node will be activated if the feature is present in the corresponding local receptive field's feature map. The feature map has the same size as the local receptive field and can be represented by an image with pixel brightness intensities proportional to the weight of that position. Features may include edges, textures or any other type of shape.

Since realistic images include more than one type of localised feature, multiple feature maps are required in a complete CNN. For simplicity, only three feature maps used in convolution are illustrated in Fig. 4.5 (the layer with dimensions 3 x 24 x 24). Following the convolution, pooling is performed (this is how data is transferred to the 3 x 12 x 12 layer). There are multiple types of pooling layers, all of which simplify the information

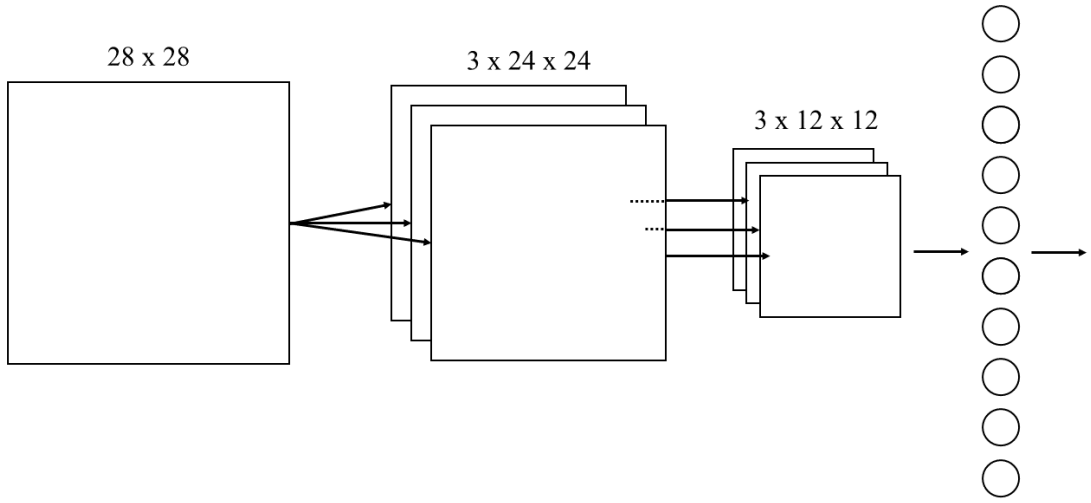


Figure 4.5: Structure of a CNN used to classify digits in the MNIST dataset (image adapted from Nielsen [82]). The layers shown are as follows: input layer, convolutional layer, max pooling layer and fully connected layer. The arrow extending from the fully connected layer leads to the output layer (not shown in this figure).

output from convolutional layers. One unit in the pooling layer can be used to summarise a larger region in the convolutional layer, thereby reducing the size of the data. A common form of pooling is max-pooling, which outputs the maximum activation in the region that it represents. The method of max-pooling is demonstrated in Fig. 4.6 for a small number of data points using a 2 x 2 region. The region is moved across each feature map, and in every position the largest number contained by the region is transferred to the corresponding placement in the max-pooling layer. Additional hidden layers follow the pooling layer before the output layer. Different CNNs may have different size feature maps, pooling region and/or stride length and have a different architecture following the pooling layer.

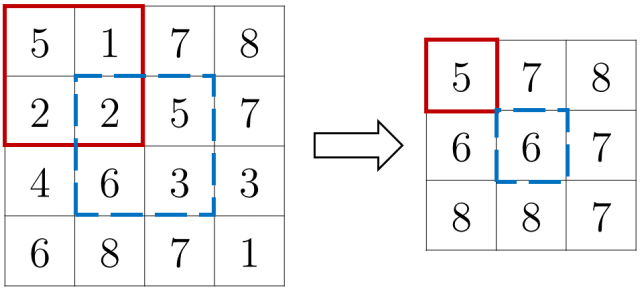


Figure 4.6: Max pooling using a 2 x 2 region.

Common leading-edge applications of neural networks include computer vision for self-driving cars and identifying features in medical imaging [87–89], among many

others [61–63, 75–81]. In self-driving cars, even in a simple scenario where there are no other vehicles/moving objects, real-time image processing is needed to identify the road and tell the steering how to remain on the road. Adding components of a more realistic scenario means recognising pedestrians, crossing zones, cyclists, other cars, road signs etc. as in Fig. 4.7 as well as controlling acceleration and braking.



Figure 4.7: Example of semantic segmentation (the *output* image here is labelled data showing the ground truth, not an actual prediction from ResNet-18) [90].

4.3 Droplet Detection Methodology

This section describes the methodology implemented to detect droplets in HS images taken on the BSR. Large numbers of droplets per frame combined with long imaging sequences make manual droplet identification unfeasible. Example images are shown in Section 3.2. Automated image processing is needed to deal with the high quantity of image data and convert it into a numerical format to allow droplet tracking and quantitative analysis.

4.3.1 CNN Droplet Detection Process Overview

The process used to extract numerical data from high speed images for quantitative analysis is outlined in Fig. 4.8 and detailed below:

1. A background removal step is used to generate the input image for the CNN.
2. The CNN detects droplets and outputs a binary mask indicating where droplets exist in each image in the sequence. This is a colour-coded image where white indicates a droplet has been detected in the given pixel position and black indicates there is not a droplets.

3. Droplet position data and equivalent diameter is extracted from the masks and accumulated into an array with columns for the following data:
   (a) x coordinate of centroid position
   (b) y coordinate of centroid position
   (c) equivalent diameter
   (d) frame in which droplet was detected
4. A tracking algorithm assigns an ID to each droplet, allowing temporal data to be obtained and enabling analysis of the number of droplets rather than the number of instances of droplet detection.
5. All distance measurements are converted from pixels to SI units and droplet velocities are calculated. Quantitative analysis follows.

4.3.2 Image Pre-Processing

Some of the difficulty in droplet detection arises from the complexity of the image background and the variation in brightness intensity across time and in separate test runs – even when no changes are made to the lighting or high-speed camera setup. Preprocessing the images before feeding them into the CNN can help reduce this issue. It should be highlighted that the images used to train a CNN must have the same preprocessing as those for which predictions are to be made i.e. the network needs to learn what the input images are expected to look like if it is to make accurate predictions.

A relatively simple way to reduce the image complexity and variation is to perform background removal. This is achieved by subtracting the temporal median value from each image in the sequence. The stages of background removal are shown in Fig. 4.9.

Preprocessing images in this way means that the images input to the CNN are of a more consistent brightness and have reduced appearance of background features; both from solid parts of the test rig and regions where the bubbly film persists. This does not eliminate all non-droplet features, only those that do not move.

4.3.3 Transfer Learning From a Pre-Trained CNN

An alternative to building and training a new network is to use transfer learning from a pre-trained network. This means taking a CNN that has already been trained for a different application and training it to perform droplet detection in the context of the

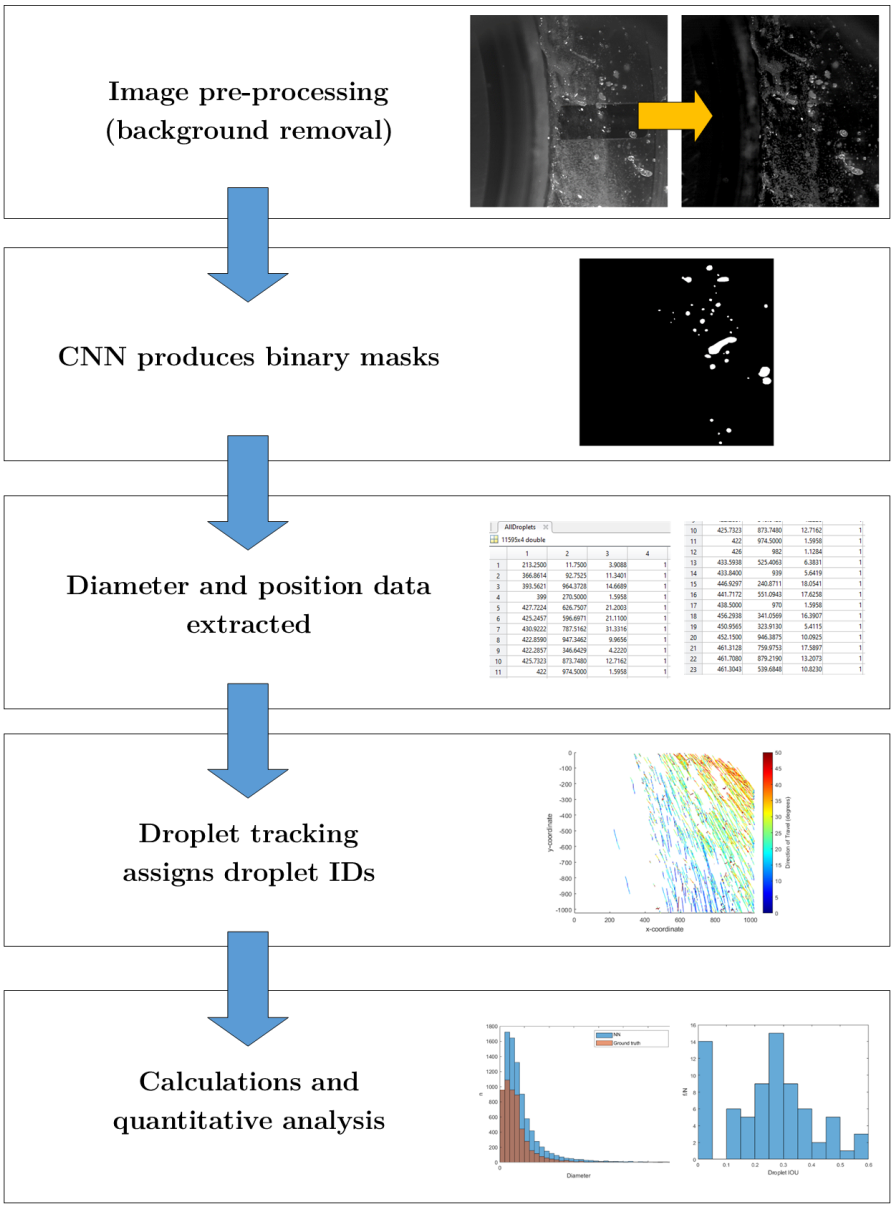


Figure 4.8: Flow diagram of the droplet detection and quantitative analysis process.

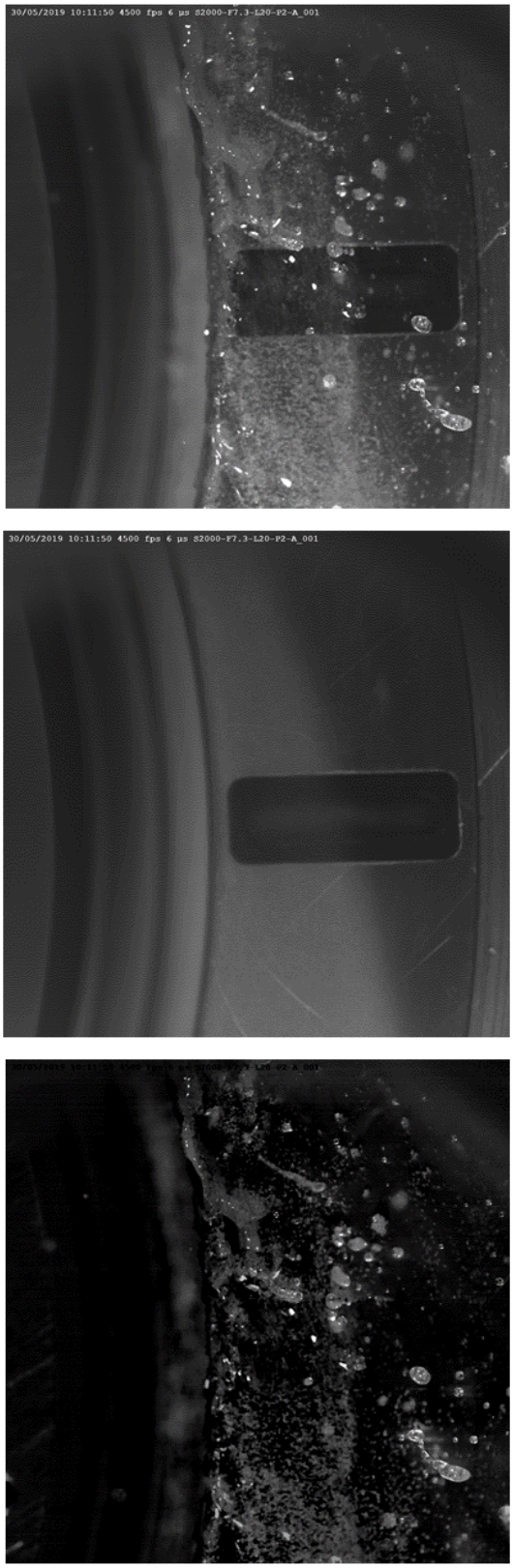


Figure 4.9: *Top:* original image taken on the BSR using high-speed camera. *Middle:* temporal median image. *Bottom:* preprocessed image (temporal median image subtracted from the original image - note that brightness and contrast are modified for better visibility).

high-speed images taken using the BSR. Training a newly built CNN requires a very large quantity of training data to facilitate recognition of both high and low level features, whereas a pre-trained CNN already has reasonable values for activation weights in the earlier layers and is therefore able to recognise features of the image. Transfer learning normally requires far less training data than would be required to train a new network to achieve the same level of accuracy since a new CNN is initialised from random weights and biases rather than from reasonable values which need only small adjustments for the new application.

4.3.4 Labelled Data for Training the CNN

Manual image labelling is performed to produce a training set of 326 images plus 109 validation images and 109 test images. Assuming 40 droplets per image, training data includes approximately 13000 droplets and validation and test images contain approximately 4300 droplets each. A comparison between a sample original image and its ground truth mask is shown in Fig. 4.10. Images used in training must be representative of the whole dataset, therefore images were selected from a range of operating conditions. Since multiple images are labelled for each operating condition, consecutive images are avoided to prevent the same liquid feature being present in more than one training image.

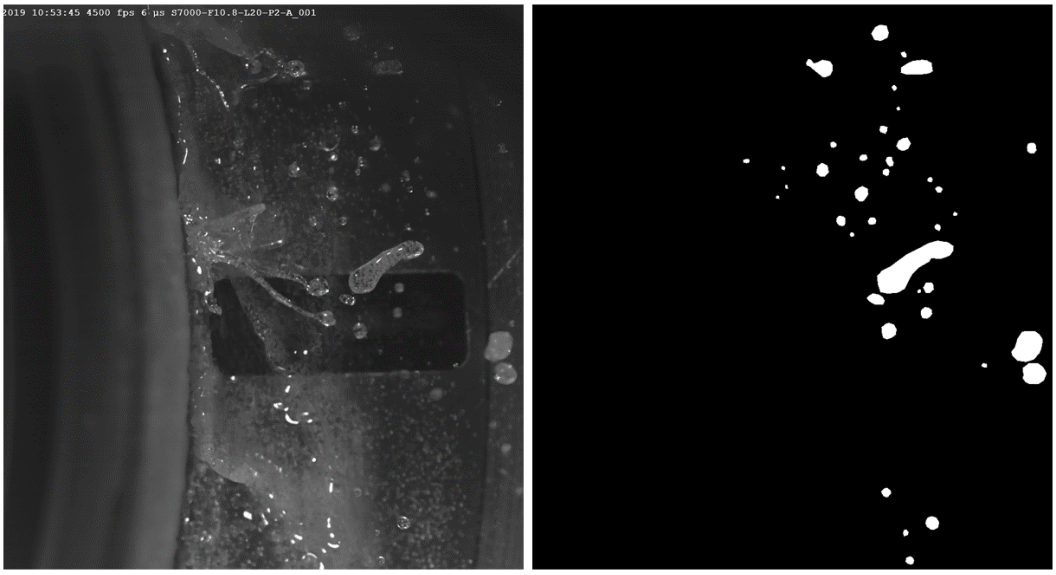


Figure 4.10: Original image alongside the ground truth labelled mask.

4.3.5 Selection of Potential Pre-Trained CNNs

Chaussonnet et al. [60] looks at segmentation of atomised droplets in degraded optical conditions using CNNs. VGG-16 was found to detect more droplets than the ResNet architecture, however little information is provided as to how significant the difference was. Comparison between the CNN data (VGG-16) and ground truth shows good agreement, meaning the methodology is suitable for droplet detection in the application considered by Chaussonnet et al. [60].

MathWorks [91] provides a comparison of pretrained networks' performances on the ImageNet [69] validation set. The networks shown in Fig. 4.11 have been trained on over a million images to classify 1000 object categories. An ideal network is high accuracy and runs quickly. ResNet-18, VGG-16 and VGG-19 achieve a similar accuracy, however ResNet-18 has a significantly lower relative prediction time. For this reason, ResNet-18 is selected in favour of VGG-16 or VGG-19, despite the findings of Chaussonnet et al. [60]. Deeper ResNet networks (ResNet-50 and ResNet-101) achieve higher accuracy at the expense of being slower to run - however these both have a shorter relative prediction time than the VGG architectures. For this reasoning, the three ResNet networks are considered in this work. Details of each are given below.

ResNet-18 This is an 18 layer deep CNN. A pre-trained version of ResNet-18, available in *MATLAB*, is able to perform semantic segmentation for the 32 classes from Brostow et al. [92]. The CNN accepts an image input size of 224x224 pixels in RGB. However, images from the BSR are 1024x1024 pixel greyscale images. The following changes are needed for this application:

- change the number of semantic segmentation classes to two (*droplet* and *not droplet*), as per MathWorks [90].
- Change the CNN input image size to 1024 x 1024 pixels, as per MathWorks [90].
- Convert high-speed images from greyscale to RGB - this means duplicating the greyscale data into the three RGB layers to make the data 1024x1024x3 instead of 1024x1024x1 (image still appears as greyscale but data format is accepted by the CNN).

ResNet-50 ResNet-50 is very similar to ResNet-18 apart from being 50 layers deep. The greater number of layers allows higher accuracy [93], but also increases relative prediction time.

ResNet-101 This is another very similar pre-trained CNN except this is 101 layers deep. Again, more layers means a higher prediction accuracy [93] with increased relative prediction time.

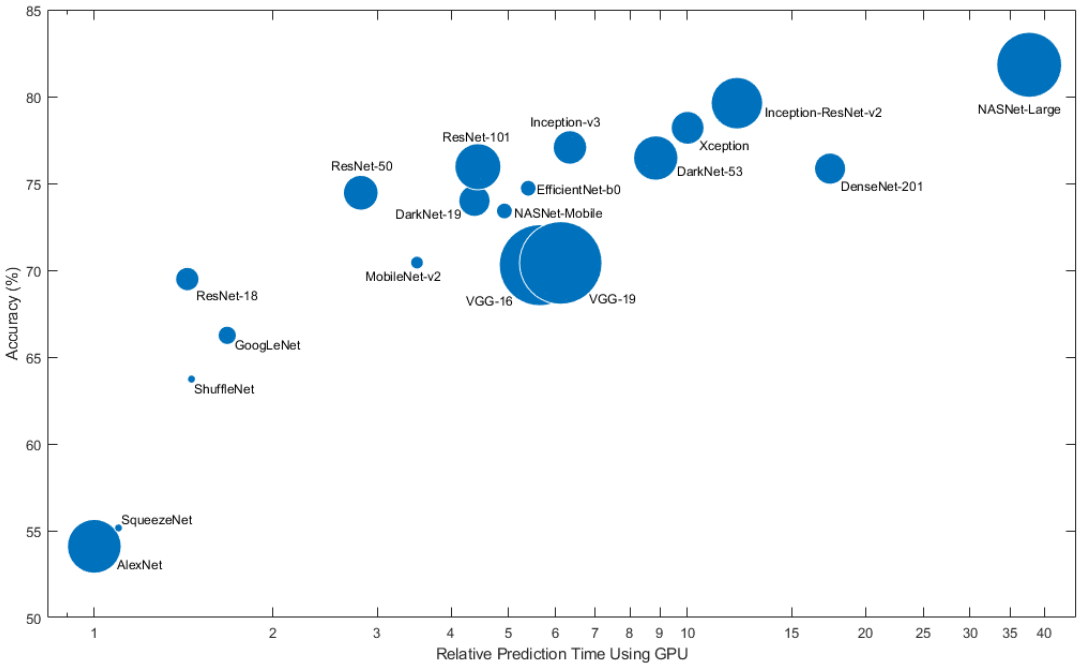


Figure 4.11: Comparison of pretrained networks' accuracy on the ImageNet [69] validation set and relative prediction time using a GPU [91].

4.3.6 CNN Implementation and Data Extraction

The fully trained CNN is applied to an image sequence to produce a series of predictions/output masks. Note that two partially overlapping droplets are treated as a single overly large droplet. Numerical droplet data is extracted from the output masks using the *MATLAB* function *regionprops* to produce an array containing the following information:

- x-position of the centroid
- y-position of the centroid
- equivalent diameter
- image number in which the detection occurred

Droplet tracking and subsequent calculations can be performed using this information as described in Sections 4.3.7 and 4.3.8.

4.3.7 Droplet Tracking

Calculating droplet velocity without assigning droplet IDs (by matching droplets across neighbouring frames of an images sequence within a set distance of the starting position) has several significant disadvantages:

- There is no way to correlate velocity and diameter of droplets.
- Incidences of a single droplet may be incorrectly paired across frames.
- Droplet statistics use the number of instances of detection rather than the number of droplets with given characteristics.

To prevent these issues, a tracking method which assigns an ID to each droplet is implemented. The tracking function available from Blair and Dufresne [71] is used. Droplets are tracked through time and an ID is assigned to each incidence of detection. The ID is maintained for a droplet for as long as it can be identified as the single droplet moving through time. There are cases where the droplet may not be able to be matched to its earlier path, in which case a new ID is generated for the same droplet. Once droplet IDs are assigned, further calculations can be performed.

4.3.8 Calculation and Quantitative Analysis

Spatial calibration is needed for the conversion of droplet diameters and distance displacement between images (for calculation of droplet in-plane speed) from pixels in standard units. The spatial calibration factor is obtained by finding the pixel distance between two points with a known separation - physical features in the BSR can be used for this. The detected area of a single droplet varies from frame to frame, so the mean diameter value is assigned to each droplet ID. This is done to minimise the effect of one inaccurate detection of the observed droplet area and to give the best representation of true droplet diameter. In-plane direction of travel and droplet speed is then calculated. It should be noted that the axial velocity component is not included due to the two-dimensional nature of the HS imaging approach.

Droplet ID is maintained for these parameters, allowing correlation of behaviours for individual droplets to be examined. Paths taken by the droplets can be plotted and coloured by diameter, speed or direction to allow visualisation of any trend in the parameters with spatial positioning in the bearing chamber. Probability distributions and correlations between droplet diameter, speed and direction are also plotted in Chapter 5.

4.4 Assessment of Droplet Detection CNNs

A method of assessing the accuracy of droplet detection by the CNN is needed to provide an indication of whether the data can be treated as representative, and allow comparison of the different networks' capability. A comparison to ground truth data is used for this purpose, alongside a number of metrics commonly used in literature as discussed in Sections 4.4.1 and 4.4.2.

4.4.1 Comparison of Detection Data to Ground Truth

Comparison of droplet data from CNN detection to the ground truth is made to examine how accurately the data obtained from the experimental work using the CNN represents true droplet behaviour in the bearing chamber. Droplet data from each of the three CNNs discussed in Section 4.3.3 is considered in this way.

Ground truth data is obtained by extracting quantitative droplet data from manually labelled masks using the same approach that is used in normal data processing following CNN implementation. The process of manually labelling *ground truth* data is itself subject to error due to human variability. Interobserver variability was investigated by Webb et al. [94] for segmentation of ultrasound images. Three experts labelled the same data, segmenting the region of the image containing benign or malignant masses, and achieved a mean Fleiss kappa value of 0.78, indicating good but imperfect agreement. Comparatively, including the optimised deep learning model increased the mean Fleiss kappa value to 0.79. Sanders et al. [95] considered interobserver variability in labelling 50 test MRIs. A lower variability was found in measurements by three radiation oncologists (specialists) compared to four other clinical observers. This indicates significance of observer familiarity with images and means that the data considered to be ground truth in this work is subject to the understanding of the two phase flow behaviour in the images that the expert performing the labelling process has. Based on the findings of Webb et al. [94], Sanders et al. [95], reasonable confidence in ground truth labelling by a single expert can be assumed.

Droplet diameter distribution data from the CNN is plotted against ground truth for the 75 test images in Figs. 4.12 and 4.13. In all cases, the CNN over predicts the number of droplets. Despite the over prediction of the number of droplets, the shape of the diameter distribution detected is very similar to that of the ground truth. The networks trained from ResNet-50 and ResNet-101 more closely match the ground truth. ResNet-50 is the computationally cheaper of the two and is therefore more appropriate given it produces the same results.

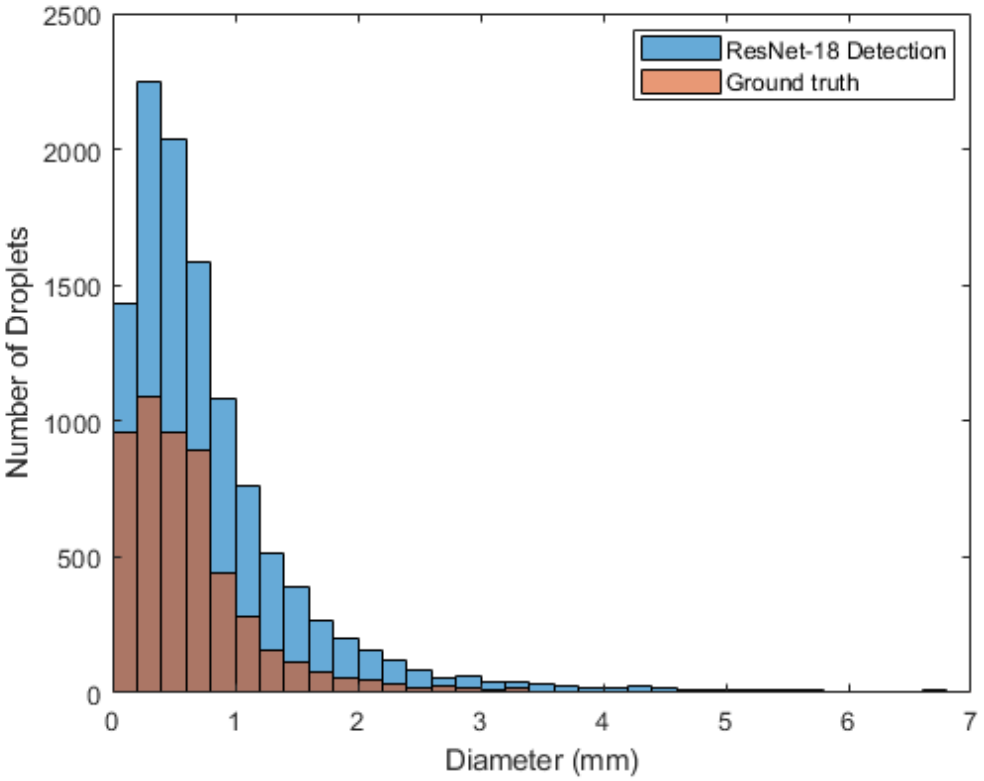


Figure 4.12: Diameter distribution of droplets detected by the CNN trained from ResNet-18 compared to ground truth solution for the 75 test images.

It is likely that many features causing a false positive are not consistently detected through time (e.g. a transient effect such as a brightly reflected region on the oil film), meaning that the tracking process used to assign droplet IDs is able to remove these. The tracker assigns an ID to every droplet detected allowing the droplets with a low number of instances of detection to be excluded from the data. For this reason, comparison between the raw CNN prediction and ground truth is not sufficient to assess the agreement between the data used for calculations and real behaviour. Droplets are tracked across a range either side of the test image for a better comparison with ground truth. A sequence of 101 images centred on each test image is used to track the droplets. Once tracking has been performed for all 75 of the test images, droplet data from each test image can be combined into a single array and compared to the ground truth and to the raw detection to see how implementing the tracking process affects agreement with ground truth.

Fig. 4.14 presents a comparison of the raw CNN predictions (untracked), the droplet data following tracking (tracked) and ground truth. The tracking process can be seen to have removed a large number of droplets from the data, producing a closer agreement with ground truth. Near-perfect agreement occurs for droplets with a diameter above

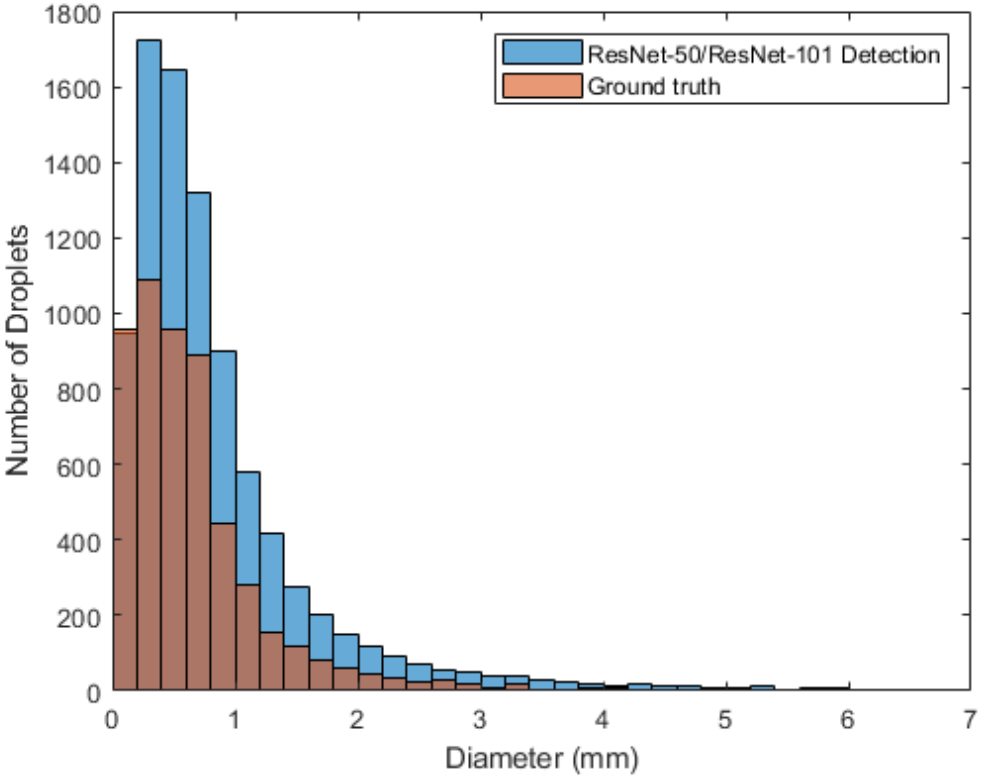


Figure 4.13: Diameter distribution of droplets detected by the CNN trained from ResNet-50 and ResNet-101 compared to ground truth solution for the 75 test images.

0.8 mm, while smaller droplets are under-detected. Droplets with a diameter between 0.2 mm and 0.8 mm are predicted reasonably well, but droplets smaller than 0.2 mm are significantly under predicted. Implementing droplet tracking and the associated filters puts the Sauter Mean Diameter (SMD) in much closer agreement with ground truth. SMD is calculated as in Eq. (4.1). Tracked CNN data has an SMD of 0.77 mm compared to the untracked data of 0.79 mm and the ground truth of 0.75 mm. The accuracy of detection for very small droplets is likely limited by the image resolution and therefore the number of pixels per droplet. Higher resolution imaging, as could be achieved using a long-distance microscope, may resolve this issue, but would mean compromising on the size of imaging area that can be considered for droplet tracking. This would mean that only a small portion of the bearing chamber could be considered and individual droplets would be tracked for a shorter period of time.

$$SMD = \frac{\mu d^3}{\mu d^2} \tag{4.1}$$

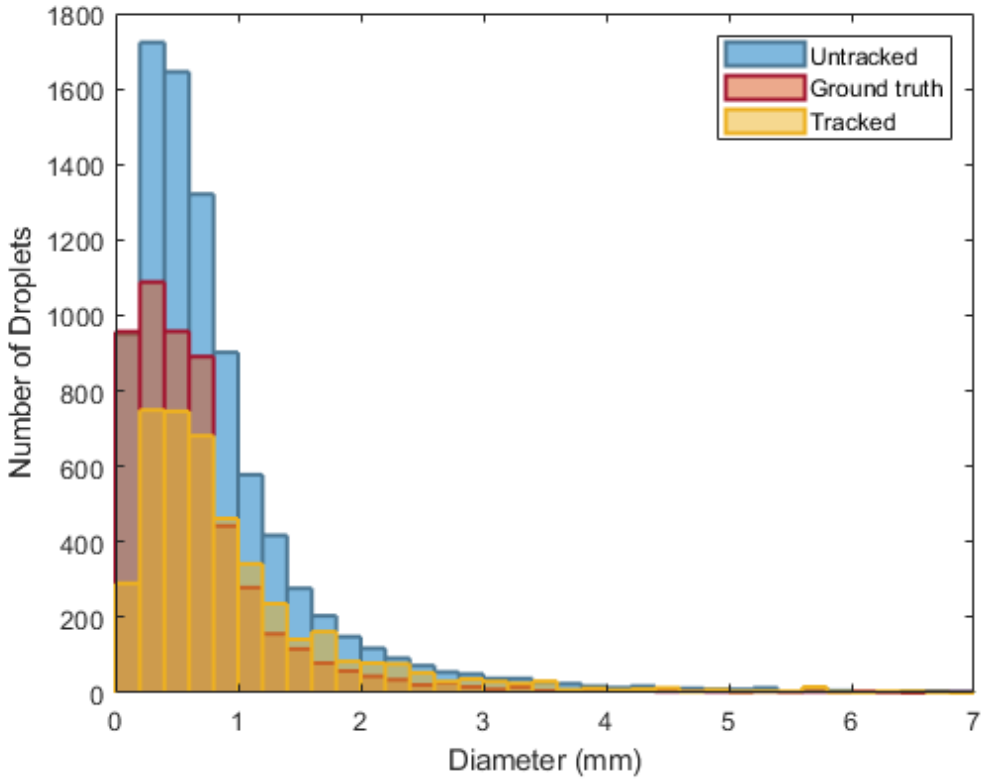


Figure 4.14: Diameter distribution of droplets detected by the CNN trained from ResNet-50, before and after excluding detections using the tracking process, compared to ground truth solution for the 75 test images.

The droplet diameter distribution detected by a conventional method for a test set of

75 images is shown in Fig. 4.15 compared to ground truth values and CNN droplet detection (for the CNN trained from ResNet-50). The diameter distribution detected by the CNN is a significantly better representation of ground truth values compared to the detection by the conventional method which fails to detect the vast majority of droplets with diameter less than 0.8 mm. Therefore, the approach is deemed less viable for droplet detection in this application. The Sauter Mean Diameter (SMD) calculated from the conventional detection method is very close to that from CNN detection (both at 0.79 mm compared to the ground truth value of 0.75 mm) despite the obvious difference in the shape of diameter distribution shown in Fig. 4.15, where the CNN data is a much closer fit to ground truth.

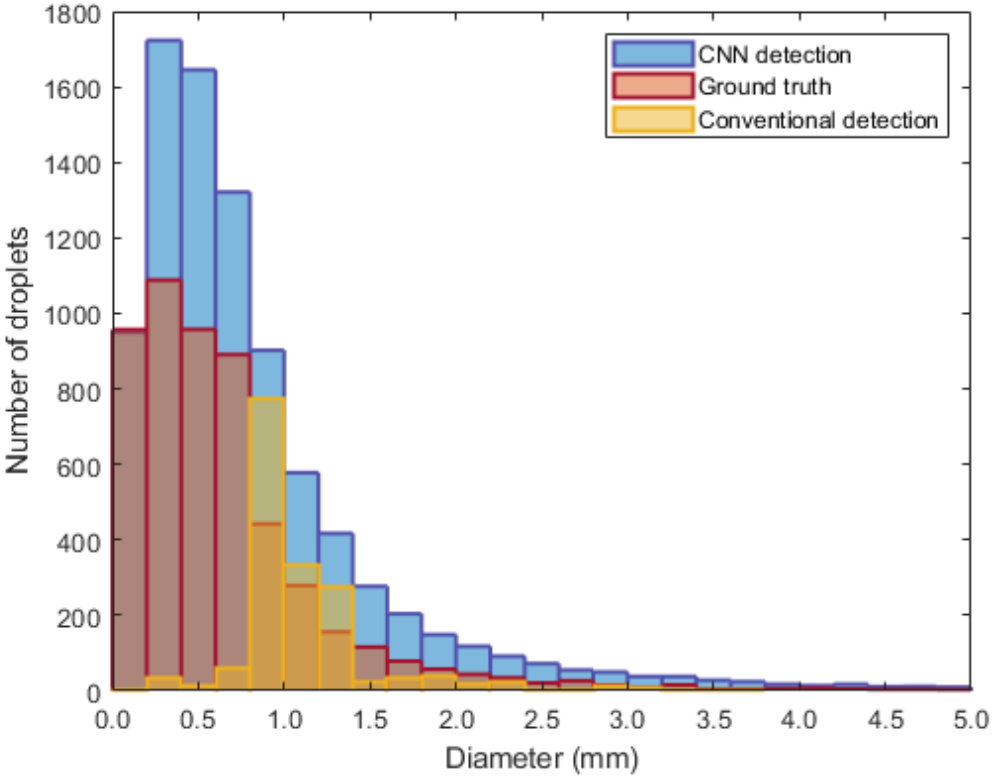


Figure 4.15: Diameter distribution in 75 test images as detected by conventional droplet detection and CNN droplet detection compared to the ground truth values.

4.4.2 Metrics

Intersect over Union (IoU) is often used to assess the level of agreement between the prediction and ground truth in semantic segmentation problems. This metric gives a score between zero and one, where zero indicates no overlap and one indicates ex-

act agreement. IoU is calculated as in Eq. (4.2), and the concept is shown visually in Fig. 4.16. The IoU gives a good indication of overall agreement with the ground truth, but has the following limitations:

- A low score does not indicate whether the total area of droplets detected in an image is greater or less than that of the ground truth.
- There is no relation to the number of droplets detected or how well individual droplets are detected (i.e. how close the detection is to the true size and shape of the droplet).
- There is no way to distinguish between a false positive pixel detection being a random pixel in the image or an over prediction of a droplet diameter - the former is much worse in this application.

Therefore, it is necessary to use additional metrics alongside IoU to assess droplet detection accuracy.

$$IoU = \frac{\text{Area of Intersection}}{\text{Area of Union}} \tag{4.2}$$

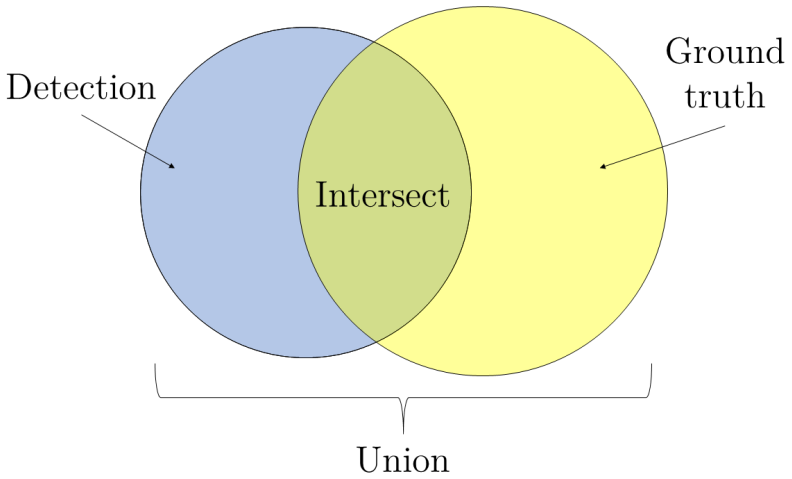


Figure 4.16: Representation of Intersect over Union (IoU) for a single droplet.

The Boundary F1 score (denoted as BF) indicates how well boundaries between classes are captured. The BF score is the average of F_1 scores of all classes. F_1 for each class is calculated as in Eq. (4.3), where precision (P) and recall (R) are defined in Eqs. (4.4) and (4.5) respectively [83]. Variables which are specific to a class are denoted with superscript c. BF has a value between zero and one, where one indicates that the boundaries perfectly match the ground truth boundaries.

$$F_1^c = \frac{2 \cdot P^c \cdot R^c}{P^c + R^c} \tag{4.3}$$

$$P^c = \frac{1}{|B_{ps}|} \sum_{z \in B_{ps}^c} [\![d(z, B_{gt}^c) < \theta]\!] \tag{4.4}$$

$$R^c = \frac{1}{|B_{gt}|} \sum_{z \in B_{gt}^c} [\![d(z, B_{pst}^c) < \theta]\!] \tag{4.5}$$

Csurka et al. [83] investigated the use of metrics to assess CNN accuracy and how they compare to human assessment of the same CNN predictions. Using these metrics separately, the IoU has higher correlation to human ranking of a CNN prediction than the BF achieves. However, the BF score becomes more important for predicting human ranking for CNNs that are ranked more highly by humans. Therefore, using a combination of IoU and BF is recommended. Csurka et al. [83] also suggests using per image scores rather than global scores. Considering the metrics for each individual image allows differentiation between a CNN which produces mediocre predictions across the board and one that is highly accurate for some images and very poor for others. Therefore, the proportion of images with a value above a given value threshold for each metric can be assessed. Additionally, using this approach reduces the bias with respect to large objects which would otherwise have a disproportionate impact.

A set of 75 labelled images (not seen by the CNN during training, testing or validation) are selected to test the ability of the CNN to detect droplets. Accuracy and loss are plotted throughout the training process for each of the CNNs in Figs. 4.17 to 4.19. Accuracy is defined as the number of correct predictions over the total number of predictions (in this case each pixel is a prediction). Loss is another metric calculated by MATLAB to indicate how well the prediction matches ground truth - lower numbers correspond to improved prediction. The gradient descent algorithm is updated towards minimizing the loss function after each iteration, which corresponds to an increase in prediction accuracy. In each case the accuracy quickly approaches maximum within the first epoch (an epoch is one pass of the entire training data set) and improves only a small amount up to the 6th epoch. Training stops automatically after validation loss stops decreasing (at 6 epochs in this case). ResNet-50 and ResNet-101 achieve a higher validation accuracy at the end of training than ResNet-18 (98.33% compared to 97.86%). Table 4.1 shows how the metrics change throughout the training process after 2, 4 and 6 epochs while training from ResNet-50. Improved metrics after more epochs in this range indicates there is benefit for training up to 6 epochs even though the change to validation accuracy and loss is relatively small.

The resulting networks trained from both ResNet-50 and ResNet-101 score more highly for the majority of images for IOU and BF than achieved by the network trained from ResNet-18, as seen in Figs. 4.20 to 4.23. Again, no difference is seen between ResNet-50 and ResNet-101 for the per image IoU and BF scores meaning it is most appropriate to use the less computationally expensive of the two.

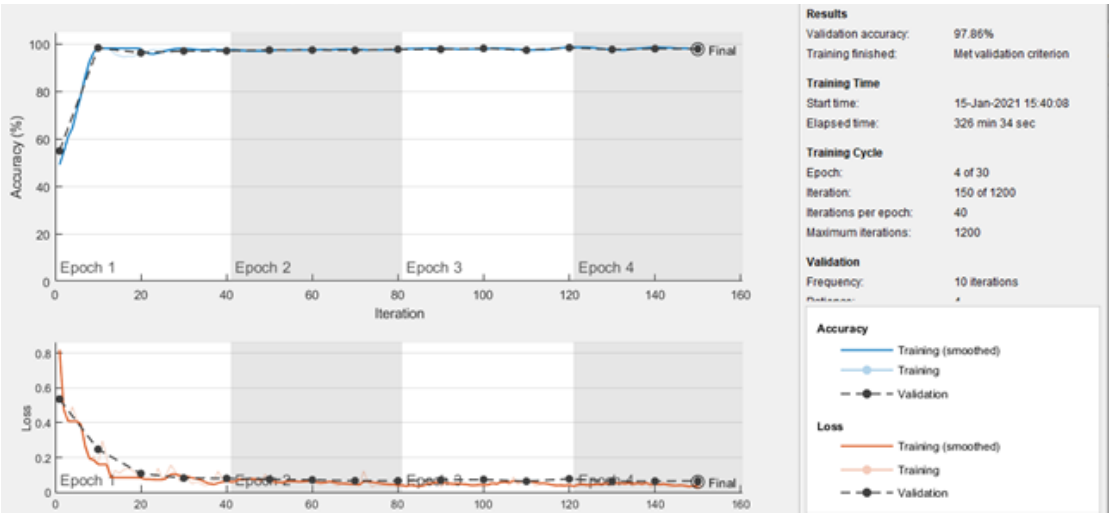


Figure 4.17: Accuracy and loss during training the CNN from ResNet-18.

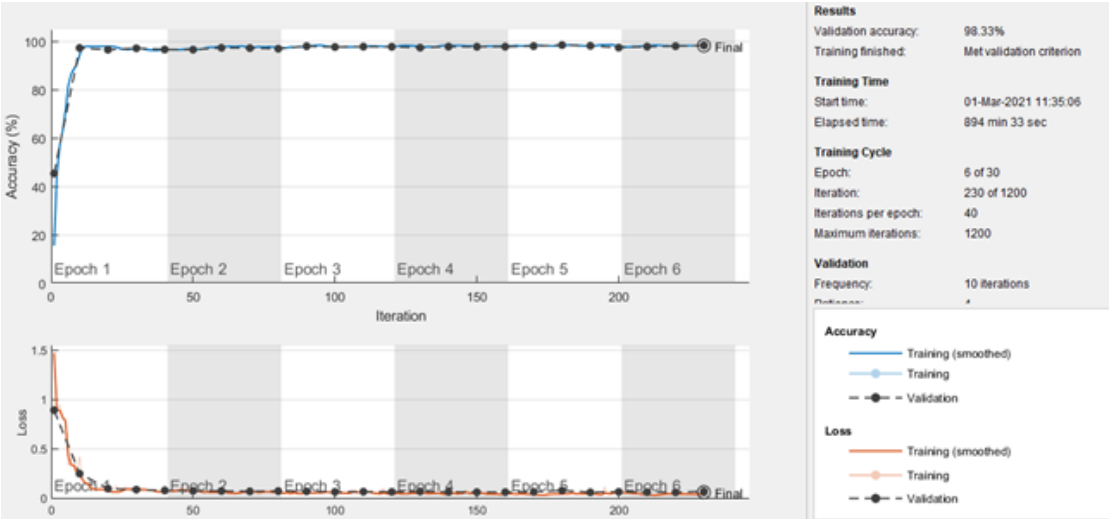


Figure 4.18: Accuracy and loss during training the CNN from ResNet-50.

Fig. 4.24 shows an example prediction alongside ground truth for an image that achieved very low IoU ($\leq$ 0.05). Inspection of these images reveals that many of the small droplets' diameters are overpredicted. This will be a major contribution to the poor IoU score. A scratch on the solid surface of the rotating stub shaft has also been incorrectly identified as a droplet. It can be noted that some of the "false positives" are in fact droplets that have been deemed to be too out of focus to be labelled in ground truth. However, it is not unreasonable for them to be included since the division be-

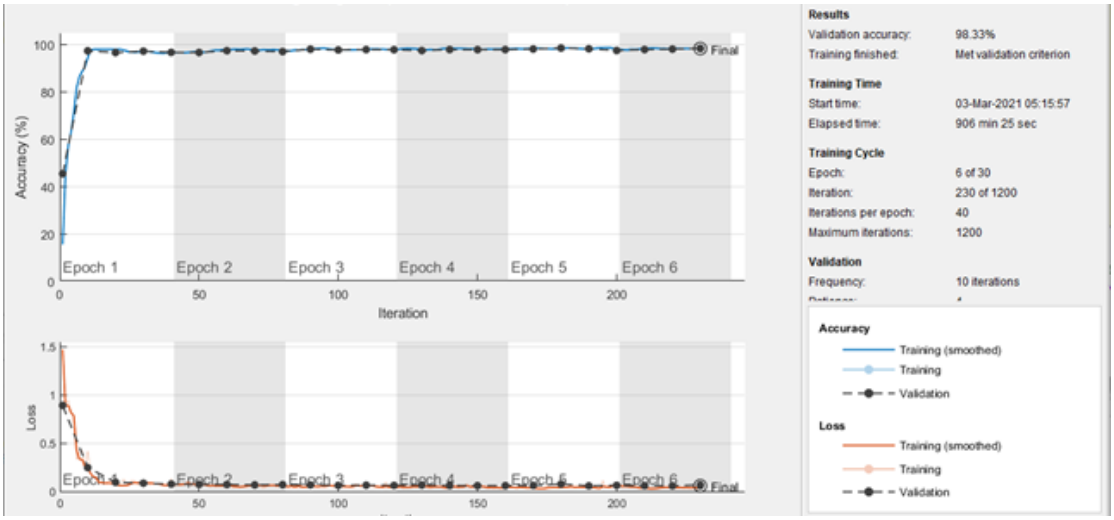


Figure 4.19: Accuracy and loss during training the CNN from ResNet-101.

Table 4.1: Change in droplet IoU and BF score generated for a set of 75 test images not previously seen by the networks throughout the training process for ResNet-50 after 2, 4 and 6 epochs.

Number of Epochs	Droplet IoU	Droplet BF
2	0.161	0.424
4	0.199	0.449
6	0.236	0.471

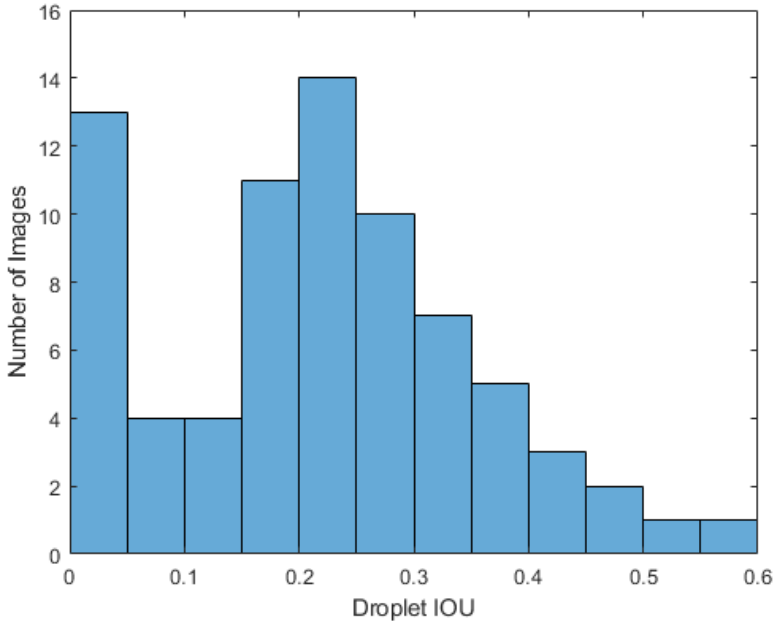


Figure 4.20: Histogram of per-image IoU scores for predictions made by the CNN trained from ResNet-18.

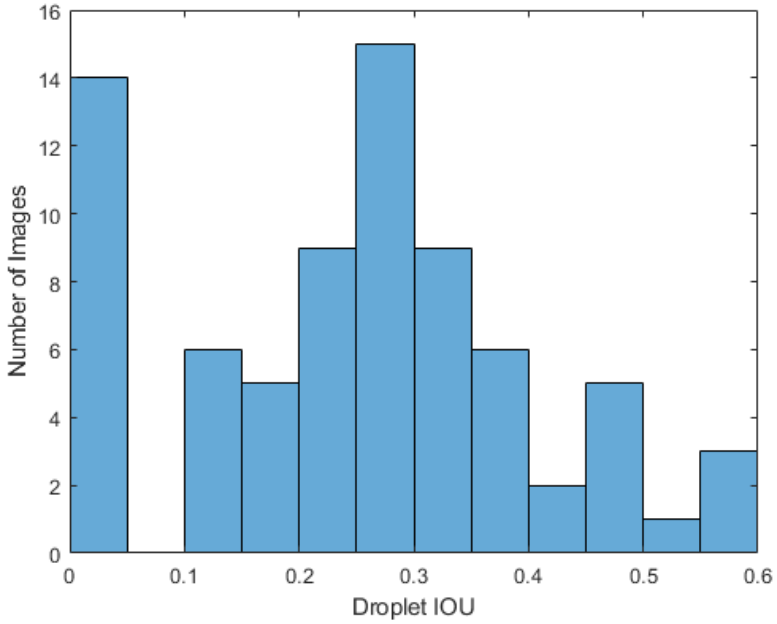


Figure 4.21: Histogram of per-image IoU scores for predictions made by the CNN trained from ResNet-50 and ResNet-101 (plots are identical).

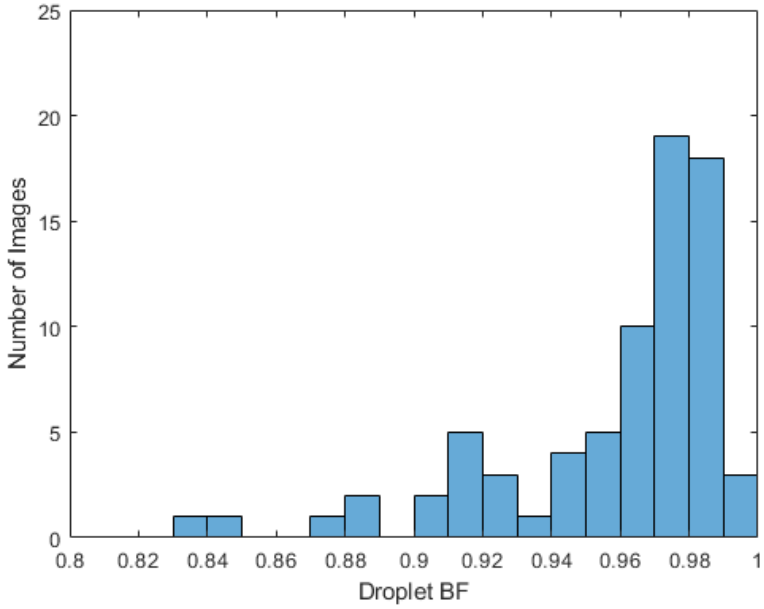


Figure 4.22: Histogram of per-image BF scores for predictions made by the CNN trained from ResNet-18 on the 75 test images.

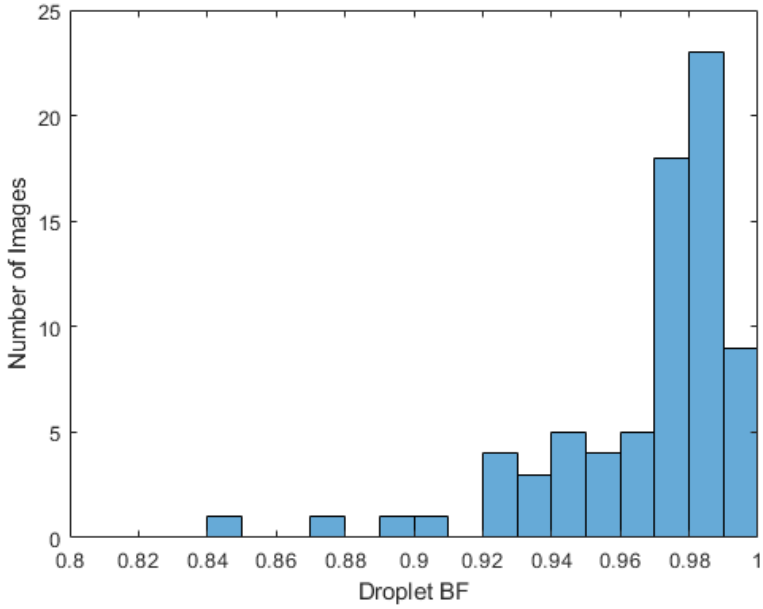


Figure 4.23: Histogram of per-image BF scores for predictions made by the CNN trained from ResNet-50 and ResNet-101 (plots are identical).

tween in focus and not in focus is difficult to define for ground truth labelling. It is estimated that droplets defined as out of focus in human labelling are in the region of 8 mm or more away from the plane of focus (towards the camera). At this distance, the effect on perceived droplet diameter due to being closer to the camera is judged to be insignificant.

An additional source of false positives comes from the detection of ligaments as droplets. While this is not strictly correct, approximating a ligament as a droplet still represents the quantity of oil in the chamber, and the ligament is likely to break up into droplets after a short period of time. Overall, while the IoU for this image is low enough to cause possible concern, a visual comparison of the prediction and the ground truth shows that the droplet detection is reasonable, meaning that applying this to a practical problem it is still a valid approach. Fig. 4.25 is an example of an image with an IoU score between 0.55 and 0.60 (the highest bin of Fig. 4.21). This image can be seen to be a much simpler case, with far fewer droplets. Therefore, a small overprediction of the size of each droplet has a lesser effect on the IoU than it does for images with a greater number of droplets.

Fig. 4.26 is an example of an image with a low BF score. A visual inspection of the prediction compared to the ground truth shows a significant difference. The original image in this case is very complex. There are a large number of droplets in the slot and the film covering the front face is very bubbly, with some three-dimensional features

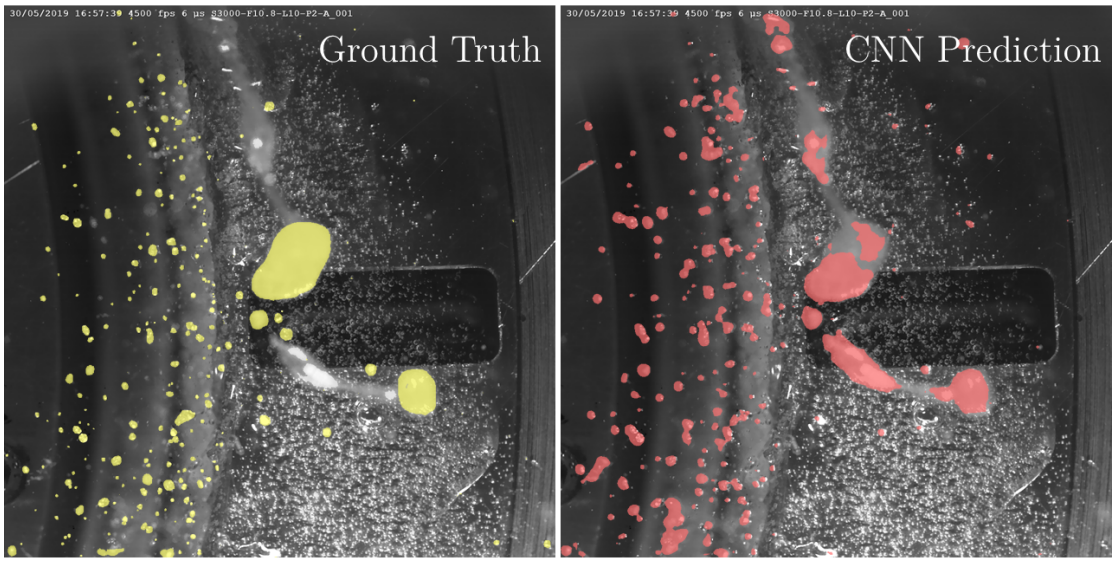


Figure 4.24: Comparison of ground truth and droplet detection by the CNN trained from ResNet-50 for a test image that scored in the lowest IoU bin ($0.00 \leq IoU < 0.05$) in Fig. 4.21.

towards the bottom of the image. These features all make detection of the droplets more challenging, so it is expected that this image would score lower than many others. Many bubbles in the film are falsely detected as droplets and a large number of the droplets in the slot are over predicted and merged together so that analysis would not be able to distinguish them as separate droplets. The lack of distinction between droplets, and poor boundaries around the edge of the ground truth droplets, is what causes the BF score to be low in this image. This is of far greater concern than the issues arising in images with a low IoU. However, it can be seen that larger droplets in the image are still detected with reasonable accuracy. For comparison, Fig. 4.27 is an example of an image with a high BF score. In this image the boundaries of the droplets detected (true positives) are very clear, although there are also some false positive detections where bubbles attached to the front face have been incorrectly identified as droplets - this does not have a significant impact on the BF score.

4.4.3 CNN Selection

A greater number of layers in the CNN correlates to greater computational expense, meaning that ResNet-50 takes longer to train/implement than ResNet-18 and ResNet-101 takes longer to train/implement than ResNet-50. The CNN trained from ResNet-50 outperforms the one trained from ResNet-18, both for similarity to ground truth

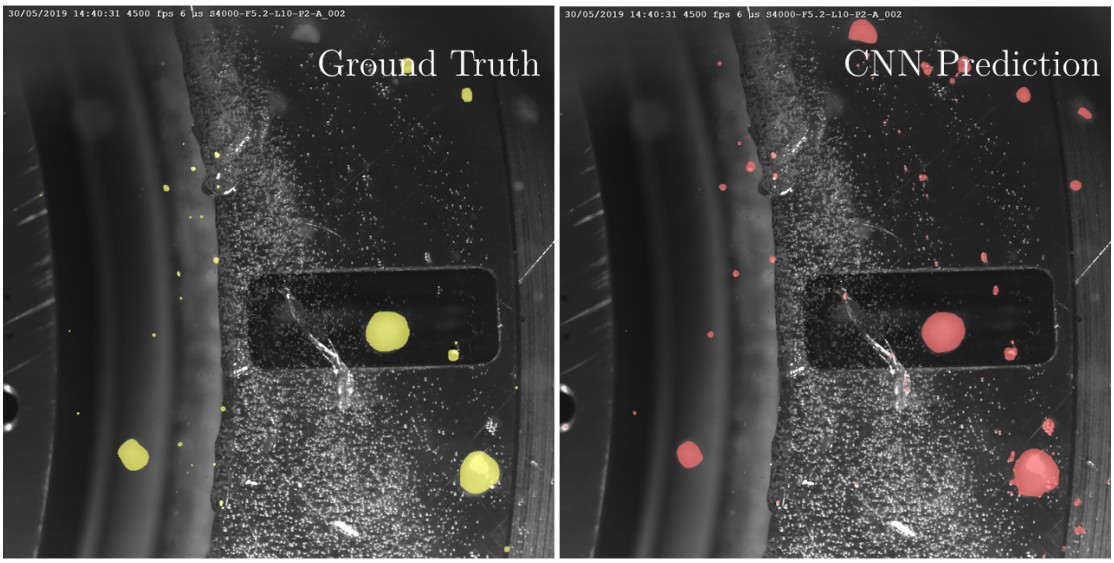


Figure 4.25: Comparison of ground truth and droplet detection by the CNN trained from ResNet-50 for a test image that scored in the highest IoU bin ($0.55 \leq IoU < 0.60$) in Fig. 4.21.

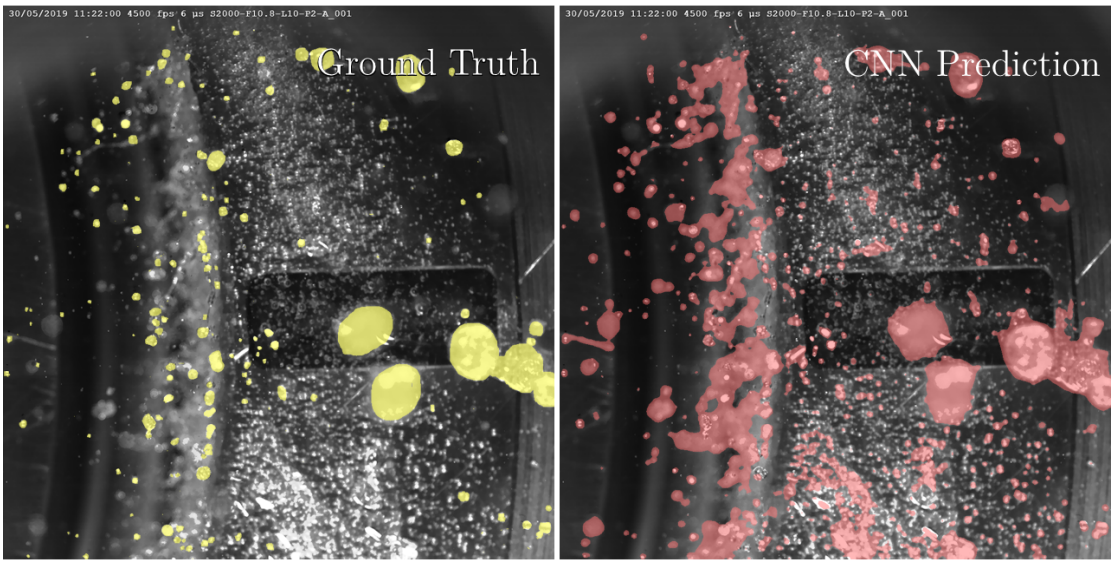


Figure 4.26: Comparison of ground truth and droplet detection by the CNN trained from ResNet-50 for a test image that scored in the lowest BF bin ($0.84 \leq BF < 0.85$) in Fig. 4.23.

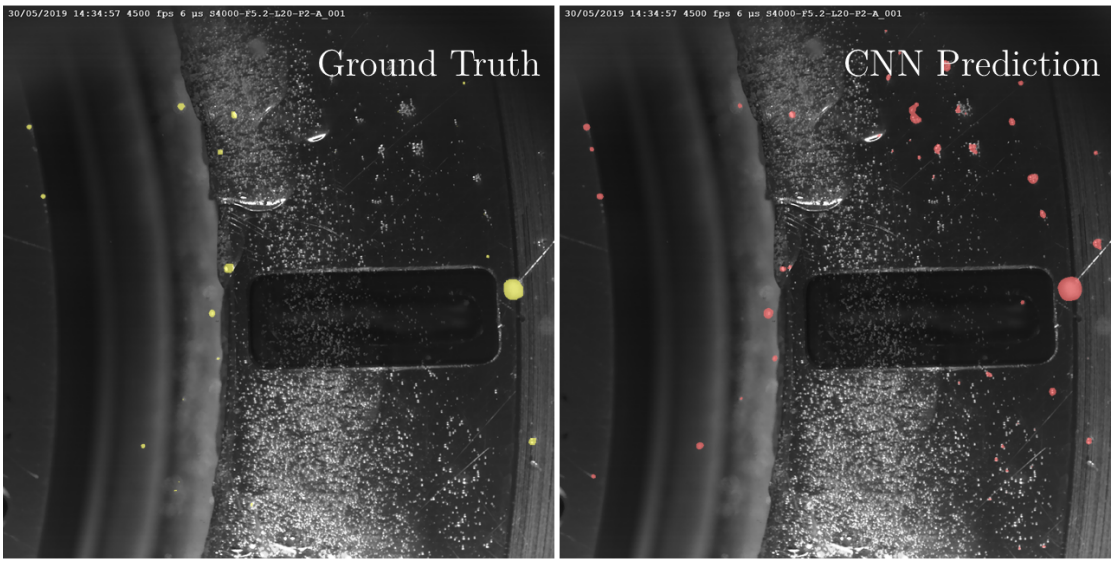


Figure 4.27: Comparison of ground truth and droplet detection by the CNN trained from ResNet-50 for a test image that scored in the highest BF bin ($0.99 \leq BF < 1.00$) in Fig. 4.23.

droplet diameter distribution and IoU and BF scores. However, it is seen that the CNNs trained from ResNet-50 and ResNet-101 achieve the same metrics and droplet diameter distributions as one another, meaning that the cheaper of the two is favourable. The CNN trained from ResNet-50 is selected for this application.

4.4.4 Validity and Applicability of Method

The CNN is trained only on images in the BSR at the 3 o'clock position. Good applicability is indicated by the CNN's ability to predict droplets accurately in this region and in other operating cases without the need for further training. Fig. 4.28 shows the droplet prediction for an example image at the 9 o'clock position. The main issue with the detection is the CNN interpreting some of the complex three-dimensional structures as droplets - these features were never before seen by the CNN. However, the true droplets are predicted with good accuracy. Even with no further training, this prediction could be used to give a good indication of droplet behaviour in this region of the bearing chamber.

The validity of this approach for droplet detection is demonstrated by the strong agreement with ground truth droplet diameter distributions. Limitations in the raw CNN predictions are compensated for by implementing droplet tracking so that false detections seen for only a small number of instances are removed from the data, increasing

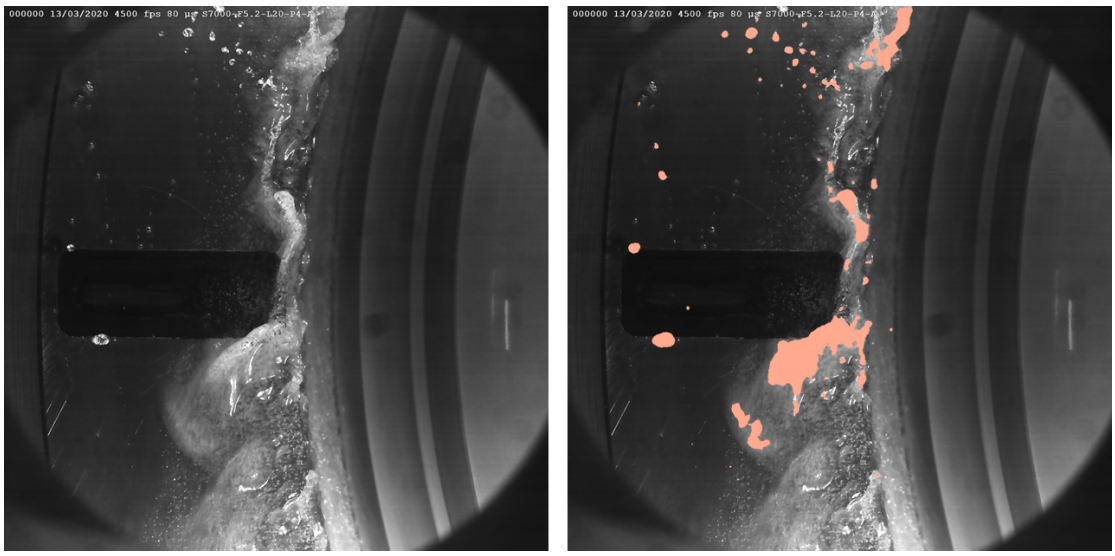


Figure 4.28: Comparison of original image *(left)* and droplet prediction *(right)* at the 9 o'clock bearing chamber position (7000 rpm, 5.2 lpm oil flow rate and 20 kN axial load) using the CNN trained only on images from 3 o'clock.

agreement with ground truth.

4.5 Droplet Detection Method Summary

CNNs can be used to detect droplets in images taken from a realistic bearing chamber experimental test rig with a good level of accuracy, outperforming the conventional method. The minimum feasible droplet diameter for detection is limited by spatial resolution of images at around four pixel diameter for this application - approximately 0.25 mm. Droplets larger than this threshold can be detected and tracked to give a good representation of ground truth. Therefore, the method for droplet detection and tracking developed in this project is considered to be appropriate for experimental work of this type. The described methodology is applied to high speed images from the BSR and results are presented in Chapter 5.

CHAPTER 5

Experimental Results and Discussion

This chapter presents the experimental results obtained using the methodology described in Chapter 3 and processed as in Chapter 4. Shedding behaviour is investigated both quantitatively and qualitatively, assessing droplet diameter, speed and path through the bearing chamber in addition to trends in two phase flow behaviour.

High-speed imaging has been performed and quantitatively assessed at the 3 o'clock and 9 o'clock positions for the following conditions to investigate the effect of speed, oil flow rate and axial load.

- **Speed:** 1000 rpm, 3000 rpm, 5000 rpm, 7000 rpm and 9000 rpm with an oil flow rate of 7.3 l min^{-1} and axial load of 10 kN as per Chapter 3. Additionally, high speed image data has been obtained for these test points plus 10 000 rpm, 11 000 rpm and 12 000 rpm with an imaging area of 576 x 908 pixels.
- **Oil flow rate:** 5.2 l min^{-1}, 7.3 l min^{-1} and 10.8 l min^{-1} with a speed of 9000 rpm and axial load of 10 kN.
- **Axial load:** 10 kN, 20 kN and 30 kN with a speed of 9000 rpm and an oil flow rate of 7.3 l min^{-1}.

Additionally, the droplet behaviour is examined in detail for a single operating condition (7000 rpm, 5.2 lpm oil flow rate and 20 kN axial load) in Section 5.2. Qualitative analysis is performed for speeds up to 7000 rpm on the 3 o'clock position and behavioural regimes are identified.

5.1 Qualitative Analysis

Trends in the change in flow phenomena on the 3 o'clock side of the bearing chamber as a result of variation in operating speed, axial load and oil flow rate are qualitatively assessed in this section. Sample images for operating speeds of 1000 rpm, 3000 rpm, 5000 rpm and 7000 rpm are shown in Figs. 5.1 to 5.3 for all combinations of axial load and oil flow rate tested.

5.1.1 Change in Operating Speed

Increasing the operating speed means that the oil film covers a greater area across the static front face and appears more bubbly. At low operating speeds, the droplets generated are generally smaller and less numerous than at higher speeds. Increasing the operating speed appears to facilitate the development of ligaments and complex three-dimensional structures. This is clearly visible for the higher flow rates shown in Figs. 5.1 to 5.3.

At lower shaft speeds the shear air flow accelerating the film is slower, leading to a lower velocity film approaching shedding edge. A smaller proportion of film is expected to separate from the wall when velocity is low due to the reduced ratio of inertial force to restoring force [39], whereas a higher velocity film is expected to have a higher proportion of separation. Formation of ligaments and complex three-dimensional oil structures occurs more prevalently when more of the film separates. These structures are often seen to breakup into droplets, contributing to the higher number of droplets observed at higher speeds. This mechanism of droplet breakup tends to produce larger droplets which explains the shift in typical droplet diameter with increased operating speed. Large droplets are less likely to become entrained in the circulating gas flow and are expected to reach the chamber wall more rapidly, leading to lower residence time and reduced oil degradation (as discussed in Section 2.8).

5.1.2 Change in Oil Flow Rate

Increasing the oil flow rate causes the film attached to the static front face to cover a larger area, extending further in the radial direction. Droplet production at low oil flow rates appears to give way to the production of larger, and more complex three-dimensional ejecta at higher oil flow rates. The phenomena is most easily observed at high speeds which facilitate the production of these structures. It is also apparent in Fig. 5.2 when operating at 7000 rpm and 20 kN axial load, that the ejecta originat-

ing from the lip of the bearing slot is relatively sparse at a low flow rate and is far more dense at the highest flow rate, originating from the whole of the visible lip on the 3 o'clock side. For a given operating speed the proportion of oil separation that occurs is expected to remain constant [39], however the increase in oil flow rate equates to a higher mass of separated oil,accounting for the increased number of droplets seen. At lower speeds, there is less of a visible effect of increasing oil flow rate beyond the change in the area covered by the oil film attached to the front face. Visual assessment of Figs. 5.1 to 5.3 indicates a strong correlation between the oil flow rate and the mass of oil droplets observed in the bearing chamber, in addition to an increase in the wetted area of the static front face.

5.1.3 Change in Axial Load

Increasing the axial load from 10 kN to 20 kN produces waves in the oil film on the front face. These move with the film flow and have a wavefront perpendicular to the direction of motion. Note that these waves are more easily visible in video form than in the still images presented here. However, of the still images, the phenomena is most easily seen at 3000 rpm in Fig. 5.2 for all values of oil flow rate tested. Waves can also be seen at higher speeds, although the wavefronts are less clearly visible, but are not seen at 1000 rpm.

At a 30 kN load, there are again no waves observed in the oil film on the front face when operating at 1000 rpm, but waves begin to appear at speeds of 3000 rpm and over. In the case of high-speed, high load and low flow rate (7000 rpm, 30 kN and 5.2 l min^{-1} respectively), a different three-dimensional phenomena is observed in the oil film: a ripple extends from the top left to the bottom right of the front face. In this situation, The apparent wave front is perpendicular to those seen most clearly at 3000 rpm.

Increasing the axial load within the range investigated encourages a greater number of droplets to be shed in the bearing chamber. This may be related to the phenomena causing the change in wave behaviour in the film but is not yet fully understood.

5.1.4 Shedding Regimes

Four distinct shedding regimes have been identified for conditions investigated at speeds up to 7000 rpm on the 3 o'clock side of the bearing chamber. They are defined as follows:

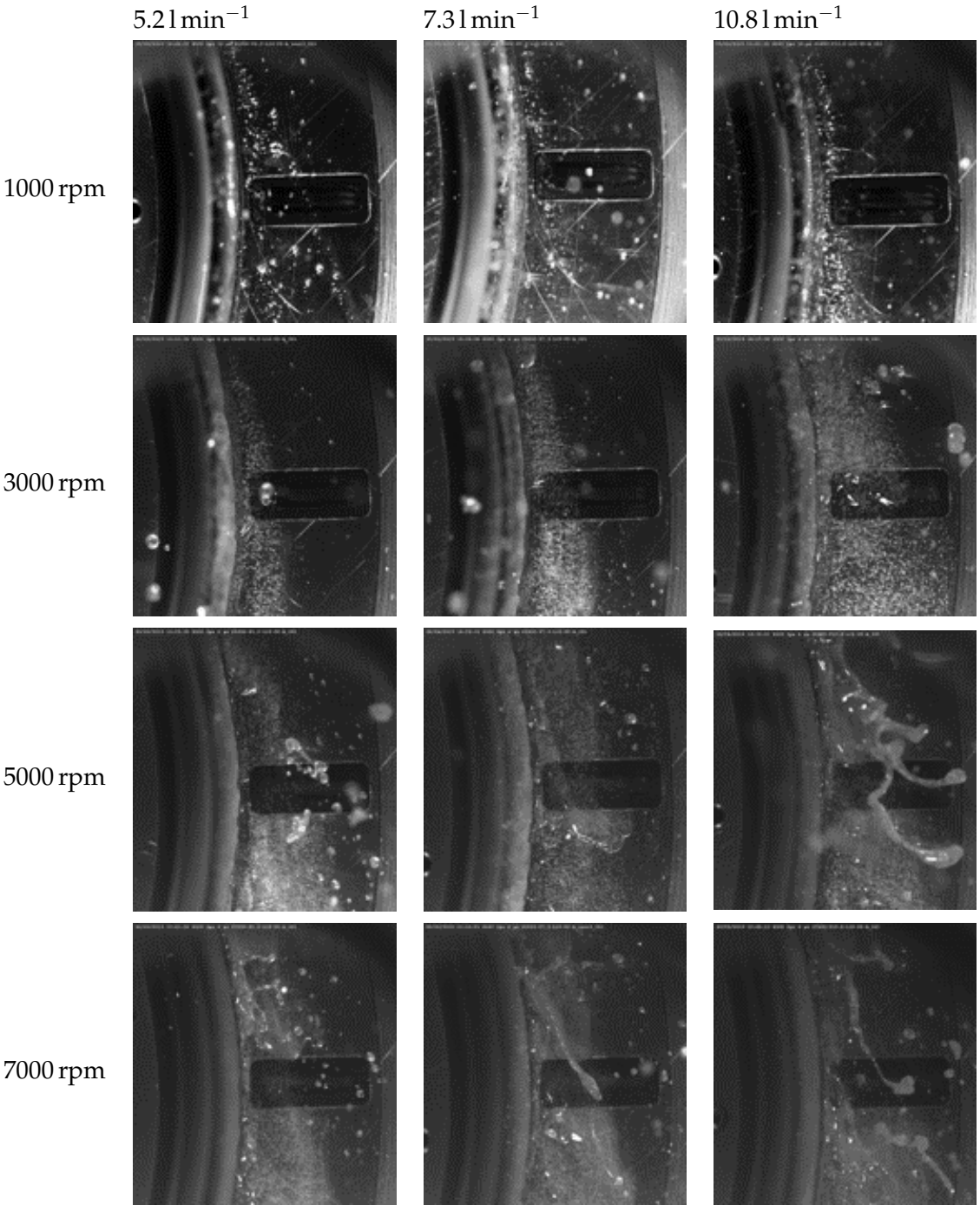


Figure 5.1: Sample HS images taken at different combinations of operating speed (in rpm) and oil flow rate (in l min^{-1}), all at an axial load of 10 kN.

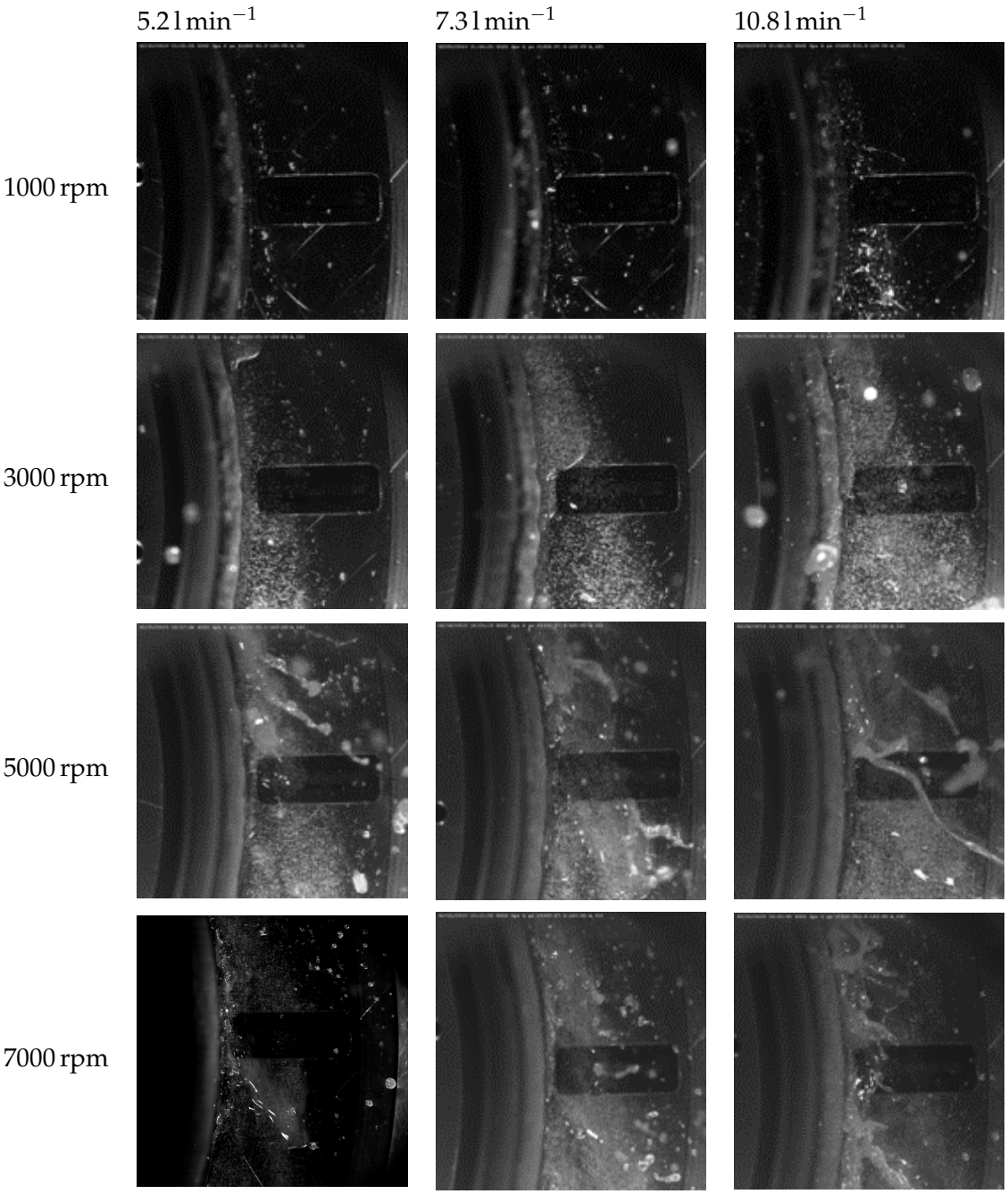


Figure 5.2: Sample HS images taken at different combinations of operating speed (in rpm) and oil flow rate (in l min^{-1}), all at an axial load of 20 kN.

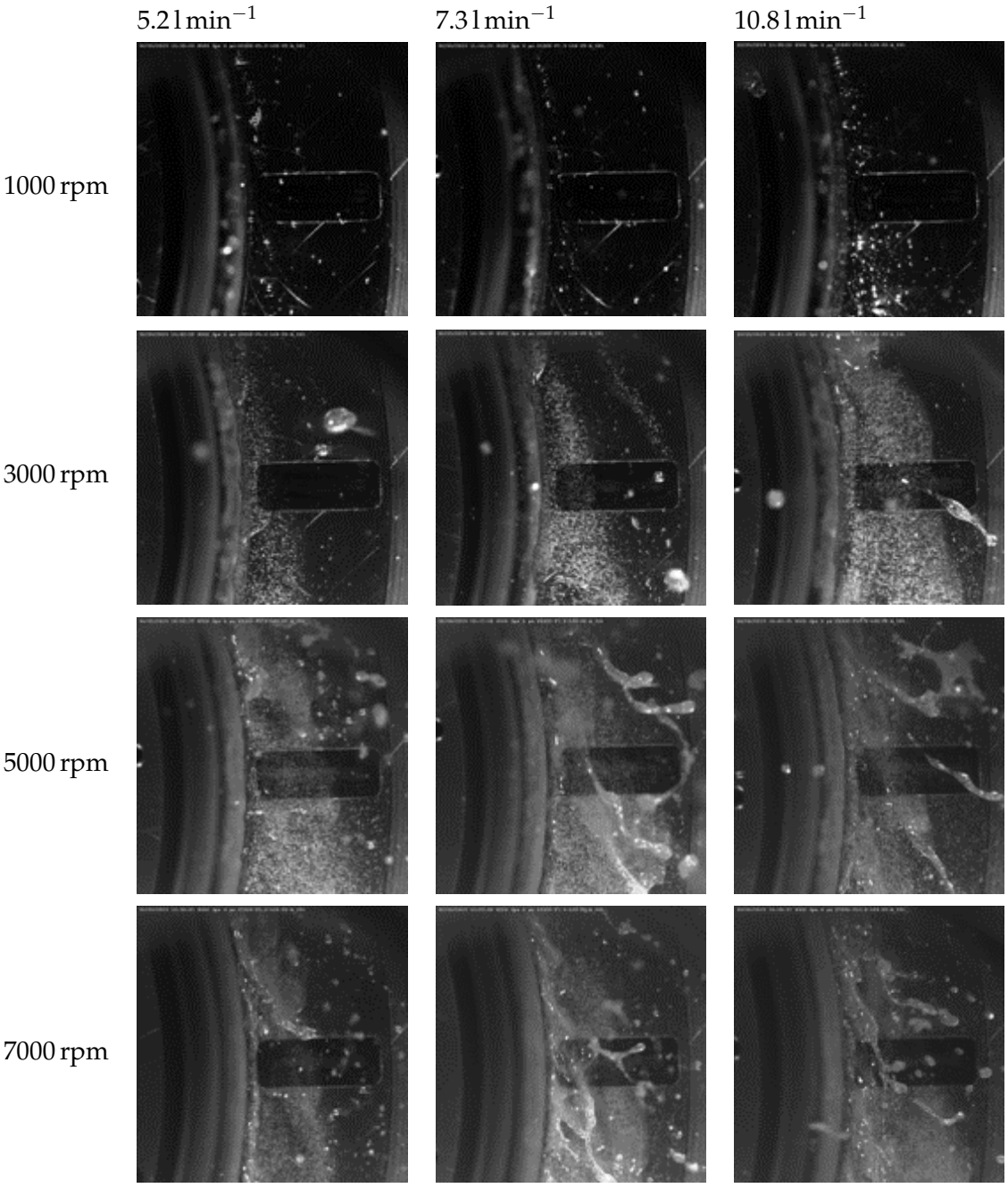


Figure 5.3: Sample HS images taken at different combinations of operating speed (in rpm) and oil flow rate (in l min^{-1}), all at an axial load of 30 kN.

Regime 1: Droplets are present and there is no/minimal film on the front face - illustrated by Fig. 5.4

Regime 2: Droplets are present and a small film coverage on front face (bubbles are contained in the film) - illustrated by Fig. 5.5

Regime 3: Droplets are present and there is a large film coverage (film is thicker and more wavy than in regime 2) - illustrated by Fig. 5.6

Regime 4: All features of regime 3 are present, in addition to large complex oil structures passing through the bearing chamber (breakup of these structures is often observed) - illustrated by Fig. 5.7

The regimes are mapped in Figs. 5.8 and 5.9. Both operating speed and oil flow rate supplied to the bearing significantly influence the change of regime. Increasing either variable can lead to a regime change. At low speed (1000 rpm) increasing oil flow rate can only change from regime 1 to 2, whereas at moderate speed (7000 rpm) change in oil flow rate in the range investigated can only change from regime 3 to 4. At a fixed low oil flow rate ($5.2\,\mathrm{l\,min^{-1}}$) increasing operating speed can influence change between regimes 1 to 3 but not regime 4. Whereas at a fixed high oil flow rate ($10.8\,\mathrm{l\,min^{-1}}$) increasing operating speed can influence change between regimes 2 to 4 but not regime 1. For regime 1 oil flow rate must be low to moderate ($\leq 7.3\,\mathrm{l\,min^{-1}}$) while operating at low speed (≤ 2000 rpm). Regime 4 only occurs at moderate to high oil flow rate ($\geq 7.3\,\mathrm{l\,min^{-1}}$) while operating at moderate speed. This demonstrates that both operating speed and oil flow rate are critical to behaviour observed in the bearing chamber.

Axial load has much less of an impact on the behavioural regimes observed. The only differences between the regime maps at 10 kN and 20 kN are as follows:

- At 3000 rpm behaviour transitions to regime 3 at a lower flow rate when operating at 30 kN ($7.3\,\mathrm{l\,min^{-1}}$ instead of $10.8\,\mathrm{l\,min^{-1}}$) and to regime 4 at $10.8\,\mathrm{l\,min^{-1}}$.
- At 4000 rpm flow transitions to regime 4 at lower flow rate when operating at 30 kN ($7.3\,\mathrm{l\,min^{-1}}$ instead of $10.8\,\mathrm{l\,min^{-1}}$).

Regime maps at 20 kN and 30 kN are identical. Increasing axial load tends to a minor shift towards transition to higher regimes at lower flow rates, but does not have a major influence on observed behaviour. Physically, the change in axial load means a change in contact angle in the bearing so it is not expected to have a major affect on oil film thickness or velocity at the shedding edge.

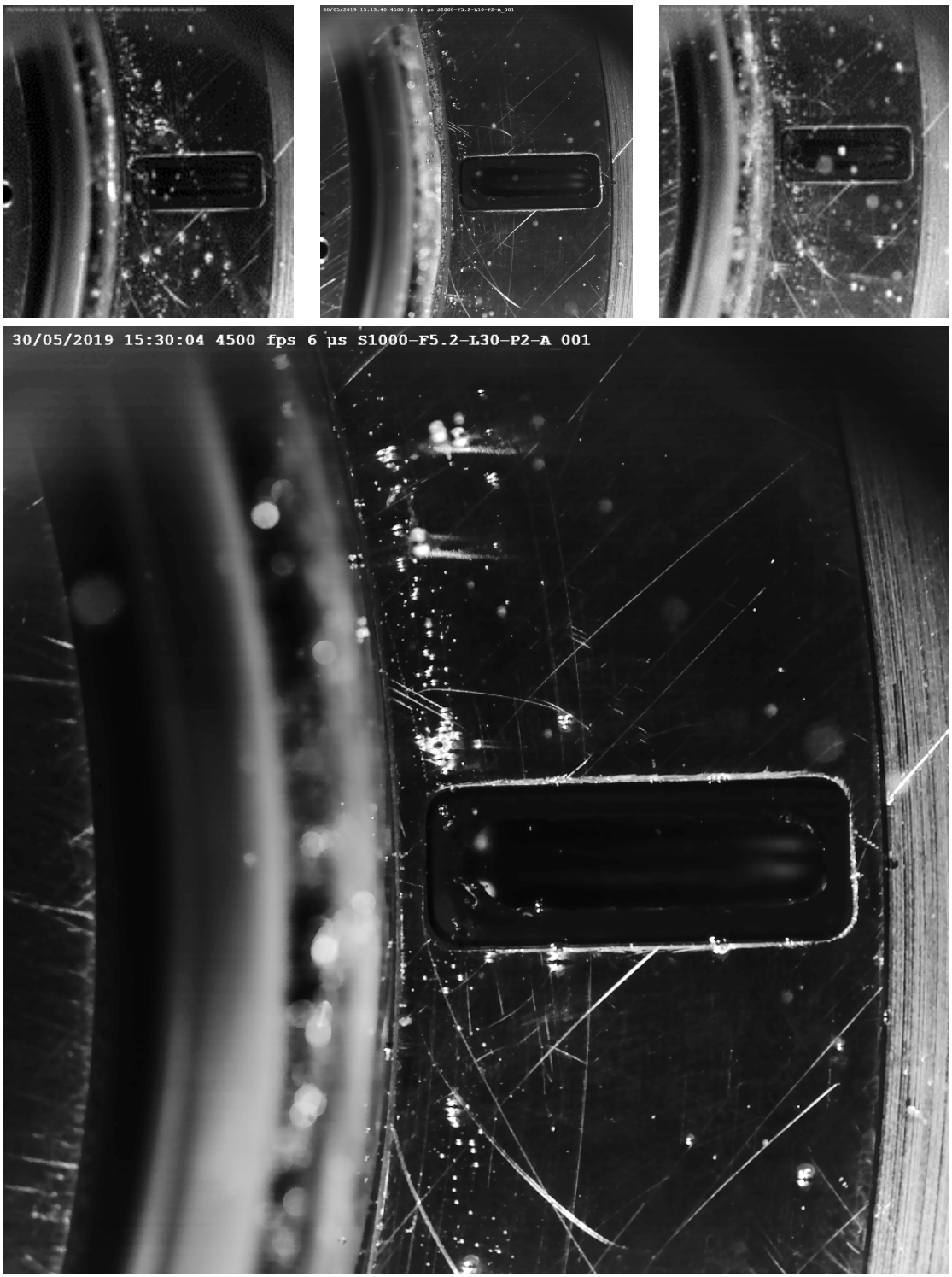


Figure 5.4: Examples of regime 1 physical behaviour.

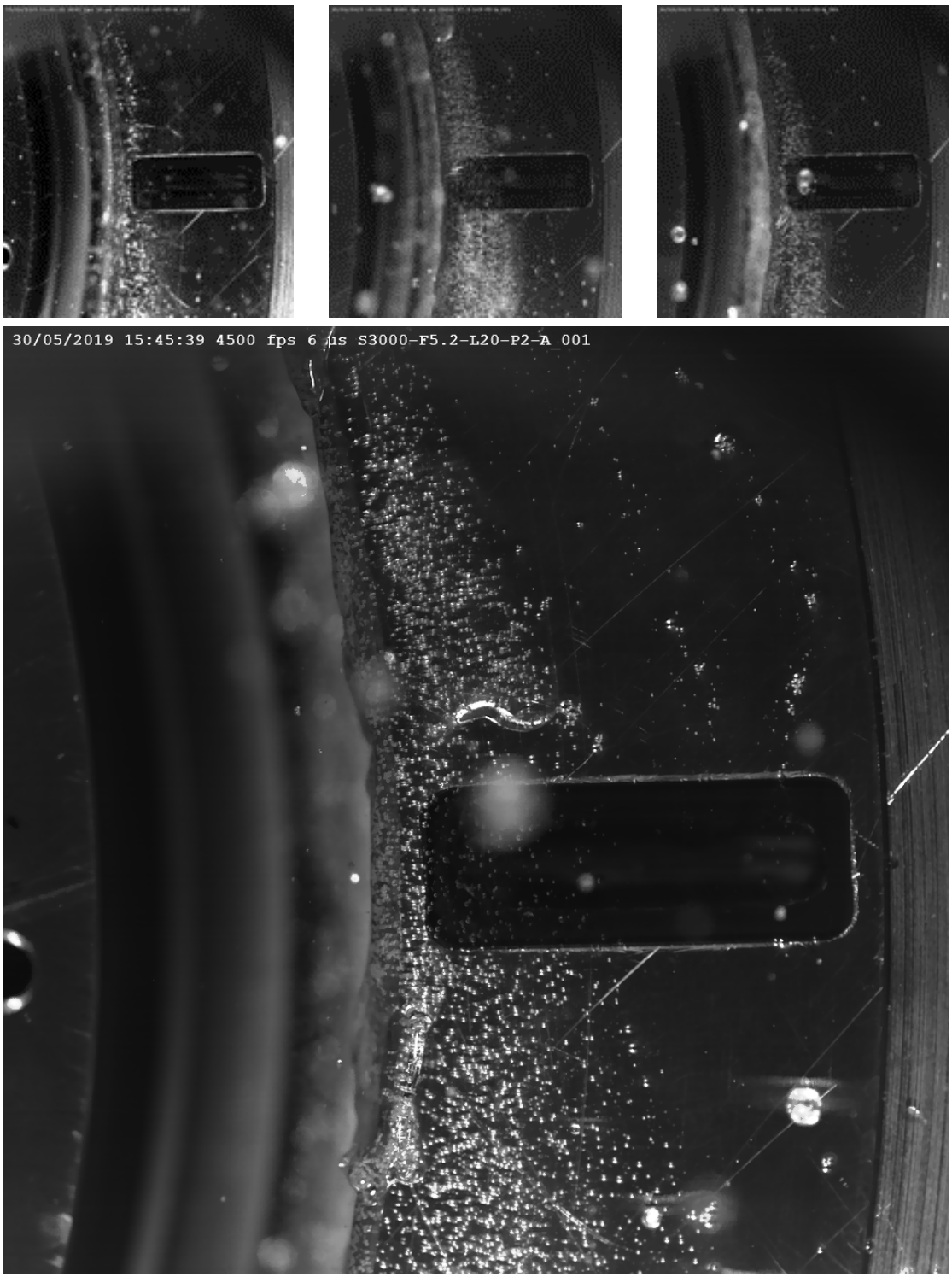


Figure 5.5: Examples of regime 2 physical behaviour.

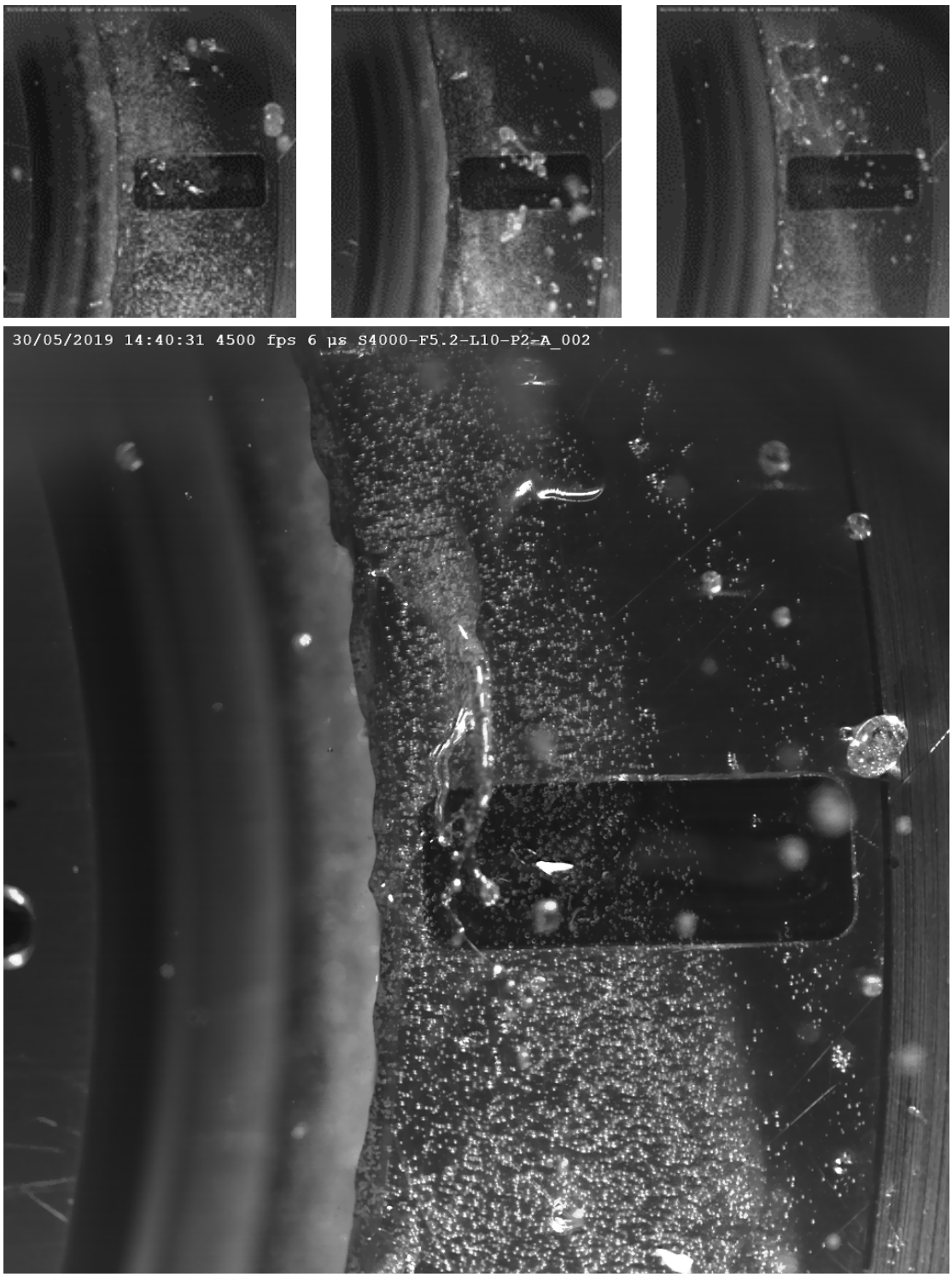


Figure 5.6: Examples of regime 3 physical behaviour.

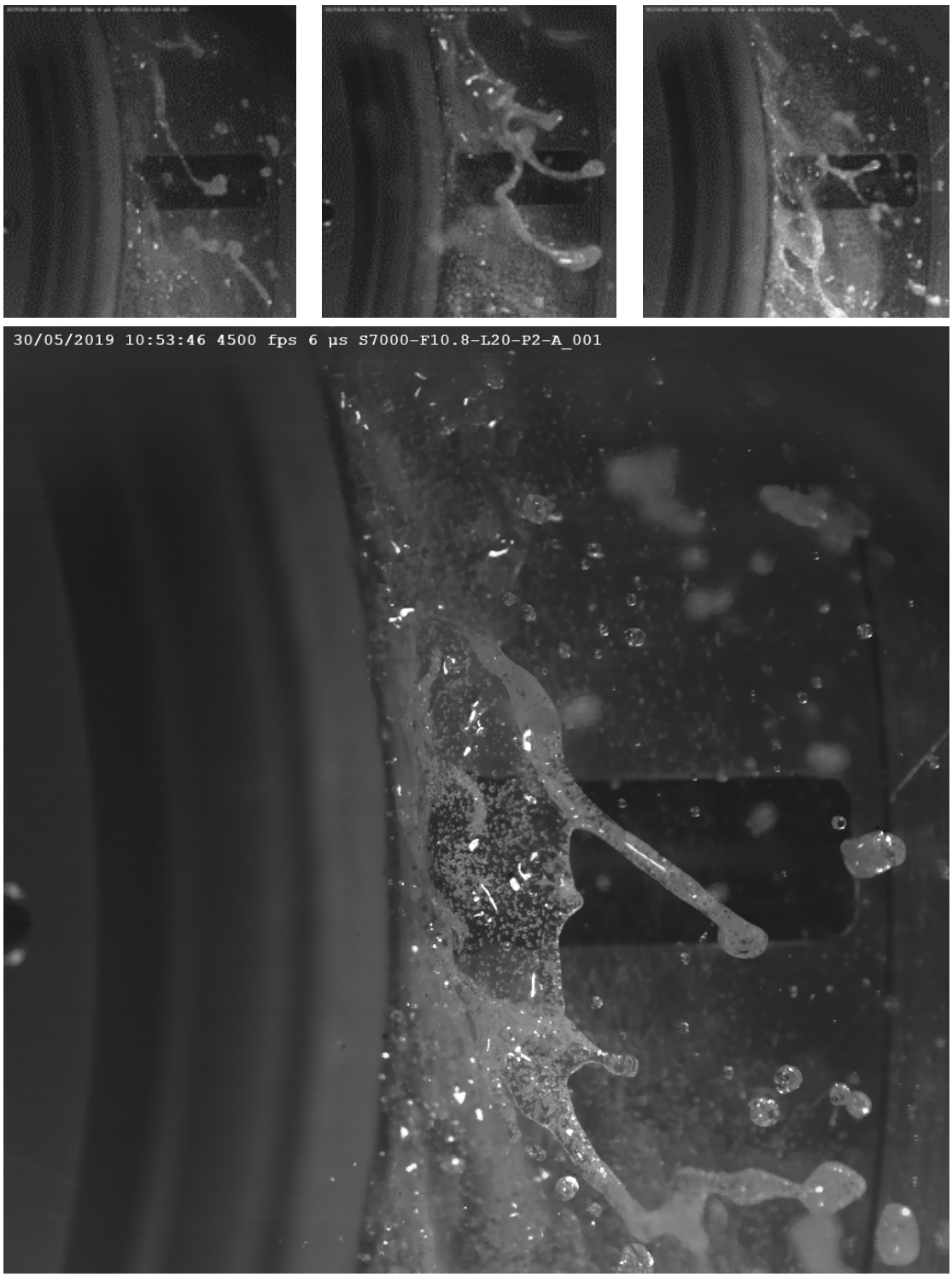


Figure 5.7: Examples of regime 4 physical behaviour.

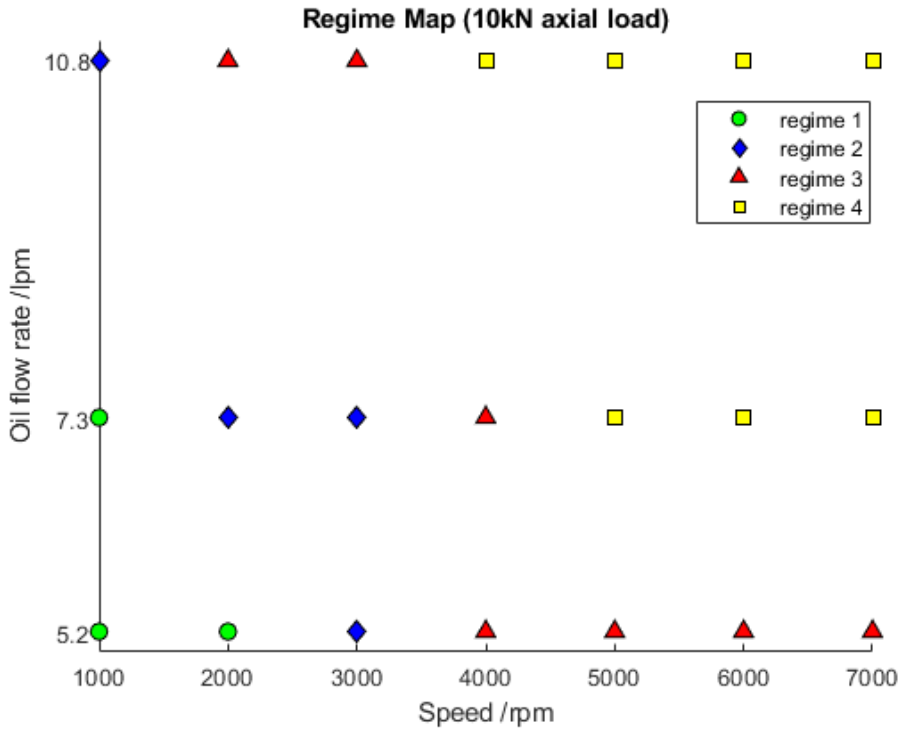


Figure 5.8: Regime map for flow on the 3 o'clock side of the BSR when operating with an axial load of 10 kN.

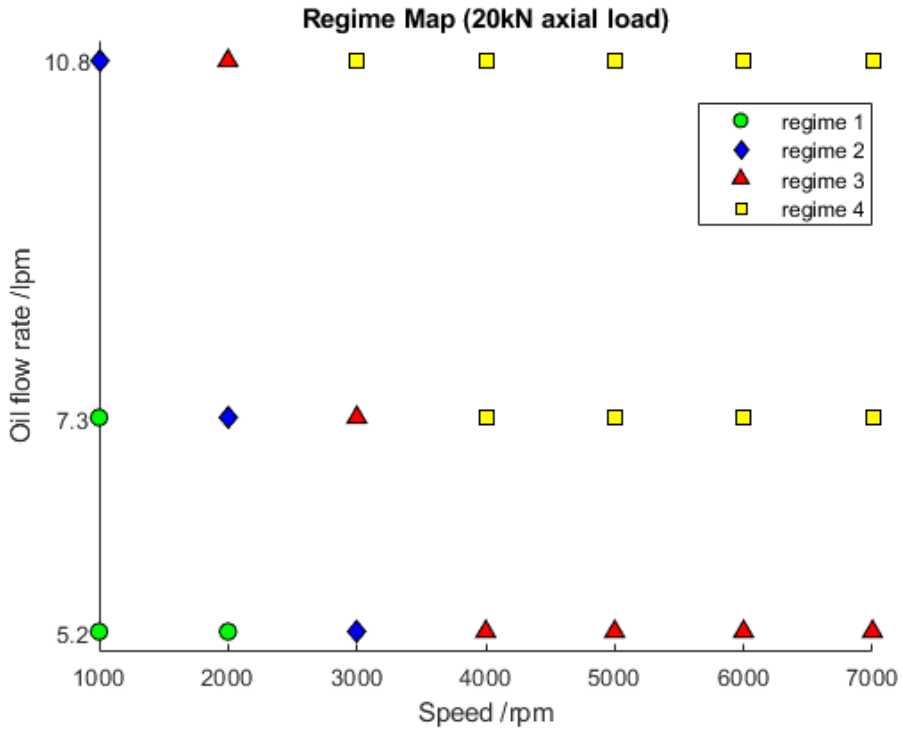


Figure 5.9: Regime map for flow on the 3 o'clock side of the BSR when operating with an axial load of 20 kN or 30 kN (regime maps are identical in both cases).

5.2 Results From a Single Operating Condition

Data from a single test point (7000 rpm, 5.2 lpm oil flow rate and 20 kN axial load) is presented here in detail to demonstrate what can be achieved using this method before comparisons are made to other operating conditions. This test condition was selected as it is moderate speed and the middle of the range of axial loads investigated (not showing extremes of behaviour due to speed or axial load), but is a low flow rate meaning there is a lower volume of oil in the bearing chamber. This is useful in early development of the detection technique, hence the detailed investigation into this test condition. One second worth of high-speed image data (recorded at 4500 fps) is analysed for the single test point. An example image is shown in Fig. 5.10.



Figure 5.10: Sample high-speed image taken at 7000 rpm with an oil flow rate of 5.2 lpm axial load of 20 kN.

The probability distribution of droplet diameter is shown in Fig. 5.11. The majority of droplets have a diameter below 2.0 mm, with the most common being in the 0.6 mm to 0.80 mm range. Very few droplets with a diameter larger than 3.0 mm are observed. The Rosin-Rammler distribution (discussed in detail in Section 5.3) is found to be a good representation of the droplet diameter probability distribution at this test point.

In prior work Glahn et al. [40], Ahmed and Youssef [96] investigated oil disintegration from the rim of a spinning disc and spinning cup respectively and presented correlations for droplet diameters generated. Similar work was performed for oil disintegration from axial and radial passages in a rotating cylinder [45, 46]. These geometries

are similar to oil shedding in parts of the bearing chamber (e.g. oil shedding from the cage), but are not representative of oil shedding from the static edge. Comparison of non-dimensional droplet diameters in the literature and those calculated from experimental droplet data highlights the difference between shedding from rotating and static surfaces. The non-dimensional Sauter Mean Diameter (SMD) predicted by the spinning disc approximation of Glahn et al. [40] is 0.07, compared to 0.03 at R/D of 0.1, 0.08 at R/D of 0.5, 0.12 at R/D of 1.0 given by the correlation from Ahmed and Youssef [96] (where R/D is the downstream tangential distance over disk diameter). Comparison to Fig. 5.11 shows that predictions from either of these correlations under-predict the droplet diameter at the 3 o'clock position in the bearing chamber. This is not unexpected given that the work by Paleo Cageao et al. [43] showed a significant difference in behaviour when oil is shed via a static element compared to directly from a rotating element.

Two peaks are found in the droplet speed probability distribution shown in Fig. 5.12. The smaller of the peaks centres around the $1.00\,\mathrm{m\,s^{-1}}$ to $1.14\,\mathrm{m\,s^{-1}}$ range and the larger around the $2.85\,\mathrm{m\,s^{-1}}$ to $3.00\,\mathrm{m\,s^{-1}}$ range. The split suggests there may be two types of droplet behaviour and/or shedding mechanisms. Further investigation is needed on this matter to determine the source of droplets in these two groups. This will likely require analysis of high-speed image data at additional circumferential positions. Droplet speed in this investigation is approximately 2% of the shaft speed. This is significantly lower than found by Farbrother et al. [97] for experimental work using a simplified bearing chamber geometry, where droplet speed was approximately 5% of the shaft speed. In the simplified test rig droplets are shed from a rotating cup via a static surface. A significant difference in the two geometries is that the test rig used by Farbrother et al. [97] has a shaft running through the bearing chamber (as in the actual engine) but the BSR has a stub shaft. This difference significantly affects the acceleration of airflow in the bearing chamber and may explain the difference in droplet speed observed.

Examination of droplet diameter and speed together can be done using Fig. 5.13. The two distinct peaks, primarily separated by difference in speed, are also seen to cover a slightly different droplet diameter range. The lower speed peak (approximately $1.00\,\mathrm{m\,s^{-1}}$) consists of small droplets of around 0.5 mm in diameter, whereas the higher speed peak (approximately $3.00\,\mathrm{m\,s^{-1}}$) includes a larger range of droplet diameters, extending up to around 2.0 mm It is also notable that droplets greater than 1.0 mm in diameter are only detected for speeds greater than approximately $2.00\,\mathrm{m\,s^{-1}}$ This suggests a slight positive correlation between droplet speed and diameter, likely either

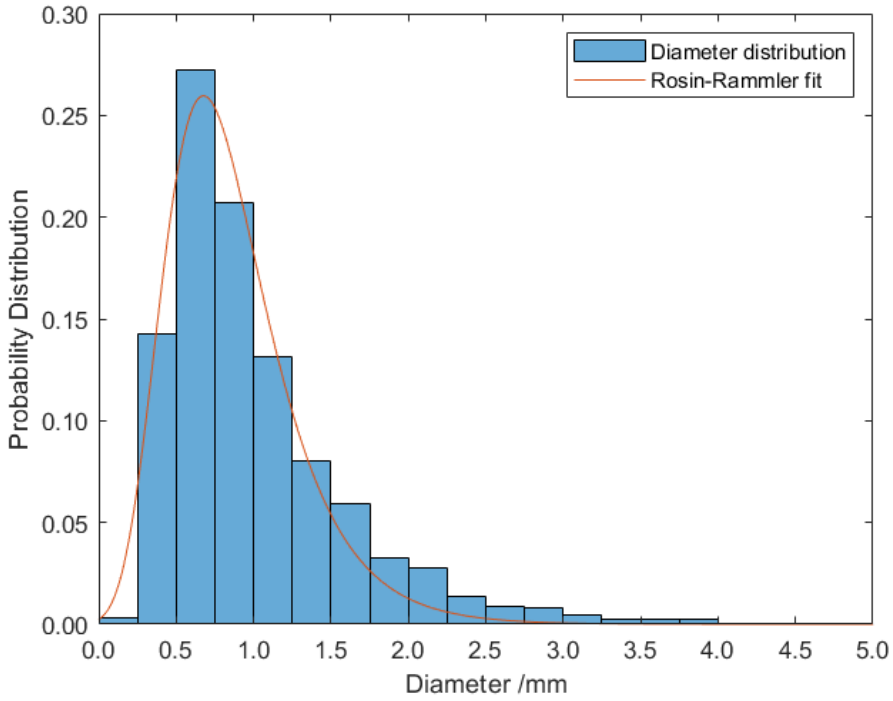


Figure 5.11: Droplet diameter distribution overlaid with a Rosin-Rammler fit for 7000 rpm with an oil flow rate of 5.2 lpm axial load of 20 kN.

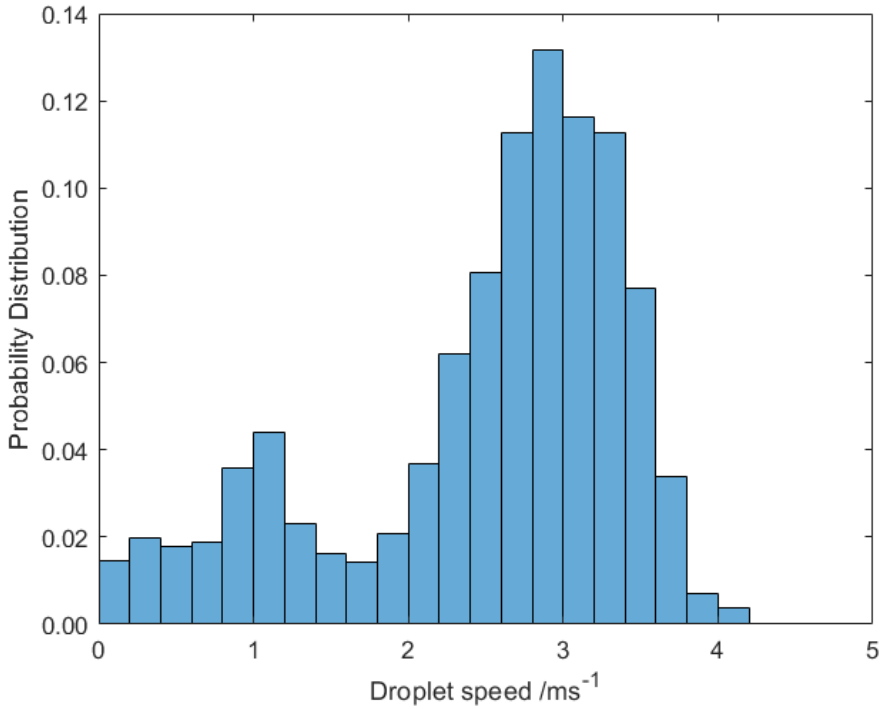


Figure 5.12: Droplet speed distribution for 7000 rpm with an oil flow rate of 5.2 lpm axial load of 20 kN.

due to the increased drag of larger droplets causing them to be accelerated to a greater extent by the rotating airflow or by a different mode of droplet generation - e.g. being shed from a different location or splashing from the oil film on the bearing housing(as discussed in Section 2.5) leading to generation of smaller droplets which pass directly into the bearing chamber.

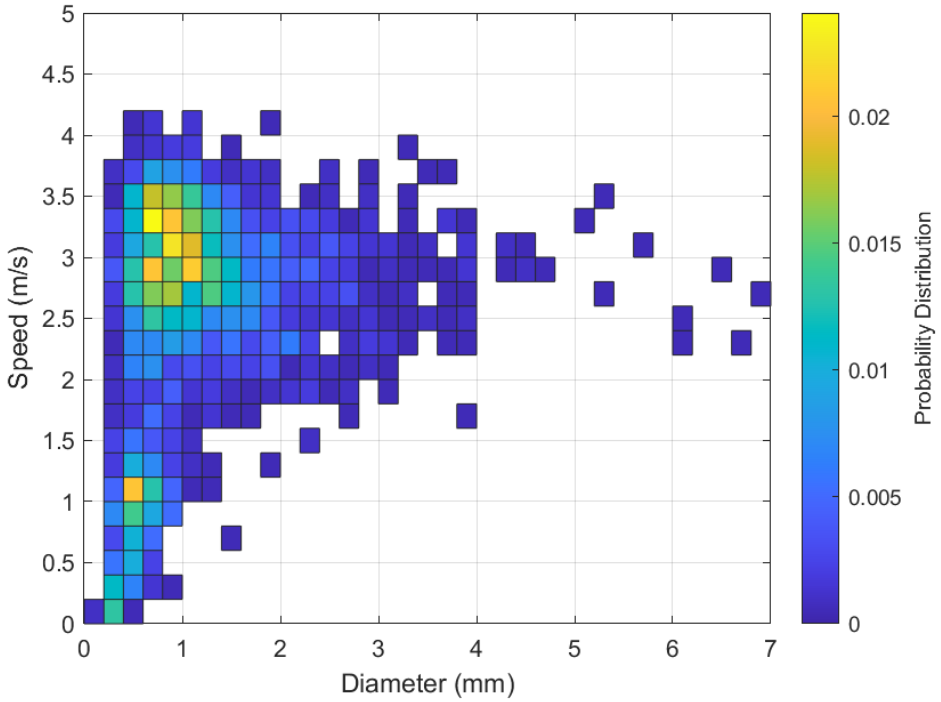


Figure 5.13: Tile plot of droplet speed and diameter distribution for 7000 rpm with an oil flow rate of 5.2 lpm axial load of 20 kN.

Droplet paths are plotted in Figs. 5.14 and 5.15 coloured by diameter and speed respectively. This type of plot allows visual inspection of variation of droplet properties with in-plane position in the bearing chamber. No obvious trend is seen for droplet diameter with spatial position, but there is a noticeable difference in speed in different regions. The majority of fast-moving droplets appear to exist at a greater radial distance from the centre. A particularly high concentration of fast droplets occurs in the upper right corner of the imaging region. Many of these droplets look to have originated from elsewhere in the bearing chamber, giving an indication that generally higher speed droplets may exist at other circumferential positions. Slower droplets closer to the centre of rotation are likely to experience a higher residence time and have a higher risk of becoming entrained in the airflow (as discussed in Section 2.8). Further investigation is required to develop a more complete understanding of droplets in the entirety of the bearing chamber and how shedding mechanisms/circumferential positions may affect droplet speed. Processing of high-speed images from additional circumferential

positions is needed for this.

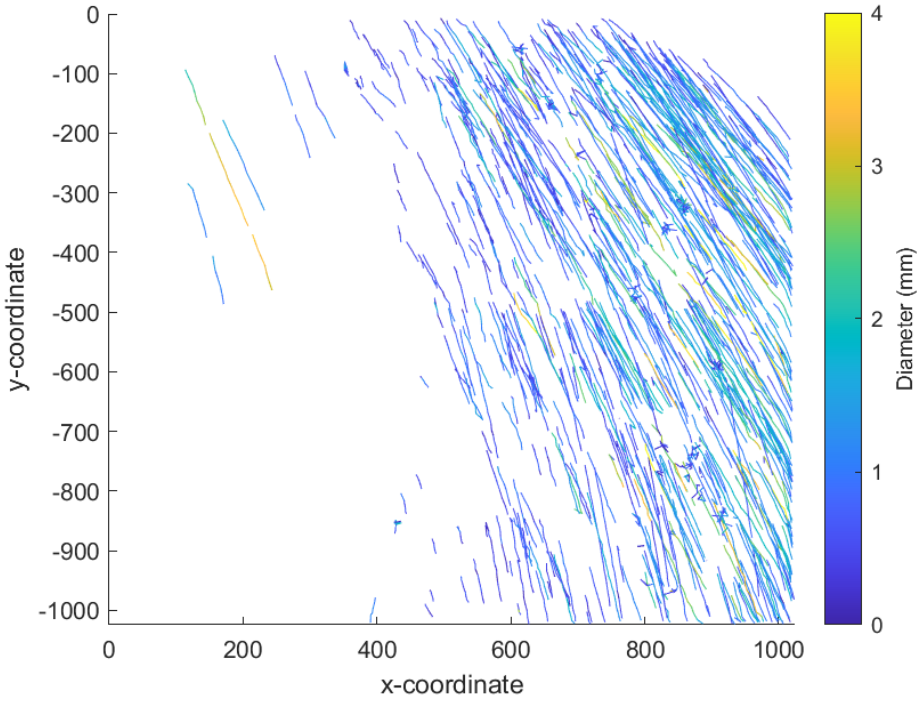


Figure 5.14: Plot of droplet tracks, coloured by diameter for 7000 rpm with an oil flow rate of 5.2 lpm axial load of 20 kN.

5.3 Diameter Distribution

The diameter distribution of droplets is investigated for multiple operating conditions and circumferential positions using the method described in Chapter 3 and analysed as in Chapter 4. The Rosin-Rammler distribution is presented as a method of representing the diameter distribution of droplets in the bearing chamber. This means that the distribution can be described using the three variables ϕ, β and k in Eq. (5.1).

$$F(x;\phi,\beta,k) = \frac{k}{\beta} e^{-(z+e^{-z})} \tag{5.1}$$

Where $z = \dfrac{x-\phi}{\beta}$, ϕ is the location parameter (i.e. the modal droplet diameter), β is the scaling factor and k is a constant. The Rosin-Rammler distribution is fitted to the droplet diameter data using the curve fitting tool in MATLAB.

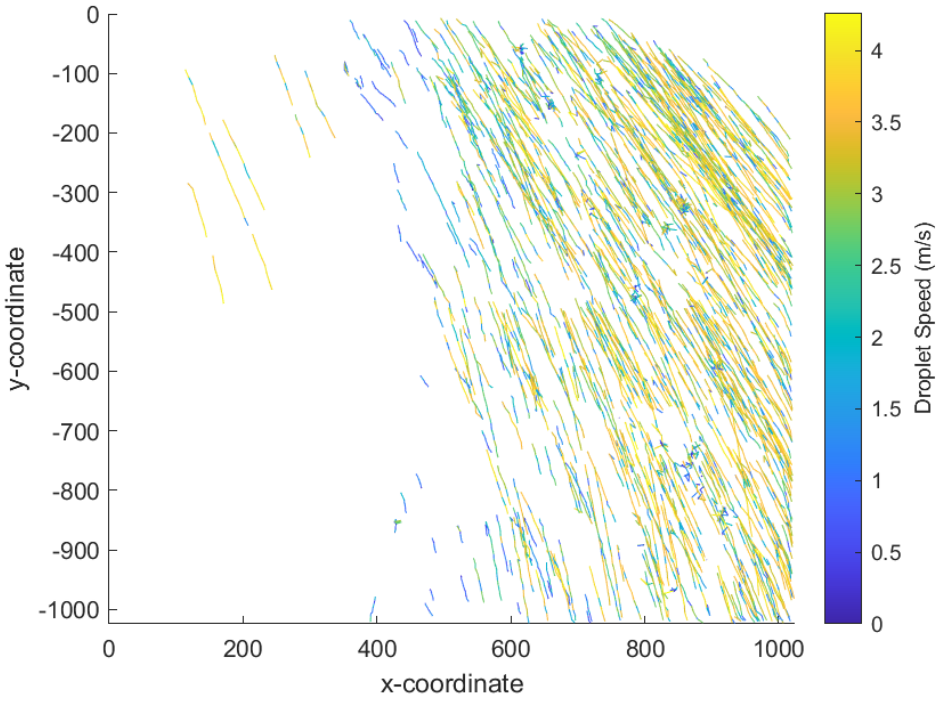


Figure 5.15: Plot of droplet tracks, coloured by droplet speed, for 7000 rpm with an oil flow rate of 5.2 lpm axial load of 20 kN.

5.3.1 Effect of Operating Speed on Diameter Distribution

The main series of data was collected as described in Chapter 3 for speeds between 1000 rpm and 9000 rpm operating with an oil flow rate of 7.3 l min^{-1} and axial load of 10 kN, in addition to a single test point at 12 000 rpm recorded at only the 9 o'clock position. However, data for additional operating speeds later became available through the Cleansky 2 funded project AERIS. This yet unpublished data extends to higher speeds, including 10 000 rpm, 11 000 rpm and 12 000 rpm but has an imaging area of 576 x 908 pixels (compared to 1024 x 1024 pixels). This difference means that the AERIS data has a lower spatial resolution than the data collected as part of this work and therefore must be considered separately for quantitative analysis. The higher spatial resolution of the main data series allows detection of smaller droplets and more accurate diameter data, however analysis of the AERIS data series adds value by showing trends in behaviour over a wider range of operating speeds including more aeroengine representative speeds. Sample images from the main and AERIS data series are shown in Figs. 5.16 and 5.17 respectively. Both data series are processed using the droplet detection and tracking method described in Chapter 4.

Qualitative discussion of the trends seen in Figs. 5.16 and 5.17 in two-phase flow behaviour with operating speed is as follows.

- At 1000 rpm there is very little oil film visible on the front face and only a small number of droplets are observed.
- Increasing the operating speed up to 5000 rpm correlates to an increase in the area of the front face covered by oil film at both the 3 o'clock and 9 o'clock position. The film covers a larger area on the 3 o'clock (co-current) side of the bearing chamber but appears thicker and more prone to forming three-dimensional structures on the 9 o'clock (counter-current) side. A larger number of droplets can be seen within the imaging area.
- At 9000 rpm more three-dimensional structures are observed on both the 3 o'clock and 9 o'clock sides of the bearing chamber - those on the 9 o'clock side become highly complex and begin to break up. The number and size of droplets appears similar to at lower speeds (i.e. not enough change to be obvious by visual inspection alone).
- At 10 000 rpm three-dimensional structures break up into droplets far more rapidly (i.e. extend a lesser distance into the bearing chamber before breakup occurs), generating a significant increase in the number of droplets.
- This trend of increasingly rapid breakup to produce droplets is continued at 11 000 rpm and 12 000 rpm.

Use of the Rosin-Rammler distribution, described in Eq. (5.1), was proposed by Nicoli [1] as a method of representing the droplet diameter distribution in the bearing chamber. Droplet diameter distribution from the main experimental dataset is plotted alongside the Rosin-Rammler for the 3 o'clock position fit in Figs. 5.18 to 5.22 and for the 9 o'clock position in Figs. 5.23 to 5.27 for speeds in the range of 1000 rpm to 9000 rpm. An additional test point on the 9 o'clock side for 12 000 rpm is shown in in Fig. 5.28. Droplet diameter distributions from the AERIS dataset are plotted in the same way and shown in Chapter A. In all cases the Rosin-Rammler fit is shown to provide a good representation of droplet diameters on both sides of the bearing chamber.

Comparison of the droplet diameter distribution at the 3 o'clock position with varying operating speeds through direct inspection of figures such as Fig. 5.22 is challenging. However, differences can be more clearly seen by inspecting the changes in the variables in the Rosin-Rammler fit used to represent the distributions and by examining the data in a box-plot - this is done in Fig. 5.29a. The key features of a box plot are as follows:

- Minimum - end of lower whisker

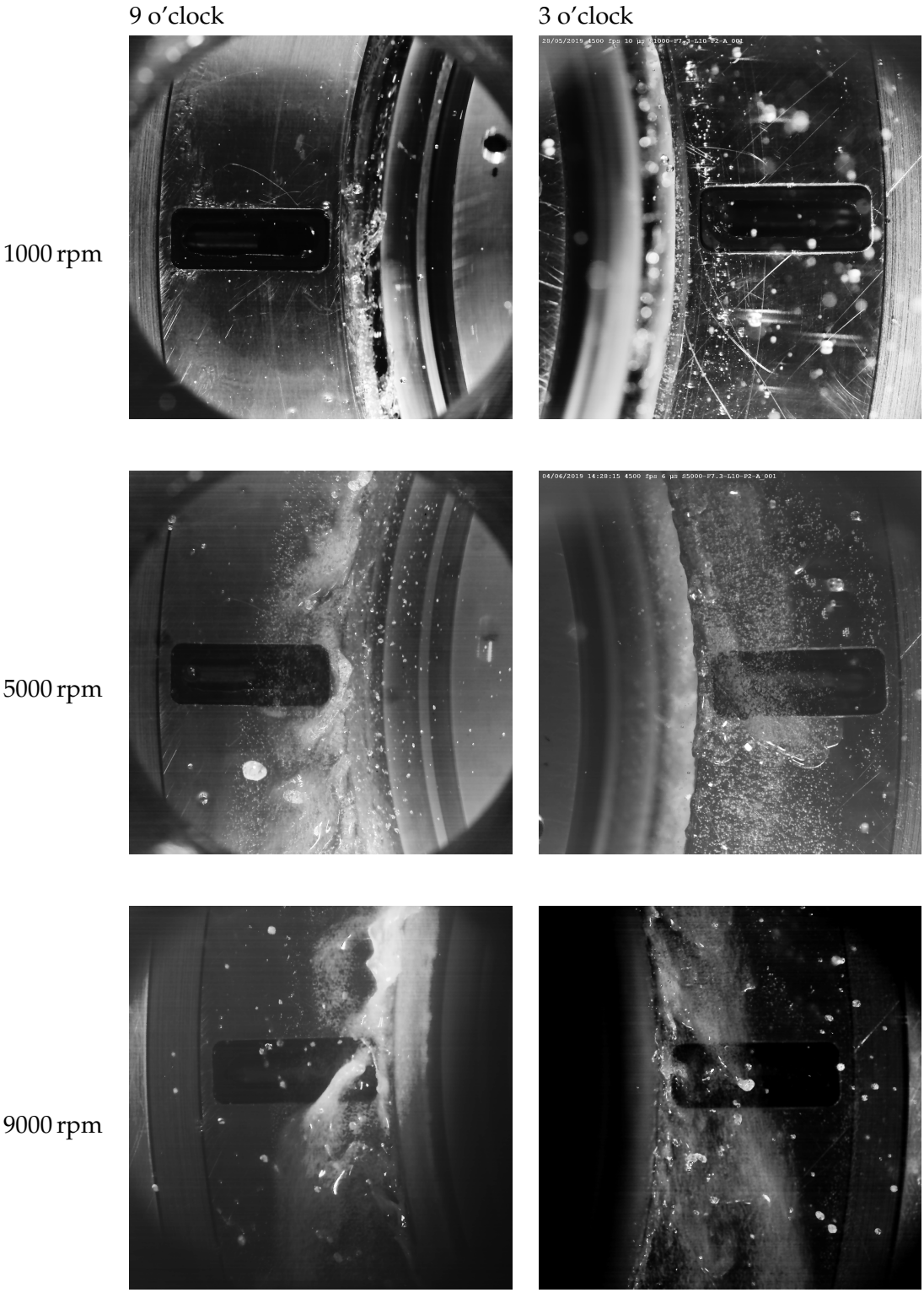


Figure 5.16: Sample high speed images from the main data series at operating speeds between 1000 rpm and 9000 rpm with an oil flow rate of 7.3 l min^{-1} and an applied axial load of 10 kN.

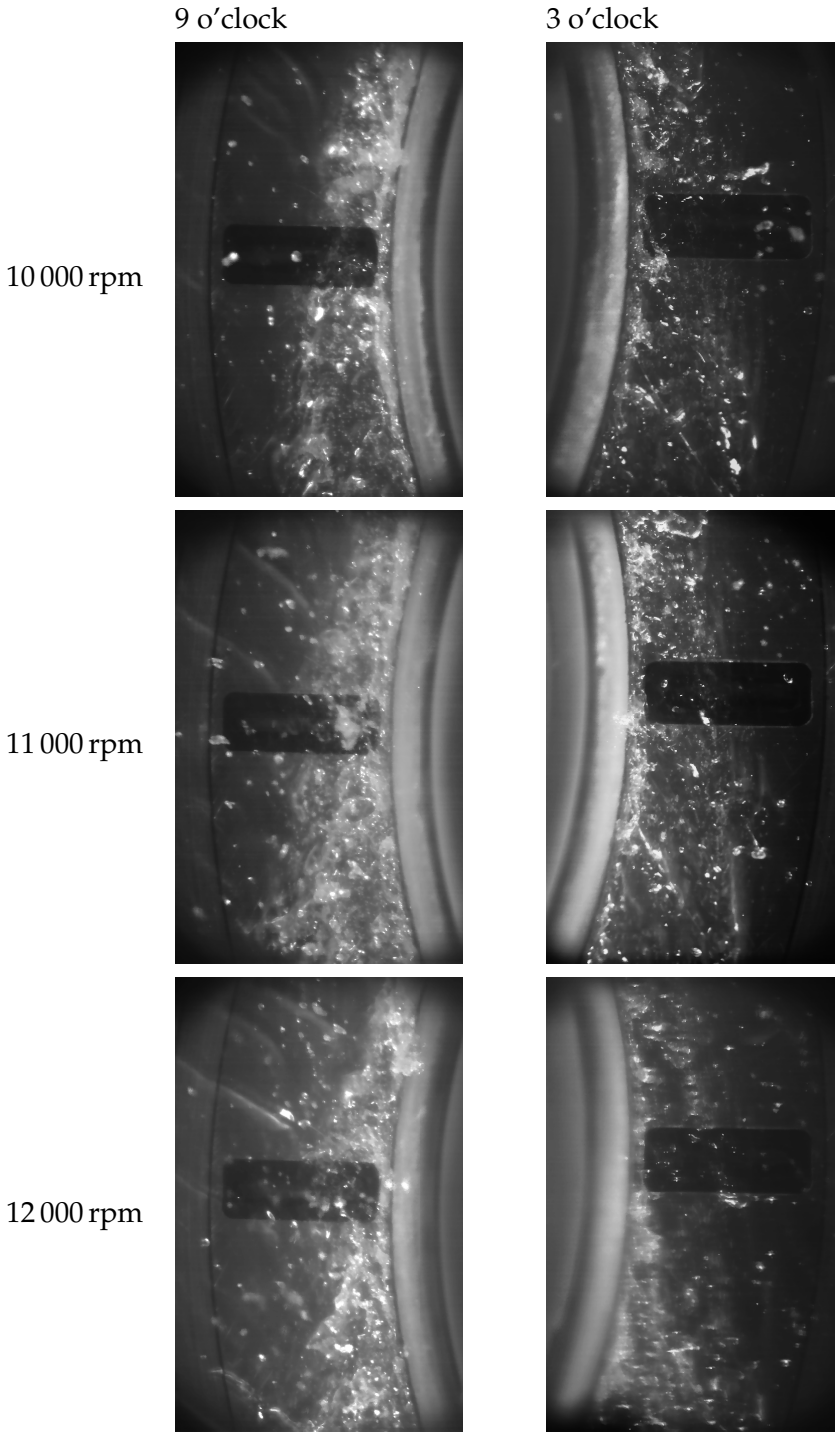


Figure 5.17: Sample high speed images from the AERIS data series at operating speeds between 10 000 rpm and 12 000 rpm with an oil flow rate of 7.3 l min^{-1} and an applied axial load of 10 kN.

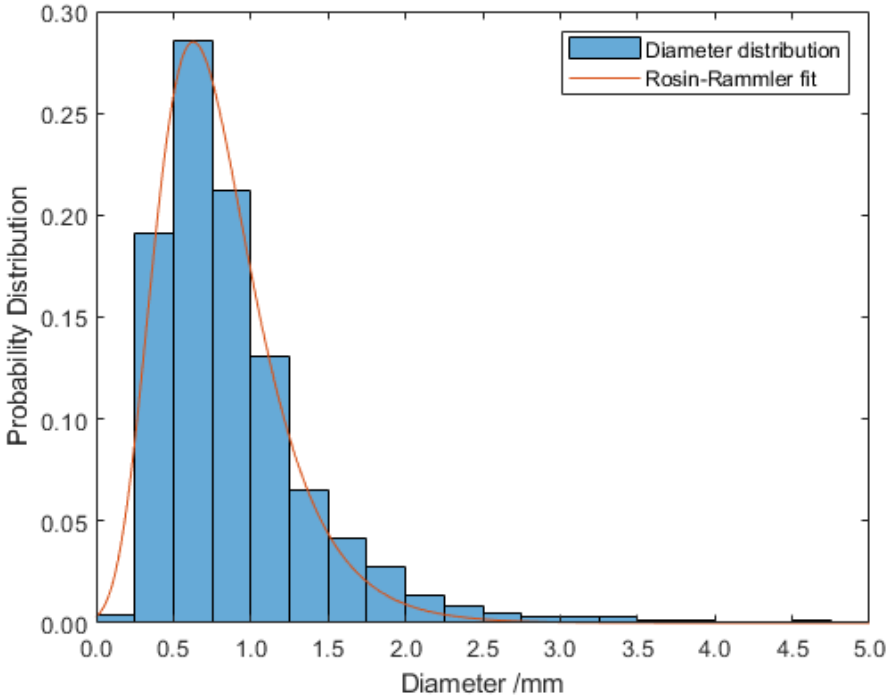


Figure 5.18: Droplet diameter distribution at the 3 o'clock position at 1000 rpm with oil flow rate 7.31 $l\,min^{-1}$ and axial load 10 kN.

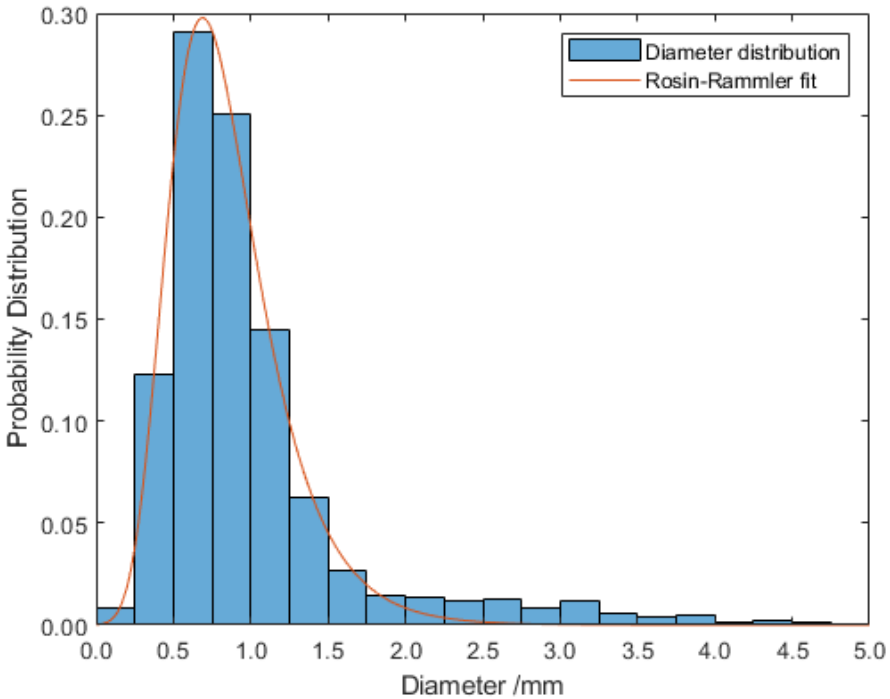


Figure 5.19: Droplet diameter distribution at the 3 o'clock position at 3000 rpm with oil flow rate 7.31 $l\,min^{-1}$ and axial load 10 kN.

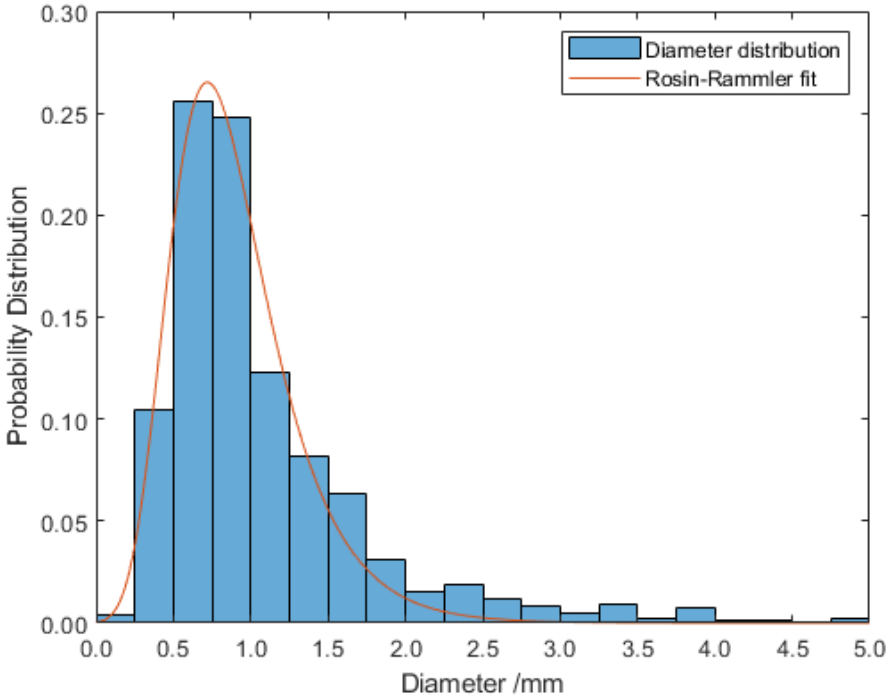


Figure 5.20: Droplet diameter distribution at the 3 o'clock position at 5000 rpm with oil flow rate 7.31 $l\,min^{-1}$ and axial load 10 kN.

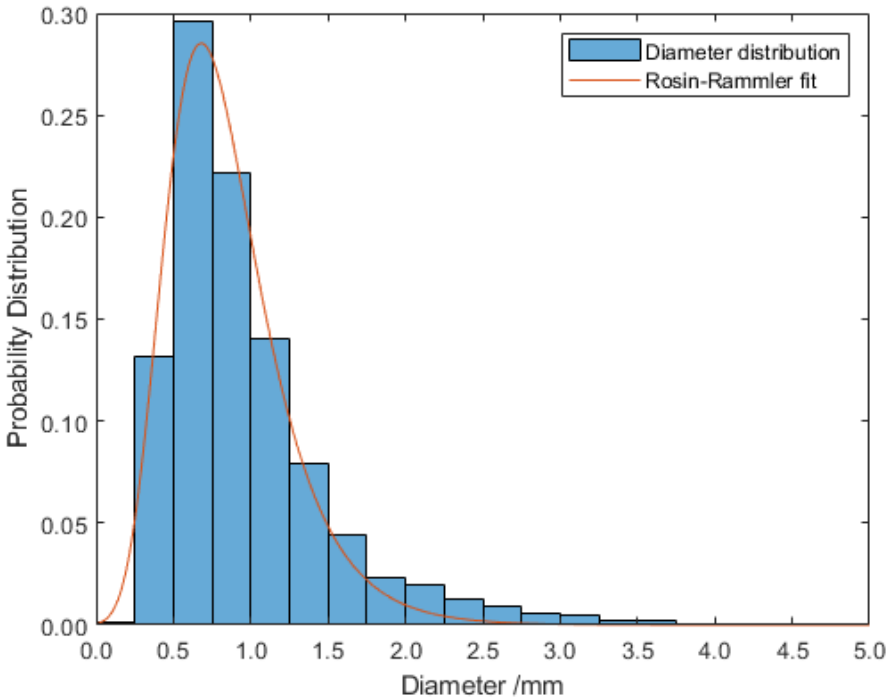


Figure 5.21: Droplet diameter distribution at the 3 o'clock position at 7000 rpm with oil flow rate 7.31 $l\,min^{-1}$ and axial load 10 kN.

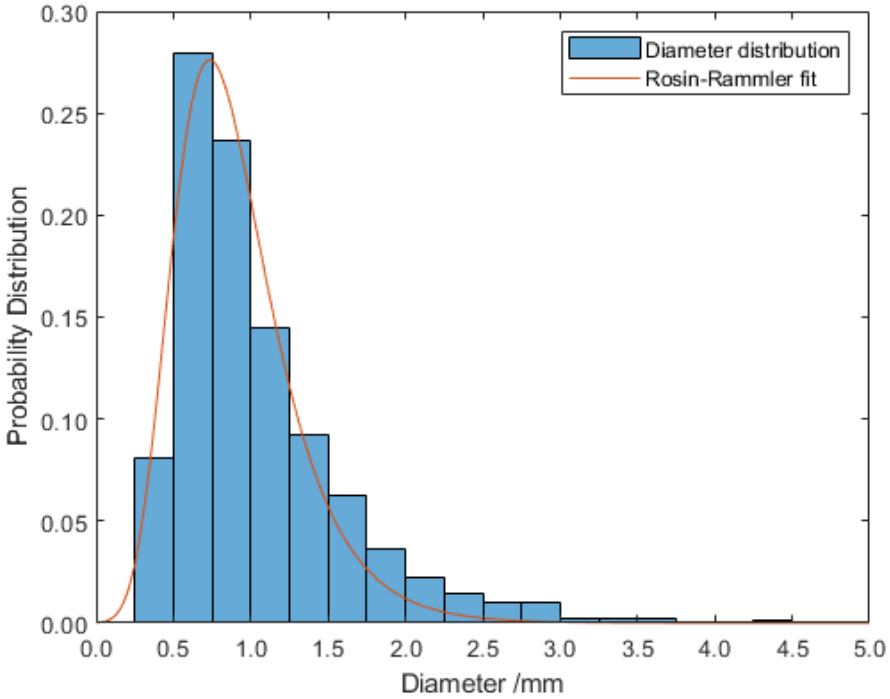


Figure 5.22: Droplet diameter distribution at the 3 o'clock position at 9000 rpm with oil flow rate 7.31 $l\,min^{-1}$ and axial load 10 kN.

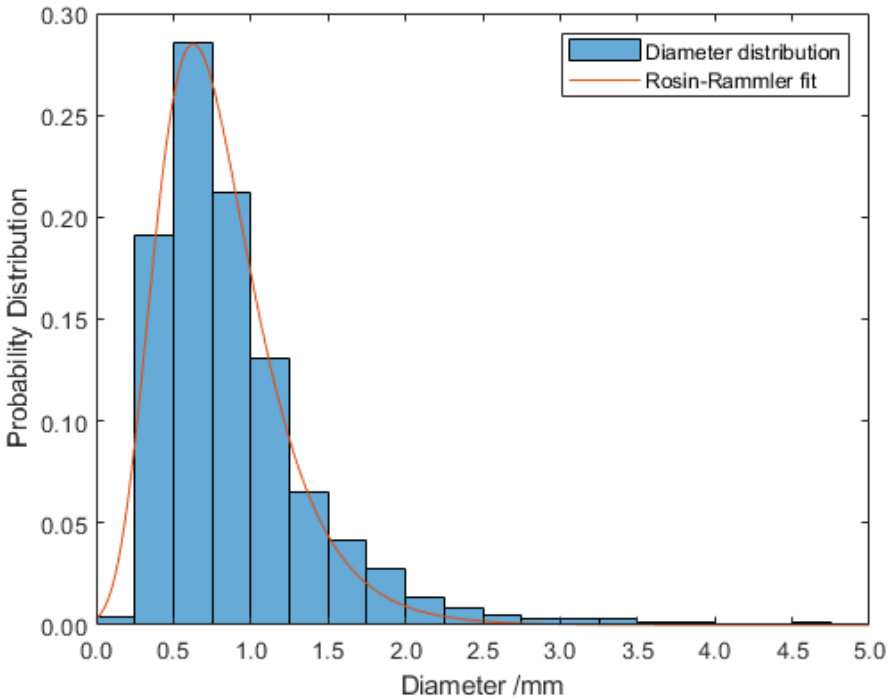


Figure 5.23: Droplet diameter distribution at the 9 o'clock position at 1000 rpm with oil flow rate 7.31 $l\,min^{-1}$ and axial load 10 kN.

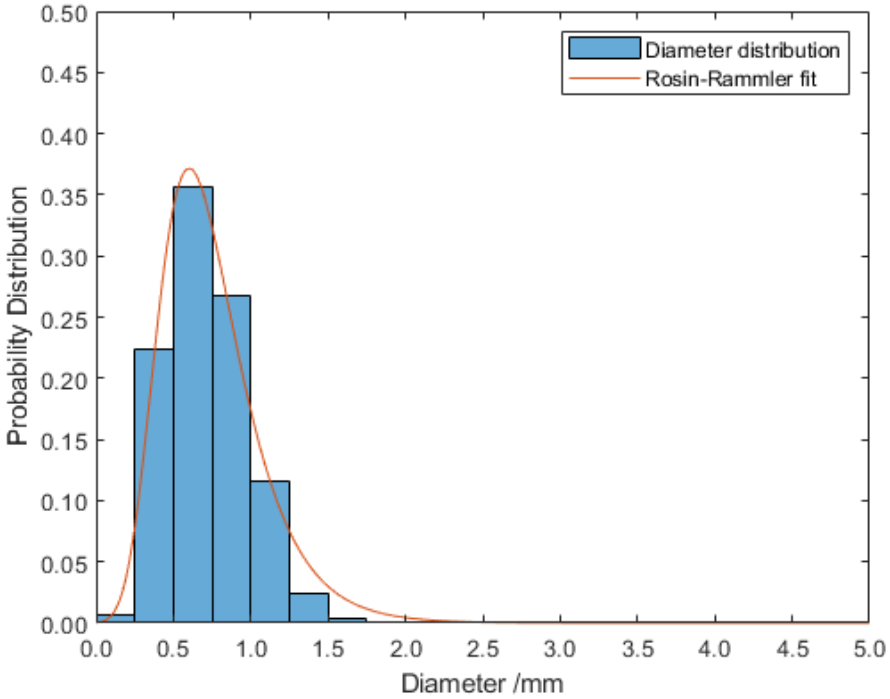


Figure 5.24: Droplet diameter distribution at the 9 o'clock position at 3000 rpm with oil flow rate 7.31 $l\,min^{-1}$ and axial load 10 kN.

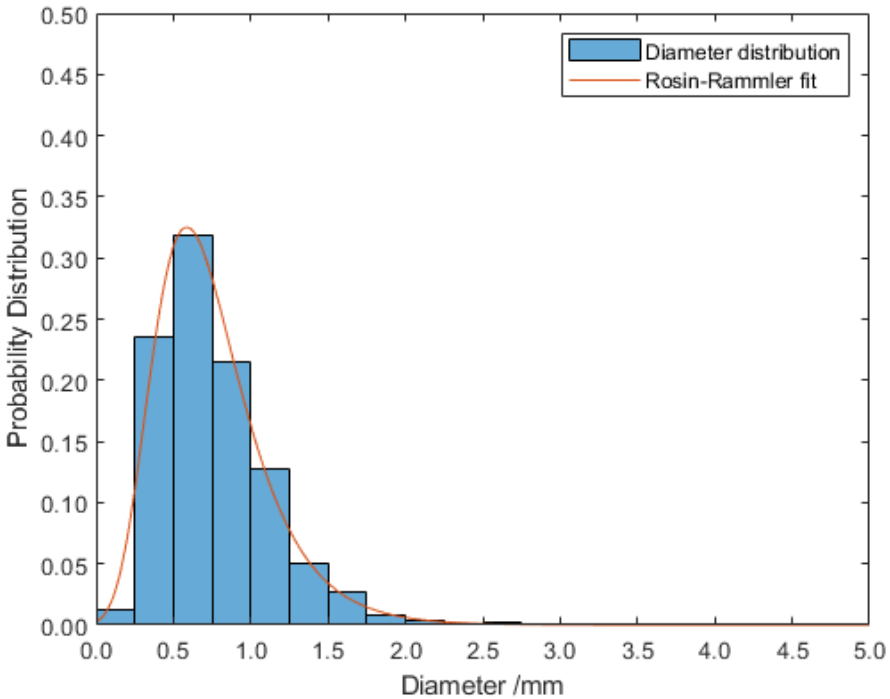


Figure 5.25: Droplet diameter distribution at the 9 o'clock position at 5000 rpm with oil flow rate 7.31 $l\,min^{-1}$ and axial load 10 kN.

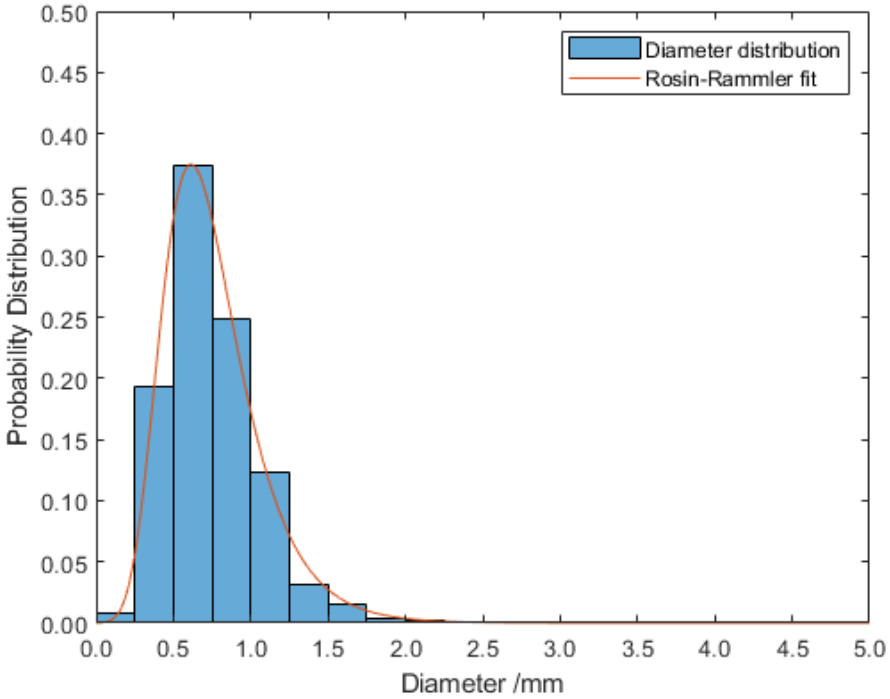


Figure 5.26: Droplet diameter distribution at the 9 o'clock position at 7000 rpm with oil flow rate 7.31 $\mathrm{l\,min^{-1}}$ and axial load 10 kN.

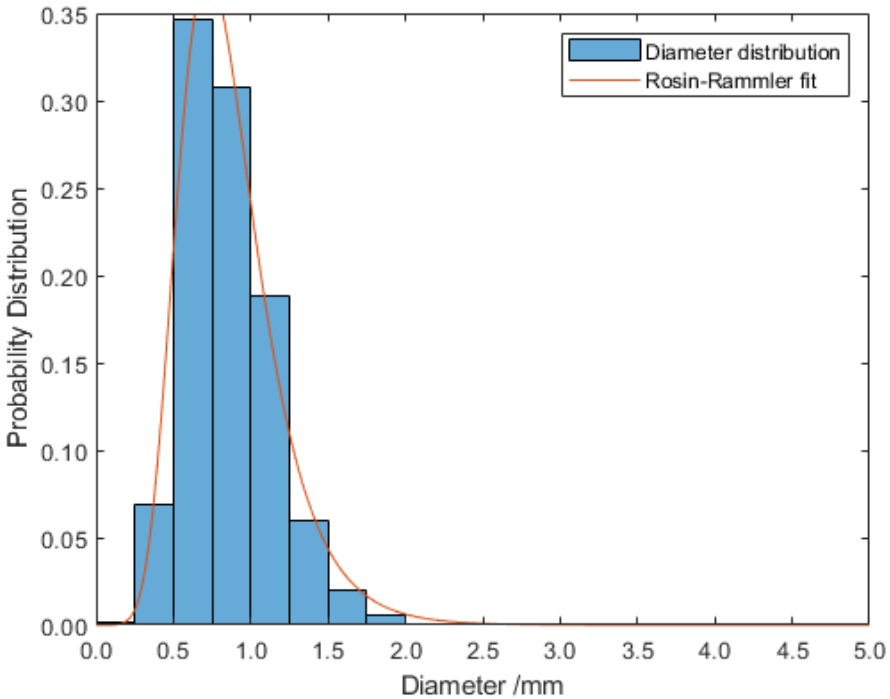


Figure 5.27: Droplet diameter distribution at the 9 o'clock position at 9000 rpm with oil flow rate 7.31 $\mathrm{l\,min^{-1}}$ and axial load 10 kN.

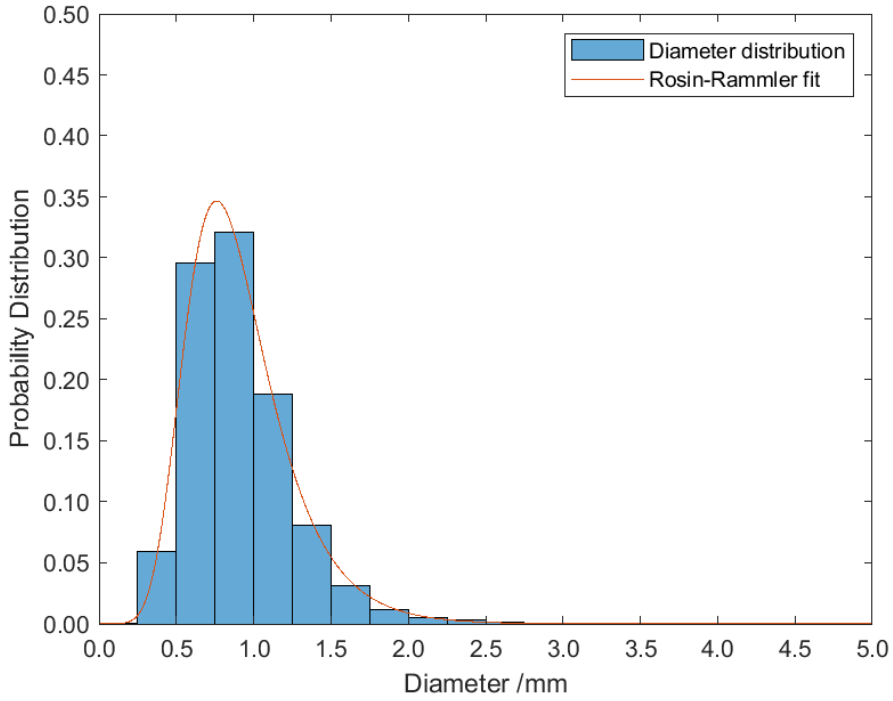


Figure 5.28: Droplet diameter distribution at the 9 o'clock position at 12 000 rpm with oil flow rate 7.3 l min^{-1} and axial load 10 kN.

- Q1/lower quartile - bottom of box
- Median - horizontal red line
- Q3/upper quartile - top of box
- Maximum - end of upper whisker
- Outliers - red crosses (outlier test is $Q1 - (Q3 - Q1)$ and $Q3 + (Q3 - Q1)$)

Additionally, the mean diameter and SMD are plotted as cyan and green Xs respectively. Fig. 5.29a shows very little change in droplet diameter with increased operating speed. There is a small increase in median droplet diameter between 1000 rpm and 5000 rpm but is then relatively constant up to 9000 rpm.

The Rosin-Rammler variables are shown in Fig. 5.30a. β (scaling factor) and k (constant) do not vary significantly over the speed range for either data series, remaining at approximately 0.30 and 0.24 respectively. However, ϕ (location parameter) is relatively constant for operating speeds up to 7000 rpm where a distinct change occurs. The increase in ϕ at higher speeds above 7000 rpm corresponds to an increase in droplet diameter and is more clearly seen as the operating speed increases from 7000 rpm to

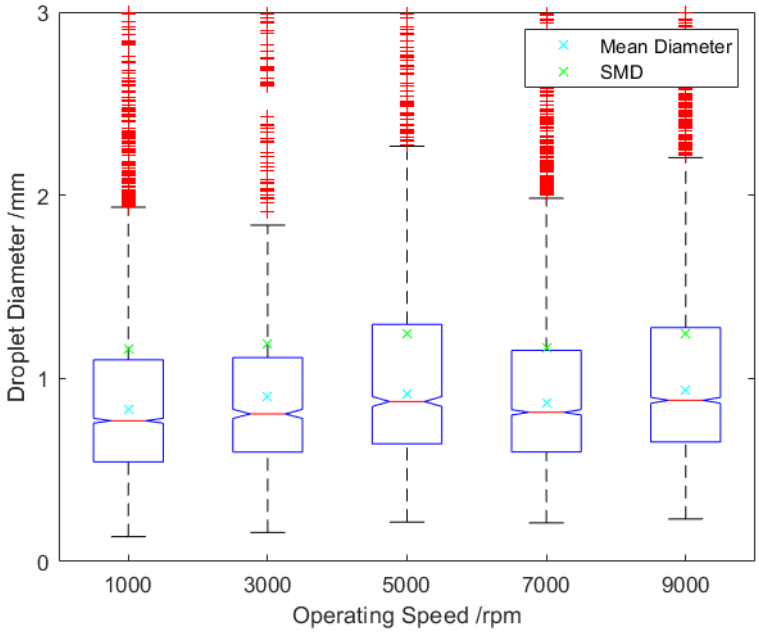
12 000 rpm in the AERIS data series - the beginning of this increasing trend is also observed between 7000 rpm to 9000 rpm in the main data series. The change from a steady value of ϕ to an increasing trend corresponds to the regime change in the oil film on the static close to the bearing seen by Sinha et al. [24] at 8000 rpm, before which the film thickness reduces with increased shaft speed and after which, the film thickness asymptotically approaches a constant value as the film is accelerated to it's maximum speed. An exception to these trends is seen in the AERIS data series at 5000 rpm, where β and ϕ are anomalously high. This may be due to detection of uncharacteristically large droplet diameters within the high-speed image sequence.

Similarly, Fig. 5.29b shows a small increase in median droplet diameter with increasing operating speed between 1000 rpm and 5000 rpm at the 9 o'clock position. However the change in diameter with operating speed is small. Droplets are generally slightly larger on the 3 o'clock side but there is considerable overlap in the diameter distribution on either side of the bearing chamber. Some of the smaller droplets seen on the 9 o'clock side may be generated by shear stripping from the oil film on the bearing housing. As discussed in Section 2.4.2, this is unlikely to occur on the co-current side but is a very likely mechanism of droplet generation on the counter-current side of the bearing chamber.

The changes in Rosin-Rammler variables representing the diameter distribution at the 9 o'clock position are shown in Fig. 5.30b. k remains constant at 0.25 however there is more variation in β (scaling factor) than seen at 3 o'clock. This is the case for both the main data series and the AERIS data series. The value of β for the main data series varies between 0.18 and 0.30 with no obvious trend with speed, other than having a notably lower value at 1000 rpm, meaning that the droplet diameter is less concentrated around the peak probability distribution than at other operating speeds. However, the value of β for the AERIS data series appears to increase with operating speed - particularly notable are the very low value at 1000 rpm (closely matching that of the main data series) and the increasing values between 9000 rpm and 12 000 rpm, potentially indicating a regime change at each of these boundaries. ϕ (location parameter) is lower at 1000 rpm for both data series, then increases to a stable value at operating speeds between 3000 rpm and 7000 rpm.

Again aligning with the change in film thickness Sinha et al. [24] observed for speeds above 8000 rpm (discussed in greater detail in Section 2.4.1), ϕ increases with operating speed above this point, meaning droplets are generally larger diameter. Considering this information alongside previously discussed qualitative analysis, the change in modal droplet diameter (ϕ) is likely due to a different mechanism of droplet gener-

a)



b)

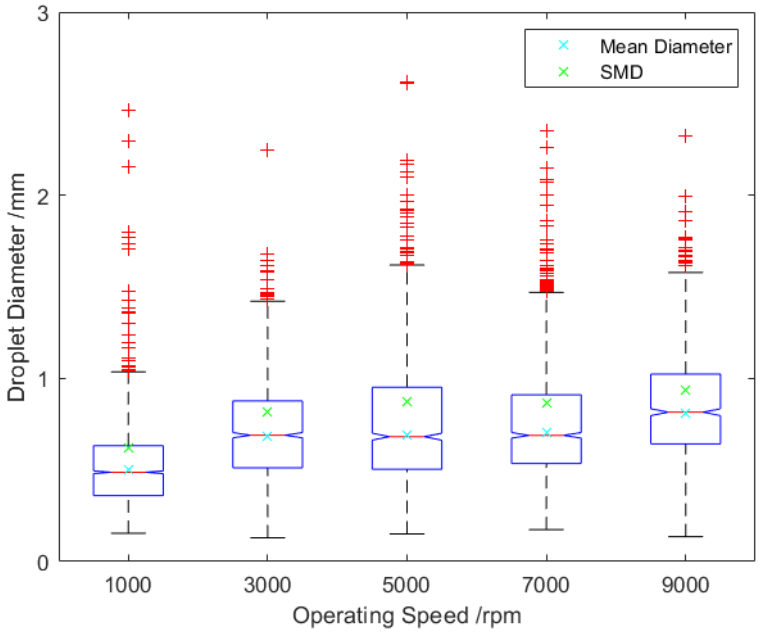
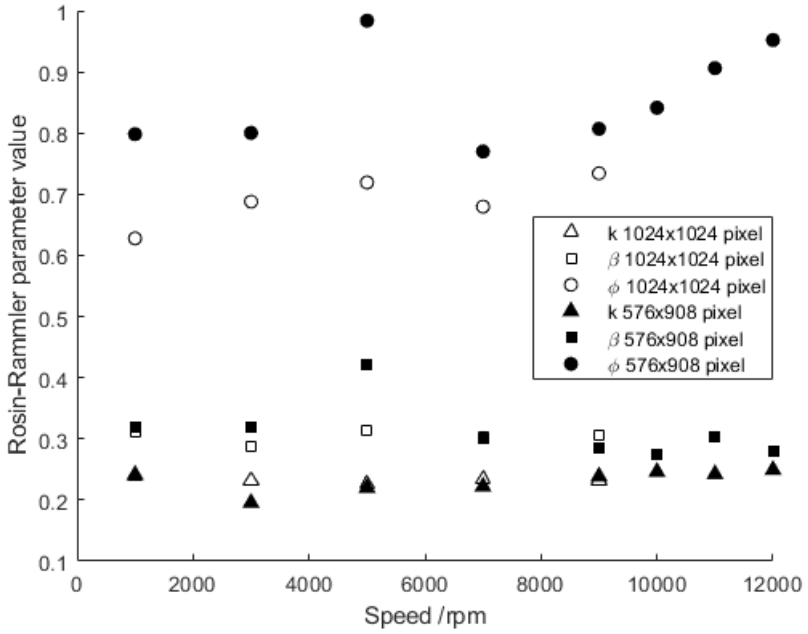


Figure 5.29: Effect of operating speed on the droplet diameter distribution on a) the 3 o'clock and b) the 9 o'clock sides of the bearing chamber.

a)



b)

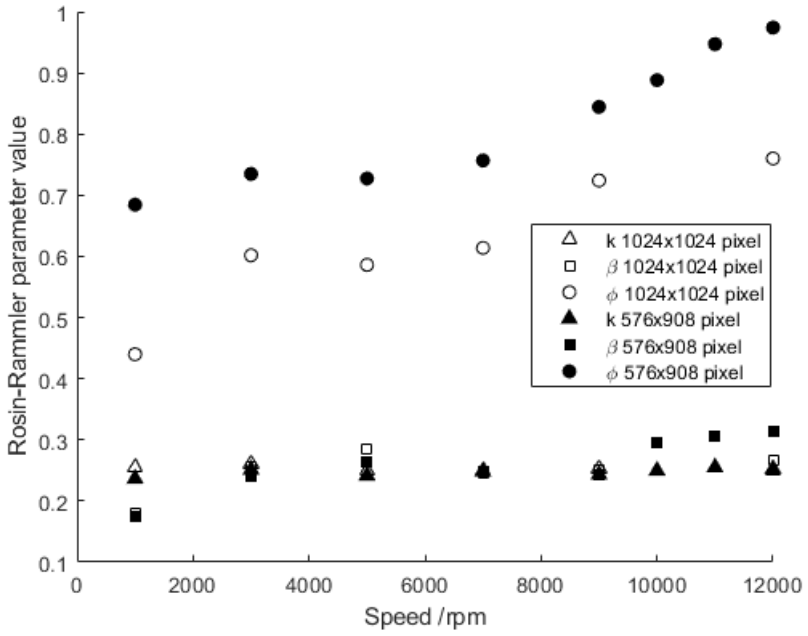


Figure 5.30: Effect of operating speed on the three variables in the Rosin-Rammler distributions representing droplet diameter on a) the 3 o'clock and b) the 9 o'clock sides of the bearing chamber. Note that data for the 1024 x 1024 pixel data series only exists for speeds up to 9000 rpm apart from a single test point at 12 000 rpmat the 9 o'clock position.

ation becoming more prevalent. This may be an increased number of droplets being generated from breakup of the oil film and complex three-dimensional structures that extend into the bearing chamber compared to droplet generation by other means such as film stripping. This mechanism of breakup (discussed in Section 2.6) generates larger droplets than those produced by shear stripping [18], which would explain the shift in droplet diameters observed.

There is a very small increase in droplet diameter between 1000 rpm and 5000 rpm in the main dataset then there is no further change in diameter up to 7000 rpm. This is true for both sides of the bearing chamber. There is not an observable increase in droplet diameter at low speeds in the AERIS dataset. Droplet diameter increases between 7000 rpm and 12 000 rpm in the AERIS dataset. The main dataset has a larger droplet diameter at 9000 rpm compared to 7000 rpm, suggesting the same trend would be seen in both datasets for high speeds. The transition point from operating speed having little/no effect on droplet diameter to where diameter increases with speed corresponds to the change in film thickness Sinha et al. [24] observed above 8000 rpm.

5.3.2 Effect of Oil Flow Rate on Diameter Distribution

The effect of oil flow rate supplied to the bearing is investigated for three different flow rates while operating at a constant speed of 9000 rpm with an applied axial load of 10 kN as per the methodology described in Chapter 3. Sample images from the three operating conditions are shown in Fig. 5.31 for both sides of the bearing chamber. Increasing oil flow rate correlates to an increasingly thick and three-dimensional oil film passing into the bearing chamber attached to the front face.

The diameter distribution for the three oil flow rates investigated is shown with the Rosin-Rammler fit of the distribution in Figs. 5.32 to 5.37. The effect of oil flow rate on droplet diameter distribution can be examined using the box-plots shown in Fig. 5.38 and by inspecting the three variables describing the Rosin-Rammler distribution plotted together in Fig. 5.39. The Rosin-Rammler fit representing the droplet diameter distribution does not change significantly on either side of the bearing chamber with increasing oil flow rate. This is unsurprising given that film thickness at the shedding edge is expected to correlate to droplet diameter and change in oil flow rate was not found to significantly affect film thickness on the bearing housing in the BSR in the investigation by Hee [8] - this is the film that breaks up to generate many of the droplets in the bearing chamber.

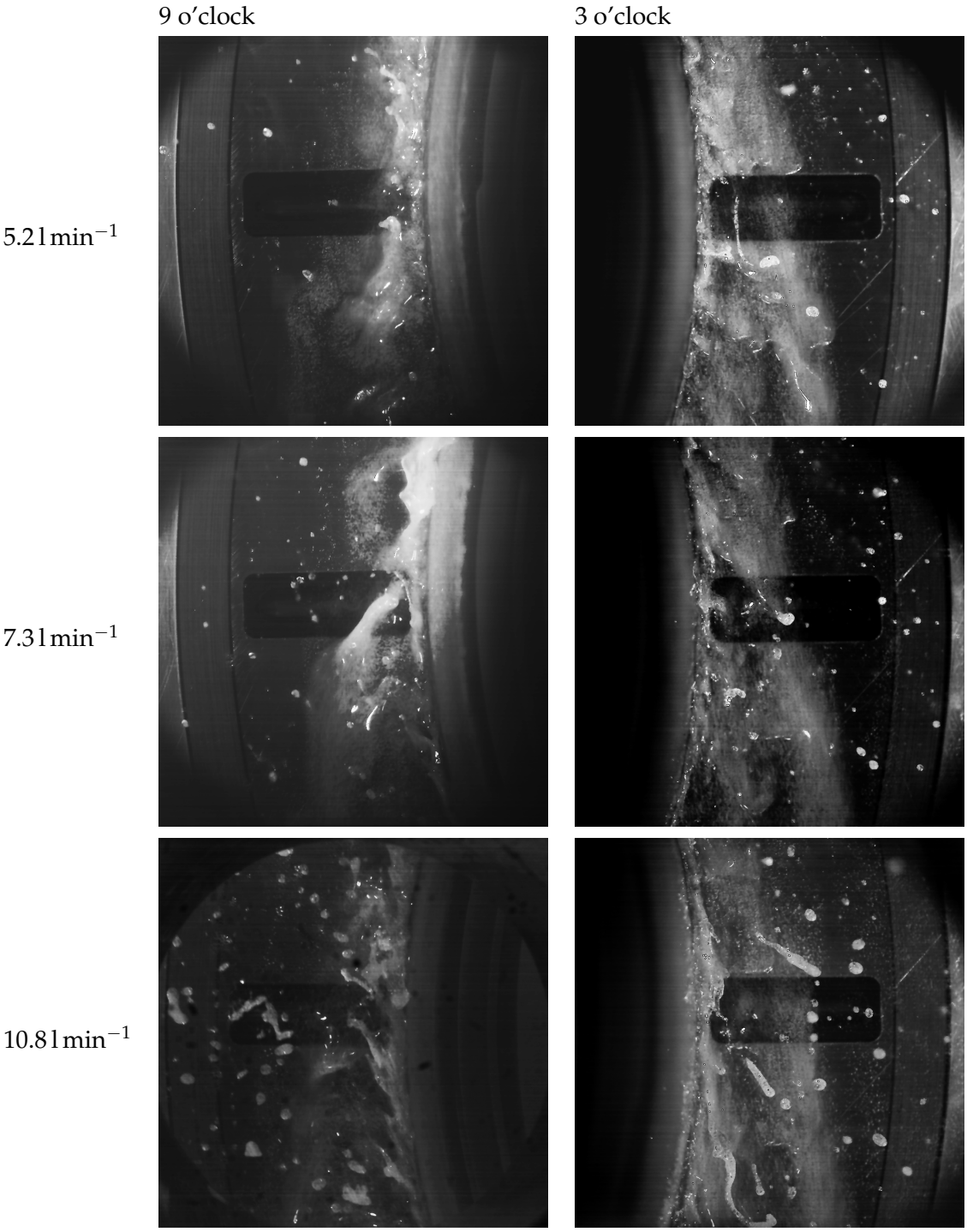


Figure 5.31: Sample high speed images from the main data series operating at 9000 rpm with an applied axial load of 10 kN and an oil flow rate between 5.21 min^{-1} and 10.81 min^{-1}.

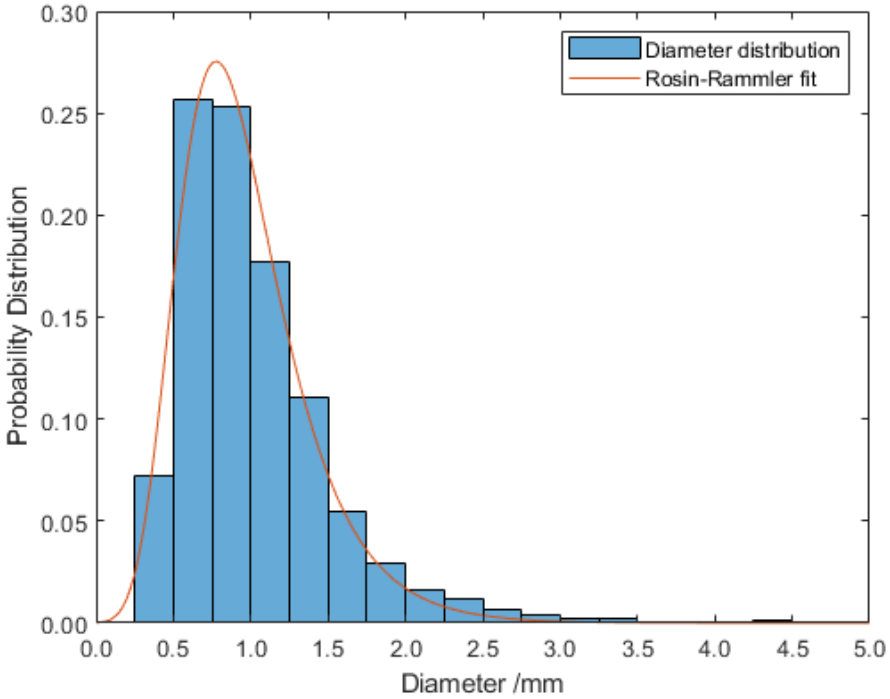


Figure 5.32: Droplet diameter distribution at the 3 o'clock position at 9000 rpm with oil flow rate 5.2 l min^{-1} and axial load 10 kN.

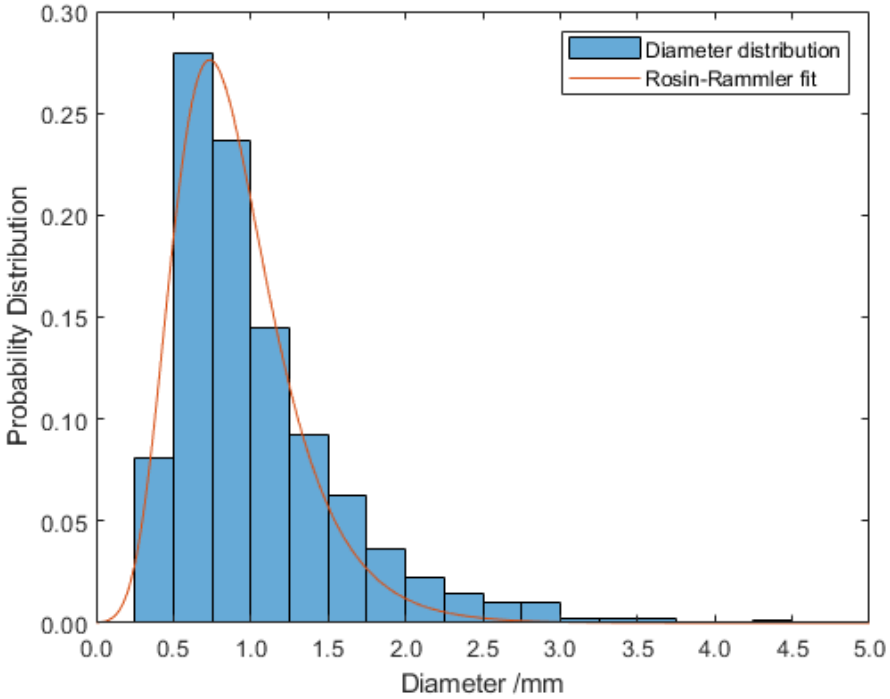


Figure 5.33: Droplet diameter distribution at the 3 o'clock position at 9000 rpm with oil flow rate 7.3 l min^{-1} and axial load 10 kN.

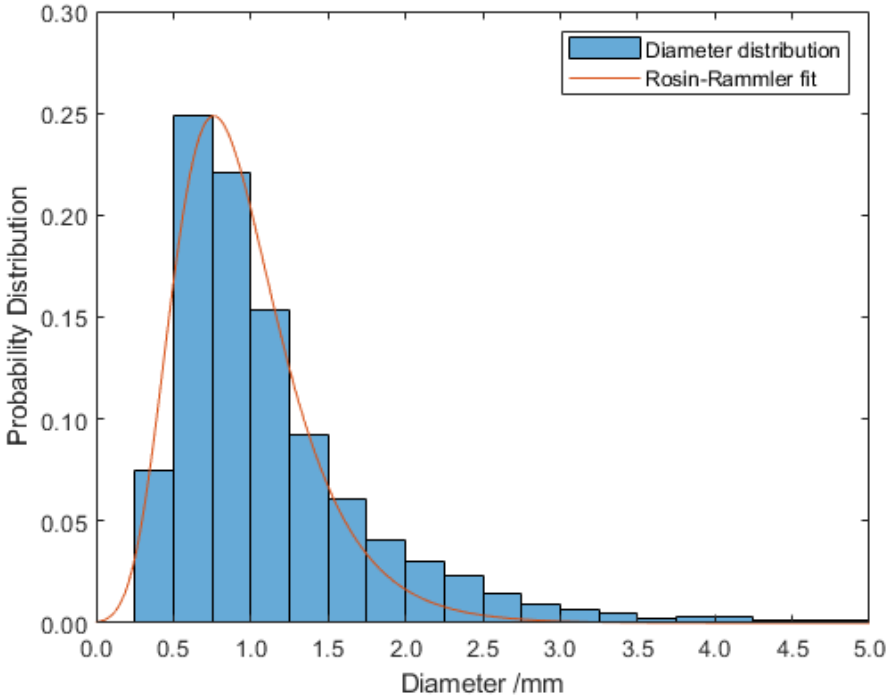


Figure 5.34: Droplet diameter distribution at the 3 o'clock position at 9000 rpm with oil flow rate 10.8 l min^{-1} and axial load 10 kN.

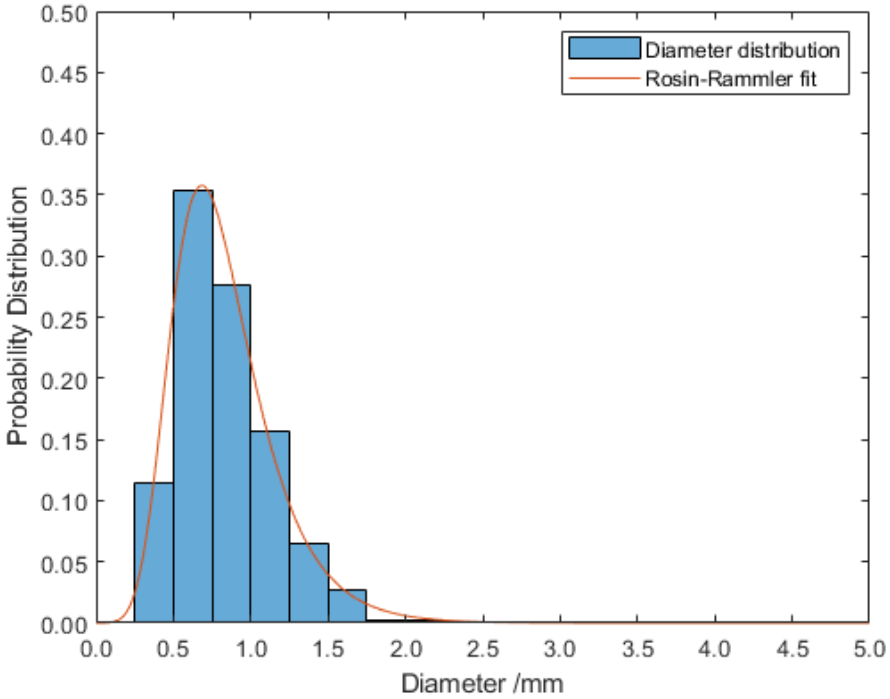


Figure 5.35: Droplet diameter distribution at the 9 o'clock position at 9000 rpm with oil flow rate 5.2 l min^{-1} and axial load 10 kN.

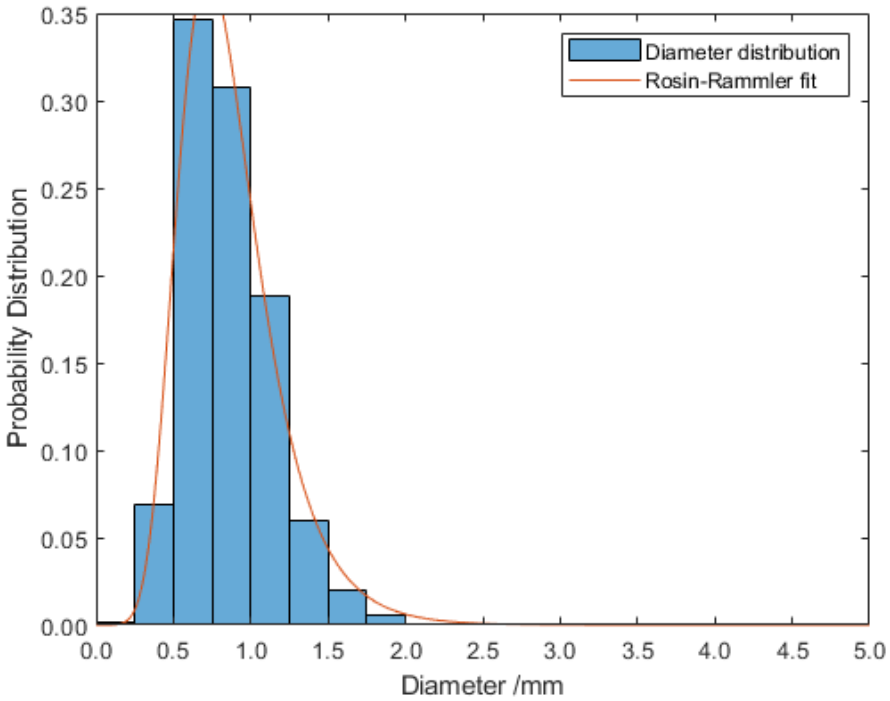


Figure 5.36: Droplet diameter distribution at the 9 o'clock position at 9000 rpm with oil flow rate 7.31 l min^{-1} and axial load 10 kN.

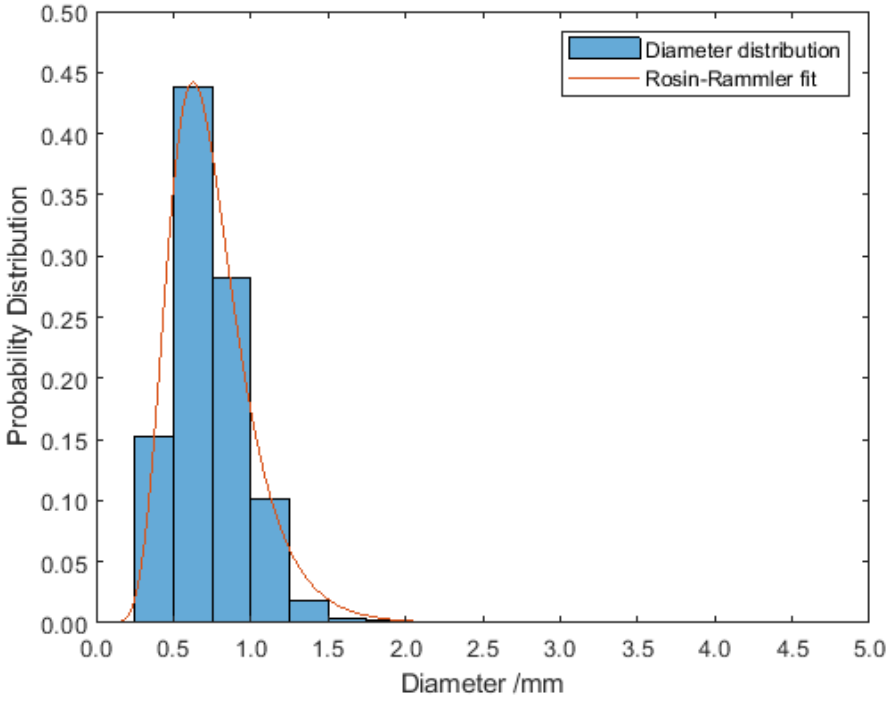
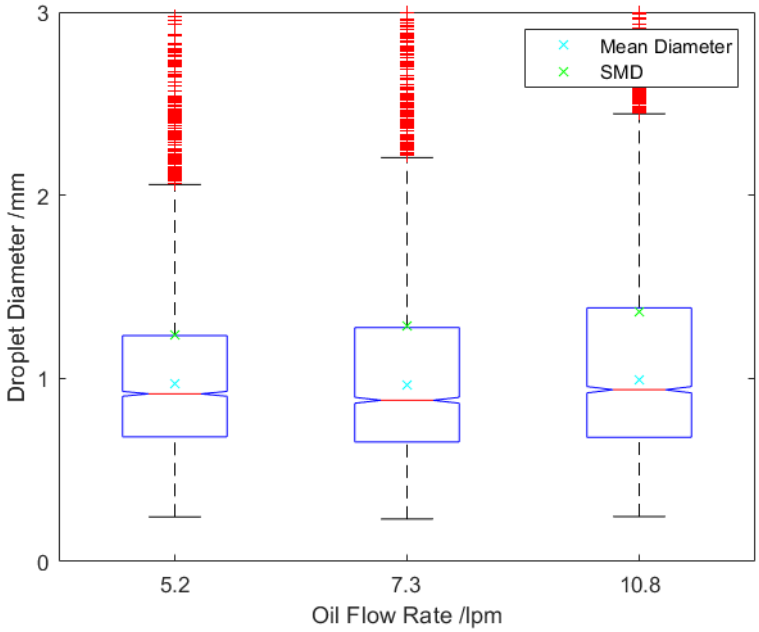


Figure 5.37: Droplet diameter distribution at the 9 o'clock position at 9000 rpm with oil flow rate 10.81 l min^{-1} and axial load 10 kN.

a)



b)

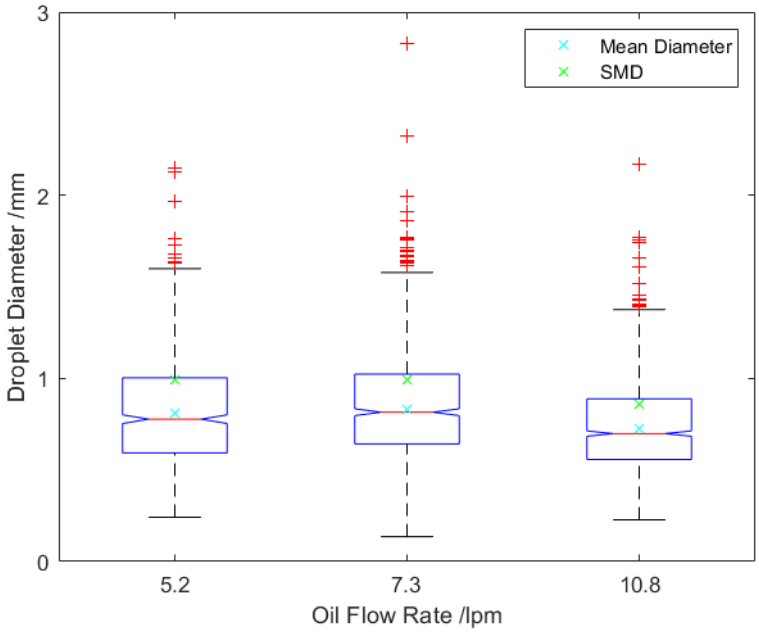


Figure 5.38: Effect of oil flow rate on the droplet diameter distribution on a) the 3 o'clock and b) the 9 o'clock sides of the bearing chamber.

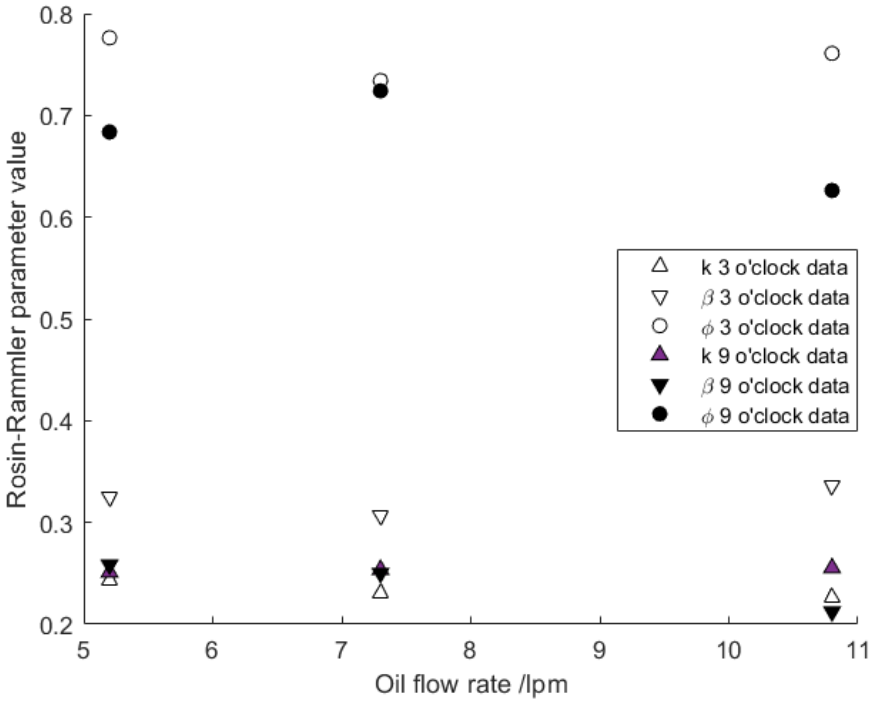


Figure 5.39: Effect of oil flow rate on the three variables in the Rosin-Rammler distributions representing droplet diameter on the 3 o'clock and 9 o'clock sides of the bearing chamber.

5.3.3 Effect of Axial Load on Diameter Distribution

High speed image data is obtained at 9000 rpm with an oil flow rate of 7.3 l min^{-1} with varying applied axial load using the method described in Chapter 3. Axial loads of 10 kN, 20 kN and 30 kN are considered in this investigation. Fig. 5.40 shows sample high speed images from the main data series on either side of the bearing chamber. Qualitative inspection of Fig. 5.40 shows no significant trends in the size and quantity of droplets seen. This is not unexpected given the findings in Section 5.1 considering the 3 o'clock side of the bearing chamber for operating speeds between 1000 rpm and 7000 rpm.

The diameter distribution is shown with the Rosin-Rammler fit for the axial loads investigated in Figs. 5.41 to 5.46. The three variables, k, β and ϕ, that describe the Rosin-Rammler fit of the diameter distribution are shown for all axial load conditions investigated at the 3 o'clock and 9 o'clock position in Fig. 5.47. No obvious trend can be seen in the droplet diameter distribution with change in applied axial load. The physical effect of change in axial is a change in contact angle in the bearing, which is not expected to have a major affect on oil film thickness or velocity at the shedding edge and therefore not expected to significantly affect droplet diameter.

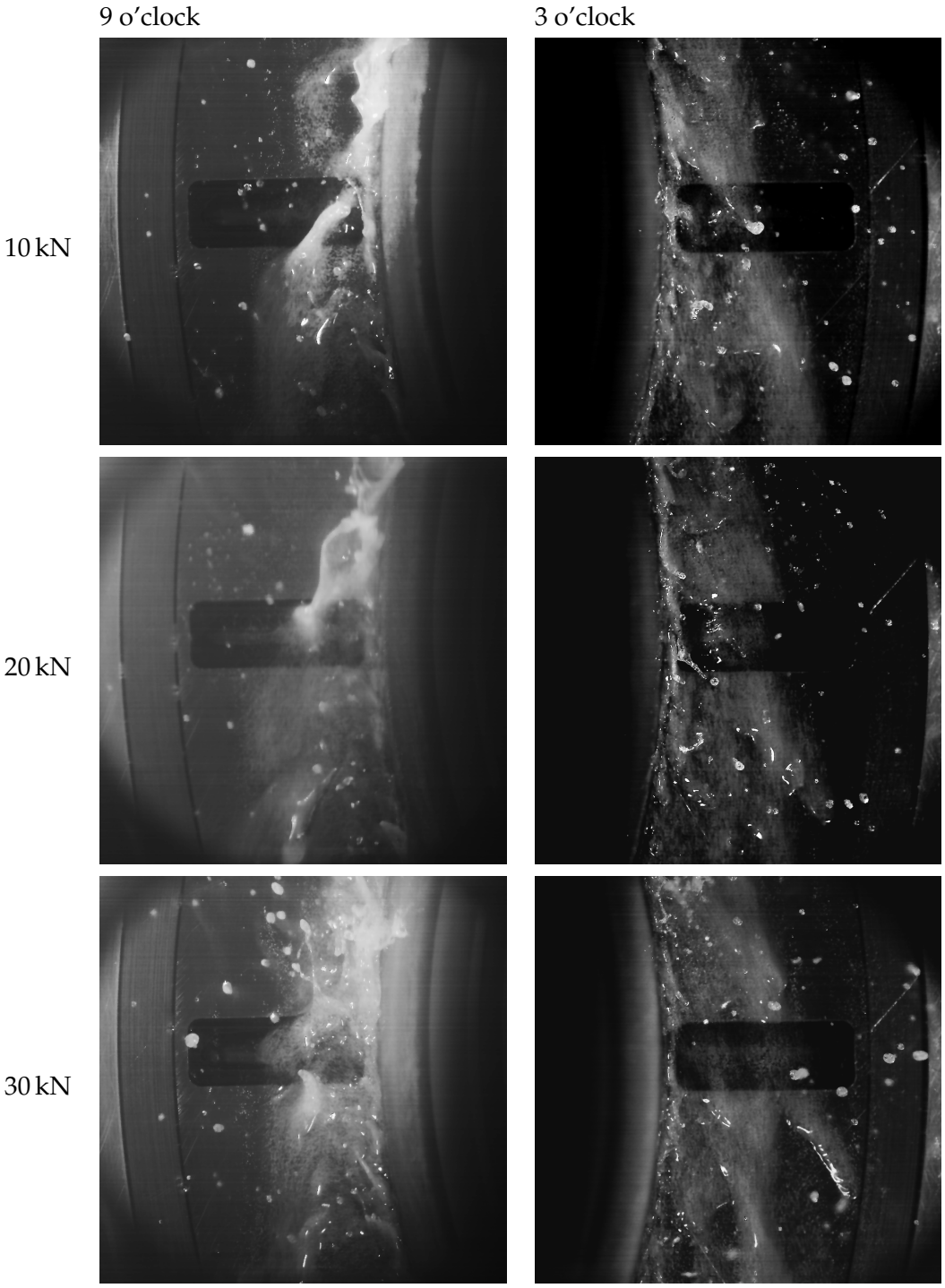


Figure 5.40: Sample high speed images from the main data series operating at 9000 rpm with an oil flow rate of 7.3 l min^{-1} and applied axial load between 10 kN and 30 kN.

5.3.4 Diameter Distribution Summary

Operating speed has the most significant effect on droplet diameter of the variables investigated. Increasing shaft speed has little effect on droplet diameter until high speeds

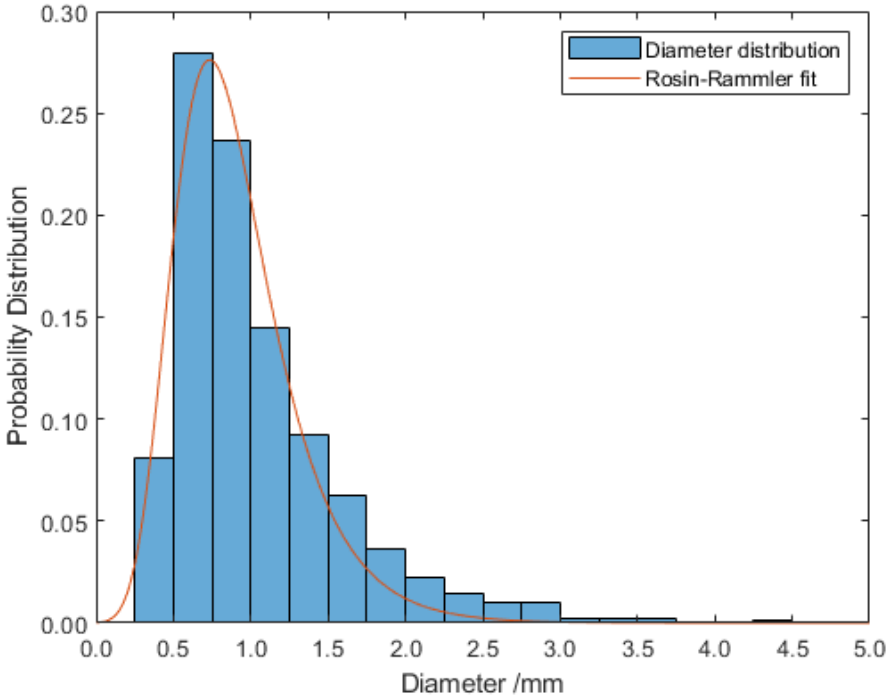


Figure 5.41: Droplet diameter distribution at the 3 o'clock position at 9000 rpm with oil flow rate 7.31 $l\,min^{-1}$ and axial load 10 kN.

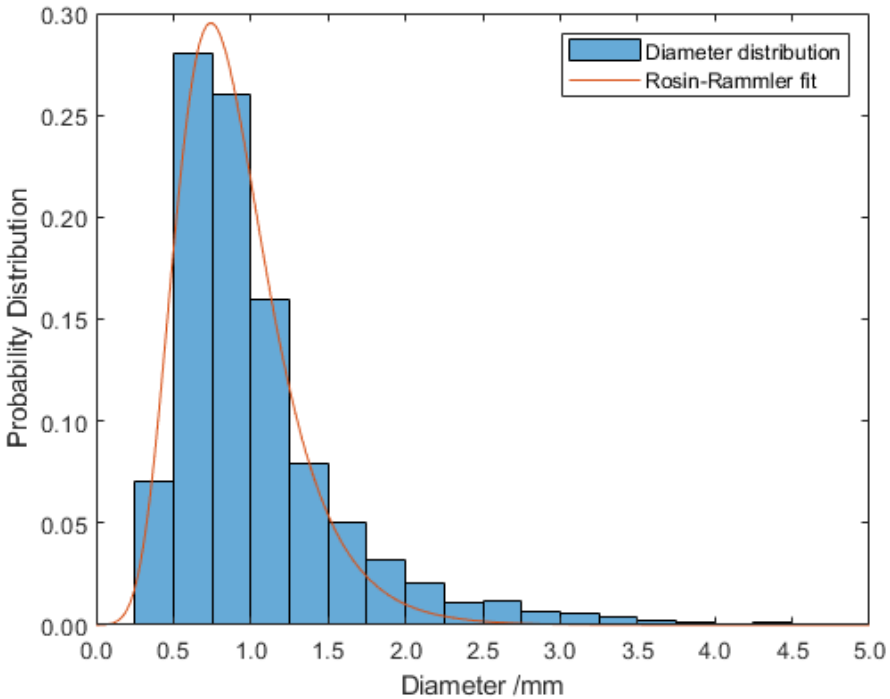


Figure 5.42: Droplet diameter distribution at the 3 o'clock position at 9000 rpm with oil flow rate 7.31 $l\,min^{-1}$ and axial load 20 kN.

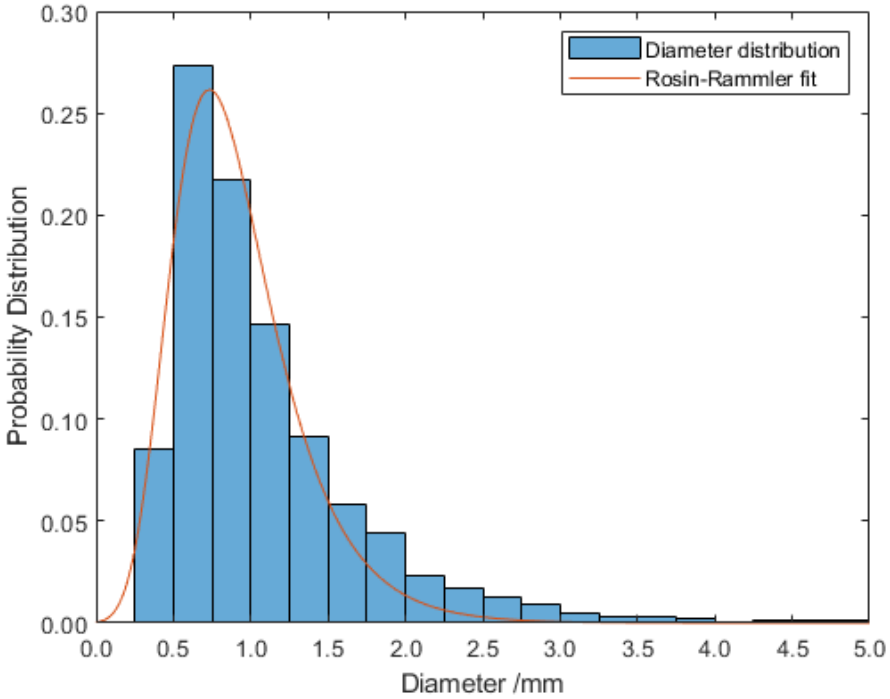


Figure 5.43: Droplet diameter distribution at the 3 o'clock position at 9000 rpm with oil flow rate 7.31 $l\,min^{-1}$ and axial load 30 kN.

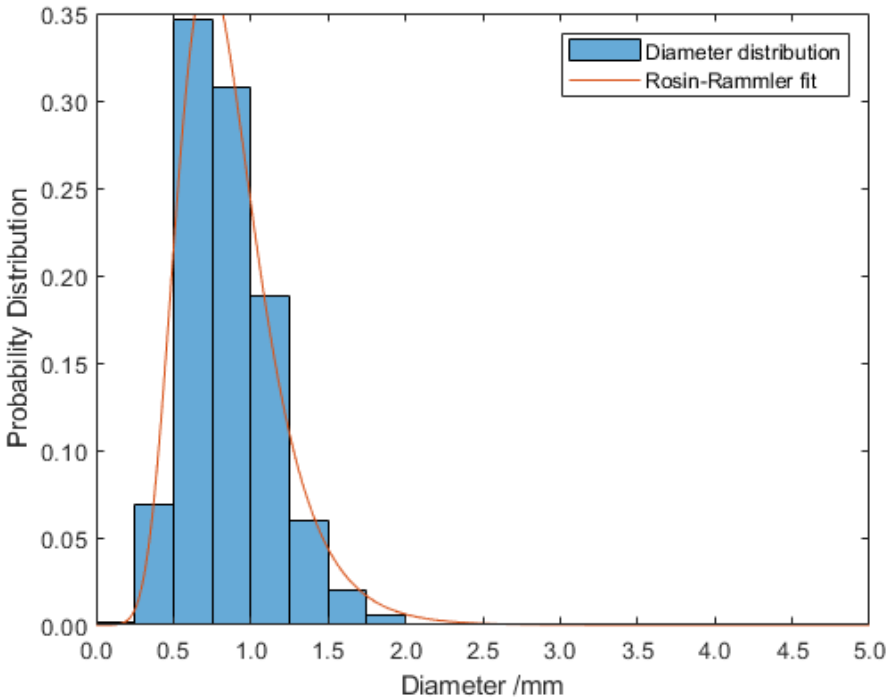


Figure 5.44: Droplet diameter distribution at the 9 o'clock position at 9000 rpm with oil flow rate 7.31 $l\,min^{-1}$ and axial load 10 kN.

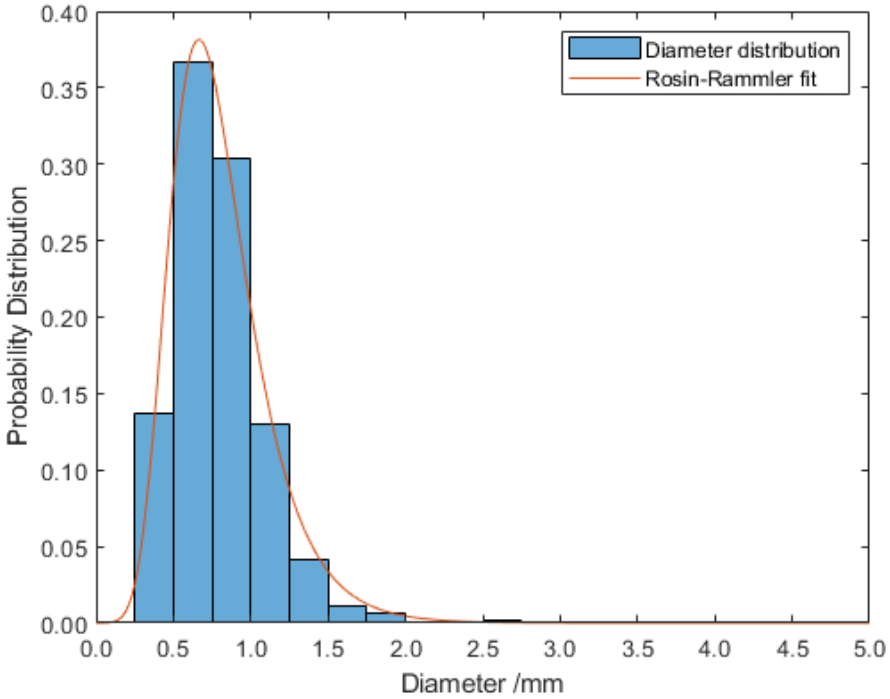


Figure 5.45: Droplet diameter distribution at the 9 o'clock position at 9000 rpm with oil flow rate 7.31 $l\,min^{-1}$ and axial load 20 kN.

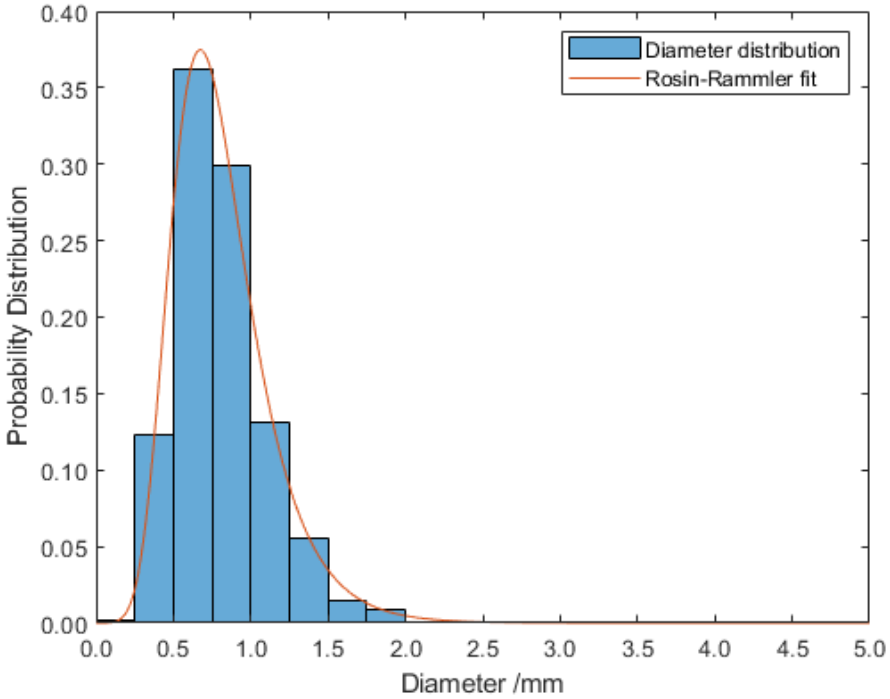


Figure 5.46: Droplet diameter distribution at the 9 o'clock position at 9000 rpm with oil flow rate 7.31 $l\,min^{-1}$ and axial load 30 kN.

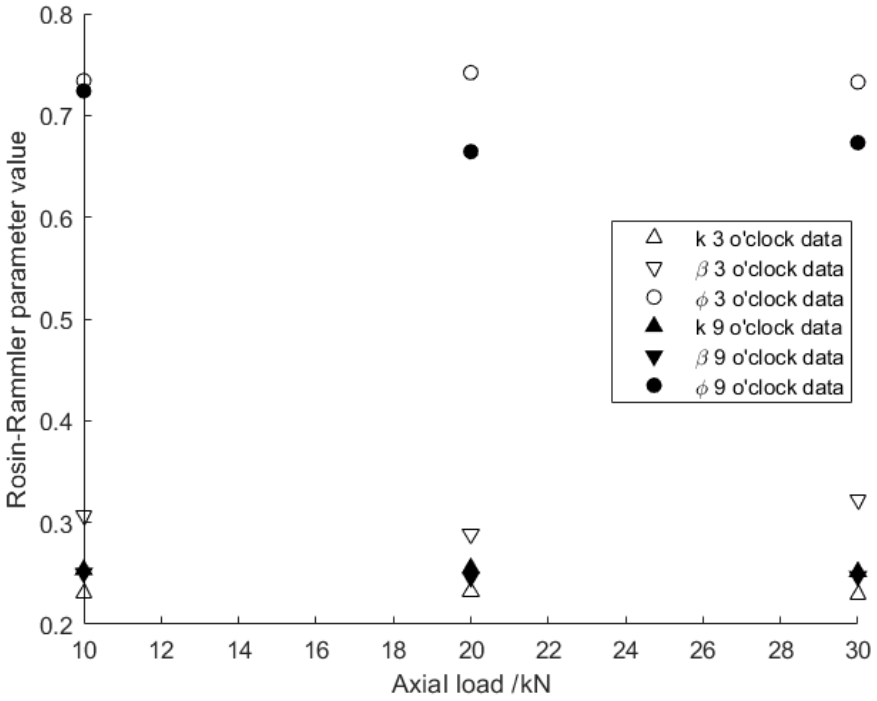


Figure 5.47: Effect of axial load on the three variables in the Rosin-Rammler distributions representing droplet diameter on the 3 o'clock and 9 o'clock sides of the bearing chamber.

are reached. Droplet diameter is relatively constant up to 7000 rpm and begins increasing at speeds over 9000 rpm. This transition aligns with a regime change reported by [24] in the film before the shedding edge, indicating a change in film behaviour may be contributing to the way droplets are generated and consequently the diameter distribution seen.

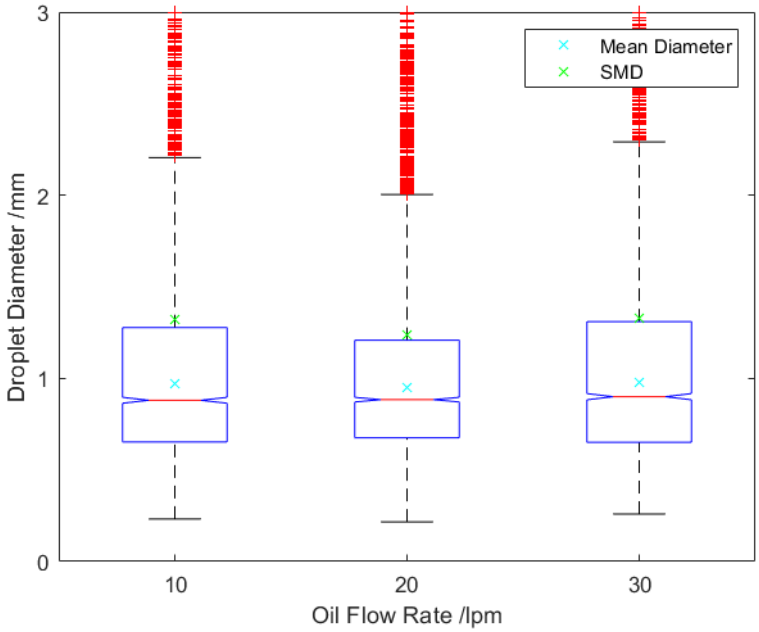
Neither oil flow rate or applied axial load were found to have a significant effect on droplet diameter distribution.

5.4 Droplet Speed Distribution

The droplet speed distribution is investigated for multiple operating conditions (varying operating speed, oil flow rate supplied to the bearing and applied axial load). High speed imaging is performed at the 3 o'clock and 9 o'clock positions using the experimental methodology and processing approach described in Chapters 3 and 4. Note that only radial and tangential components are included in droplet speed.

Air speed is not measured in the BSR but the shaft operates with surface speeds up to approximately 150 m s^{-1}. The shaft rotation accelerates air in the chamber to a lesser

a)



b)

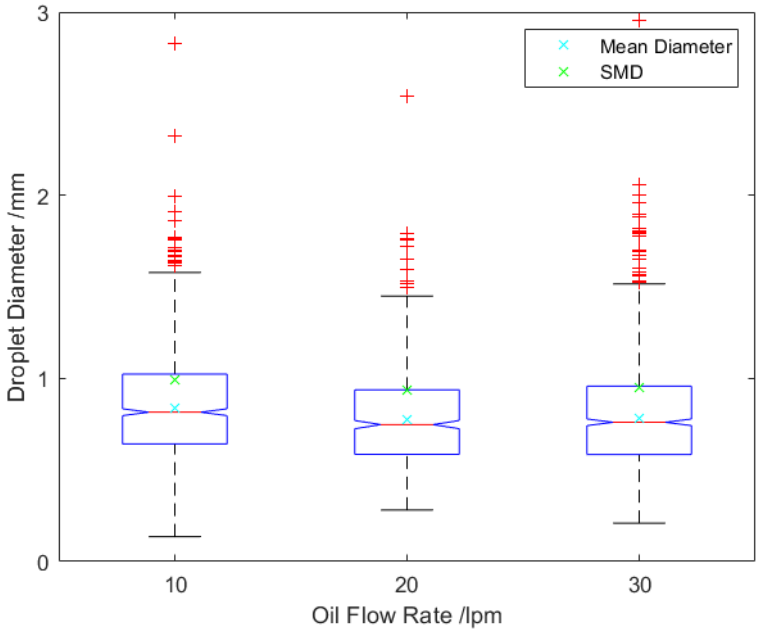


Figure 5.48: Effect of axial load on the droplet diameter distribution on a) the 3 o'clock and b) the 9 o'clock sides of the bearing chamber.

extent than would be expected with a through-shaft (the BSR has a stub shaft). Droplet speeds are expected to be significantly lower than the surface shaft speed since the shedding edge is a static surface.

Giles et al. [98] performed a study investigating the axial movement of droplets in the bearing chamber using high speed imaging from the side of the chamber, as in Fig. 5.49. This work is done using the bearing chamber rig with static insert described in Farbrother et al. [97]. The position of droplet impact is plotted in Fig. 5.50 where increasing horizontal position means the impact occurs at a greater axial distance from the static. The probability distribution of droplet impact angle (Fig. 5.51) shows the majority of droplets impact the outer wall at 40°-45° when operating at 8100 rpm from the edge of the static insert and 35°-45° when operating at 12 000 rpm. Assuming that the shedding angle in the BSR is similar, this information can be combined with droplet diameter and radial-tangential plane velocity data for fuller understanding of behaviour and for computational modelling of droplets in a bearing chamber.

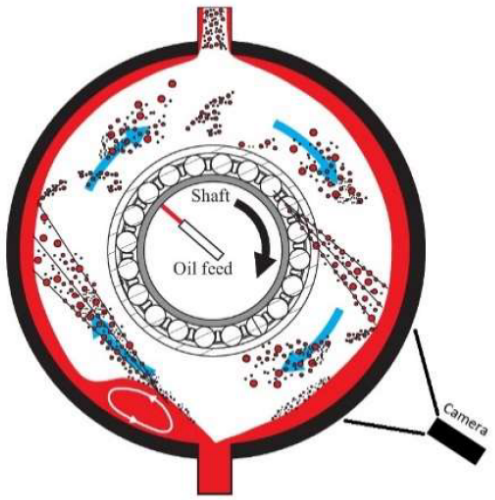


Figure 5.49: Experimental imaging position for investigation of axial droplet movement [98].

5.4.1 Effect of Operating Speed on Droplet Speed Distribution

High speed images from the main data series discussed in Section 5.3.1 are used to investigate the effect of operating speed on droplet speed distribution between 1000 rpm and 9000 rpm, operating with an oil flow rate of 7.3 l min^{-1} and axial load of 10 kN, in addition to a single test point at 12 000 rpm recorded at only the 9 o'clock position.

The speed distribution of droplets in each operating condition is represented in Figs. 5.52 to 5.61. Easier comparison can be made across the range of operating speeds using

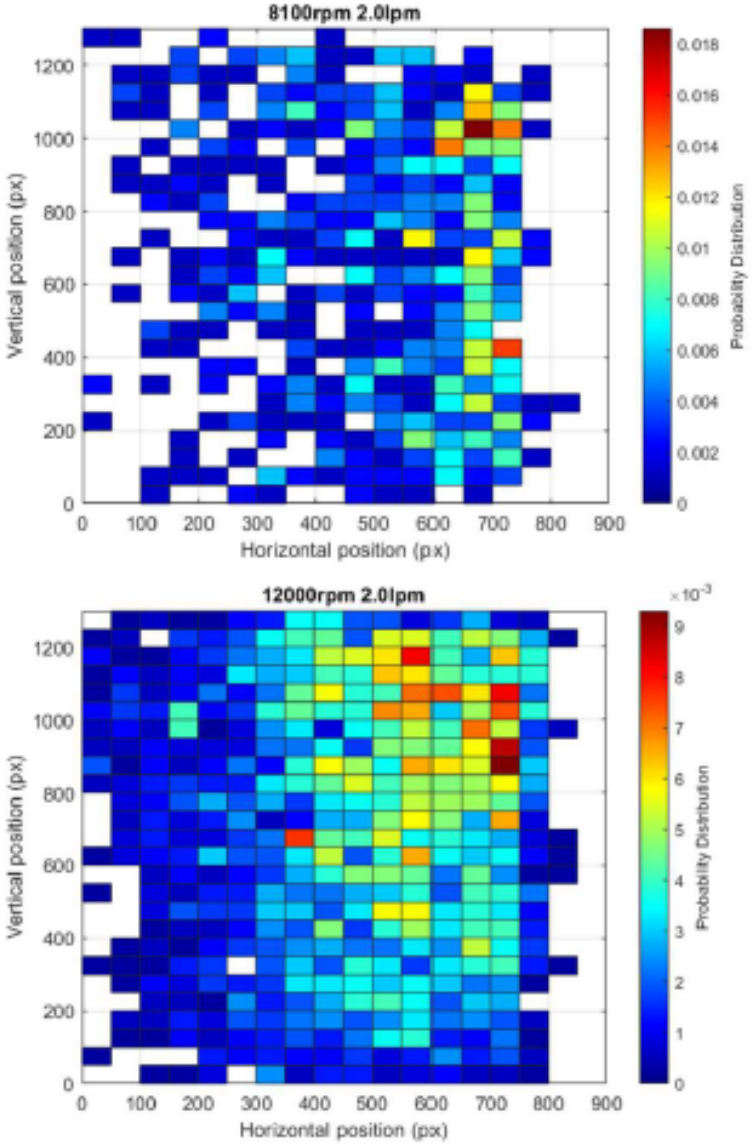


Figure 5.50: Impact positions of droplets against the outer wall, where horizontal position is in the axial plane [98].

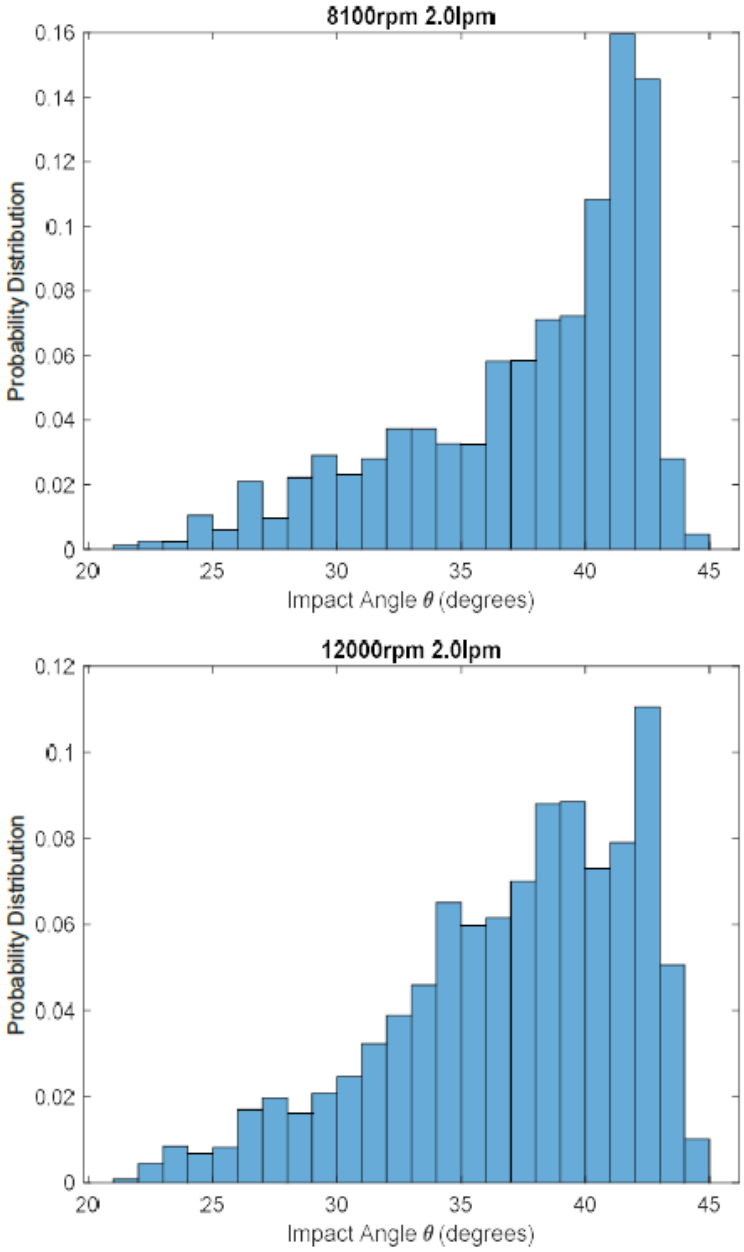


Figure 5.51: Probability distribution of impact angles of droplets against the outer wall, where 0° means zero axial velocity [98].

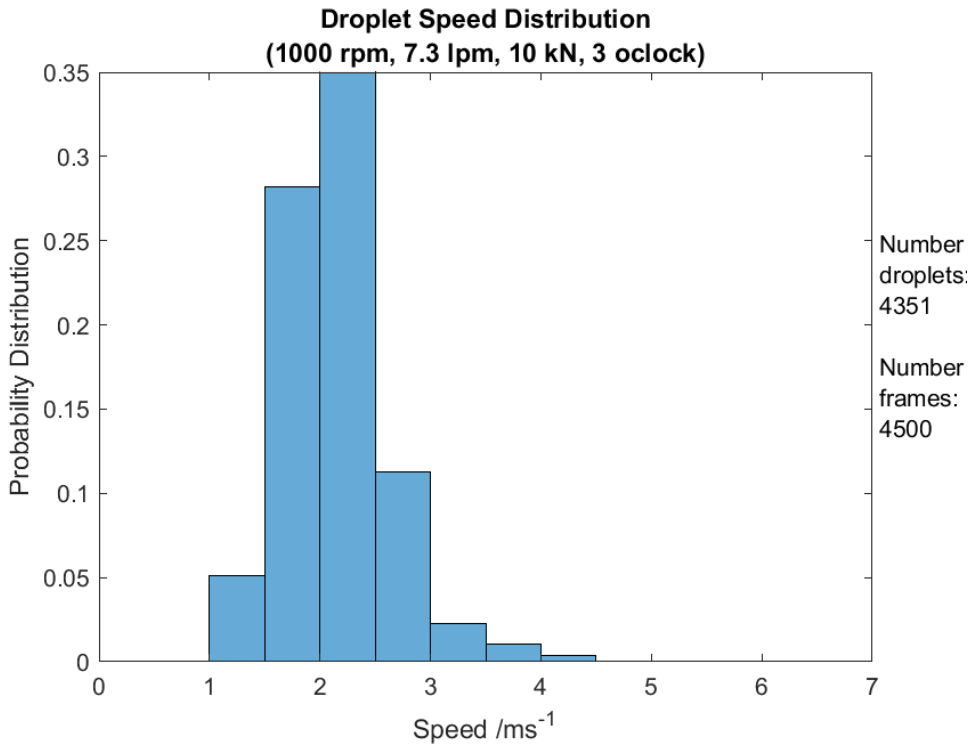


Figure 5.52: Droplet speed distribution at the 3 o'clock position at 1000 rpm with oil flow rate 7.3 l min^{-1} and axial load 10 kN.

Fig. 5.63 for the 3 o'clock and 9 o'clock positions respectively. It is difficult to identify an overall trend with operating speed on either side of the bearing chamber, however there is a notable difference in speed distribution at 1000 rpm compared to the rest of the data series. In this case, most droplets are significantly slower than at other operating speeds (in the order of 1 m s^{-1} slower).

Droplet speeds are generally fairly similar on both sides of the bearing chamber for each operating speed, although they tend to higher speeds at the 3 o'clock position where gravity and shear act in the same direction - approximately 0.5 m s^{-1} faster than on the 9 o'clock side where shear and gravity act in opposite directions. This corresponds to the faster film on the static elements of the bearing seen by Sinha et al. [24] on the co-current side of the bearing chamber. Also of interest is the smaller interquartile range of droplets on the 9 o'clock side, indicating that droplet diameters are more consistent on this side of the chamber. This is also represented by the Rosin-Rammler fit in that the scaling factor β is smaller for droplet diameter distributions on the 9 o'clock side.

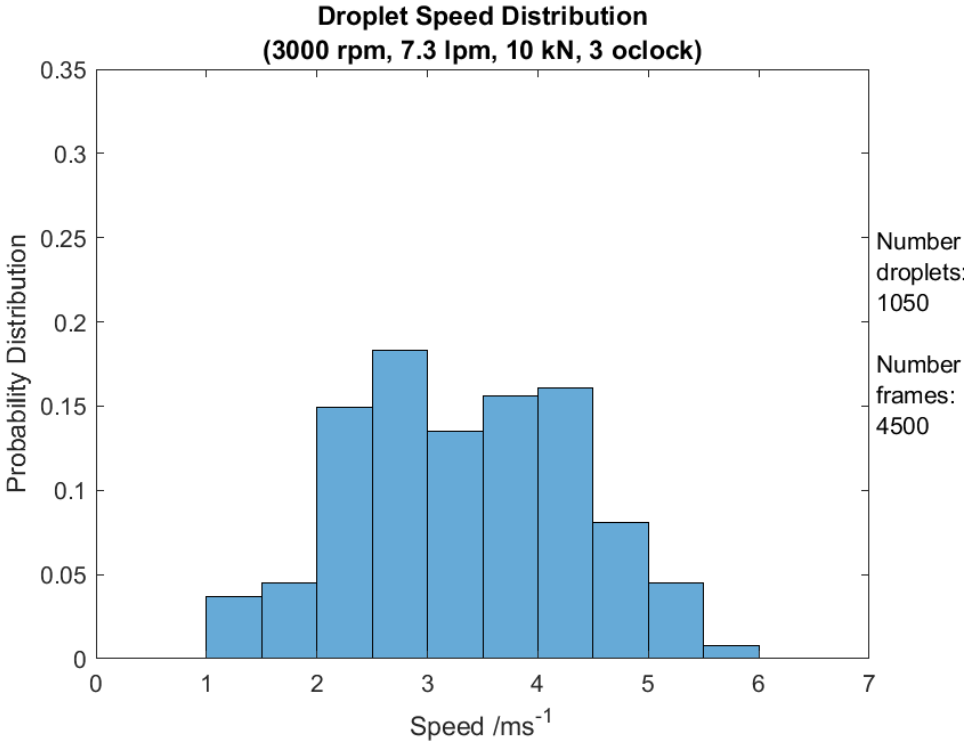


Figure 5.53: Droplet speed distribution at the 3 o'clock position at 3000 rpm with oil flow rate 7.31 min^{-1} and axial load 10 kN.

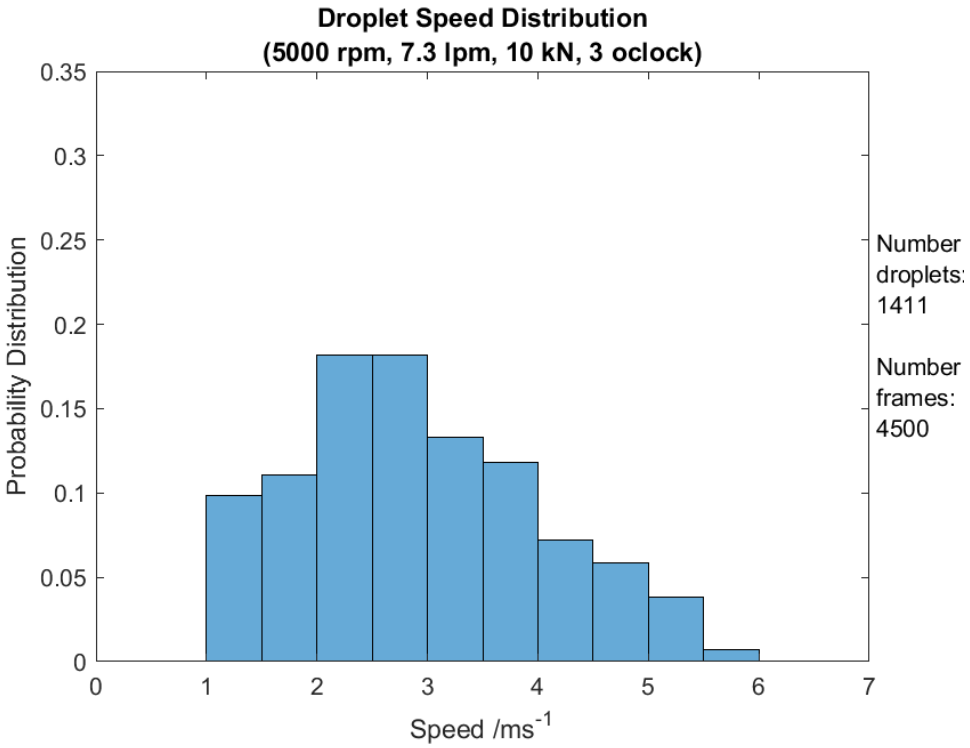


Figure 5.54: Droplet speed distribution at the 3 o'clock position at 5000 rpm with oil flow rate 7.31 min^{-1} and axial load 10 kN.

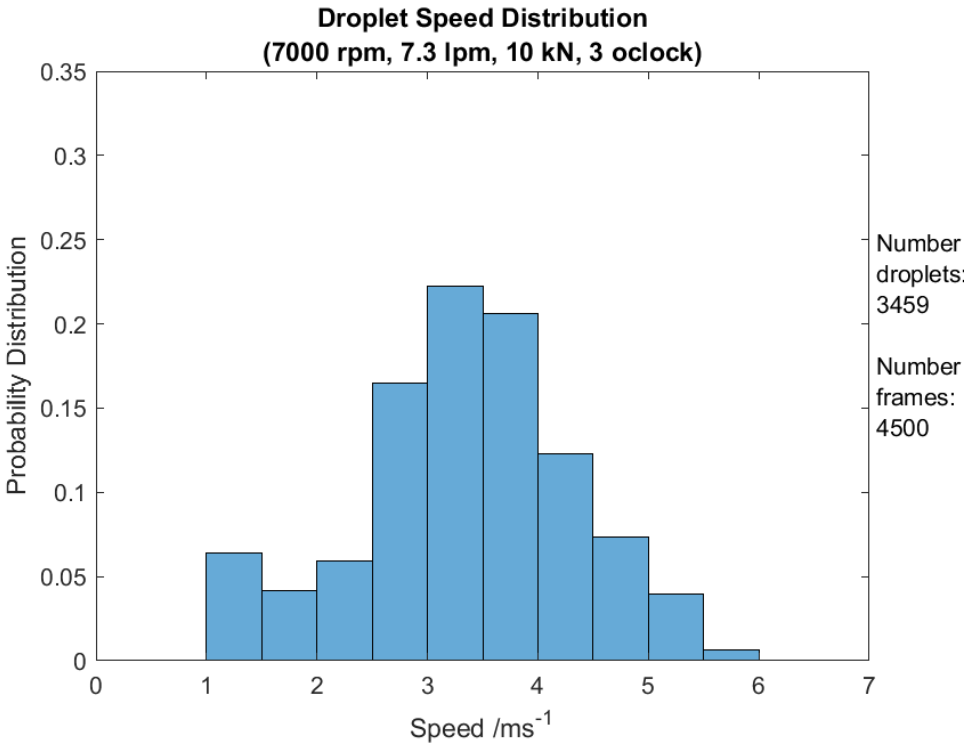


Figure 5.55: Droplet speed distribution at the 3 o'clock position at 7000 rpm with oil flow rate 7.3 l min^{-1} and axial load 10 kN.

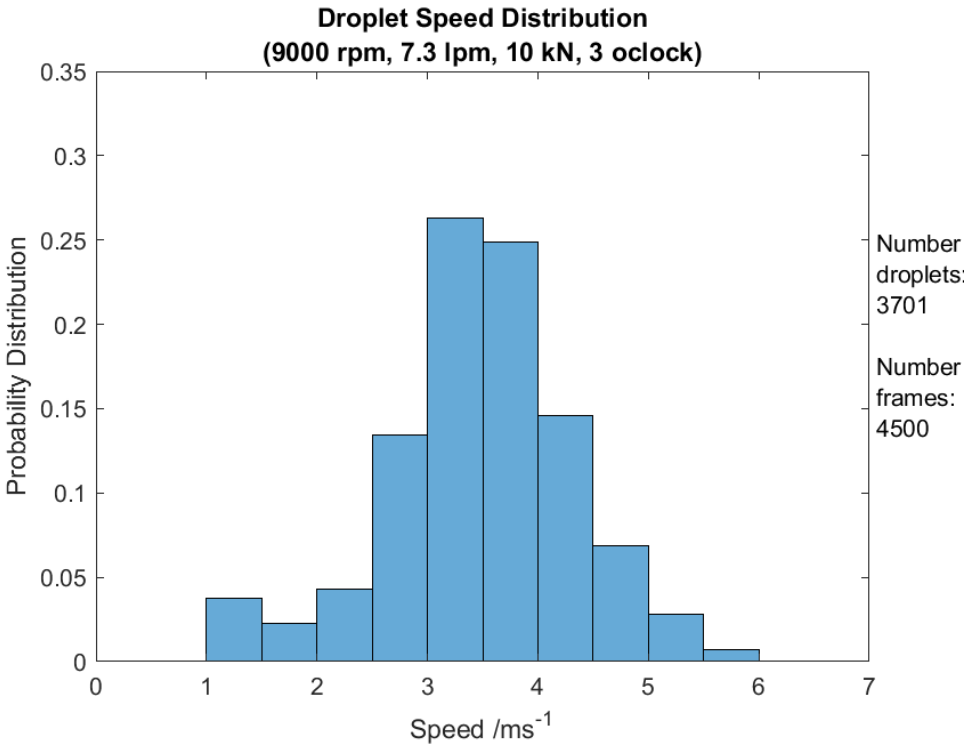


Figure 5.56: Droplet speed distribution at the 3 o'clock position at 9000 rpm with oil flow rate 7.3 l min^{-1} and axial load 10 kN.

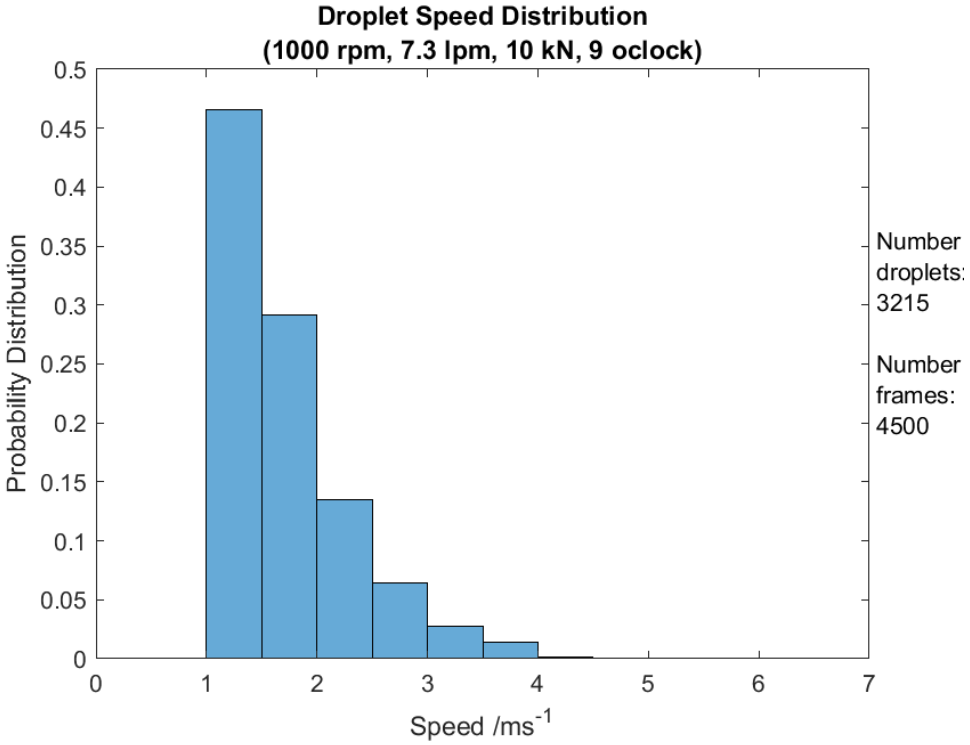


Figure 5.57: Droplet speed distribution at the 9 o'clock position at 1000 rpm with oil flow rate 7.31 min^{-1} and axial load 10 kN.

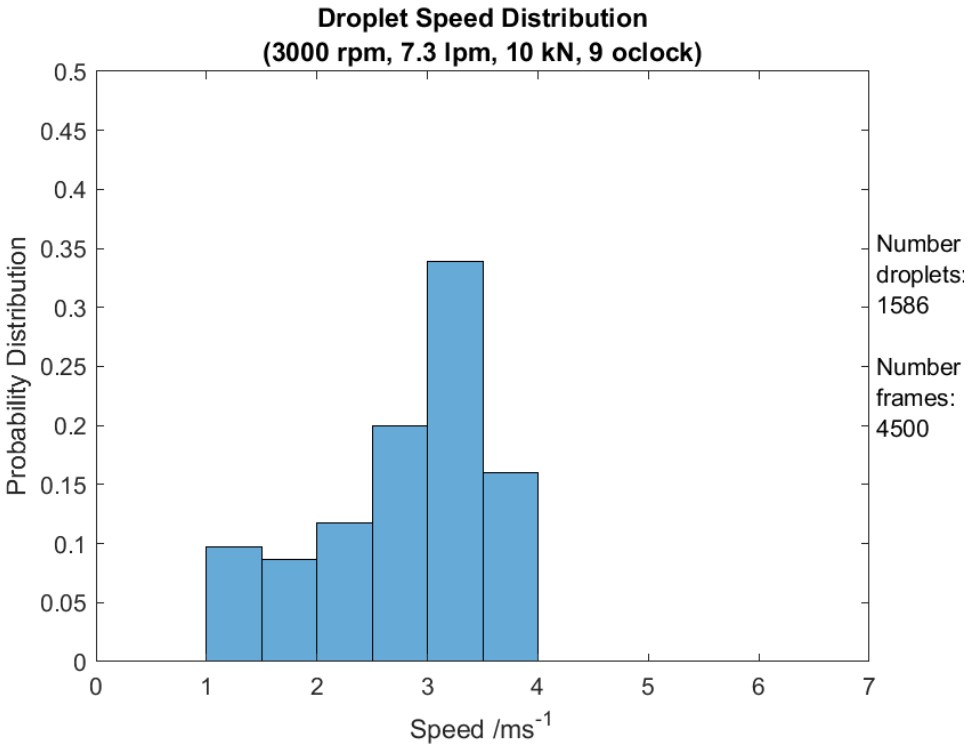


Figure 5.58: Droplet speed distribution at the 9 o'clock position at 3000 rpm with oil flow rate 7.31 min^{-1} and axial load 10 kN.

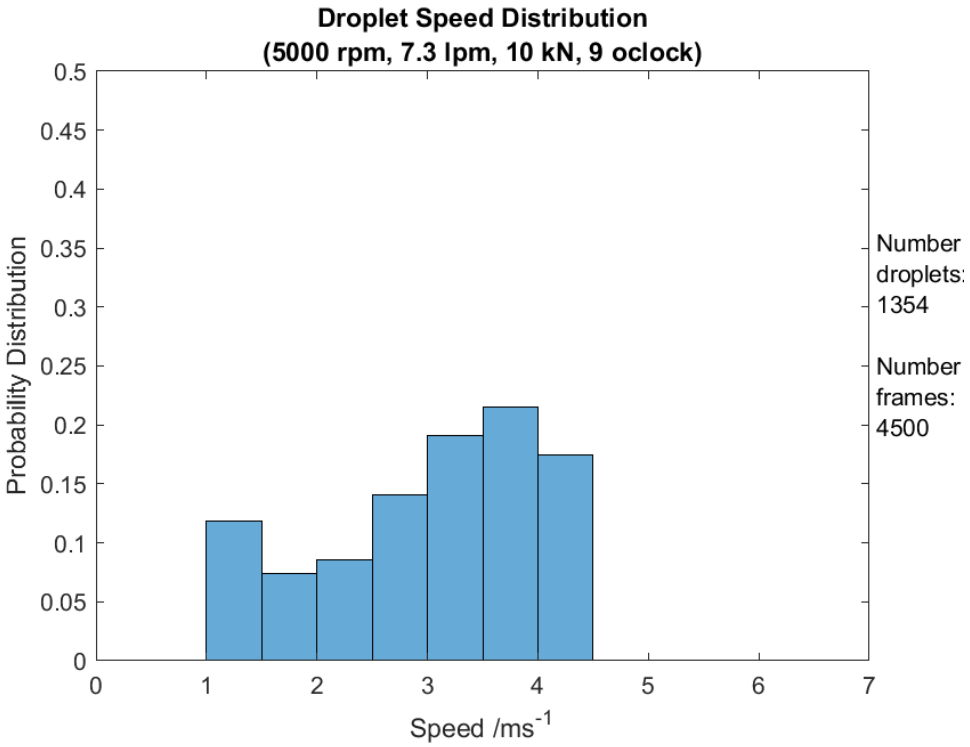


Figure 5.59: Droplet speed distribution at the 9 o'clock position at 5000 rpm with oil flow rate 7.31 min^{-1} and axial load 10 kN.

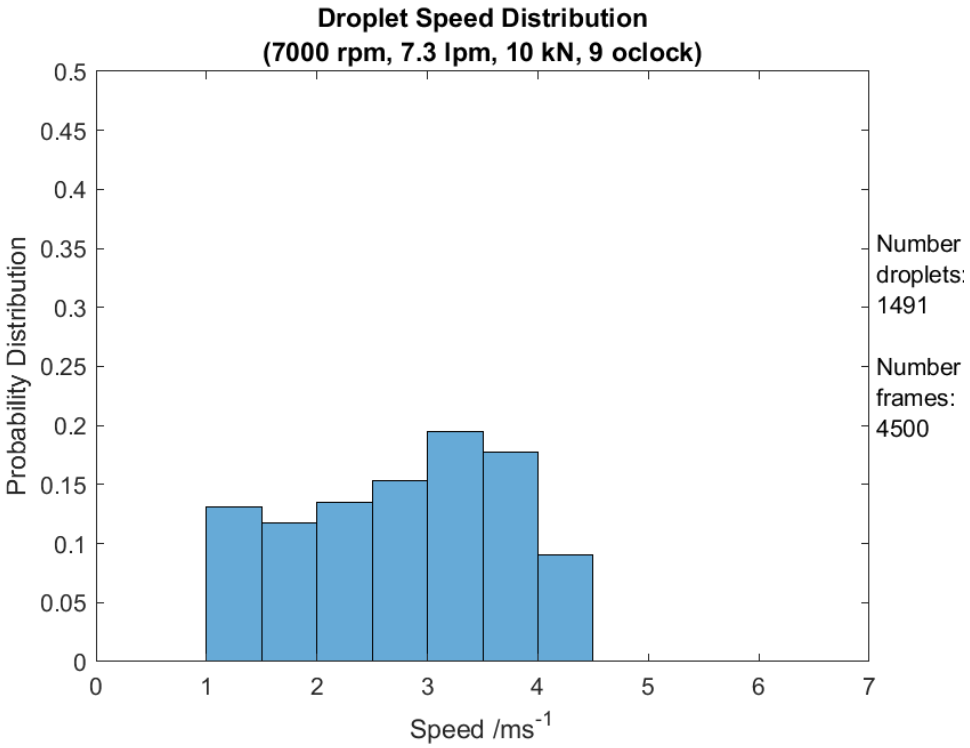


Figure 5.60: Droplet speed distribution at the 9 o'clock position at 7000 rpm with oil flow rate 7.31 min^{-1} and axial load 10 kN.

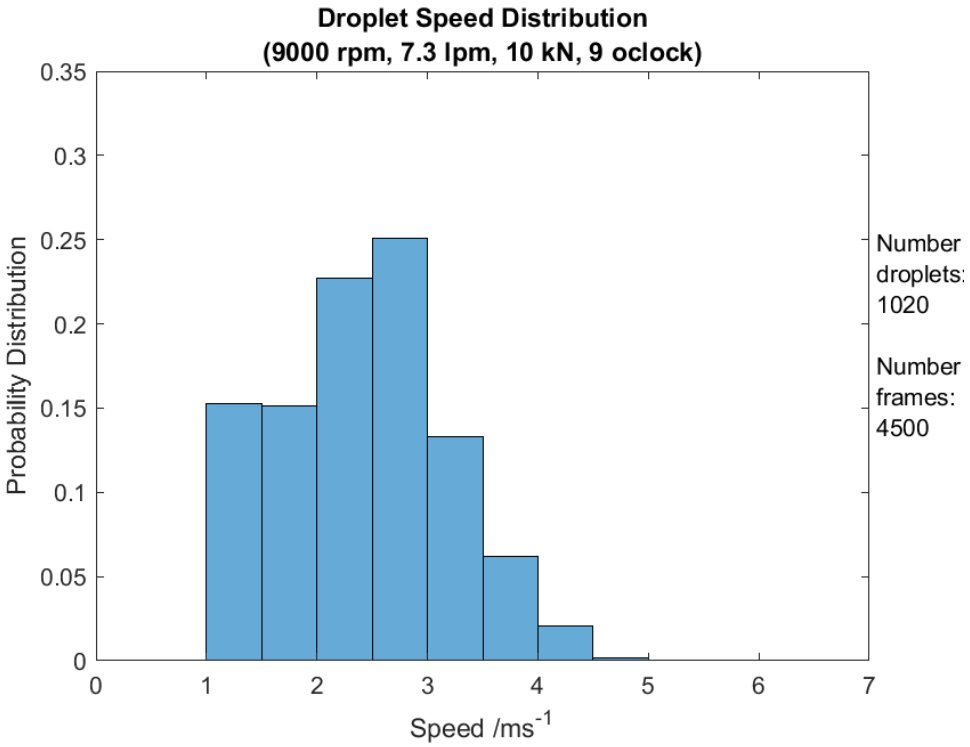


Figure 5.61: Droplet speed distribution at the 9 o'clock position at 9000 rpm with oil flow rate 7.31 min^{-1} and axial load 10 kN.

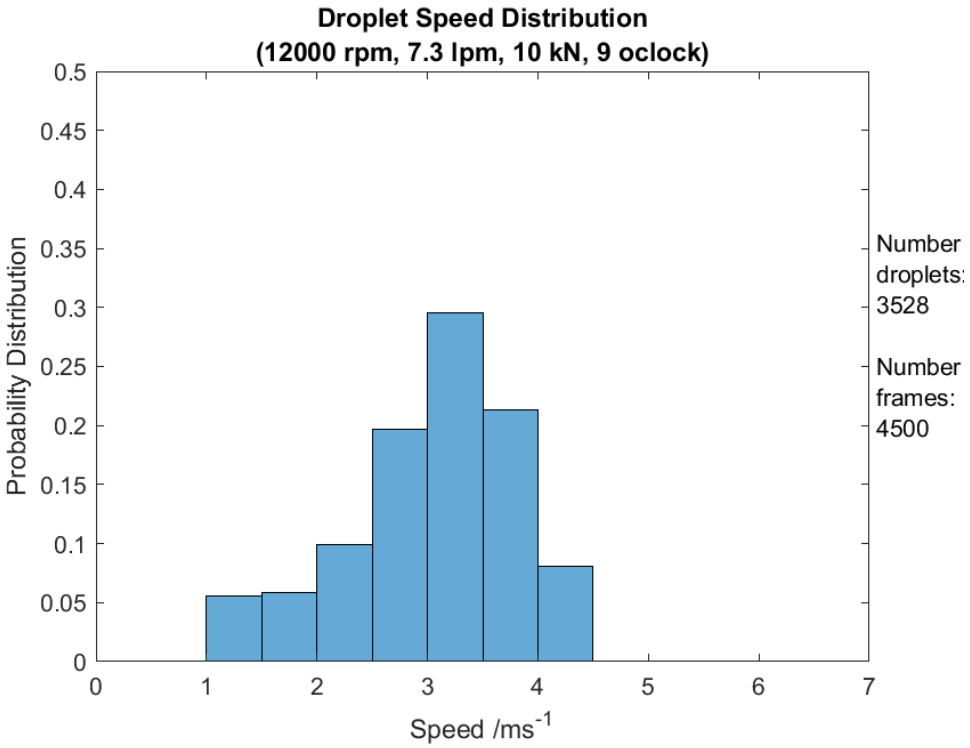
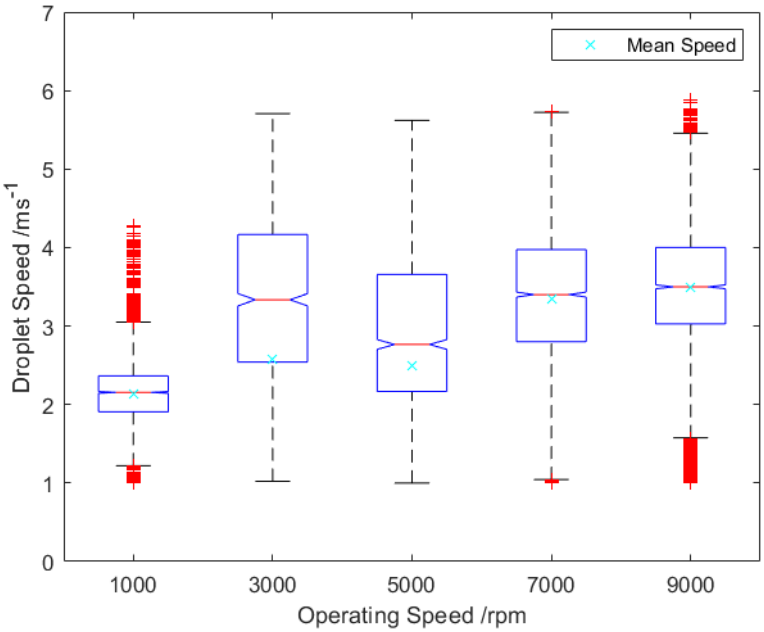


Figure 5.62: Droplet speed distribution at the 9 o'clock position at 12 000 rpm with oil flow rate 7.31 min^{-1} and axial load 10 kN.

a)



b)

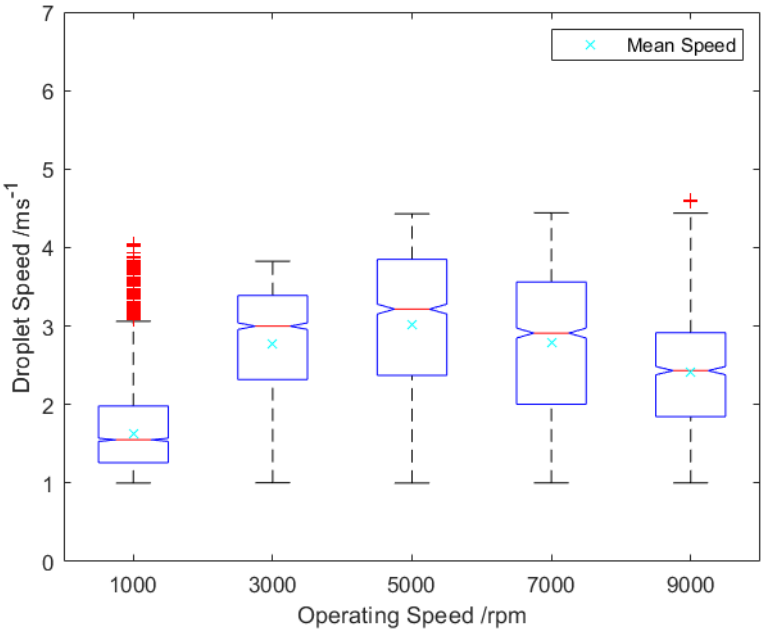


Figure 5.63: Effect of operating speed on the droplet speed distribution on a) the 3 o'clock and b) the 9 o'clock sides of the bearing chamber.

5.4.2 Effect of Oil Flow Rate on Droplet Speed Distribution

The effect of oil flow rate supplied to the bearing is investigated for three oil flow rates: $5.2\,\mathrm{l\,min^{-1}}$, $7.3\,\mathrm{l\,min^{-1}}$ and $10.8\,\mathrm{l\,min^{-1}}$. In all cases the test rig was operating at 9000 rpm with an applied axial load of 10 kN. The droplet speed distribution is shown for each case in Figs. 5.64 to 5.69. Comparison of droplet speed distributions with varying oil flow rate can be made using Fig. 5.70 for the 3 o'clock and 9 o'clock positions respectively. Increasing oil flow correlates to lower droplet speeds (mean and median values reduce, as does the value of the upper and lower quartiles). This trend occurs on both sides of the bearing chamber.

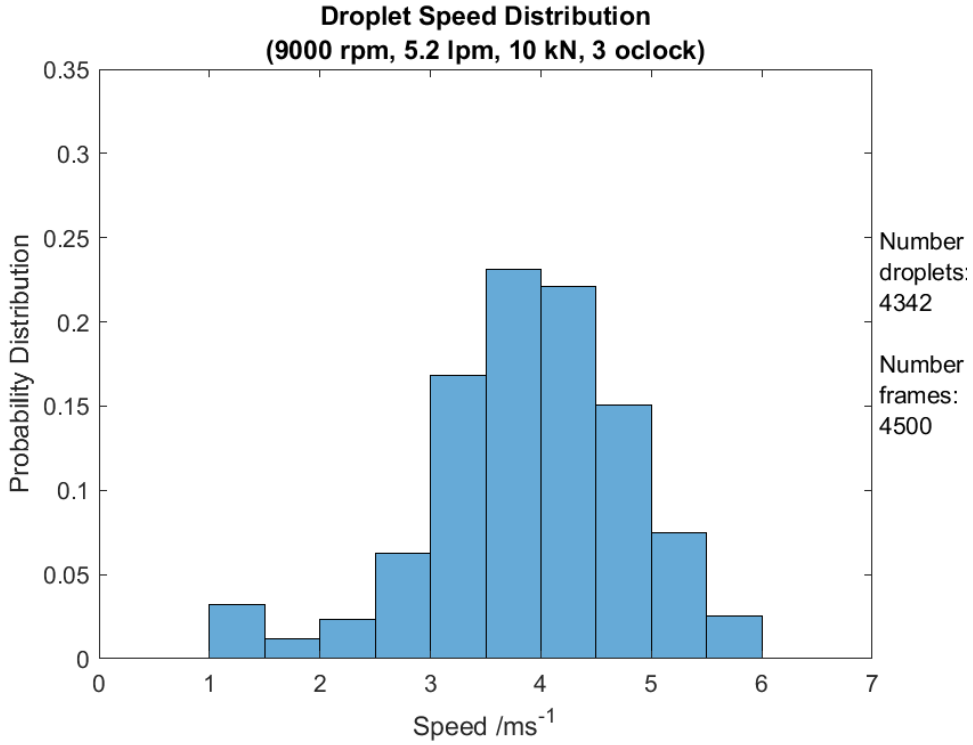


Figure 5.64: Droplet speed distribution at the 3 o'clock position at 9000 rpm with oil flow rate $5.2\,\mathrm{l\,min^{-1}}$ and axial load 10 kN.

5.4.3 Effect of Axial Load on Droplet Speed Distribution

Droplet speed is investigated for axial loads of 10 kN, 20 kN and 30 kN while operating at 9000 rpm with an oil flow rate of $7.3\,\mathrm{l\,min^{-1}}$. No obvious trend in droplet speed with axial load can be seen in Fig. 5.71, which shows droplet diameter has little/no dependency on axial load applied to the bearing in the range investigated. As with other operating conditions, droplets have a generally higher speed on the 3 o'clock side than on the 9 o'clock side - a difference of approximately $1\,\mathrm{m\,s^{-1}}$.

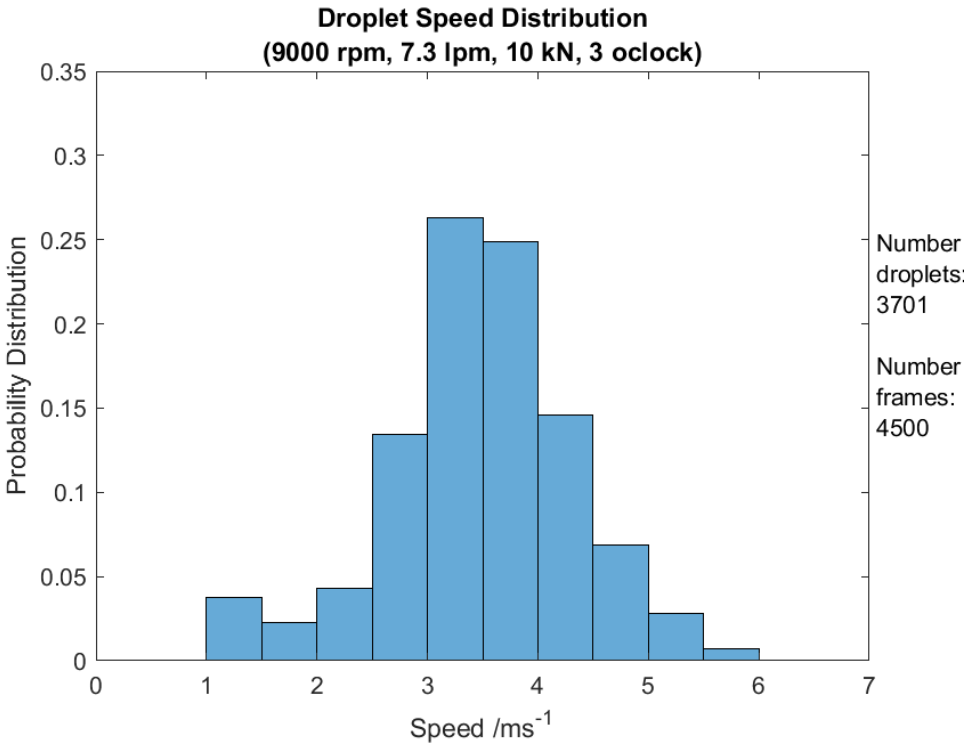


Figure 5.65: Droplet speed distribution at the 3 o'clock position at 9000 rpm with oil flow rate 7.3 l min^{-1} and axial load 10 kN.

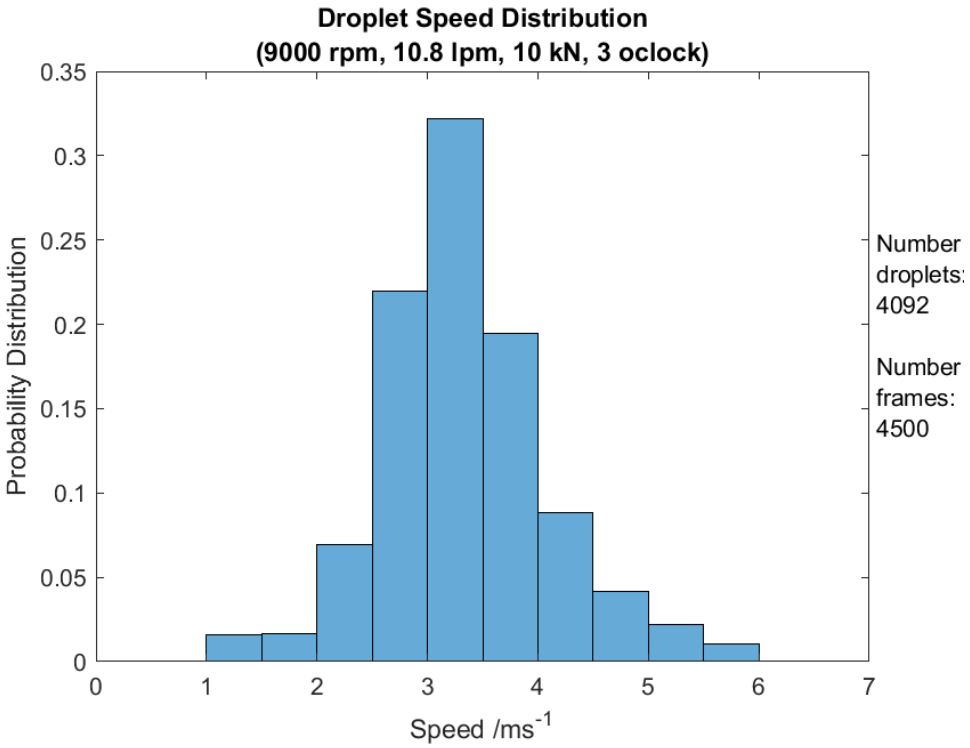


Figure 5.66: Droplet speed distribution at the 3 o'clock position at 9000 rpm with oil flow rate 10.8 l min^{-1} and axial load 10 kN.

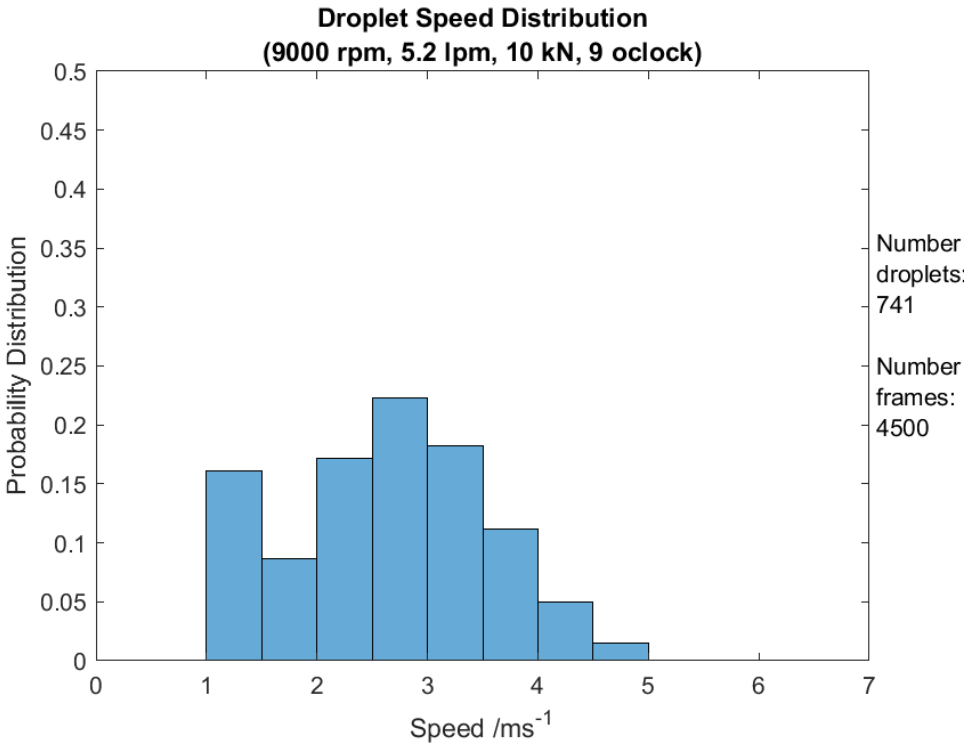


Figure 5.67: Droplet speed distribution at the 9 o'clock position at 9000 rpm with oil flow rate 5.2 l min^{-1} and axial load 10 kN.

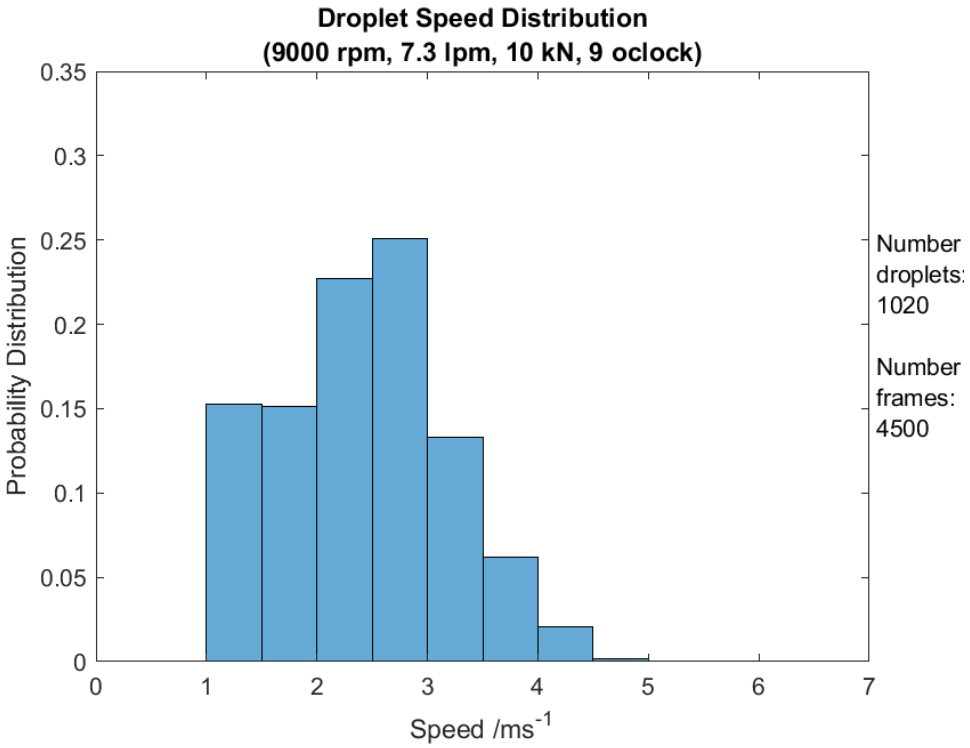


Figure 5.68: Droplet speed distribution at the 9 o'clock position at 9000 rpm with oil flow rate 7.3 l min^{-1} and axial load 10 kN.

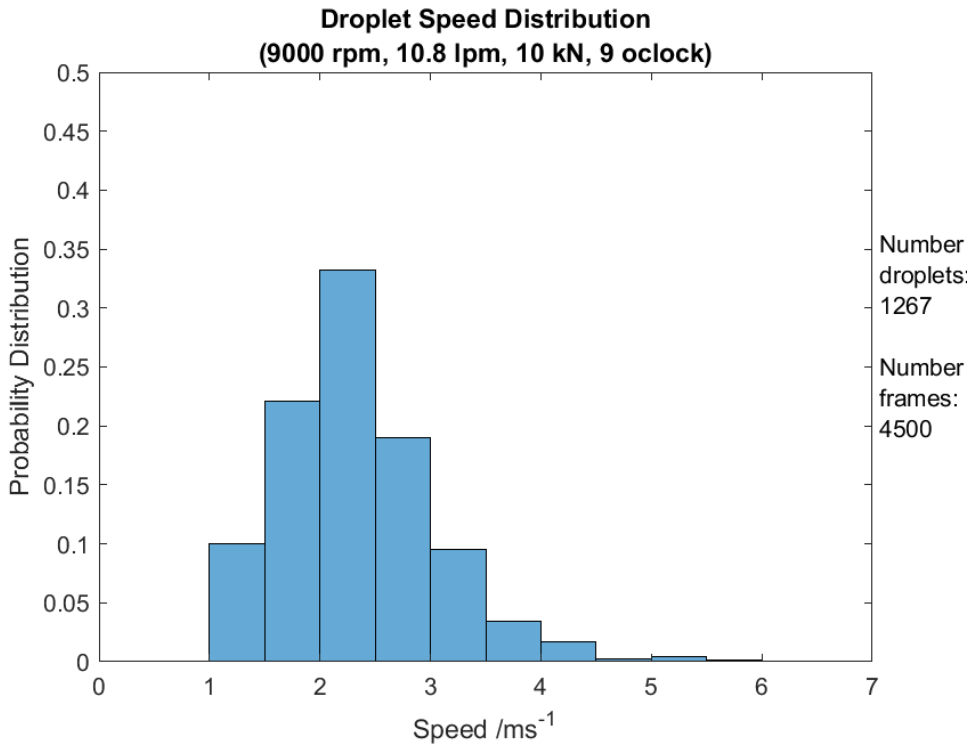


Figure 5.69: Droplet speed distribution at the 9 o'clock position at 9000 rpm with oil flow rate 10.8 l min^{-1} and axial load 10 kN.

5.5 Experimental Results Summary

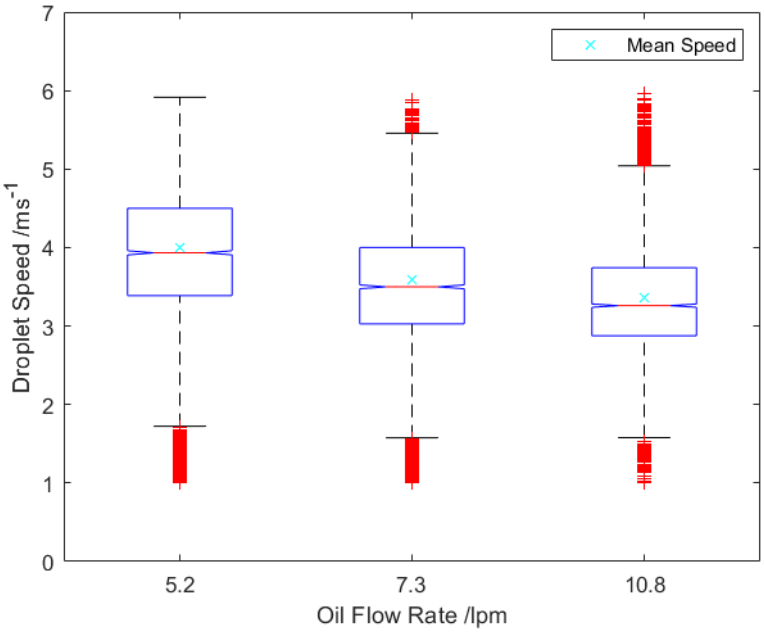
Experimental results are obtained using the experimental methodology and processing techniques presented in Chapters 3 and 4, including both quantitative and qualitative analysis of two phase flow behaviour in an aeroengine bearing chamber.

Qualitative analysis of images shows a change in wetted surface area of the front face with increasing operating speed and/or higher oil flow rate. Increasing either of these variables or applying a greater axial load correlates to increased production of ligaments and complex three-dimensional structures and higher number of droplets in the bearing chamber.

Four behavioural regimes have been identified for conditions investigated at speeds up to 7000 rpm on the 3 o'clock side of the bearing chamber. These are defined in Section 5.1.

Detailed analysis of a single test point (7000 rpm, 5.2 lpm oil flow rate and 20 kN axial load) shows that most droplets have a diameter below 2.0 mm , with the most common being in the 0.6 mm to 0.8 mm range. Very few droplets with diameter larger than 3.0 mm are observed. This data is in good agreement with ground truth, indicating that the CNN droplet detection approach produces representative droplet data.

a)



b)

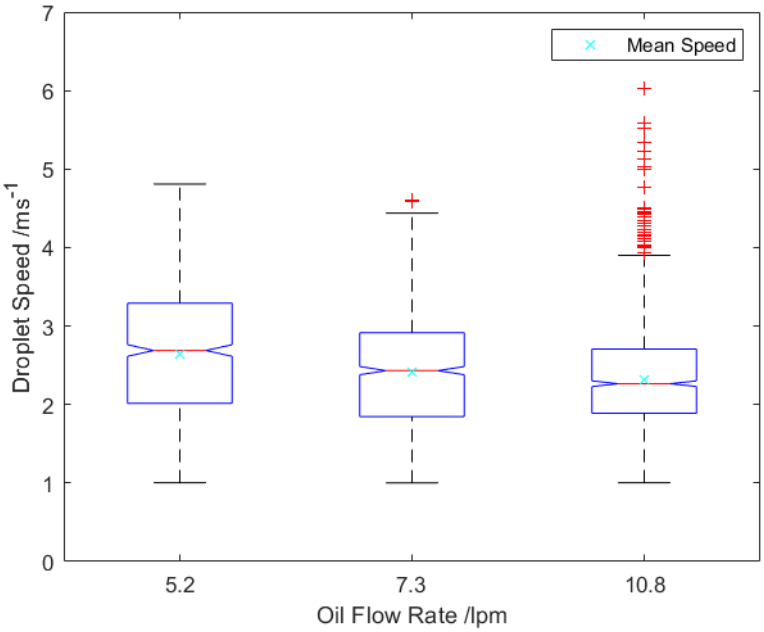
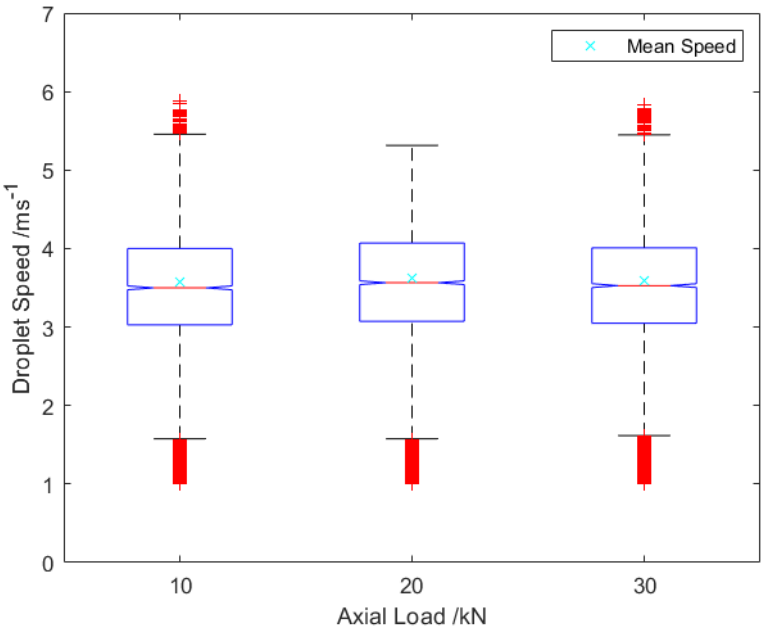


Figure 5.70: Effect of oil flow rate on the droplet speed distribution on a) the 3 o'clock and b) the 9 o'clock sides of the bearing chamber.

a)



b)

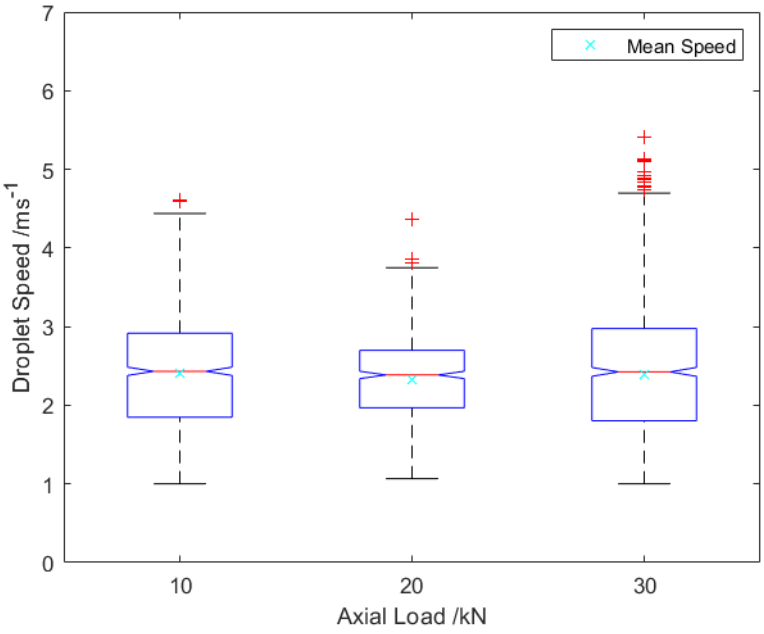


Figure 5.71: Effect of axial load on the droplet speed distribution on a) the 3 o'clock and b) the 9 o'clock sides of the bearing chamber.

Two peaks in the droplet speed probability distribution were identified at each test point suggesting there may be multiple mechanisms of droplet generation in the bearing chamber. The lower speed peak consists of generally smaller diameter droplets compared to the higher speed peak which is made up of a greater range of droplet diameters.

Increased operating speed correlates to an increased film surface area on the front face. The film also becomes more prone to forming complex three-dimensional oil structures. Greater three-dimensionality is observed on the 9 o'clock (countercurrent side) compared to the 3 o'clock (co-current side) where the oil film on the front face is generally thinner and covers a larger surface area. This difference in behaviour is due to the combined effect of shear and gravity in the bearing chamber - i.e. forces act in the same direction on the co-current side and in opposing directions on the counter-current side. At higher operating speeds, a greater number of droplets are observed - some of which are seen to be generated from rapid breakup of the three-dimensional structures.

The Rosin-Rammler fit is shown to provide a good representation of the droplet diameter probability distribution on both sides of the bearing chamber. This is a method of representing droplet diameters that was previously proposed by Nicoli [1] for computational modelling of two phase flow in an aeroengine bearing chamber. It has been shown in this work to be representative of experimental droplet diameter data. The spread of the distribution (indicated by the scaling factor) does not vary significantly or with an identified trend in relation to operating conditions, meaning that a similarly shaped diameter distribution is seen at all operating conditions investigated. However, modal droplet diameter (indicated by location parameter) is found to be constant for speeds up to 7000 rpm, after which droplet diameter increases with operating speed. This change corresponds to a regime change seen by Sinha et al. [24] in the oil film on the static close to the bearing at 8000 rpm before which the film thickness ranged from 2.3 mm to 0.4 mm with increased shaft speed and after which, the film thickness on the static elements of the bearing asymptotically approaches a constant value as the film is accelerated to it's maximum speed. Hee [8] similarly found film thickness to reduce significantly between 3000 rpm and 7000 rpm (from 2.1 mm to 0.7 mm) in prior work investigating film thickness on the bearing housing using the same test rig.

Droplet diameter was expected to increase with film thickness so it is somewhat surprising that diameter was constant in the operating speed range in which film thickness reduces and then begins to increase when film thickness becomes constant. It is likely that the phenomena that occur after the film regime change observed by Sinha et al. [24] also affect the way in which film breakup occurs over the shedding edge, explaining

the increase in droplet diameters observed at higher speeds.

Both increasing oil flow rate and applied axial load correlate to an increasingly thick and three-dimensional oil film that remains attached to the front face. However, no significant effect on droplet diameter is observed with change in either of these variables. This is as expected given that Hee [8] did not find oil flow rate or axial load to have a substantial effect on the thickness of the film close to the bearing. The insensitivity of droplet diameter to oil flow rate and axial load means that these variables do not need to be considered in changes to future bearing design with respect to the size of droplets generated in the bearing chamber. This does however indicate that a higher mass of oil remains in the form of a film and in contact with the static front face, allowing heat transfer to occur. The oil in the film does not have the same risk of becoming entrained in the circulating airflow that droplets have, meaning this may be a desirable behaviour.

Droplet speeds are generally fairly similar on both sides of the bearing chamber for each operating speed, but tend to higher speeds at the 3 o'clock position where gravity and shear act in the same direction - approximately $0.5\,\mathrm{m\,s^{-1}}$ faster than on the 9 o'clock side where shear and gravity act in opposite directions.

No correlation is identified between droplet speed and operating speed, with the exception of 1000 rpm where droplets observed were in the order of $1\,\mathrm{m\,s^{-1}}$ slower than at other operating speeds. Variation in applied axial load did not affect droplet speed. However, lower droplet speeds are seen at higher oil flow rates.

CHAPTER 6

Conclusions and Future Work

This chapter presents the main findings of the oil shedding process in a ball bearing and proposed future work for continued improvement of heat and oil management for more efficient aeroengines.

6.1 Main Findings From the Thesis

A gap in the literature exists around droplet generation as oil enters the bearing chamber, including data regarding droplet diameter, speed and path taken to the outer wall before scavenge. Experimental droplet data from a representative geometry, such as the University of Nottingham's Bearing Shedding Rig (BSR), is of great value for validation of existing and future computational modelling as well as providing direct understanding of two phase flow behaviour in an aeroengine bearing chamber. Image data is captured using a high-speed camera, allowing droplets to be visualised.

6.1.1 Qualitative Work

High-speed imaging has been successfully performed on the Bearing Shedding Rig (BSR), allowing visualisation of two phase flow behaviour at the 3 o'clock and 9 o'clock positions. Qualitative analysis of the images shows that some oil remains attached to the front face of the bearing chamber forming an oil film. Entrained air bubbles can be seen within the film. Some droplets are seen to exists in the bearing slot before passing into the bearing chamber – these are generally smaller diameter droplets. As oil passes over the lip of the front face into the bearing chamber, droplets (or three-dimensional structures which often subsequently break up into droplets) are formed. At higher operating speeds the oil film on the front face becomes more three-dimensional and complex structures become more prevalent – these are often the source of larger droplets

observed.

Qualitative analysis of the high-speed images shows that the oil film covers a greater area of the front face at higher operating speeds, as well ass becoming more prone to forming complex three-dimensional oil structures. Greater three-dimensionality is observed on the 9 o'clock (countercurrent side) compared to the 3 o'clock (co-current side) where the oil film on the front face appears thinner and covers a larger surface area. Rapid breakup of three-dimensional structures at high operating speeds leads to a greater number of droplets in the imaging area. Increasing oil flow rate and axial load correlate to an increasingly thick and three-dimensional oil film passing into the bearing chamber. However, no significant effect on droplet diameter is observed with change in either oil flow rate supplied to the bearing chamber or applied axial load.

6.1.2 Development of the Convolutional Neural Network (CNN)

Convolutional Neural Networks (CNNs) are found to be an effective tool for accurate droplet detection from high-speed experimental images, outperforming the conventional method. This is a key finding and facilitates the processing of large quantities of data that would be unfeasible manually without compromising on accuracy. The minimum feasible detectable droplet diameter is limited by spatial resolution of images at around four pixel diameter for this application - approximately 0.25 mm for droplets in the main data series. Droplets larger than this threshold can be detected and tracked to give a good representation of ground truth. Therefore, the method for droplet detection and tracking developed in this project is considered to be appropriate for experimental work of this type.

The droplet detection CNN was trained via transfer learning from the pre-trained network ResNet-50. This outputs a semantic segmentation mask, showing the locations of all detected droplets in white (and all non-droplets in black). Droplet diameter is and positions are extracted from the output masks for analysis. A strong level of agreement is found in diameter distribution of detected droplets compared to ground truth. Detected droplets are tracked through time using script from Blair and Dufresne [71], allowing calculation of in-plane droplet speed (excluding the axial component) and correlations between droplet diameter and speed to be identified. Droplet in-plane speed is typically found to be in the order of $2\,\mathrm{m\,s^{-1}}$ to $5\,\mathrm{m\,s^{-1}}$. Analysis has been performed for the following conditions at both the 3 o'clock and 9 o'clock positions to give a representation of two-phase flow behaviour:

- Operating speeds between 1000 rpm and 12 000 rpm (fixed axial load of 10 kN

and oil flow rate of 7.3 l min^{-1}).

- Oil flow rate supplied to the bearing of 5.2 l min^{-1}, 7.3 l min^{-1} and 10.8 l min^{-1} (fixed speed of 9000 rpm and axial load of 10 kN).
- Applied axial load of 10 kN, 20 kN and 30 kN (fixed speed of 9000 rpm and an oil flow rate of 7.3 l min^{-1}).

6.1.3 Quantitative Work

Detailed analysis of a single test point (7000 rpm, 5.2 l min^{-1} oil flow rate and 20 kN axial load) shows that most droplets have a diameter below 2.0 mm, with the most common being in the 0.6 mm to 0.8 mm range. Very few droplets with diameter larger than 3.0 mm are observed. Data is in good agreement with ground truth, showing that the droplet detection CNN provides representative data from the high-speed images. The inclusion of two distinct peaks in the droplet speed probability distribution at this test point suggests multiple mechanisms of droplet generation may occur in the bearing chamber. The lower speed peak consists of generally smaller diameter droplets compared to the higher speed peak which is made up of a greater range of droplet diameters.

The use of the Rosin-Rammler fit to describe the droplet diameter distribution, proposed by Nicoli [1], is found to provide a good representation of experimental data on both sides of the bearing chamber. The spread of the distribution (indicated by the scaling factor) does not vary significantly or with any identified trend in relation to operating conditions.

Operating speed was seen to have significantly more effect on droplet diameter then change in applied axial load or oil flow rate. Below the threshold value of 7000 rpm modal droplet diameter is relatively constant at 0.8 mm on the 3 o'clock side of the bearing chamber and 0.7 mm on the 9 o'clock side, however above 7000 rpm droplet diameter increases with operating speed to approximately 1.0 mm on both sides of the bearing chamber. Conversely, no trends in droplet diameter were seen with changing applied axial load or oil flow rates supplied to the bearing.

Droplets tend to have higher speeds at the 3 o'clock position where gravity and shear act in the same direction - approximately 0.5 m s^{-1} faster than on the 9 o'clock side where shear and gravity act in opposite directions. No correlation is identified between droplet speed and either operating speed or applied axial load within the conditions examined in this work. Lower droplet speeds are seen as oil flow rate increases.

It is anticipated that droplet speeds in a real aeroengine bearing may be higher due to increased windage caused by the difference in geometry compared to the BSR. Air in the bearing chamber will be accelerated to a greater extent by a through-shaft (as in an actual aeroengine) than by a stub-shaft (as in the BSR). However, droplet speed data from this work is still considered to be strongly informative.

6.2 Contribution to Knowledge

The work presented in this thesis demonstrates a significant improvement to the understanding of two phase flow in an aeroengine bearing chamber. The key contributions to knowledge are detailed below.

- Improved qualitative understanding of the effect of operating speed, oil flow rate and axial load on flow behaviour at the shedding edge on the co-current side of the bearing chamber, including the definition of four behavioural regimes.
- Delivery of an analysis tool for droplet detection in a visually complex aeroengine representative environment, meaning that automated processing is possible for large quantities of data.
- The droplet detection CNN is validated against manually labelled experimental data, showing that droplet diameters are detected with good accuracy.
- Droplet diameter and speed data has been obtained on the co-current and counter-current sides of the bearing chamber for a range of operating conditions providing aeroengine relevant data for future design and validation of existing and new computational models, facilitating improved design capabilities.
- Trends in droplet diameter and speed are established for changes in operating conditions (operating speed, oil flow rate and applied axial load).

These contributions to knowledge demonstrate an enhanced understanding of two phase flow behaviour in aeroengine bearing chambers for future design and validation of computational modelling approaches, as well as having provided an analysis tool for automated droplet detection in future experimental work. Based on the findings and experience acquired throughout the work presented in this thesis, recommendations for future work are suggested to continue furthering knowledge in this area.

6.3 Recommendations for Future Work

Proposed future work includes:

- Analysis of additional circumferential positions in the bearing chamber (i.e. the 12 o'clock and 6 o'clock positions) to get a fuller understanding of two phase flow behaviour in the bearing chamber.
- High-speed imaging and analysis of additional operating speeds with a high spatial resolution. The AERIS data used for speeds over 9000 rpm has lower spatial resolution than main data set meaning the difference made by a single pixel error in droplet diameter detection is more significant. Performing additional high-speed imaging using the methodology described in Chapter 3 would allow comparison of high resolution data through the entire speed range.
- Further training of the CNN (requiring additional labelling of ground truth images) for improved detection accuracy.
- Further investigation into the mechanisms of droplet generation in the bearing chamber causing the two peaks in droplet speed distribution.
- Investigate whether the droplet speed distribution can be described by a normal distribution. This would be allow droplet speeds to be described in a representative manner using only a small number of variables.
- Development of computational modelling of two phase flow in an aeroengine bearing chamber using experimental droplet data obtained in this work for validation.

References

[1] A. Nicoli. *Development and Application of a Fully Coupled Eulerian Thin Film/Discrete Phase Approach to a Simplified Aeroengine Bearing Chamber*. PhD thesis, University of Nottingham, 2020.

[2] Department for Transport Statistics. AVI0101: Air Traffic at UK Airports, 2022. URL https://www.gov.uk/government/statistical-data-sets/aviation-statistics-data-tables-avi#activity-by-uk-airlines-avi02.

[3] S. Shparberg and B. Lange. Global Market Forecast 2022 - AIRBUS, July 2022. URL https://www.airbus.com/en/products-services/commercial-aircraft/market/global-market-forecast.

[4] ACARE. Beyond Vision 2020 (towards 2050), 2010. URL https://commission.europa.eu/research-and-innovation_en.

[5] European Commission. Flightpath 2050: Europe's Vision for Aviation. Luxembourg Publications Office of the European Union, Luxembourg, 2011.

[6] IATA. Air Passenger Market Analysis, December 2022. URL https://www.iata.org/en/iata-repository/publications/economic-reports/air-passenger-market-analysis---december-2022.

[7] Rolls Royce. *The Jet Engine*. Wiley, 5th edition, August 2015. ISBN 978-1-119-06599-9.

[8] J. L. Hee. *Experimental and Computational Investigation Into Oil Shedding From an Aeroengine Ball Bearing*. PhD thesis, University of Nottingham, 2019.

[9] C. W. Lee, P. C. Palma, K. Simmons, and S. J. Pickering. Comparison of Computational Fluid Dynamics and Particle Image Velocimetry Data for the Airflow in an Aeroengine Bearing Chamber. *Journal of Engineering for Gas Turbines and Power*, 127(4):697–703, 2005. doi: 10.1115/1.1924635.

[10] C. W. Lee. *Air and Oil Flow Investigations in an Aeroengine Bearing Chamber*. PhD thesis, University of Nottingham, 2004.

[11] J. T. Stuart. Taylor-Vortex Flow: A Dynamical System. *SIAM Review*, 1986.

[12] P. Gorse, K. Willenborg, S. Busam, J. Ebner, K. Dullenkopf, and S. Wittig. 3D-LDA Measurements in an Aero-Engine Bearing Chamber. *American Society of Mechanical Engineers, International Gas Turbine Institute, Turbo Expo (Publication) IGTI*, 5 A:257–265, 2003. doi: 10.1115/GT2003-38376.

[13] P. Gorse, S. Busam, and K. Dullenkopf. Influence of Operating Condition and Geometry on the Oil Film Thickness in Aeroengine Bearing Chambers. *Journal of Engineering for Gas Turbines and Power*, 128(1):103–110, 2006. doi: 10.1115/1.1924485.

[14] J. Aidarinis and A. Goulas. Enhanced Computational Fluid Dynamics Modeling and Laser Doppler Anemometer Measurements for the Air-Flow in an Aeroengine Front Bearing Chamber - Part I. *Journal of Engineering for Gas Turbines and Power*, 137(8), 2015. doi: 10.1115/1.4029272.

[15] A. Glahn, M. Kurreck, M. Willmann, and S. Wittig. Feasibility Study on Oil Droplet Flow Investigations Inside Aero Engine Bearing Chambers - PDPA Techniques in Combination With Numerical Approaches. *Journal of Engineering for Gas Turbines and Power*, 118(4):749–755, 1996. doi: 10.1115/1.2816990.

[16] P. Gorse, K. Dullenkopf, H. J. Bauer, and S. Wittig. An Experimental Study on Droplet Generation in Bearing Chambers Caused by Roller Bearings. *Proceedings of the ASME Turbo Expo*, 4(Part B):1681–1692, 2008. doi: 10.1115/GT2008-51281.

[17] T. A. Shedd, M. L. Corn, J. M. Cohen, M. Arienti, and M. C. Soteriou. Liquid Film Formation by an Impinging Jet in a High-Velocity Air Stream. *47th AIAA Aerospace Sciences Meeting including the New Horizons Forum and Aerospace Exposition*, January 2009.

[18] M. Arienti, L. Wang, M. Corn, X. Li, M. C. Soteriou, T. A. Shedd, and M. Herrmann. Modeling Wall Film Formation and Breakup Using an Integrated Interface-Tracking/discrete-Phase Approach. *Journal of Engineering for Gas Turbines and Power*, 133(3), 2011. doi: 10.1115/1.4002019.

[19] A. Nicoli, R. Jefferson-Loveday, and K. Simmons. A New OpenFoam Solver Capable of Modelling Oil Jet-Breakup and Subsequent Film Formation for Bearing Chamber Applications. *Proceedings of the ASME Turbo Expo 2019: Turboma-*

chinery Technical Conference and Exposition, 2C-2019, June 2019. doi: 10.1115/GT2019-90264.

[20] J. L. Hee, K. Simmons, B. Kakimpa, and D. Hann. Computationally Efficient Modelling of Oil Jet-Breakup and Film Formation for Bearing Chamber Applications. *Proceedings of the ASME Turbo Expo*, 2C-2018, 2018. doi: 10.1115/GT201876172.

[21] S. Wittig, A. Glahn, and J. Himmelsbach. Influence of High Rotational Speeds on Heat Transfer and Oil Film Thickness in Aero-Engine Bearing Chambers. *Journal of Engineering for Gas Turbines and Power*, 116(2):395–401, 1994.

[22] A. Glahn and S. Wittig. Two-Phase Air/oil Flow in Aero-Engine Bearing Chambers - Assessment of an Analytical Prediction Method for the Internal Wall Heat Transfer. *International Journal of Rotating Machinery*, 5(3):155–165, 1999.

[23] J. L. Hee, R. Santhosh, K. Simmons, G. Johnson, D. Hann, and M. Walsh. Oil Film Thickness Measurements on Surfaces Close to an Aeroengine Ball Bearing Using Optical Techniques. *Proceedings of the ASME Turbo Expo*, 7A-2017, 2017. doi: 10.1115/GT201763813.

[24] A. Sinha, D. Hann, K. Johnson, and M. Walsh. Experimental Investigation Into Oil Film Thickness and Behaviour Near an Aero-Engine Bearing. In *Proceedings of the ASME Turbo Expo*, volume 8-A, 2022. doi: 10.1115/GT2022-82180.

[25] W. Kurz and H.-J. Bauer. An approach for predicting the flow regime in an aero engine bearing chamber. *Proceedings of the ASME Turbo Expo 2014: Turbine Technical Conference and Exposition*, 5C, 2014. doi: 10.1115/GT2014-26756.

[26] A. A. Hashmi, K. Dullenkopf, H. J. Bauer, and M. Klingsporn. Experimental Investigation of Lubrication Oil Film Dynamics in a Typical Aero-Engine Bearing Chamber Environment. *Proceedings of the ASME Turbo Expo*, 5:797–807, 2011. doi: 10.1115/GT2011-45545.

[27] R. Ingle, R. Yadav, H. Punekar, and J. Cao. Modeling of Particle Wall Interaction and Film Transport Using Eulerian Wall Film Model. *ASME 2014 Gas Turbine India Conference, GTINDIA 2014*, 2014. doi: 10.1115/GTINDIA2014-8230.

[28] T. C. L. Yue. *Numerical Simulation of Multiphase Jet Fragmentation Using Smoothed Particle Hydrodynamics*. PhD thesis, University of Nottingham, 2015.

[29] T. Okawa, T. Shiraishi, and T. Mori. Production of Secondary Drops During the Single Water Drop Impact Onto a Plane Water Surface. *Experiments in Fluids*, 41: 965–974, November 2006. doi: 10.1007/s00348-006-0214-x.

[30] G. E. Cossali, A. Coghe, and M. Marengo. The Impact of a Single Drop on a Wetted Solid Surface. *Experiments in Fluids*, 22(6):463–472, 1997. doi: 10.1007/s003480050073.

[31] A. M. Worthington. *A Study of Splashes*. Longmans, Green & Co., 1908.

[32] M. Rein. Phenomena of Liquid Drop Impact on Solid and Liquid Surfaces. *Fluid Dynamics Research*, 12(2):61–93, 1993.

[33] R. Rioboo, C. Bauthier, J. Conti, M. Voué, and J. De Coninck. Experimental Investigation of Splash and Crown Formation During Single Drop Impact on Wetted Surfaces. *Experiments in Fluids*, 35(6):648–652, 2003. doi: 10.1007/s00348-003-0719-5.

[34] T. Okawa, K. Kawai, K. Kubo, and S. Kitabayashi. Fundamental Characteristics of Secondary Drops Produced by Early Splash During Single-Drop Impingement Onto a Thick Liquid Film. *Experimental Thermal and Fluid Science*, 131, 2022. doi: 10.1016/j.expthermflusci.2021.110533.

[35] T. Okawa, T. Shiraishi, and T. Mori. Effect of Impingement Angle on the Outcome of Single Drop Impact Onto a Plane Water Surface. *Experiments in Fluids*, 44(2):331–339, 2008. doi: 10.1007/s00348-007-0406-z.

[36] Z. Chen, C. Shu, Y. Wang, and L. M. Yang. Oblique Drop Impact on Thin Film: Splashing Dynamics at Moderate Impingement Angles. *Physics of Fluids*, 32(3), 2020. doi: 10.1063/5.0004142.

[37] A. Sinha, V. Ramakrishnan, and K. Johnson. Droplet Impact on a Curved Moving Liquid Film. volume 10-B, 2022. doi: 10.1115/GT2022-79505.

[38] R. Santhosh, J. L. Hee, K. Simmons, G. Johnson, D. Hann, and M. Walsh. Experimental Investigation of Oil Shedding From an Aero-Engine Ball Bearing at Moderate Speeds. *Proceedings of the ASME Turbo Expo*, 7A-2017, 2017. doi: 10.1115/GT201763815.

[39] M. A. Friedrich, H. Lan, J. L. Wegener, J. A. Drallmeier, and B. F. Armaly. A Separation Criterion With Experimental Validation for Shear-Driven Films in Separated Flows. *Journal of Fluids Engineering, Transactions of the ASME*, 130(5):0513011–0513019, 2008. doi: 10.1115/1.2907405.

[40] A. Glahn, S. Busam, M. F. Blair, K. L. Allard, and S. Wittig. Droplet Generation by Disintegration of Oil Films at the Rim of a Rotating Disk. *Journal of Engineering for Gas Turbines and Power*, 124(1):117–124, 2002. doi: 10.1115/1.1400753.

[41] J. Liu, Q. Yu, and Q. Guo. Experimental Investigation of Liquid Disintegration by Rotary Cups. *Chemical Engineering Science*, 73:44–50, 2012. doi: 10.1016/j.ces.2012.01.010.

[42] A. R. Frost. Rotary Atomization in the Ligament Formation Mode. *Journal of Agricultural Engineering Research*, 26(1):63–78, 1981. doi: 10.1016/0021-8634(81)90127-X.

[43] P. Paleo Cageao, K. Johnson, S. Ambrose, and R. Omar. Experimental Investigation Into Oil Shedding From a Rotating Cup Geometry. *Proceedings of the ASME 2022 Turbomachinery Technical Conference & Exposition*, 2022. doi: 10.1115/GT2022-82195.

[44] R. P. Fraser, N. Dombrowski, and J. H. Routley. The Filming of Liquids by Spinning Cups. *Chemical Engineering Science*, 18(6):323–337, 1963. doi: 10.1016/0009-2509(63)80026-3.

[45] A. Glahn, M. F. Blair, K. L. Allard, S. Busam, O. Schäfer, and S. Wittig. Disintegration of Oil Jets Emerging From Axial Passages at the Face of a Rotating Cylinder. *Journal of Engineering for Gas Turbines and Power*, 125(4):1003–1010, 2003. doi: 10.1115/1.1586310.

[46] A. Glahn, M. F. Blair, K. L. Allard, S. Busam, O. Schäfer, and S. Wittig. Disintegration of Oil Films Emerging From Radial Holes in a Rotating Cylinder. *Journal of Engineering for Gas Turbines and Power*, 125(4):1011–1020, 2003. doi: 10.1115/1.1586311.

[47] D. Zhu, G. Chen, L. Wang, and R. Zhang. Effects of Droplet Deformation, Evaporation, and Mutual Interaction With Air on Droplet Motion and Droplet-Film Impingement in Aeroengine Bearing Chambers. *Applied Thermal Engineering*, 224, 2023. doi: 10.1016/j.applthermaleng.2023.120008.

[48] J. O. Hinze and H. Milborn. Atomization of Liquids by Means of a Rotating Cup. *ASME Journal of Applied Mechanics*, 17(2):145–153, 1950. doi: 10.1115/1.4010093.

[49] D. F. Rutland and G. J. Jameson. A Non-Linear Effect in the Capillary Instability of Liquid Jets. *Journal of Fluids Mechanics*, 46:267–271, 1971.

[50] M. Yousefifard, P. Ghadimi, and M. Mirsalim. Numerical Simulation of Biodiesel Spray Under Ultra-High Injection Pressure Using OpenFOAM. *Journal of the Brazilian Society of Mechanical Sciences and Engineering*, 37(2):737–746, 2015. doi: 10.1007/s40430-014-0199-y.

[51] P. Ghadimi, M. Yousefifard, and H. Nowruzi. Applying Different Strategies Within OpenFOAM to Investigate the Effects of Breakup and Collision Model on the Spray and In-Cylinder Gas Mixture Attribute. *Journal of Applied Fluid Mechanics*, 9(6):2781–2790, 2016.

[52] V. Kulkarni and P. E. Sojka. Bag Breakup of Low Viscosity Drops in the Presence of a Continuous Air Jet. *Physics of Fluids*, 26(7), 2014. doi: 10.1063/1.4887817.

[53] H. Sun, G. Chen, Y. Zhang, and L. Wang. Theoretical and Experimental Studies on the Motion and Thermal States of Oil Droplet in a Bearing Chamber. *Proceedings of the Institution of Mechanical Engineers, Part G: Journal of Aerospace Engineering*, 230 (14):2596–2614, 2016. doi: 10.1177/0954410016629690.

[54] L. Fang and G. Chen. The Study of Droplet Deformation and Droplet Volume Fraction in an Aero-Engine Bearing Chamber. *Proceedings of the Institution of Mechanical Engineers, Part G: Journal of Aerospace Engineering*, 233(6):2264–2277, 2019. doi: 10.1177/0954410018777595.

[55] B. Chen, G. D. Chen, H. C. Sun, and Y. H. Zhang. Effect of Oil Droplet Deformation on Its Deposited Characteristics in an Aeroengine Bearing Chamber. *Proceedings of the Institution of Mechanical Engineers, Part G: Journal of Aerospace Engineering*, 228 (2):206–218, 2014. doi: 10.1177/0954410012467875.

[56] S. Shao, C. Li, and J. Hong. A Hybrid Image Processing Method for Measuring 3D Bubble Distribution Using Digital Inline Holography. *Chemical Engineering Science*, 207:929–941, 2019. doi: 10.1016/j.ces.2019.07.009.

[57] A. J. Mitchell, K. Simmons, and D. Hann. Experimental Investigation Into Droplet Impingement Upon Moving Films Using High Speed Video and Thermal Imaging. *ASME International Mechanical Engineering Congress and Exposition, Proceedings (IMECE)*, 1, 2015. doi: 10.1115/IMECE2015-51677.

[58] J. Vasques, A. Ibrahim, D. Hann, K. Simmons, and M. Walsh. The Effect of Surface Tension on Bubble Generation in Gas-Sheared Liquid Films. In *Proceedings of the ASME Turbo Expo 2019*, volume 5A, June 2019. doi: 10.1115/GT2019-91303.

[59] J. Ilonen, R. Juránek, T. Eerola, L. Lensu, M. Dubská, P. Zemčík, and H. Kälviäinen. Comparison of Bubble Detectors and Size Distribution Estimators. *Pattern Recognition Letters*, 101:60–66, 2018. doi: 10.1016/j.patrec.2017.11.014.

[60] G. Chaussonnet, C. Lieber, Y. Yikang, W. Gu, A. Bartschat, M. Reischl, R. Koch, R. Mikut, and H. J. Bauer. Towards DeepSpray: Using Convolutional Neural Net-

work to Post-process Shadowgraphy Images of Liquid Atomization. techreport, Karlsruher Institut für Technologie, 2019.

[61] I. Poletaev, M. P. Tokarev, and K. S. Pervunin. Bubble Patterns Recognition Using Neural Networks: Application to the Analysis of a Two-Phase Bubbly Jet. *International Journal of Multiphase Flow*, 126, 2020. doi: 10.1016/j.ijmultiphaseflow.2019.103194.

[62] L. Shu, G. R. Osinski, K. McIsaac, and D. Wang. An Automatic Methodology for Analyzing Sorting Level of Rock Particles. *Computers and Geosciences*, 120:97–104, 2018. doi: 10.1016/j.cageo.2018.08.001.

[63] J. Schäfer, P. Schmitt, M. W. Hlawitschka, and H. J. Bart. Measuring Particle Size Distributions in Multiphase Flows Using a Convolutional Neural Network. *Chemie-Ingenieur-Technik*, 91(11):1688–1695, 2019. doi: 10.1002/cite.201900099.

[64] MathWorks. Hough Transform. URL `https://uk.mathworks.com/help/images/ref/hough.html`. [last accessed 02/03/23].

[65] I. Malakhov, A. Seredkin, A. Chernyavskiy, V. Serdyukov, R. Mullyadzanov, and A. Surtaev. Deep Learning Segmentation to Analyze Bubble Dynamics and Heat Transfer During Boiling at Various Pressures. *International Journal of Multiphase Flow*, 162, 2023. doi: 10.1016/j.ijmultiphaseflow.2023.104402.

[66] O. Ronneberger, P. Fischer, and T. Brox. U-Net: Convolutional Networks for Biomedical Image Segmentation. In Nassir Navab, Joachim Hornegger, William M. Wells, and Alejandro F. Frangi, editors, *Medical Image Computing and Computer-Assisted Intervention - MICCAI 2015*, pages 234–241. Springer International Publishing, 2015. ISBN 978-3-319-24574-4. doi: 10.1007/978-3-319-24574-4_28.

[67] K. He, G. Gkioxari, P. Dollár, and R. Girshick. Mask R-CNN. In *IEEE International Conference on Computer Vision (ICCV)*, pages 2980–2988, 2017. doi: 10.1109/ICCV.2017.322.

[68] K. He, X. Zhang, S. Ren, and J. Sun. Deep Residual Learning for Image Recognition. In *Proceedings of the IEEE Computer Society Conference on Computer Vision and Pattern Recognition*, pages 770–778, December 2016. doi: 10.1109/CVPR.2016.90.

[69] Stanford Vision Lab, Stanford University, Princeton University. ImageNet, 2016. URL `http://www.image-net.org/`. [last accessed 07/09/20].

[70] A. Krizhevsky, V. Nair, and G. Hinton. The CIFAR-10 dataset, 2006. URL https://www.cs.toronto.edu/~kriz/cifar.html.

[71] D. Blair and E. Dufresne. The Matlab Particle Tracking Code Repository, 2008. URL http://site.physics.georgetown.edu/matlab/index.html. [last accessed 21/01/20].

[72] J. C. Crocker and D. G. Grier. Methods of Digital Video Microscopy for Colloidal Studies. *Journal of Colloid and Interface Science*, 179(1):298–310, 1996. doi: 10.1006/jcis.1996.0217.

[73] R. Santhosh, J. L. Hee, K. Simmons, and G. Johnson. Experimental Investigation Into Oil Shedding and Film Flow Near a Trent 1000 HP Bearing at Shaft Speeds up to 7000 rpm. Technical report, University of Nottingham, October 2016.

[74] A. J. Mitchell, D. Hann, and K. Simmons. Experimental Investigation Into Crater Morphology for Droplets Impinging on a Moving Film. *Proceedings of the ASME Turbo Expo*, 2D-2017, 2017. doi: 10.1115/GT2017-63443.

[75] M. Frei and F. E. Kruis. Image-Based Size Analysis of Agglomerated and Partially Sintered Particles via Convolutional Neural Networks. *Powder Technology*, 360: 324–336, 2020. doi: 10.1016/j.powtec.2019.10.020.

[76] S. Khodakarami, K. Fazle Rabbi, Y. Suh, Y. Won, and N. Miljkovic. Machine Learning Enabled Condensation Heat Transfer Measurement. *International Journal of Heat and Mass Transfer*, 194, 2022. doi: 10.1016/j.ijheatmasstransfer.2022.123016.

[77] G. M. Hobold and A. K. da Silva. Visualization-Based Nucleate Boiling Heat Flux Quantification Using Machine Learning. *International Journal of Heat and Mass Transfer*, 134:511–520, 2019. doi: 10.1016/j.ijheatmasstransfer.2018.12.170.

[78] G. M. Hobold and A. K. da Silva. Automatic Detection of the Onset of Film Boiling Using Convolutional Neural Networks and Bayesian Statistics. *International Journal of Heat and Mass Transfer*, 134:262–270, 2019. ISSN 0017-9310. doi: https://doi.org/10.1016/j.ijheatmasstransfer.2018.12.070.

[79] Y. Kim and H. Park. Deep Learning-Based Automated and Universal Bubble Detection and Mask Extraction in Complex Two-Phase Flows. *Scientific reports*, 11(1): 8940, 2021. doi: 10.1038/s41598-021-88334-0.

[80] Q. Wang, X. Li, C. Xu, T. Yan, and Y. Li. Bubble Recognizing and Tracking in a Plate Heat Exchanger by Using Image Processing and Convolutional Neural Network.

International Journal of Multiphase Flow, 138:103593, 2021. ISSN 0301-9322. doi: https://doi.org/10.1016/j.ijmultiphaseflow.2021.103593.

[81] H. Hessenkemper, S. Starke, Y. Atassi, T. Ziegenhein, and D. Lucas. Bubble Identification From Images With Machine Learning Methods. *International Journal of Multiphase Flow*, 155:104169, 2022. ISSN 0301-9322. doi: https://doi.org/10.1016/j.ijmultiphaseflow.2022.104169.

[82] M. A. Nielsen. Neural Networks and Deep Learning. Online Book, December 2019. URL `http://neuralnetworksanddeeplearning.com/`.

[83] G. Csurka, D. Larlus, and F. Perronnin. What is a Good Evaluation Measure for Semantic Segmentation? In *BMVC 2013 - Electronic Proceedings of the British Machine Vision Conference*, 2013. doi: 10.5244/C.27.32.

[84] K. He, G. Gkioxari, P. Dollár, and R. Girshick. Mask R-CNN. *IEEE Transactions on Pattern Analysis and Machine Intelligence*, 42(2):386–397, 2020. doi: 10.1109/TPAMI.2018.2844175.

[85] V. Badrinarayanan, A. Kendall, and R. Cipolla. SegNet: A Deep Convolutional Encoder-Decoder Architecture for Image Segmentation. *IEEE Transactions on Pattern Analysis and Machine Intelligence*, 39(12):2481–2495, 2017. doi: 10.1109/TPAMI.2016.2644615.

[86] A. B. Oktay and A. Gurses. Automatic Detection, Localization and Segmentation of Nano-Particles With Deep Learning in Microscopy Images. *Micron*, 120:113–119, 2019. doi: 10.1016/j.micron.2019.02.009.

[87] A. K. Jaiswal, P. Tiwari, S. Kumar, D. Gupta, A. Khanna, and J. Rodrigues. Identifying Pneumonia in Chest X-Rays: A Deep Learning Approach. *Measurement*, 145:511–518, 2019. ISSN 0263-2241. doi: https://doi.org/10.1016/j.measurement.2019.05.076. URL `https://www.sciencedirect.com/science/article/pii/S0263224119305202`.

[88] B. Liang, Y. Zhai, C. Tong, J. Zhao, J. Li, X. He, and Q. Ma. A Deep Automated Skeletal Bone Age Assessment Model via Region-Based Convolutional Neural Network. *Future Generation Computer Systems*, 98:54–59, 2019. ISSN 0167-739X. doi: https://doi.org/10.1016/j.future.2019.01.057. URL `https://www.sciencedirect.com/science/article/pii/S0167739X18326153`.

[89] H Chen, K. Zhang, P. Lyu, H. Li, L. Zhang, J. Wu, and C. H. Lee. A Deep Learning Approach to Automatic Teeth Detection and Numbering Based on Ob-

ject Detection in Dental Periapical Films. *Scientific Reports*, 9, 03 2019. doi: 10.1038/s41598-019-40414-y.

[90] MathWorks. Semantic Segmentation Using Deep Learning, . URL https://uk.mathworks.com/help/vision/examples/semantic-segmentation-using-deep-learning.html. [last accessed 07/09/20].

[91] MathWorks. Pretrained Deep Neural Networks, . URL https://uk.mathworks.com/help/deeplearning/ug/pretrained-convolutional-neural-networks.html. [last accessed 22/09/22].

[92] G. J. Brostow, J. Fauqueur, and R. Cipolla. Semantic Object Classes in Video: A High-Definition Ground Truth Database. *Pattern Recognition Letters*, 30(2):88–97, 2009. doi: 10.1016/j.patrec.2008.04.005.

[93] MathWorks. Pretrained Deep Neural Networks, . URL https://uk.mathworks.com/help/deeplearning/ug/pretrained-convolutional-neural-networks.html#mw_6ab30f15-4136-46b0-b5db-4f9b3b1cfcd2. [last accessed 13/05/21].

[94] J. M. Webb, S. A. Adusei, Y. Wang, N. Samreen, K. Adler, D. D. Meixner, R. T. Fazzio, M. Fatemi, and A. Alizad. Comparing Deep Learning-Based Automatic Segmentation of Breast Masses to Expert Interobserver Variability in Ultrasound Imaging. *Computers in Biology and Medicine*, 139:104966, 2021. ISSN 0010-4825. doi: https://doi.org/10.1016/j.compbiomed.2021.104966.

[95] J. W. Sanders, H. Mok, A. N. Hanania, A. M. Venkatesan, C. Tang, T. L. Bruno, H. D. Thames, R. J. Kudchadker, and S. J. Frank. Computer-Aided Segmentation on MRI for Prostate Radiotherapy, Part I: Quantifying Human Interobserver Variability of the Prostate and Organs at Risk and Its Impact on Radiation Dosimetry. *Radiotherapy and Oncology*, 169:124–131, 2022. doi: 10.1016/j.radonc.2021.12.011.

[96] M. Ahmed and M. S. Youssef. Influence of Spinning Cup and Disk Atomizer Configurations on Droplet Size and Velocity Characteristics. *Chemical Engineering Science*, 107:149–157, 2014. doi: 10.1016/j.ces.2013.12.004.

[97] K. Farbrother, P. Paleo Cageao, K. Johnson, and S. Ambrose. Investigation of Droplet Shedding in an Aeroengine Bearing Chamber Using Convolutional Neural Networks. In *Proceedings of the ASME Turbo Expo*, volume 8-A, 2022. doi: 10.1115/GT2022-82275.

[98] G. Giles, K. Farbrother, and S. Ambrose. Analysis of Droplet Impact on the Outer

Wall of Aeroengine Bearing Chambers using Convolutional Neural Networks. Master's thesis, University of Nottingham, 2022.

Appendices

APPENDIX A

Effect of Operating Speed on Diameter Distribution for the AERIS Dataset

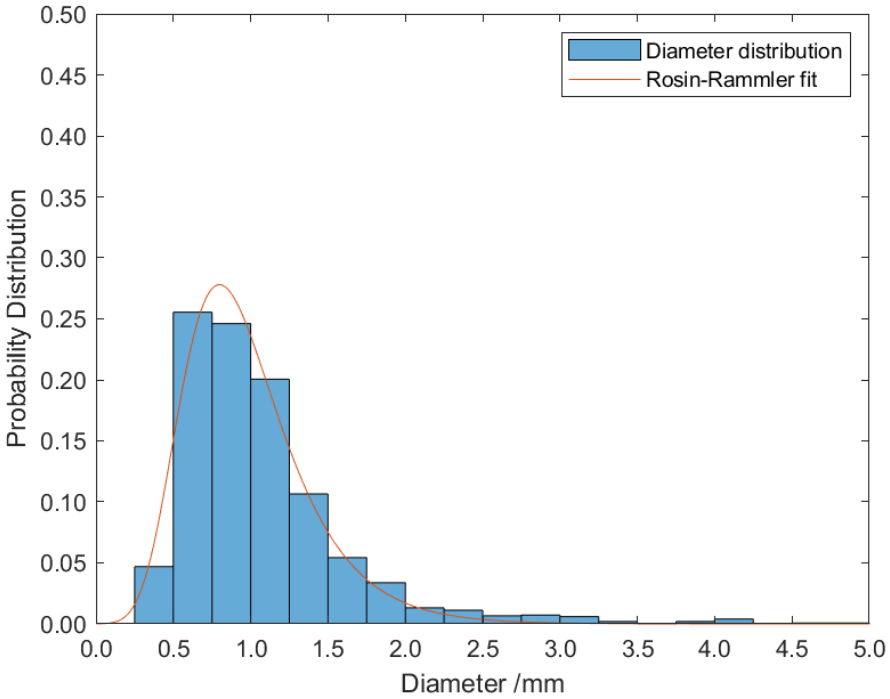


Figure A.1: Droplet diameter distribution at the 3 o'clock position at 1000 rpm with oil flow rate 7.3 l min^{-1} and axial load 10 kN taken from 576 x 908 pixel images.

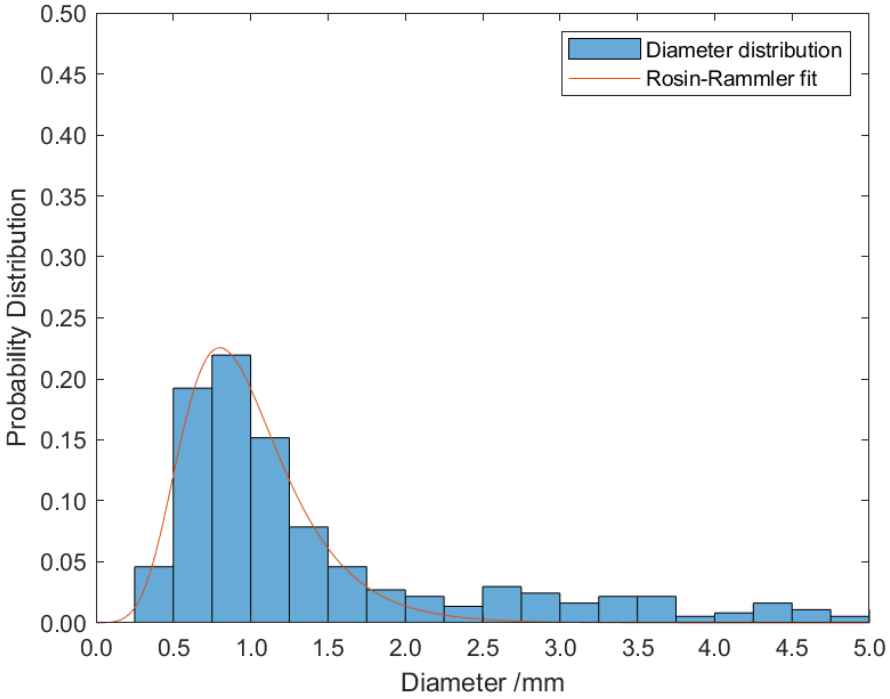


Figure A.2: Droplet diameter distribution at the 3 o'clock position at 3000 rpm with oil flow rate 7.31 $l\,min^{-1}$ and axial load 10 kN taken from 576 x 908 pixel images.

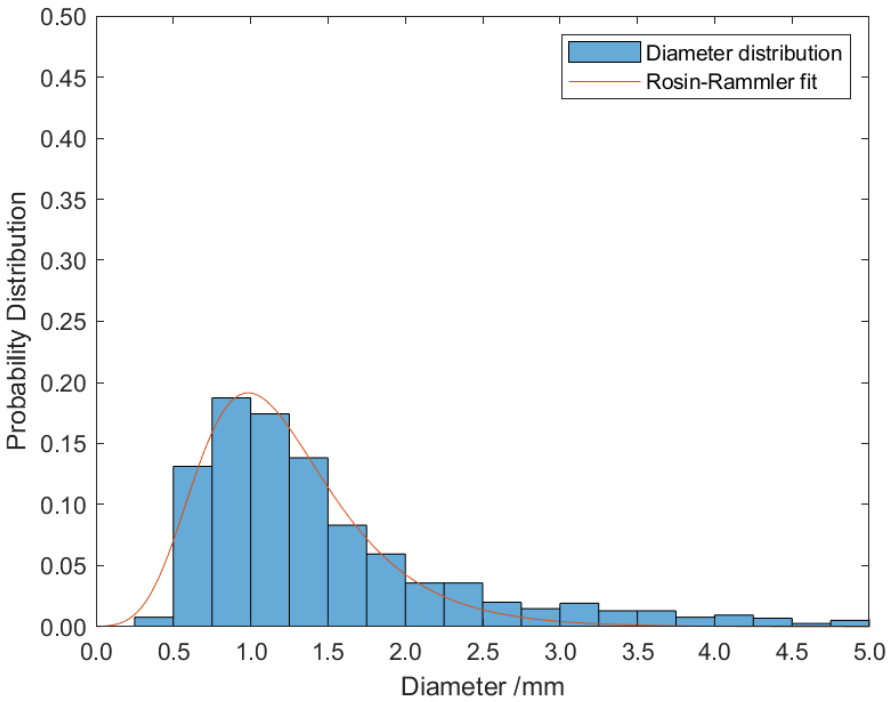


Figure A.3: Droplet diameter distribution at the 3 o'clock position at 5000 rpm with oil flow rate 7.31 $l\,min^{-1}$ and axial load 10 kN taken from 576 x 908 pixel images.

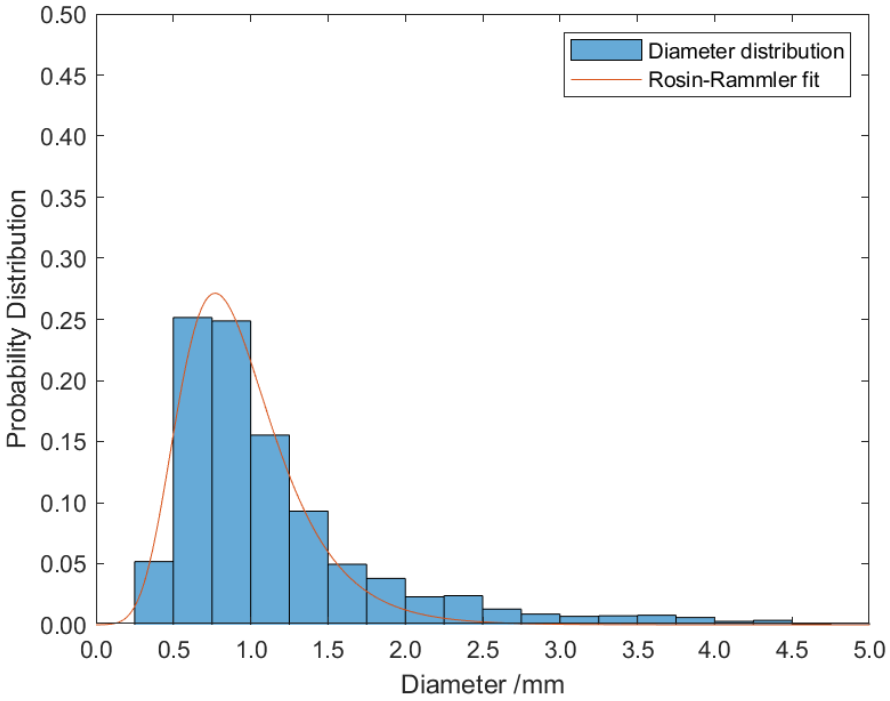


Figure A.4: Droplet diameter distribution at the 3 o'clock position at 7000 rpm with oil flow rate 7.31 $\mathrm{l\,min^{-1}}$ and axial load 10 kN taken from 576 x 908 pixel images.

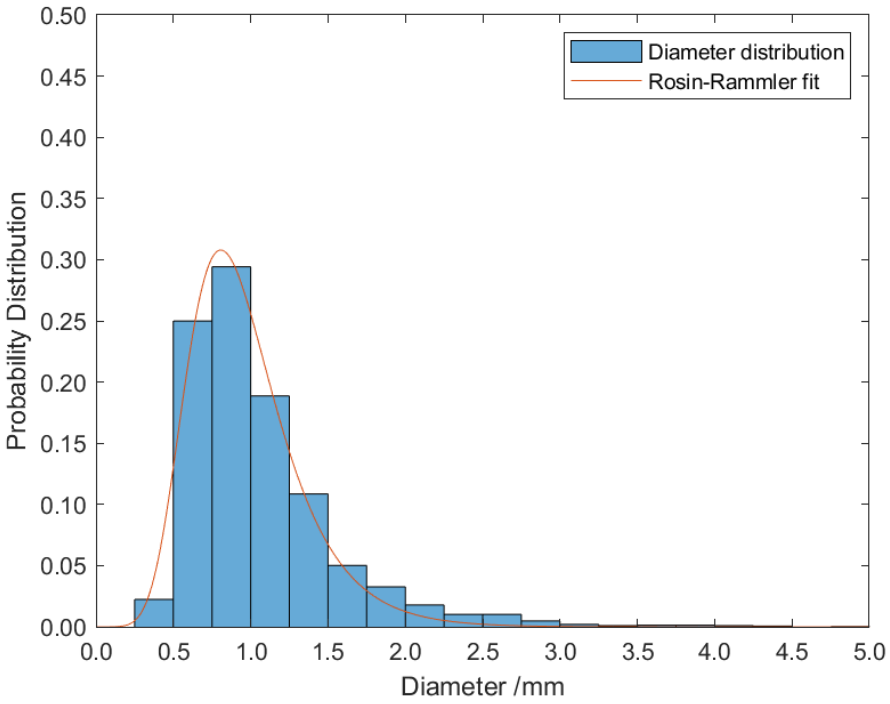


Figure A.5: Droplet diameter distribution at the 3 o'clock position at 9000 rpm with oil flow rate 7.31 $\mathrm{l\,min^{-1}}$ and axial load 10 kN taken from 576 x 908 pixel images.

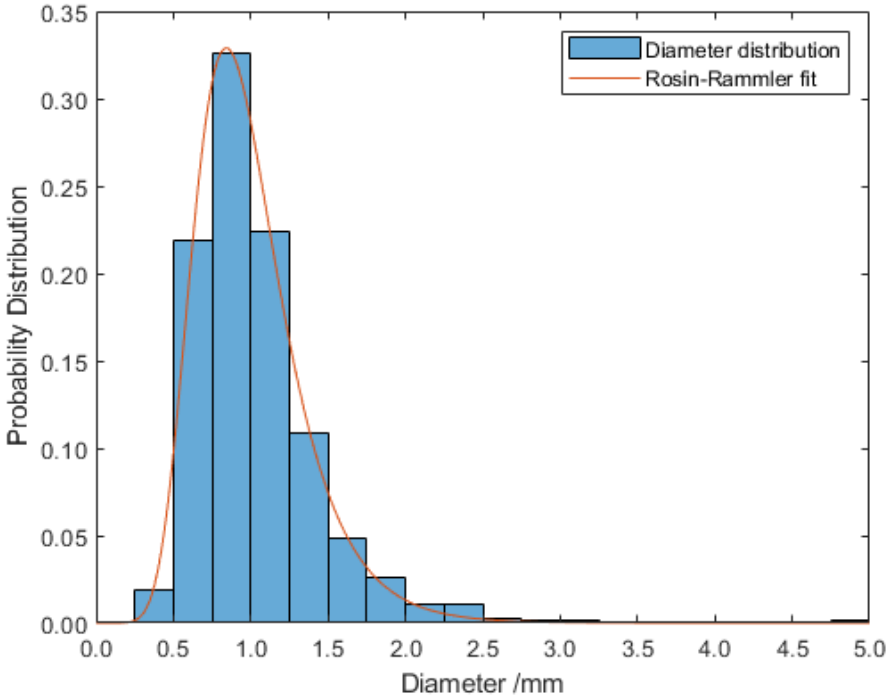


Figure A.6: Droplet diameter distribution at the 3 o'clock position at 10 000 rpm with oil flow rate 7.3 l min^{-1} and axial load 10 kN taken from 576 x 908 pixel images.

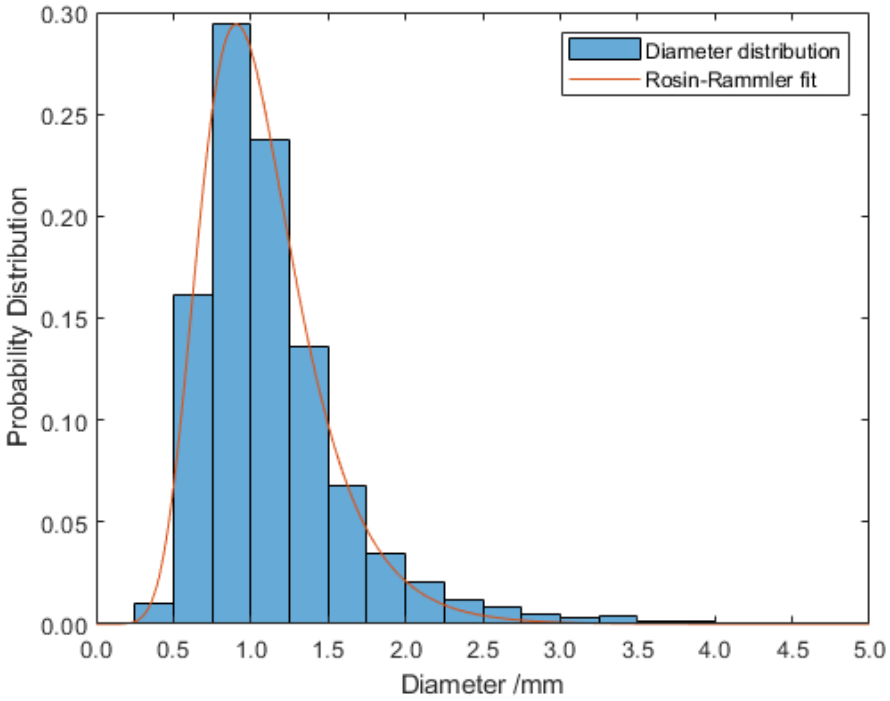


Figure A.7: Droplet diameter distribution at the 3 o'clock position at 11 000 rpm with oil flow rate 7.3 l min^{-1} and axial load 10 kN taken from 576 x 908 pixel images.

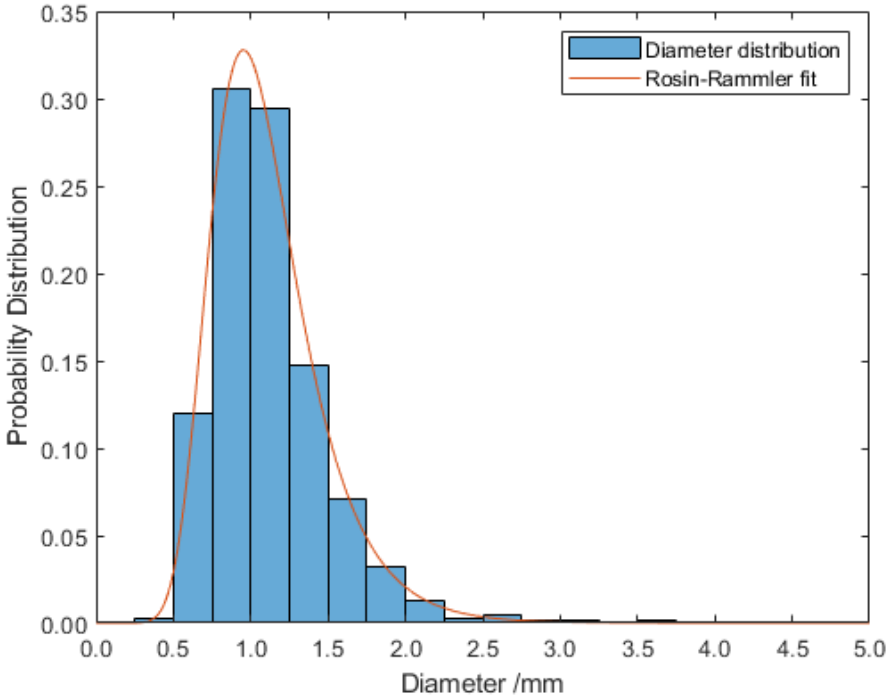


Figure A.8: Droplet diameter distribution at the 3 o'clock position at 12 000 rpm with oil flow rate 7.31 $l\,min^{-1}$ and axial load 10 kN taken from 576 x 908 pixel images.

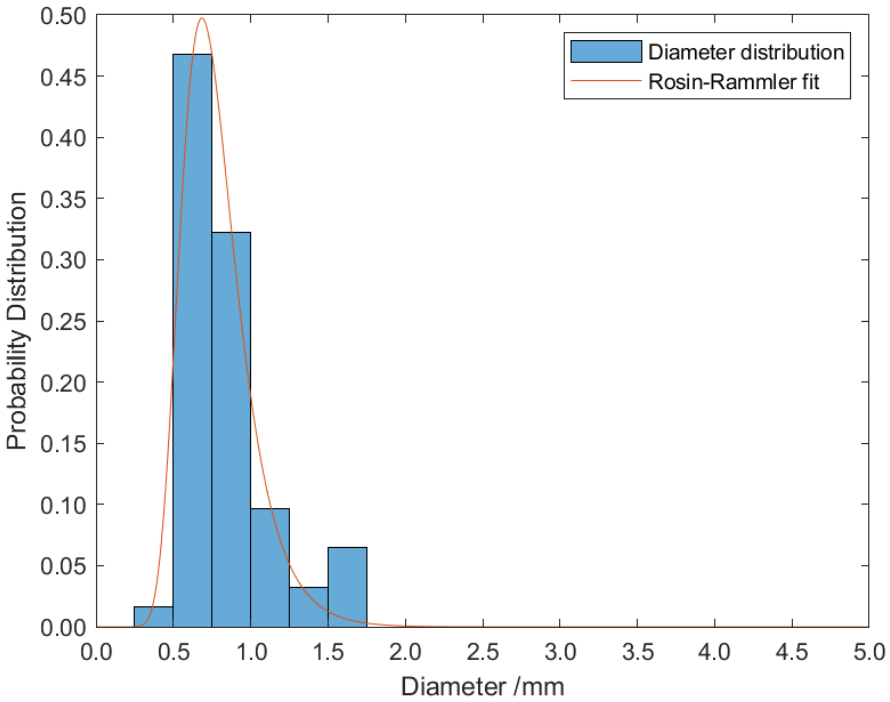


Figure A.9: Droplet diameter distribution at the 9 o'clock position at 1000 rpm with oil flow rate 7.31 $l\,min^{-1}$ and axial load 10 kN taken from 576 x 908 pixel images.

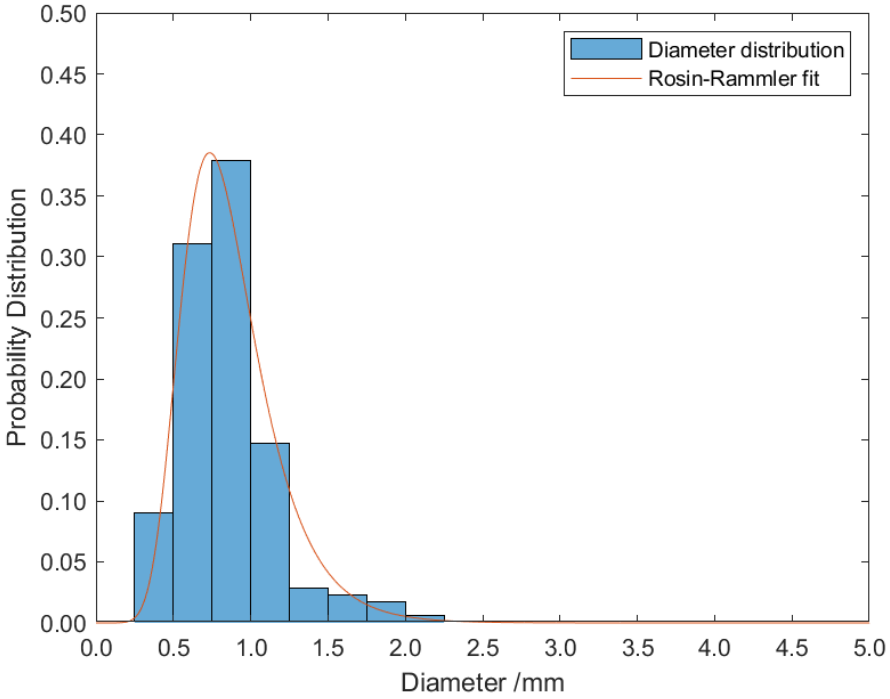


Figure A.10: Droplet diameter distribution at the 9 o'clock position at 3000 rpm with oil flow rate 7.3 l min^{-1} and axial load 10 kN taken from 576 x 908 pixel images.

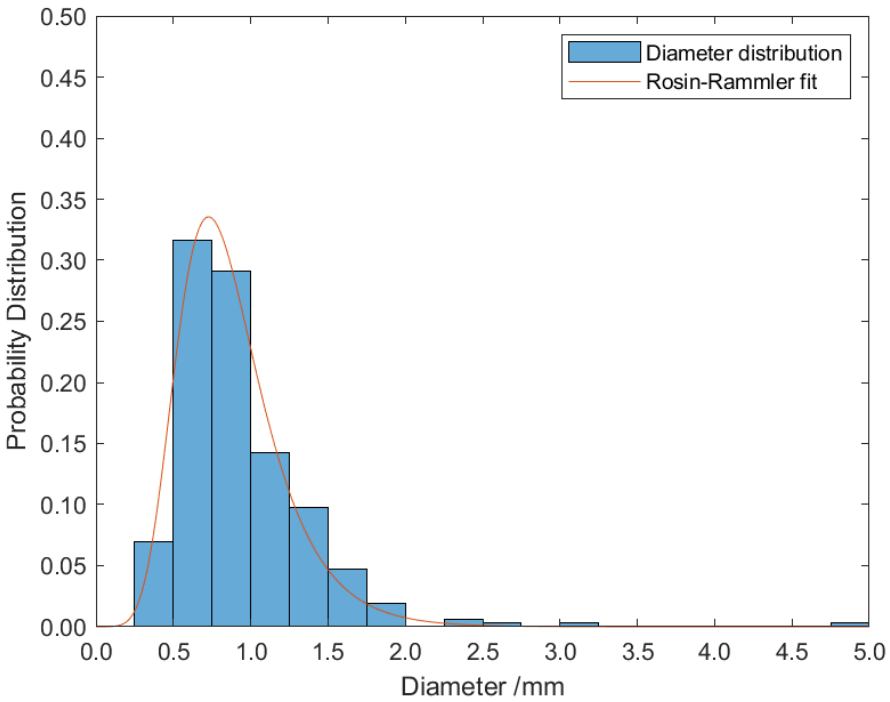


Figure A.11: Droplet diameter distribution at the 9 o'clock position at 5000 rpm with oil flow rate 7.3 l min^{-1} and axial load 10 kN taken from 576 x 908 pixel images.

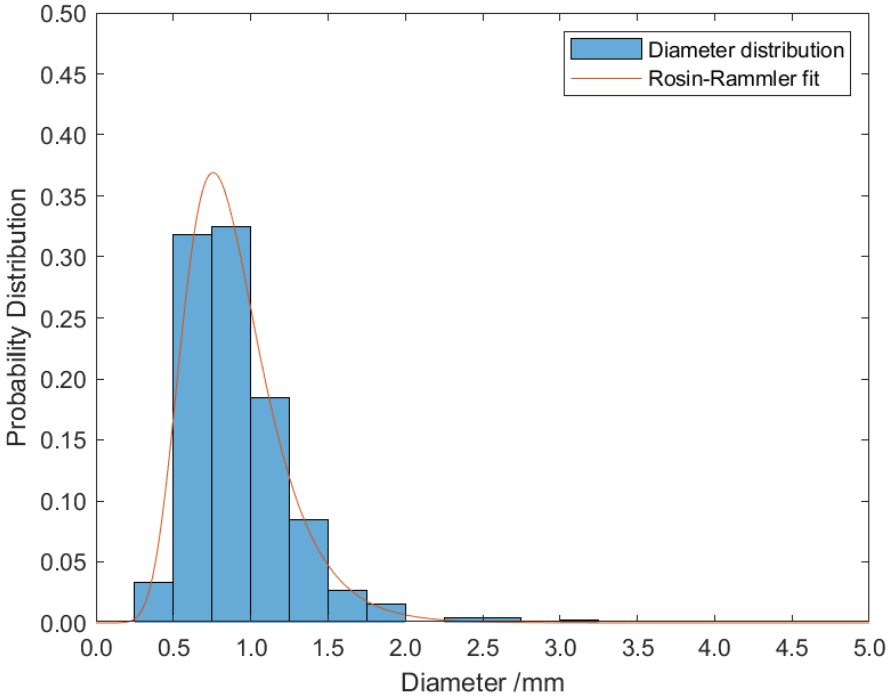


Figure A.12: Droplet diameter distribution at the 9 o'clock position at 7000 rpm with oil flow rate 7.3 l min^{-1} and axial load 10 kN taken from 576 x 908 pixel images.

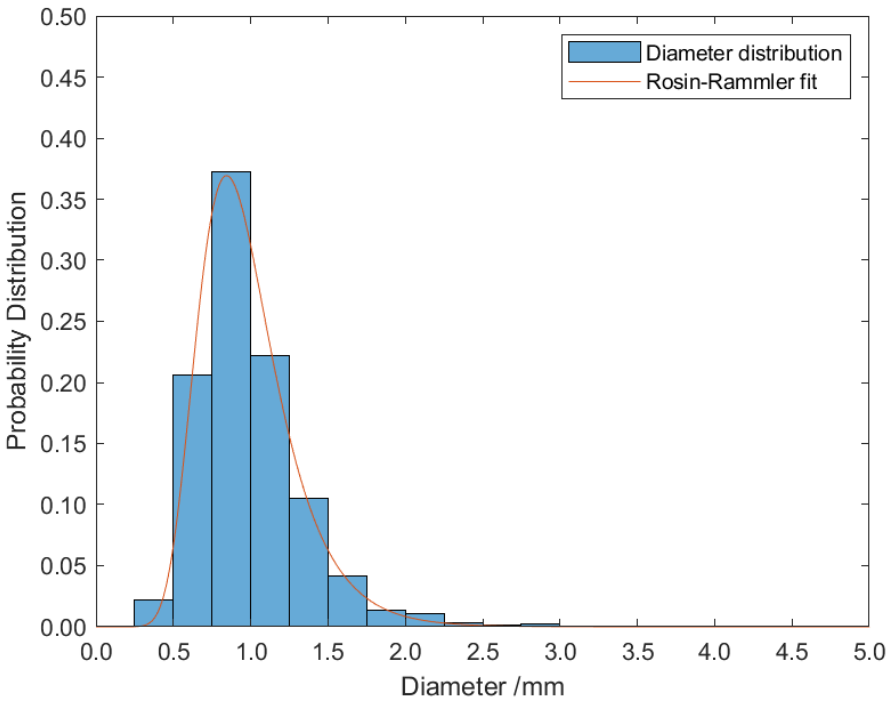


Figure A.13: Droplet diameter distribution at the 9 o'clock position at 9000 rpm with oil flow rate 7.3 l min^{-1} and axial load 10 kN taken from 576 x 908 pixel images.

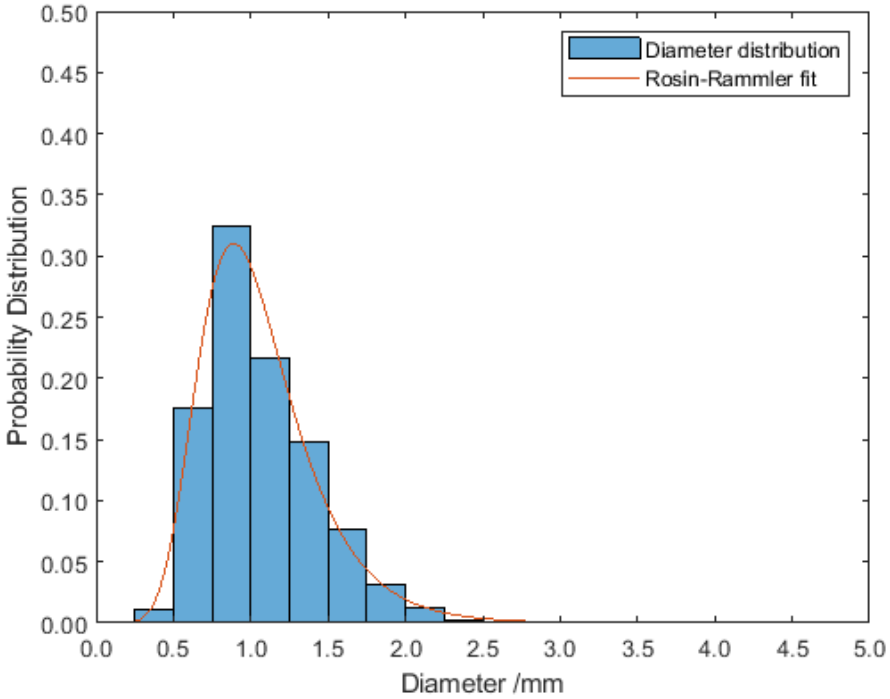


Figure A.14: Droplet diameter distribution at the 9 o'clock position at 10 000 rpm with oil flow rate 7.3 l min^{-1} and axial load 10 kN taken from 576 x 908 pixel images.

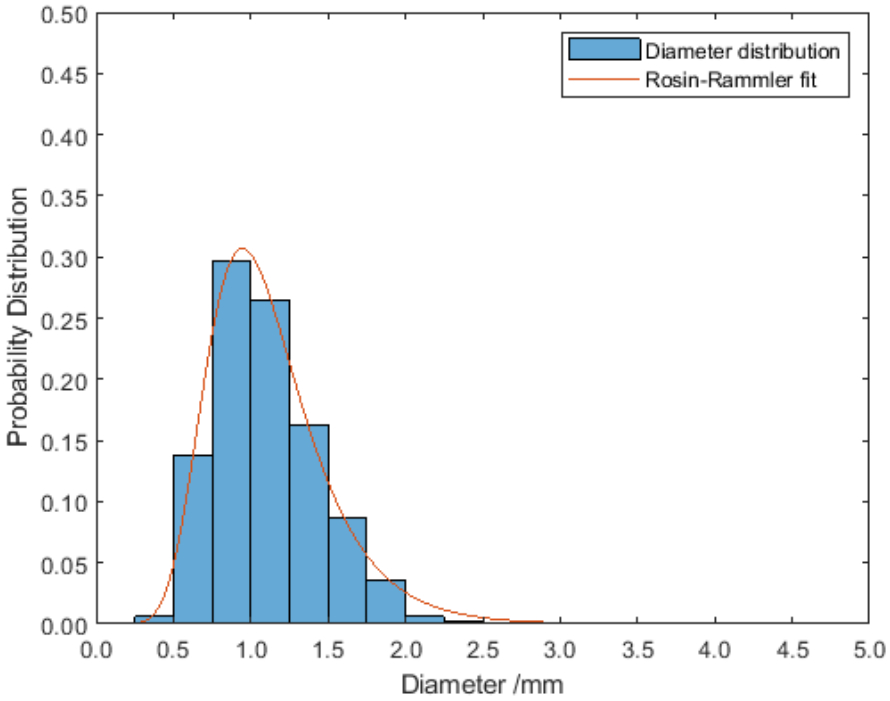


Figure A.15: Droplet diameter distribution at the 9 o'clock position at 11 000 rpm with oil flow rate 7.3 l min^{-1} and axial load 10 kN taken from 576 x 908 pixel images.

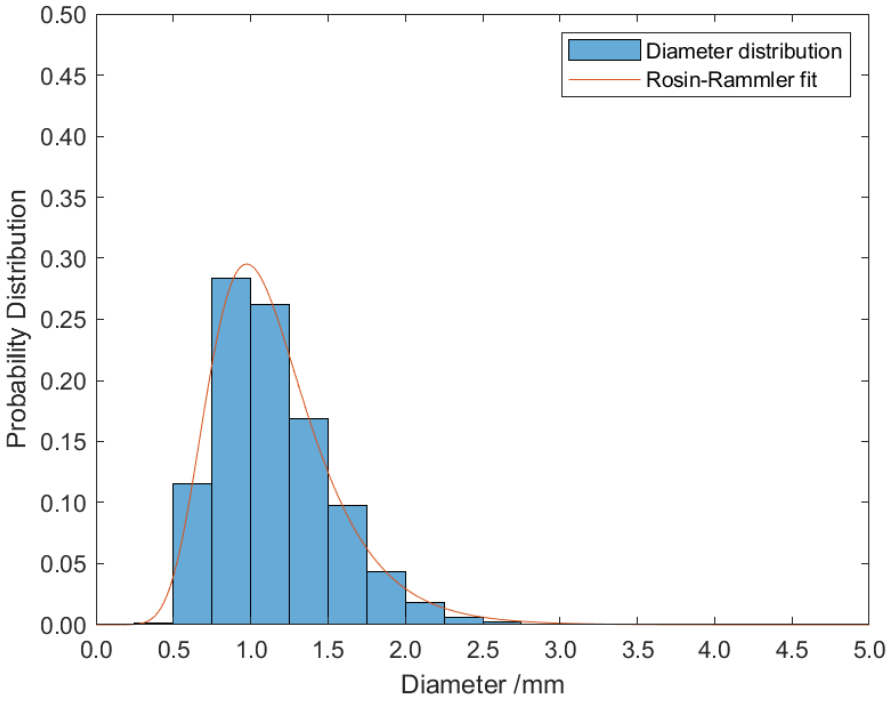


Figure A.16: Droplet diameter distribution at the 9 o'clock position at 12 000 rpm with oil flow rate 7.3 l min^{-1} and axial load 10 kN taken from 576 x 908 pixel images.

APPENDIX B

Droplet Speed Distribution

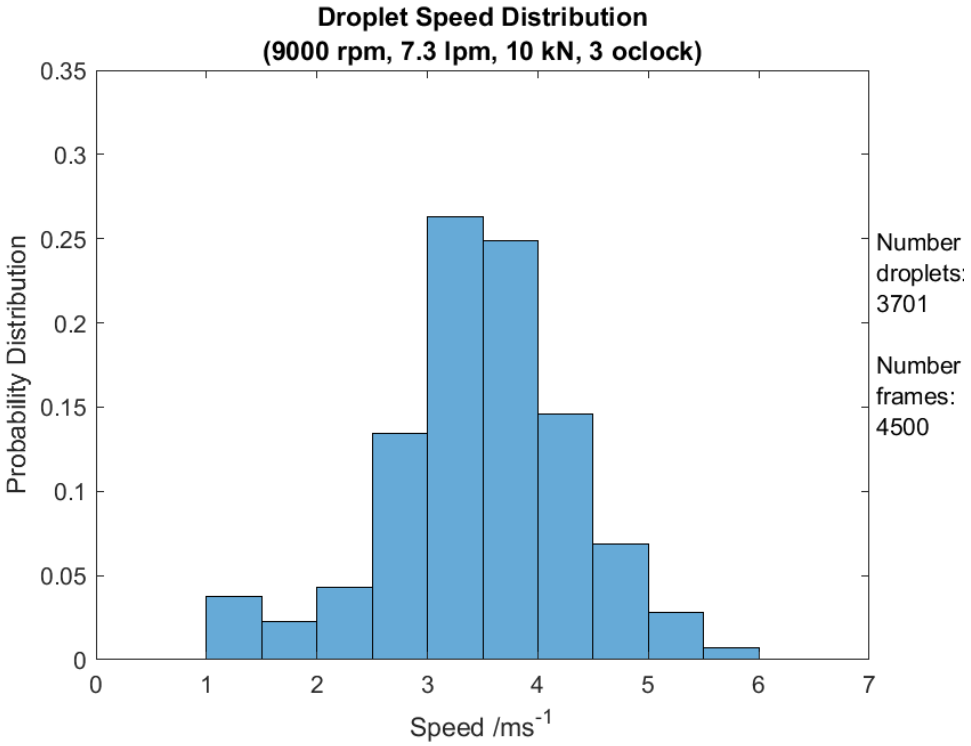


Figure B.1: Droplet speed distribution at the 3 o'clock position at 9000 rpm with oil flow rate 7.3 l min^{-1} and axial load 10 kN.

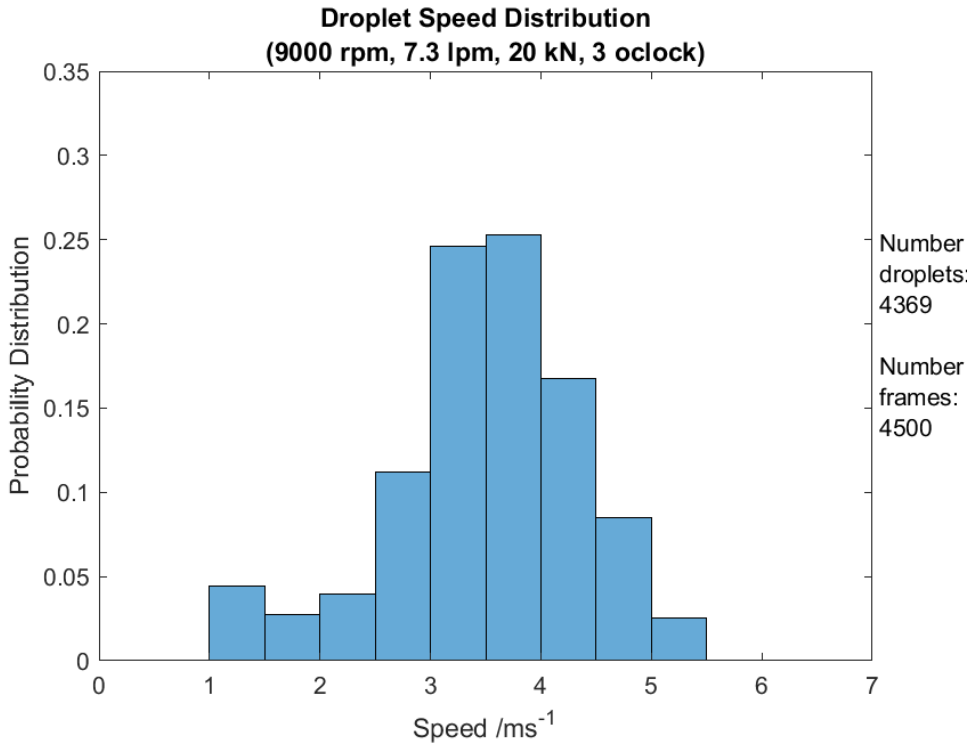


Figure B.2: Droplet speed distribution at the 3 o'clock position at 9000 rpm with oil flow rate 7.3 l min^{-1} and axial load 20 kN.

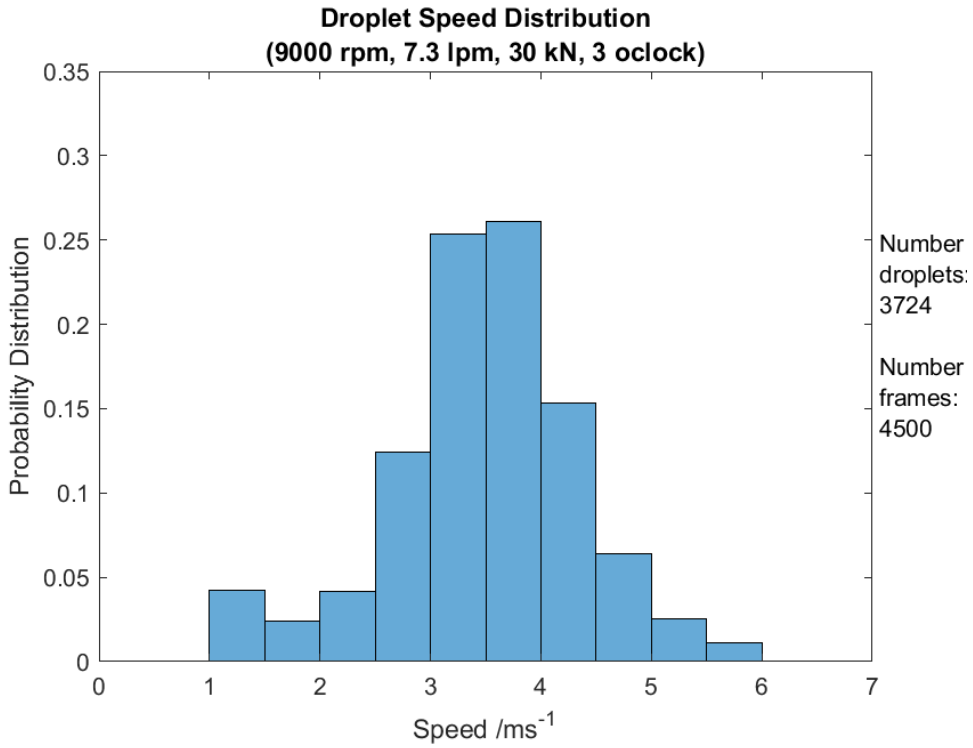


Figure B.3: Droplet speed distribution at the 3 o'clock position at 9000 rpm with oil flow rate 7.3 l min^{-1} and axial load 30 kN.

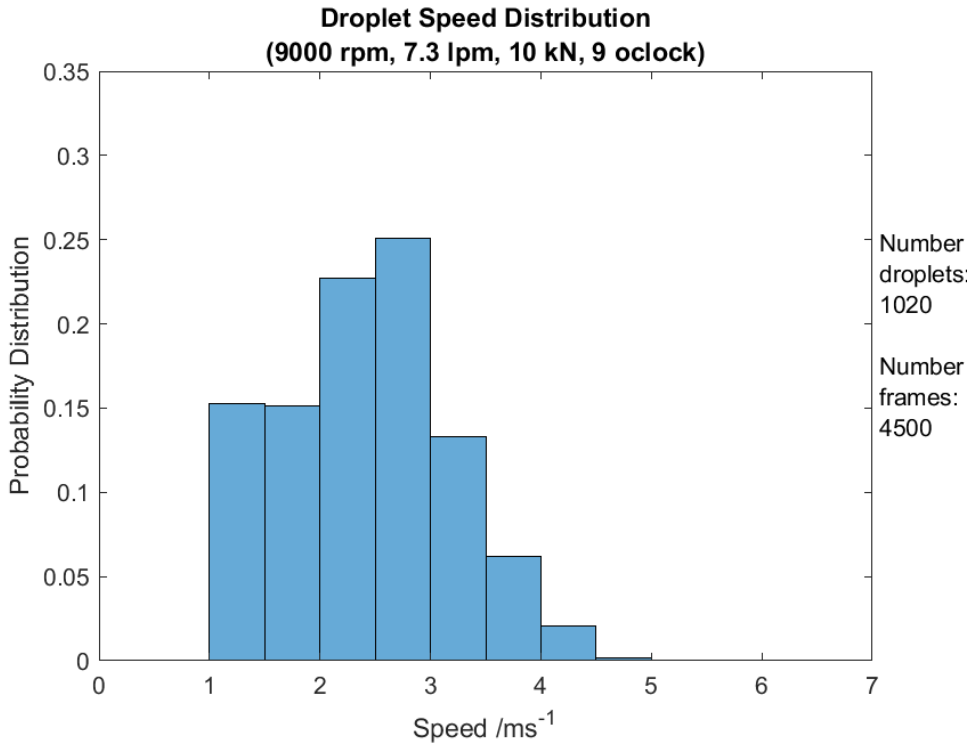


Figure B.4: Droplet speed distribution at the 9 o'clock position at 9000 rpm with oil flow rate 7.3 l min^{-1} and axial load 10 kN.

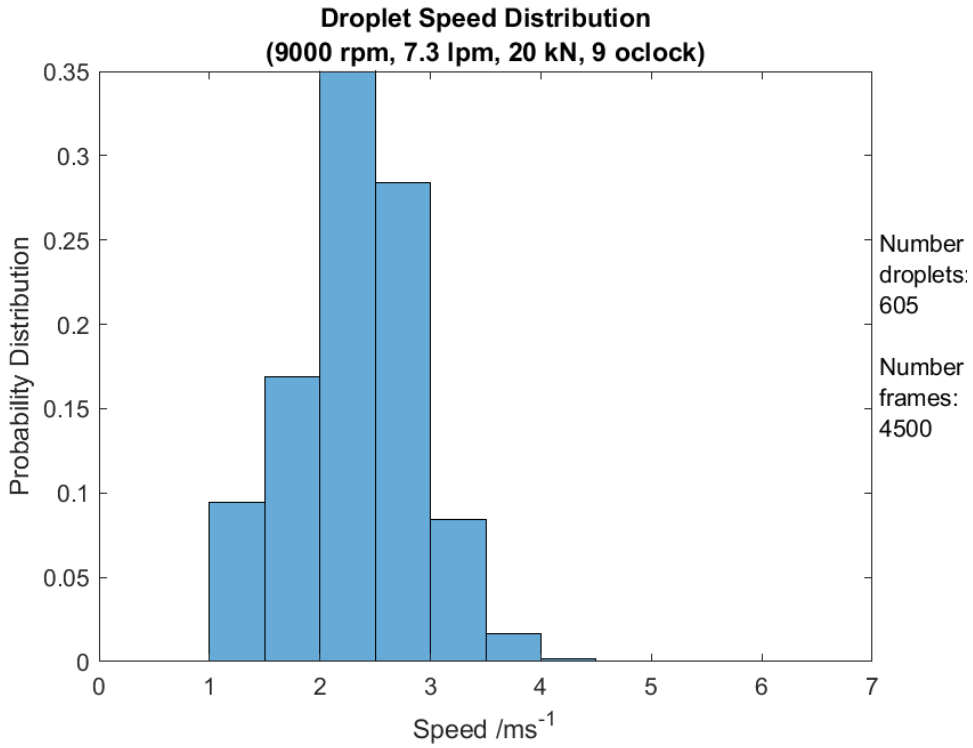


Figure B.5: Droplet speed distribution at the 9 o'clock position at 9000 rpm with oil flow rate 7.3 l min^{-1} and axial load 20 kN.

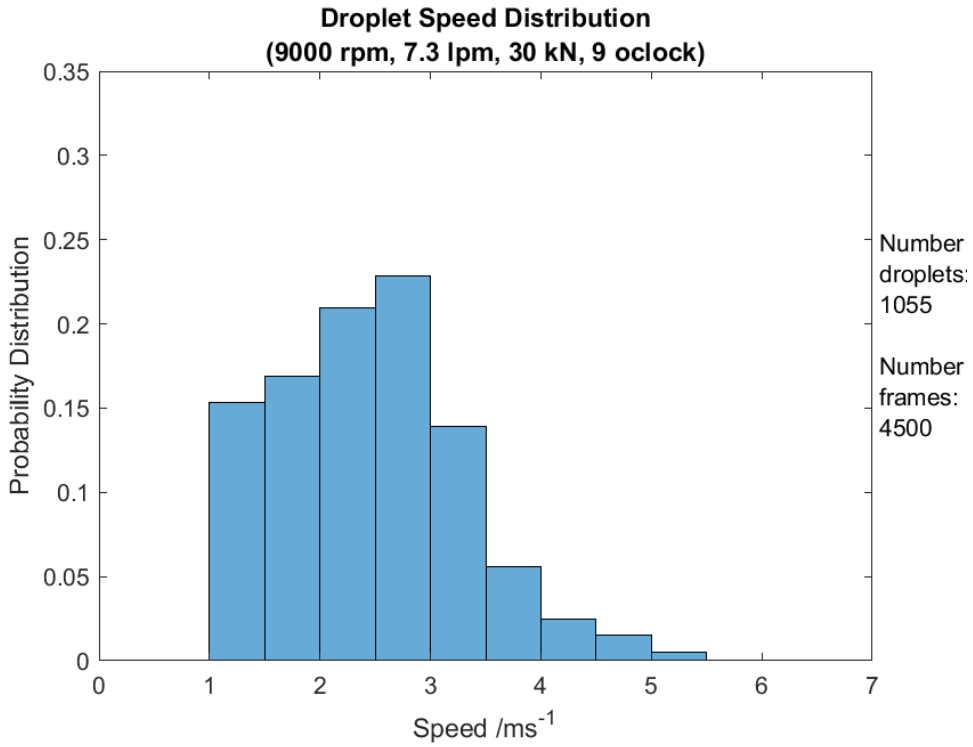


Figure B.6: Droplet speed distribution at the 9 o'clock position at 9000 rpm with oil flow rate 7.3 l min^{-1} and axial load 30 kN.